The Formation of Molecular Clouds in the Galaxy and the Small Magellanic Cloud

By

Min-Young Lee

A dissertation submitted in partial fulfillment of

the requirements for the degree of

Doctor of Philosophy

(Astronomy)

at the

UNIVERSITY OF WISCONSIN-MADISON

2013

Date of final oral examination: 05/13/13

The dissertation is approved by the following members of the Final Oral Committee:

Snežana Stanimirović, Associate Professor, Astronomy
Jay Gallagher, Professor, Astronomy
Eric Wilcots, Professor, Astronomy
Matt Haffner, Senior Scientist, Astronomy
Lisa Everett, Associate Professor, Physics
Josh Peek, Research Associate, Astronomy Columbia University

Abstract

In this thesis, I provide observational constraints on the formation of molecular clouds, precursors of star formation, by conducting high-resolution, multi-wavelength investigations of dense gas in the Galaxy and the Small Magellanic Cloud (SMC). By applying the unsharp-masking technqiue to the mid-infrared image obtained with the *Spitzer Space Telescope*, I identify 55 high-contrast regions (HCRs) in the SMC. The follow-up molecular line observations toward one of the HCRs suggest that the HCRs are likely moderately dense and trace regions where the transition from atomic to molecular hydrogen occurs in this low-metallicity galaxy.

Motivated by this result, I investigate the transition from atomic to molecular hydrogen at high resolution across the Perseus molecular cloud in the Galaxy. By deriving the atomic and molecular hydrogen column density images on sub-parsec scales, I find that the atomic gas distribution is relatively uniform across Perseus and as a result, the ratio of molecular to atomic hydrogen linearly increases with the total gas column density. These results are consistent with the theoretical perspective that formation and photodissociation of molecular hydrogen are in balance and the abundance of molecular hydrogen is controlled by the minimum gas column density required for shielding of molecular hydrogen.

Finally, I perform a detailed study of the relation between the molecular hydrogen column density and the carbon monoxide integrated intensity in Perseus and show that the ratio of the two, so called X-factor, varies spatially by up to a factor of 100. I compare the atomic/molecular hydrogen, carbon monoxide, and X-factor data with two contrasting theoretical models. I find that the steady state and equilibrium chemistry model reproduces the observations very well but requires an extended, diffuse halo around a dense core. While agreeing with the observations reasonably well, the macroturbulent and non-equilibrium chemistry model shows significant discrepancies, including a broader range of the atomic hydrogen column density and a smaller carbon monoxide integrated intensity. These discrepancies likely result from the complex spatial and kinematic structure of the gas in the macroturbulent and non-equilibrium chemistry model and require further investigations.

To my family

Acknowledgements

First, I am extremely grateful to my advisor Snežana Stanimirović. She has always been a great scientist, a caring advisor, and a dedicated educator and I cannot even describe how much I learned from her. Now as a collaborator, I am highly excited to continue our explorations of the interstellar medium and star formation in galaxies.

I would like to thank all faculty members in the department. Since I have arrived here, I have been taken care and loved. As one of few international students in the department, I couldn't go through without their warm encouragment. In particular, I would like to give special thanks to Jay Gallagher and Ellen Zweibel for their continuous interest and strong support. Also, I would like to express my heartfelt thanks to Bob Bless, Joe Cassinelli, Ed Churchwell, John Mathis, Ken Nordsieck, Ron Reynolds, and Blaire Savage. You showed me how exciting astronomy is and how to pursue it with both passion and dedication. You have been such a great inspiration for me and I will always keep what I learned from you in my heart. I have always felt that I am extremly privileged to be part of this department. If I did accomplish anything, that is only because I have been here in Madison.

I would like to give big thanks to Ayesha Begum, Bob Benjamin, John Everett, Matt Haffner, Tae-Sun Kim, Brian Morsony, and Barb Whitney. I have always benefited from discussions with them and greatly appreciate their energy that has made the department more energetic. They have been extremely friendly and approachable and conversations with them have helped me a lot nurture communication skills. I am also grateful to our administrative staffs, Steve Anderson, Angela Normington, Sheri Pittman, Aaron Teche, and Gary van Ryzin for their help. In particular, my deepest thanks go to Stephan Jansen, who had taken care of my linux machines and personal laptops throughout my time in the department.

Thanks to all graduate students in the department for being such good friends. In particular, I give my thanks to Claudia Cyganowski, Ryan Keenan, Hyeseung Lee, Matt Povich, Jennifer Stone, and Doosoo Yoon for offering a kind word and an understanding ear. And as a member of the same research group, I have really enjoyed my time with Lou Nigra and Claire Murray. Sharing the same passion and interest, I have learned a lot from them and deeply appreciate their heart-warming words. My warmest thanks also go to Blakesley Burkhart, who is an extremely inspiring women and a good collegues. I am looking forward to working on research projects together as co-workers. I have also been tremendously lucky to have Paul Sell and Isak Wold in the same class at school. I have had so much fun with them and will keep those good

memories wherever I go. And Ann, I cannot even describe how much I feel appreciated and honored to have you around me in the last couple years. You have been such a great friend, a thoughtful mentor, and a strong scientist. I will always remember what I learned from you and do my best to follow the footstep of you as a fine example of a good radio astronomer.

Thanks to all my collaborators for their brilliant insights and suggestions. In particular, I would like to give my deepest thanks to the GALFA-HI survey team, Kevin Douglas, Steven Gibson, Jana Grcevich, Carl Heiles, Eric Korpela, Josh Peek, Mary Putman, and Destry Saul. Since I have arrived here, I have learned so much from them and am so proud of being a member of such a great survey team. The GALFA-HI rocks!

And above all, thanks to my family. Without your support, patience, and love, I couldn't make it through. This is as much your accomplishments as mine.

Contents

List of Tables

List of Figures

Chapter 1

Introduction

Molecular clouds are unique places in the Universe. At small scales, they are nurseries for stars and planets. A cold and dense molecular cloud fragments into smaller cores and each core collapses inward due to its strong gravity. As the core collapses, it spins faster and flattens into a disk with a central bulge. The bulge eventually changes into a star and planets form within the disk through the progressive agglomeration of gas, ices, and dust grains. The formed star and planets make up a planetary system such as our Solar System. At large scales, on the other hand, molecular clouds play a significant role in the evolution of baryonic matter in galaxies. The massive stars formed in molecular clouds inject a large amount of energy via intense radiation fields, strong stellar winds, and powerful supernovae explosions, ungratefully destroying their parent clouds. At the same time, the material sent back to the interstellar medium, including heavy elements fused inside the stars, is used for new generations of molecular cloud and star formation.

Since the first surveys of Galactic molecular clouds in the rotational transition of carbon monoxide (CO) at 2.6-mm wavelength (e.g., Scoville & Solomon 1975; Gordon & Burton 1976; Cohen & Thaddeus 1977), the developement of large and sensitive (sub-)millimeter telescopes, e.g., the Owens Valley Radio Observatory (OVRO) interferometer, the Berkeley-Illinois-Maryland Association (BIMA) array, the Nobeyama Radio Observatory (NRO) 45-m, the Institut de Radio Astronomie Millimétrique (IRAM) 30-m, the James Clerk Maxwell Telescope (JCMT) 15-m, etc., have enabled us to investigate the properties of molecular clouds in Local Group galaxies at spatial scales of $\lesssim$ 50 pc (e.g., Fukui & Kawamura 2010), as well as to make remarkable progress in the study of gas content of high-redshift galaxies (e.g., Carilli & Walter 2013). Despite these dramatic advances, however, some fundamental questions remain to be fully answered:

1. What are the physical processes responsible for the formation of molecular clouds?
2. How much are the formation and evolution of molecular clouds influenced by the global and local conditions in galaxies?
3. What is the role of stellar feedback in the formation and evolution of molecular clouds?
4. What is the link between the physical, chemical, and dynamical properties of molecular clouds and star formation?

This thesis focuses on the first three questions.

In this chapter, I summarize previous observational and theoretical efforts made toward the understanding of molecular clouds. I review the physical and dynamical properties of molecular clouds in Sections 1.1.1 and 1.1.2 and focus on the formation of the most abundant molecular speices in the Universe, molecular hydrogen (H_2), in Section 1.1.3. I then provide a detailed discussion of the "CO-to-H_2 conversion factor" or "X-factor", widely used for inferring the properties of molecular clouds, in Section 1.1.4. Next, I summarize two main theoretical perspectives on the origin and lifetime of molecular clouds in Section 1.2. Finally, I finish the chapter by providing an overview of this thesis in Section 1.3.

1.1 Observed Properties of Molecular Clouds

1.1.1 Physical Properties

Molecular clouds correspond to the coldest ($T \lesssim 10$ K) and densest ($n \gtrsim 100$ cm^{-3}) phase of the interstellar medium, composed of mainly H_2 with additional contributions from He ($\sim$36%) and dust grains ($\sim$1%). The typical size of molecular clouds ranges from $\sim$50 pc to several hundred parsecs and their mass ranges from $\sim 10^4$ M$_\odot$ to $\sim 10^7$ M$_\odot$ (e.g., Fukui & Kawamura 2010). The mass distribution of molecular clouds has been observed to have a power-law distribution with a sharp cutoff:

$$\frac{dN}{d\ln M} \propto \left(\frac{M_{\rm u}}{M}\right)^{\alpha}, \tag{1.1}$$

where N is the number of molecular clouds and $M_{\rm u}$ is the upper mass limit. For molecular clouds inside the solar circle, $M_{\rm u} = 6 \times 10^6$ M$_\odot$ and $\alpha = 0.6$ were derived (Williams & McKee 1997). Observations of most Local Group galaxies have found similar mass distributions (e.g., Engargiola et al. 2003; Leroy et al. 2006; Rosolowsky 2007; Fukui et al. 2008; Figure 1.1). The implications of this fairly similar mass distribution are as follows. First, most of the molecular gas is contained in massive clouds ($\gtrsim 80$% in clouds with $M \gtrsim 10^5$ M$_\odot$), while numerically most clouds are of low-mass. Second, the upper limit of the mass distribution is sharp, suggesting a physical limit to cloud formation or destruction processes.

A close look at individual molecular clouds reveals that they are remarkably filamentary. For example, the K-band extinction image of the Taurus, Perseus, and California molecular clouds shows that they have indeed highly irregular shapes (Figure 1.2). When the distribution of total gas column density is measured, however, molecular clouds share surprisingly similar properties. Studies of Galactic molecular clouds have found that the probability distribution function (PDF) of total gas column density (traced by either dust

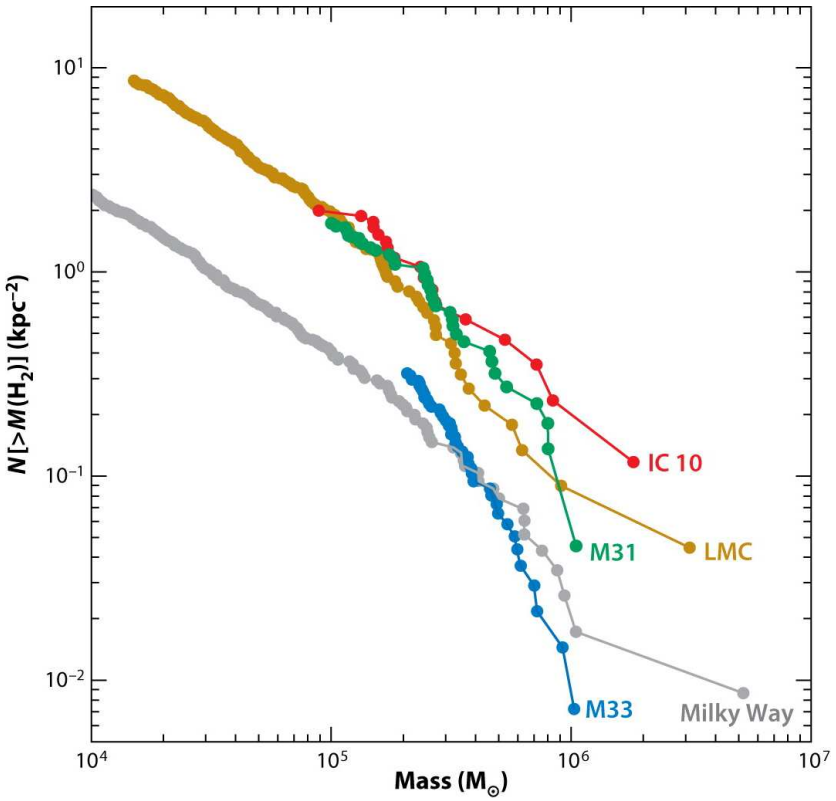

Fig. 1.1. — Cumulative mass distributions of molecular clouds in the Galaxy, the Large Magellanic Cloud (LMC), IC10, M31, and M33 (Fukui & Kawamura 2010).

extinction at near-infrared (NIR) wavelengths or dust emission at far-infrared (FIR) wavelengths) is close to a lognormal function at small column densities ($A_V \lesssim 3$–5 mag), while showing a non-lognormal wing at large column densities ($A_V \gtrsim 3$–5 mag) (e.g., Lombardi et al. 2008; Kainulainen et al. 2009; Schneider et al. 2012). The lognormal column density PDF has been traditionally attributed to cloud internal supersonic turbulence (e.g., Vázquez-Semadeni 1994; Ostriker et al. 1999; Federrath et al. 2008), although it has been recently pointed out that several different physical processes can reproduce the observed column density PDF (Tassis et al. 2010). The non-lognormal wing, on the other hand, was found almost exclusively among star-forming molecular clouds (Figure 1.2). A detailed analysis showed that dense clumps correponding to the non-lognormal wing are confined by the external pressure from their diffuse surroundings (Kainulainen et al. 2011). In addition, the amount of mass at $A_V \gtrsim 3$–5 mag is highly correlated with the star formation rate, suggesting that pressure-confined clumps are a prerequisite for star formation. Similar thresholds for star formation, $A_V \gtrsim 7$–8 mag, have been proposed by other studies of young stellar objects (YSOs) in Galactic molecular clouds (Heiderman et al. 2010; Lada et al. 2010).

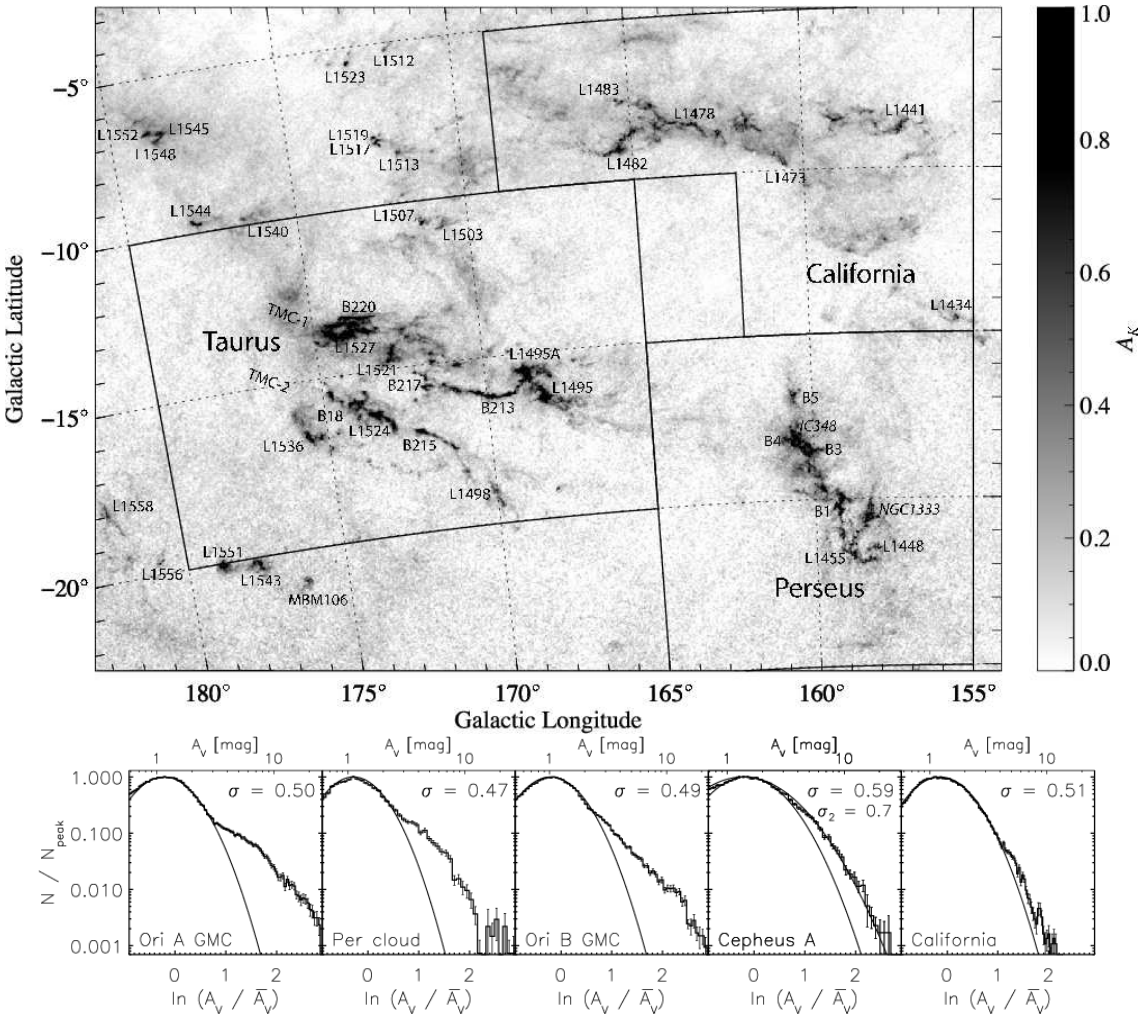

Fig. 1.2. — (Top) The K-band extinction image of the Taurus, Perseus, and California molecular clouds (Lombardi et al. 2010). (Bottom) The probability density functions (PDFs) of a normalized column density for the Orion, Perseus, Cepheus A, and California molecular clouds (Kainulainen et al. 2009). Note that non-lognormal wings are most prominent for active star-forming clouds such as Orion and Perseus.

1.1.2 Dynamical Properties

Molecular clouds appear to share their dynamical properties as well as internal structure. In his seminal paper, Larson (1981) summarized three fundamental dynamical properties of molecular clouds, which are often referred to as "Larson's laws".

(1) *The first law*: molecular clouds obey a linewidth-size relation such that their velocity dispersion, commonly measured by the width of molecular spectral lines, increases as a power of the cloud size. For molecular clouds in the solar circle, Solomon et al. (1987) found

$$\sigma_{\rm v} = (0.72 \pm 0.07) R_{\rm pc}^{0.5\pm0.05} \text{ km s}^{-1}, \tag{1.2}$$

where $R_{\rm pc}$ is the cloud radius in pc. Bolatto et al. (2008) found a similar relation, $\sigma_{\rm v} = 0.44^{+0.18}_{-0.13} {R_{\rm pc}}^{0.60\pm0.10}$ km s^{-1}, for molecular clouds in a number of external galaxies (Figure 1.3). Interestingly, this cloud-to-cloud relation holds for sub-structure within individual clouds as well (Heyer & Brunt 2004), suggesting that there is no preferred length scale for the relation. All these results have been interpreted mainly as the presence of universal turbulence in molecular clouds.

(2) *The second law*: molecular clouds are gravitationally bound such that their virial parameter,

$$\alpha_{\rm vir} = \frac{5\sigma_{\rm v}^2 R}{G M_{\rm vir}}, \tag{1.3}$$

is $\sim$1 (G = the gravitational constant and $M_{\rm vir}$ = the virial mass). However, deriving $\alpha_{\rm vir}$ is nontrivial due to the uncertainty in the measurements of cloud mass and radius (e.g., Maloney 1990; Heyer et al. 2001, 2009) and other effects missing in Equation (1.3) such as magnetic fields and projection effects (e.g., Shetty et al. 2010). In addition, recent large-scale simulations of molecular clouds in spiral galaxies, where the formation of molecular clouds is regulated by cloud-cloud collisions and stellar feedback, have found that most parts of molecular clouds are gravitationally unbound (e.g., Dobbs et al. 2011). The question whether molecular clouds are in virial equilibrium or not is deeply related with the physical processes involved in the formation of molecular clouds (Section 1.2) and still under debate.

(3) *The third law*: molecular clouds have similar mean column densities. For the molecular clouds considered by Solomon et al. (1987), the mean column density is $\langle N({\rm H}) \rangle = (1.5 \pm 0.3) \times 10^{22} R_{\rm pc}^{0.0\pm0.1}$ or

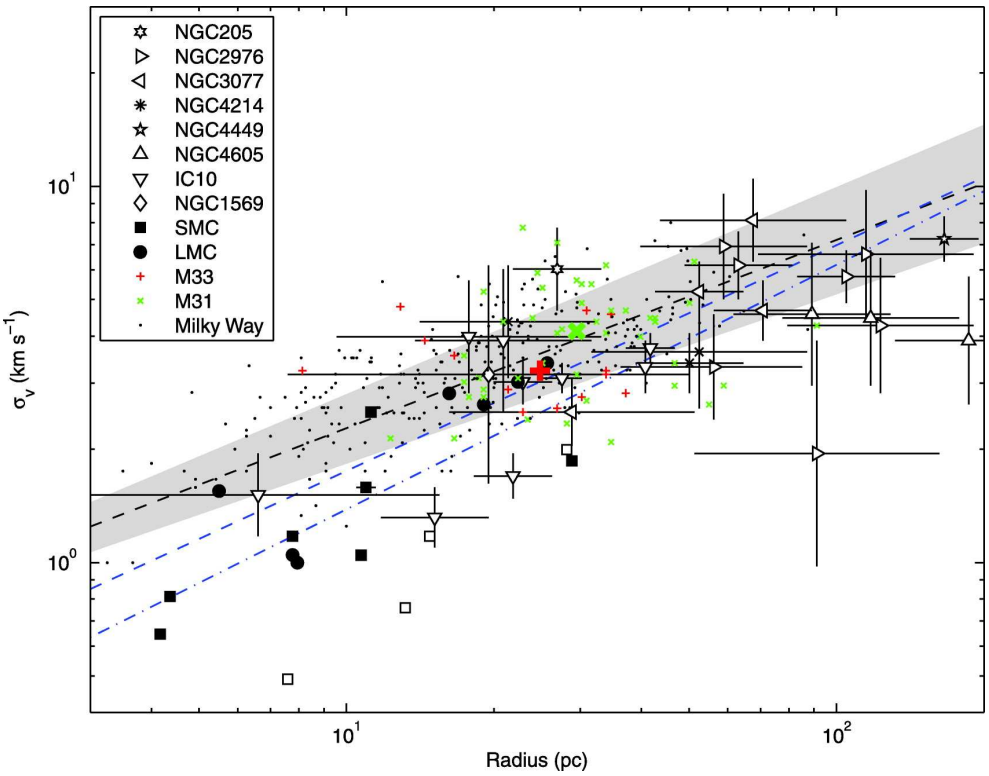

Fig. 1.3. — Extragalactic linewidth-size relation (Bolatto et al. 2008). The open and filled symbols indicate measurements based on CO($J = 1 \rightarrow 0$) and CO($J = 2 \rightarrow 1$) observations. The black dashed line and the grey area illustrate the relation for the Galaxy found by Solomon et al. (1987), $\sigma_{\rm v} = (0.72 \pm 0.07) {R_{\rm pc}}^{0.5\pm0.05}$. The relation for the sample of extragalactic molecular clouds, $\sigma_{\rm v} \sim 0.44 R_{\rm pc}^{0.60}$ km s^{-1}, is shown as the blue dashed line. Finally, the blue dot-dashed line indicates the fit to the dwarf galaxies only.

surface density $\langle\Sigma\rangle \sim 170$ M$_\odot$ pc^{-2}. A recent study using higher resolution and better sensitivity data of the Galaxy found a slightly smaller value, $\langle\Sigma\rangle \sim 80$–$120$ M$_\odot$ pc^{-2} (Heyer et al. 2009), and this is consistent with the extragalactic study by Bolatto et al. (2008).

It is important to note that Larson's three laws are not independent. If the linewidth-size relation is expressed as $\sigma_{\rm v} = \sigma_{\rm v,pc} R_{\rm pc}^{0.5}$, then the following equation relates all three scaling relations (McKee & Ostriker 2007):

$$\alpha_{\rm vir} = \left(\frac{5}{\pi \text{ pc}}\right) \frac{\sigma_{\rm v,pc}^2}{G\Sigma} = 3.7 \left(\frac{\sigma_{\rm v,pc}}{1 \text{ km s}^{-1}}\right)^2 \left(\frac{100 \text{ M}_\odot \text{ pc}^{-2}}{\Sigma}\right). \quad (1.4)$$

Indeed, the relatively uniform observed normalization factor, $\sigma_{\rm v,pc} \sim 1$ (Equation 1.2), implies that Σ is similar for molecular clouds with $\alpha_{\rm vir} \sim 1$.

1.1.3 The Formation of Molecular Hydrogen

As the most dominant constituent, H_2 plays a central role in determining the chemical and physical properties of molecular clouds. The presence of H_2 in the interstellar medium was first indicated by rich absorption spectra at far-ultraviolet (FUV) wavelengths (e.g., Spitzer & Jenkins 1975; Figure 1.4). The absorption spectra were obtained toward early-type stars using the *Copernicus* telescope and the measured H_2 column densities showed a sharp increase at the color excess of $E(B-V) \sim 0.1$ mag (Figure 1.4). With the total-to-selective extinction ratio of $R_V = 3.1$ for the diffuse interstellar medium (Mathis 1990), $E(B-V) \sim 0.1$ mag corresponds to $A_V \sim 0.3$ mag. This observed threshold for H_2 was consistent with theoretical models where H_2 formation on dust grains is in equilibrium with H_2 photodissociation by FUV photons and H_2 remains shielded by absorption in the H_2 lines ("self-shielding") and grain extinction ("dust shielding") (e.g., Hollenbach et al. 1971; Jura 1975; Black & Dalgarno 1977). Further FUV absorption measurements using more background sources (stars + AGNs) have confirmed the previous results: the H_2 fraction, $f = 2N(H_2)/(N(HI) + 2N(H_2)$ undergoes a transition from $\sim 10^{-5}$ to $\gtrsim 10^{-2}$ at $N(H) \sim$ (3–5) $\times$ 10^{20} cm^{-2} in the Galaxy (e.g., Savage et al. 1977; Rachford et al. 2002; Gillmon et al. 2006).

As a homonuclear diatomic molecule, however, H_2 lacks a permanent electric dipole moment and even the lowest (electric quadrupole) rotational transitions require temperatures and densities much higher than those found in typical molecular clouds. Therefore, the presence of H_2 in individual molecular clouds has been inferred by indirect measurements. For example, FIR observations of interstellar clouds have found a significant deviation from a linear relation between the 100 μm intensity and the HI column density at $N(HI) \gtrsim 4 \times 10^{20}$ cm^{-2} (e.g., Reach et al. 1994; Douglas & Taylor 2007). In addition, comparisons between the HI column density and other molecular gas tracers (e.g., CO, OH, dust extinction) have shown that $N(HI)$ saturates to a few $\times$ 10^{20} cm^{-2} for high values of total hydrogen column density $N(H)$ deduced by the tracers (e.g., Knapp 1974; Sancisi et al. 1974; Gir et al. 1994; Williams & Maddalena 1996; Barriault et al. 2010a,b). All these results suggest that much of the hydrogen in molecular clouds is in molecular form above the threshold column density $N(H) \sim N(HI) \sim$ a few $\times$ 10^{20} cm^{-2}, which is consistent with the results from the FUV absorption studies of individual lines of sight through the Galaxy.

The saturation of $N(HI) \sim$ a few $\times$ 10^{20} cm^{-2} or $\Sigma_{HI} \sim 10$ M$_\odot$ pc^{-2} has been found in external galaxies at kpc-scales (e.g., Martin & Kennicutt 2001; Wong & Blitz 2002; Blitz & Rosolowsky 2004, 2006; Bigiel et al. 2008; Wong et al. 2009; Schruba et al. 2011; Figure 1.5). While having poor spatial

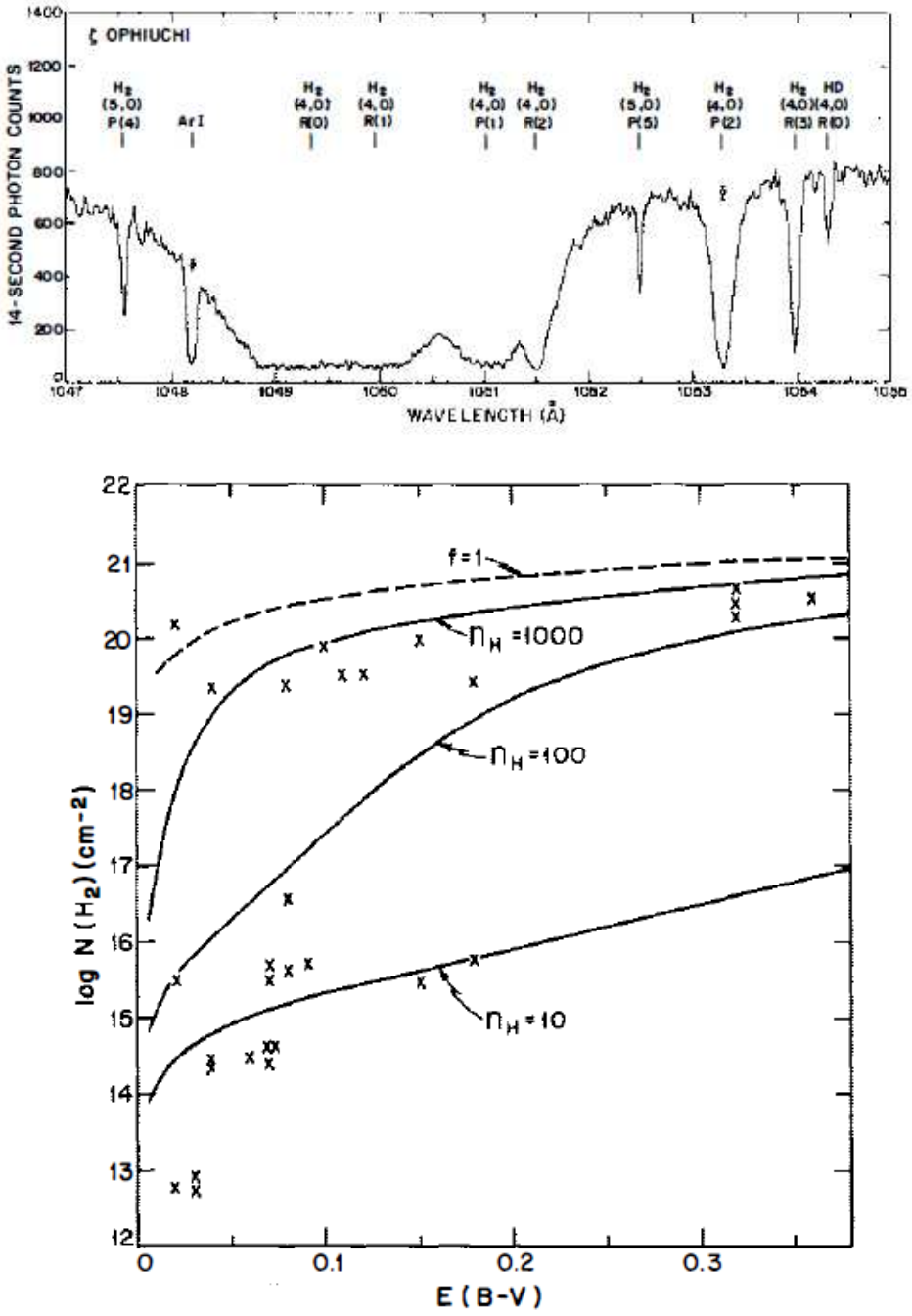

Fig. 1.4. — (Top) The FUV spectrum obtained toward the O9.5 V-type star ζ Oph using the *Copernicus* telescope (Spitzer & Jenkin 1975). The wavelengths of various rotational transitions in the Lyman bands for H_2 and HD are indicated by the vertical lines. (Bottom) H_2 column densities plotted against color excesses (Spitzer & Jenkins 1975). With a dust-to-gas ratio of $N(\mathrm{H})/E(B-V) = 1.6 \times 10^{-22}$ cm^{-2} mag (Jenkins & Savage 1974), the dashed curve represents $2N(\mathrm{H_2}) = N(\mathrm{H})$ (fully molecular gas). The three solid curves are theoretical predictions from Hollenbach et al. (1971) calculated based on the balance between H_2 formation on dust grains and H_2 dissociation by FUV photons.

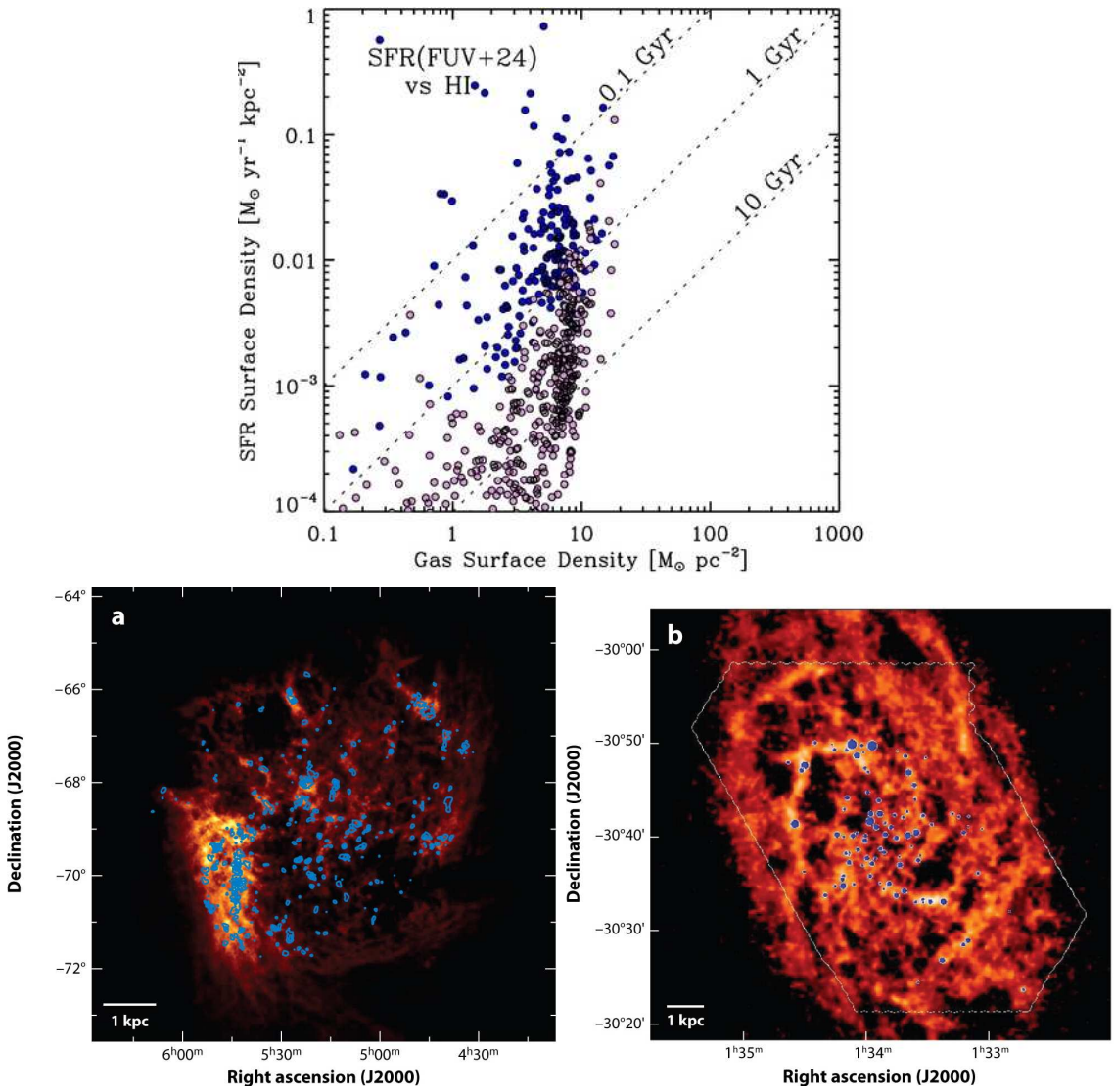

Fig. 1.5. — (Top) The surface densities of star formation rate derived for 33 nearby galaxies are plotted against HI surface densities (Schruba et al. 2011). Each circle represents a value averaged over some radial extent and the HI-dominated and H_2-dominated regions are shown in light red and dark blue symbols. Note a sharp saturation of $\Sigma_{\rm HI} \sim 10$ $M_\odot$ pc^{-2}. (Bottom) The HI integrated intensity images of the LMC (Left) and M33 (Right). To indicate the locations of molecular clouds, CO emission is overlaid in the case of the LMC, while blue circles whose areas are scaled to CO integrated intensities are shown for M33 (Fukui & Kawamura 2010).

resolution for detailed studies, extragalactic observations offer a unique view of the large-scale distribution of molecular clouds. For example, the CO and HI images of two face-on galaxies in the Local Group, the Large Magellanic Cloud (LMC) and M33, clearly show a strong correlation between the atomic and molecular gas (Figure 1.5). Almost all molecular clouds in these galaxies are located in bright HI filaments but the reverse is not true: there are many bright HI filaments without any association with molecular clouds. This suggests that HI is required but not a sufficient condition for the formation of molecular clouds. In addition, the fact that HI is much more widespread than CO implies that molecular clouds are formed out of HI, rather than HI being primarily a dissociation product of molecular clouds, as some have previously argued (e.g., Allen 2001; Heiner et al. 2009, 2011). Similar conclusions have been reached for other galaxies in the Local Group (e.g., Fukui & Kawamura 2010) and the emerging picture is that the assembly of HI filaments likely regulates the formation of molecular clouds in galaxies, even though the detailed physical processes of the assembly and the conversion of HI filaments into molecular clouds in various galactic environments still remain to be understood.

1.1.4 *X*-factor

As described in Section 1.1.3, H_2 is not directly observable under the typical conditions in molecular clouds. Therefore, alternative tracers are required to measure the abundance and distribution of H_2 and CO has been one of the most commonly used tracers due to its large abundance and low rotational transitions that are easily excited even in cold molecular clouds. In particular, its lowest rotational transition CO($J = 1 \rightarrow 0$) is often observed to estimate $N(H_2)$ via the "CO-to-H_2 conversion factor" or "X-factor":

$$X_{\rm CO} = \frac{N(H_2)}{I_{\rm CO}}\ {\rm cm^{-2}\ K^{-1}\ km^{-1}\ s}, \tag{1.5}$$

where $I_{\rm CO}$ is the CO($J = 1 \rightarrow 0$) integrated intensity. For convenience, the normalized $X_{\rm CO,20}$ will be used throughout this chapter:

$$X_{\rm CO,20} = \frac{X_{\rm CO}}{1 \times 10^{20}\ {\rm cm^{-2}\ K^{-1}\ km^{-1}\ s}}. \tag{1.6}$$

To be used as a handy conversion factor, $X_{\rm CO}$ must be estimated first using observational methods independent of CO. In general, two types of methods have been widely used for both the Galaxy and external galaxies.

(1) X_{CO} *based on the virial theorem*: For a molecular cloud in virial equilibrium, $\alpha_{\rm vir} = 5\sigma_{\rm v}^2 R/GM_{\rm vir} \sim 1$. Even though the question whether molecular clouds are virialized or not is a subject of current debate (Section 1.1.2), measuring the size (R) and kinematics ($\sigma_{\rm v}$) is relatively easy with CO observations and the assumption of virial equilibrium allows derivation of $X_{\rm CO}$ for a large number of molecular clouds. In this case, $X_{\rm CO}$ is estimated by:

$$X_{\rm CO} = \frac{N({\rm H_2})}{I_{\rm CO}} \propto \frac{M_{\rm vir}}{L_{\rm CO}}, \tag{1.7}$$

where $L_{\rm CO}$ is the CO($J = 1 \rightarrow 0$) luminosity, which is derived by integrating $I_{\rm CO}$ over the cloud area and usually expressed in K km s^{-1} pc^2.

In their seminal paper, Solomon et al. (1987) applied this method for ∼300 Galactic molecular clouds and found a strong relation between $M_{\rm vir}$ and $L_{\rm CO}$, $M_{\rm vir} \sim 43{L_{\rm CO}}^{0.81}$. For a molecular cloud with their median $L_{\rm CO} \sim 10^5$ K km s^{-1} pc^2, this results in $X_{\rm CO,20} \sim 2.1$. As the relation is not strictly linear, $X_{\rm CO}$ depends on $L_{\rm CO}$ such that $X_{\rm CO}$ varies by ∼60% for an order of magnitude change in $L_{\rm CO}$. Extragalactic measurements of $X_{\rm CO}$ for ∼12 systems have found similar values, $X_{\rm CO,20} \sim$ 1–4 (e.g., Rosolowsky 2007; Bolatto et al. 2008; Pineda et al. 2009; Wong et al. 2011; Donovan Meyer et al. 2012, 2013). The excellent correlation between $M_{\rm vir}$ and $L_{\rm CO}$ now extends over more than three orders of magnitude in $L_{\rm CO}$ and shows a slightly sublinear slope (Figure 1.6). The galaxies studied span from grand design spirals with supersolar metallicities (e.g., inner regions of M31) to dwarf irregular galaxies with subsolar metallicities (e.g., the Small Magellanic Cloud (SMC) and IC10).

Caveats: $X_{\rm CO}$ values derived using this method are sensitive to cloud definitions and biases induced by the signal-to-noise ratio. In addition, it is not completely certain that the assumption of virialized molecular clouds is valid. But most importantly, this method preferentially probes $X_{\rm CO}$ in CO-bright regions and therefore likely misses "CO-dark" H_2 (See the following paragraphs).

(2) X_{CO} *based on dust measurements*: Another approach to independently measure $N({\rm H_2})$ is to employ optically thin tracers such as dust. Using dust to derive $N({\rm H_2})$ involves one main assumption: dust and gas are well mixed and linearly related by a dust-to-gas ratio (DGR),

$$N({\rm H}) = N({\rm HI}) + 2N({\rm H_2}) = \frac{N({\rm Dust})}{\rm DGR}, \tag{1.8}$$

where N(Dust) is the dust column density usually expressed in A_V. N(Dust) can be estimated by either

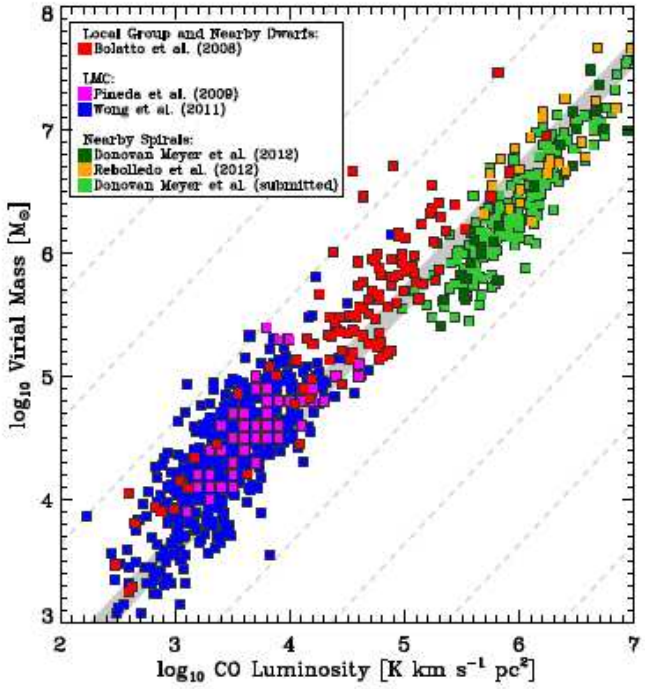

Fig. 1.6. — Relation between $M_{\rm vir}$ and $L_{\rm CO}$ for molecular clouds in external galaxies (Bolatto et al. 2013). The dashed lines represent the typical $X_{\rm CO,20} = 2$ for the Galaxy and the grey region shows ±30%. The median $X_{\rm CO,20}$ for all displayed data points is ∼2.8 and the best-fit relation has a power-law slope of ∼0.9.

measuring stellar extinction (dust in absorption) or modelling spectral energy distributions (dust in emission). As for the DGR, it is either blindly assumed or self-consistently determined. In blind determinations, a relation where a typical Galactic DGR $\sim 5.3 \times 10^{-22}$ mag cm^2 (Bohlin et al. 1978) is scaled with metallicity is usually assumed. In self-consistent determinations, on the other hand, DGR is locally estimated by comparing the measured A_V with N(HI) for HI-dominated regions. In any case, $X_{\rm CO}$ is estimated by:

$$X_{\rm CO} = \frac{N({\rm H_2})}{I_{\rm CO}} = \frac{\frac{1}{2}\left(\frac{N({\rm Dust})}{\rm DGR} - N({\rm HI})\right)}{I_{\rm CO}}. \tag{1.9}$$

For the Galaxy, Dame et al. (2001) used this method to derive $X_{\rm CO,20} \sim 2$ and found that $X_{\rm CO}$ does not significantly change with Galactic latitude. Several studies of individual molecular clouds have estimated similar values, $X_{\rm CO,20} \sim$ 1–4 (e.g., Frerking et al. 1982; Lombardi et al. 2006; Pineda et al. 2010; Abdo et al. 2010; Paradis et al. 2012). For external galaxies, on the other hand, $X_{\rm CO,20}$ shows a broader range of ∼0.4–130 (e.g., Smith et al. 1991; Israel 1997a,b; Leroy et al. 2007, 2009; Gratier et al. 2010; Leroy et al. 2011; Sandstrom et al. 2013).

Caveats: This method estimates the difference between N(H) and N(HI) and assigns it to $N(H_2)$. However, there could be contributions from other components, e.g., the high optical depth HI gas and the warm ionized medium. In addition, this method assumes that DGR does not change between HI and H_2, which has been challenged by the observed decrease in DGR for diffuse regions, suggesting the depedence of DGR on density (e.g., Bot et al. 2004; Leroy et al. 2007).

Interestingly, both methods suggest a relatively small range of $X_{CO,20} \sim 1$–4 for normal spiral galaxies. The largest discrepancy between the two methods is found for dwarf irregular galaxies with low metallicities (e.g., NGC 6822 and the SMC), where the dust-based method produces systematically larger X_{CO}. This is primarily due to the fundamental limitation of the virial-based method: its insensitivity to "CO-dark" H_2. The "CO-dark" H_2 refers to interstellar gas that is predominantly H_2 but with little or no CO. The presence of such gas has been predicted by theoretical models of photodissociation regions (PDRs), which show that the transition from CII/CI to CO occurs deeper in molecular clouds than the transition from HI to H_2 due to the less effective self-shielding for CO (e.g., Tielens & Hollenbach 1985; van Dischoeck & Black 1988; Taylor et al. 1993; Kaufman et al. 1999; Bell et al. 2006; Wolfire et al. 2010). The models also predict that the size of the "CO-dark" H_2 envelope strongly depends on metallicity. For example, in subsolar metallicity environments, CO-emitting regions are pushed further into molecular clouds to achieve dust shielding that sufficiently attenuates external dissociating photons (Figure 1.7). In this case, X_{CO} is expected to increase compared to the solar metallicity case. The dust-based measurements of X_{CO} for external galaxies indeed show such trend (Figure 1.7). The virial-based method underestimates M_{vir} and consequently X_{CO}, because it only probes the potential that is traced by CO-bright regions and misses a large amount of the "CO-dark" H_2 in the cloud outskirts. Another interesting result regarding X_{CO} is that the central parts of galaxies (including the Galaxy) frequently show suppressed X_{CO} values (e.g., Sandstrom et al. 2013; Figure 1.7). Detailed analyses of multiple CO transitions have shown that the suppressed X_{CO} likely results from broader CO linewidths and increased CO excitation (e.g., Garcia-Burillo et al. 1993; Israel et al. 2006; Israel 2009; Watanabe et al. 2011). These two effects increase CO emission per unit molecular gas and therefore result in the decreased X_{CO}. In summary, both the Galactic and extragalactic studies have found relatively constant X_{CO} values, while suggesting some degree of dependence on local conditions in the interstellar medium (e.g., metallicity, CO linewidths, and CO excitation).

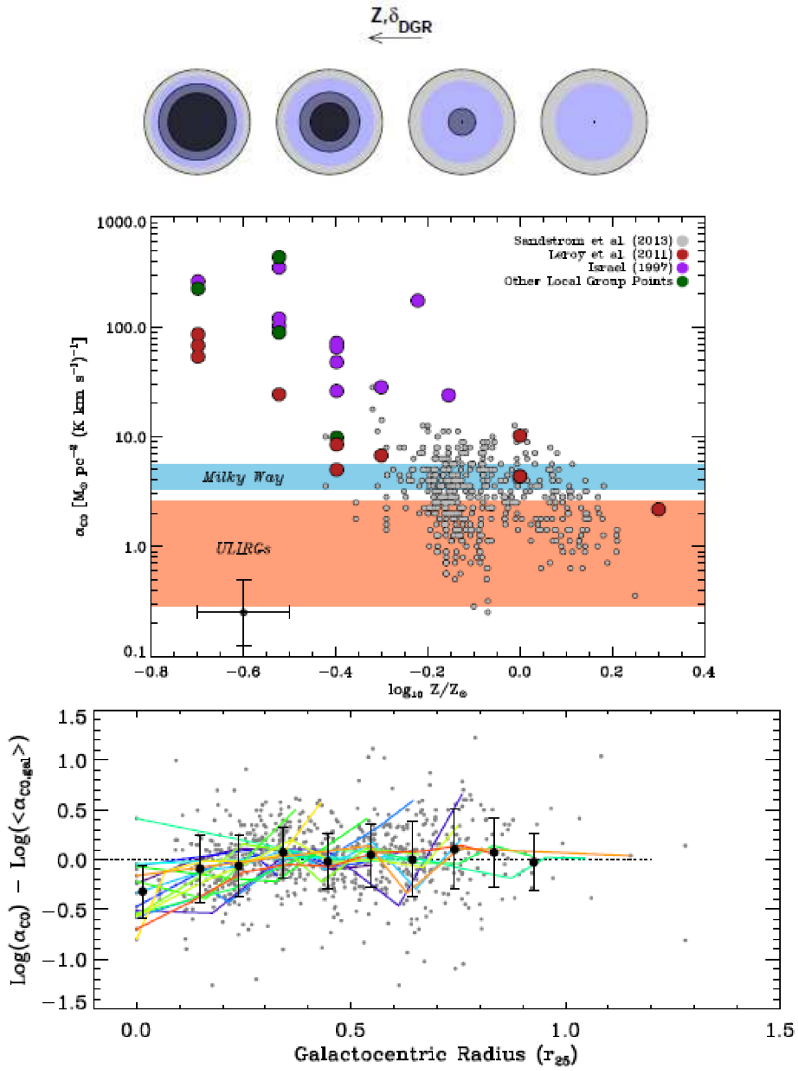

Fig. 1.7. — (Top) The effect of metallicity/DGR on the "CO-dark" H_2 envelope (Bolatto et al. 2013). Each circle represents a molecular cloud embedded in a uniform radiation field. Blue shading shows the region where gas is predominatly H_2 and darker shading indicates the regions where carbon is found as CII, CI, or CO. As metallicity/DGR decreases, the size of the CO clump decreases and the "CO-dark" H_2 envelope becomes more dominant. (Middle) The relation between (dust-based) α_{CO} and metallicity (Bolatto et al. 2013). Note that this plot shows $\alpha_{CO} = M_{H2}/L_{CO}$ instead of $X_{CO} = N(H_2)/I_{CO}$. α_{CO} is essentially same with X_{CO} and can be converted into X_{CO} by $X_{CO} = 4.6 \times 10^{19}$ α_{CO}. The data points represent the measurements of individual galaxies and the color bands show the ranges of α_{CO} observed for the Galaxy and dusty star-forming galaxies (ULIRGs). (Bottom) The normalized radial profiles of (dust-based) α_{CO} for external galaxies (Sandstrom et al. 2013). Note that a large number of galaxies show suppressed α_{CO} values in their centers.

1.2 Formation of Molecular Clouds: Theory

Currently, there are two main theoretical perspectives regarding the origin and lifetime of molecular clouds: molecular clouds are "long-lived/equilibrium" or "transient/non-equilibrium" entities. In the "long-lived/equilibrium" picture, molecular clouds are formed by large-scale instabilities in galactic disks and considered as quasi-equilibrium, self-gravitating objects. Supersonic turbulence results from a combination of the inheritance from the diffuse interstellar medium, conversion of gravitational to turbulent energy during contraction, and stellar feedback, which keeps molecular clouds from collapsing. The first proposed mechanism for the formation of molecular clouds was the Parker instability, which arises from the presence of magnetic fields in a system where the interstellar medium is supported against an external gravitational field by the thermal, magnetic, and cosmic-ray pressure (e.g., Mouschovias et al. 1974; Blitz & Shu 1980; Shibata & Matsumoto 1991). Such system is unstable to long wavelength perturbations along the direction of the magnetic field, causing the gas to move along the field lines and accumulate until sufficiently large densities are achieved for the formation of molecular clouds. Numerical simulations, however, have shown that this instability is stabilized by magnetic tension forces and density is enhanced by only a factor of $\sim$2, suggesting that molecular clouds cannot form solely by the Parker instability (e.g., Mouschovias 1974; Basu et al. 1997; Kim et al. 1998). On the other hand, the Jeans instability grows structures much faster and Kim et al. (2002) indeed found that a cloud with $M \sim 10^7$ $M_\odot$ forms rapidly by the magneto-Jeans instability (Figure 1.8). The molecular clouds formed by this self-gravitating instability are expected to live at least $\sim$3 crossing times, where $t_{\rm cross} = 2R/\sqrt{3}\sigma_{\rm v}$ (e.g., Palla & Stahler 2000; Tan et al. 2006). This lifetime corresponds to $\sim$30 Myr for massive molecular clouds in the Galaxy.

In the "transient/non-equilibrium" picture, molecular clouds are formed at the stagnation points of converging supersonic flows (e.g., Chernin et al. 1995; Ballesteros-Peredes et al. 1999; Heitsch et al. 2005; Vázquez-Semadeni et al. 2007). Contrary to the "long-lived/equilibrium" picture, the molecular clouds formed by this mechanism live only $\sim$1 crossing time and are not necessarily in equilibrium (e.g., Hartmann et al. 2001). As a result of the initial setup, the molecular clouds are naturally turbulent and their linewidth-size relation has a slope of $\sim$0.5 (due to the scaling properties of supersonic turbulence). For the diffuse interstellar medium with mean density $\langle\rho\rangle$ and relative velocity of converging flows $v_{\rm rel}$, a total column of shocked gas $\Sigma_{\rm sh}$ accumulates over time $t_{\rm accum}$ (McKee & Ostriker 2007):

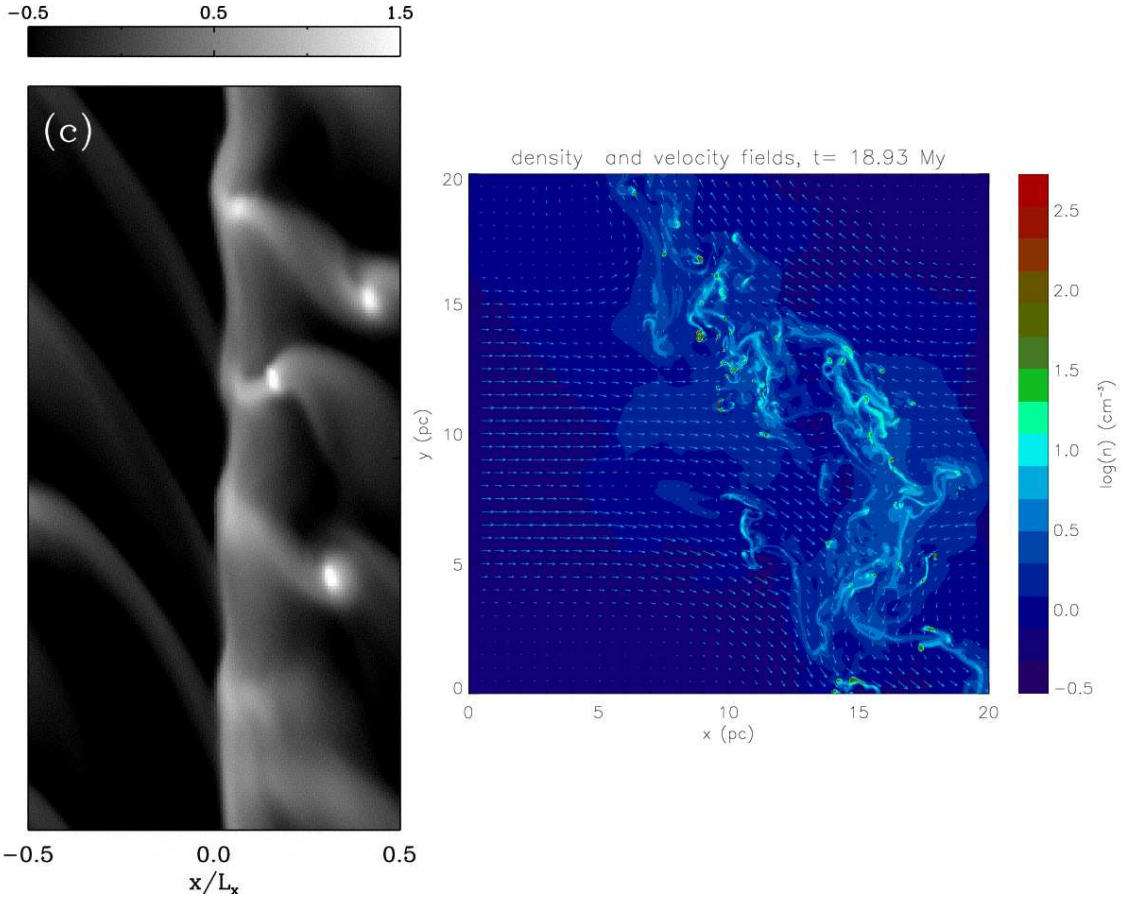

Fig. 1.8. — (Left) The vertically integrated surface density image ($\log(\Sigma/\Sigma_0)$ where Σ_0 is the initial surface density) of the structures formed by the magneto-Jeans instability in a three-dimensional galactic disk (Kim & Ostriker 2006). The simulation box in the x-y plane has a length of $L_{\rm x} = L_{\rm y} \sim 3$ kpc and the average mass of the structures is $\sim 10^7$ $M_\odot$. (Right) The density (color) and velocity (arrow) fields for the structures formed by colliding supersonic flows (Audit & Hennebelle 2005). Note that there are many small and filamentary structures in this (20 pc)^2 simulation box.

$$t_{\rm accum} = \frac{\Sigma_{\rm sh}}{\langle\rho\rangle v_{\rm rel}} = 1.6\times10^7 \left(\frac{N_{\rm sh}}{10^{21}\ {\rm cm^{-2}}}\right)\left(\frac{n}{1\ {\rm cm^{-3}}}\right)^{-1}\left(\frac{v_{\rm rel}}{20\ {\rm km\ s^{-1}}}\right)^{-1}\ {\rm years}. \quad (1.10)$$

With $v_{\rm rel} \sim 20$ km s^{-1}, $N_{\rm sh} \sim 10^{21}$ cm^{-2} accumulates over $t_{\rm accum} \sim 20$ Myr for $n \sim 1$ cm^{-3}. In this case, however, one-dimensional numerical simulations that model the formation of molecular gas behind shocks have found the H_2-to-HI ratio $R_{\rm H2} \sim 0.1$ (e.g., Bergin et al. 2004). This slow H_2 formation can be accelerated if turbulence-driven clumping is taken into account. The H_2 formation rate increases as the square of the mass-weighted mean density $\langle n\rangle_{\rm m}$, which is larger than the volume-weighted mean density $\langle n\rangle_{\rm v}$ in supersonic flows. Because $\langle n\rangle_{\rm m}/\langle n\rangle_{\rm v} \sim 10$ for the typical level of turbulence in molecular clouds, the H_2 formation timescale, $t_{\rm H2} \propto 1/\langle n\rangle_{\rm m}$, can drastically decrease down to $\sim$1 Myr.

The two perspectives on molecular clouds have led to two different approaches to model the chemical evolution of molecular clouds. In the "long-lived/equilibrium" picture, the dynamical and chemical evolution of gas are only loosely coupled and therefore can be modelled seperately. This approach corresponds to classical PDR models, where gas evolves under the assumption of thermal and chemical equilibrium (both heating-cooling and formation-dissociation are in balance) without any dynamical influences (e.g., Hollenbach et al. 1971; Tielens & Hollenbach 1985; Black & van Dishoeck 1987; Sternberg & Dalgarno 1989; Taylor et al. 1993; Ferland et al. 1998; Bensch et al. 2003; Le Petit et al. 2006; Wolfire et al. 2010). On the other hand, in the "transient/non-equilibrium" picture, the dynamical evolution of gas is rapid with its timescale comparable to that of the key chemical processes such as the transition from HI to H_2. In this case, the dynamical and chemical evolution of the gas are strongly coupled and therefore must be modelled simultaneously. This approach corresponds to recent efforts to model the formation of molecular gas in the turbulent interstellar medium by performing three-dimensional magnetohydrodynamic (MHD) simulations combined with simple chemical networks (e.g., Glover & Mac Low 2007; Glover et al. 2010; Glover & Clark 2012). Interestingly, these latest MHD simulations have found that H_2 formation does not reach chemical equilibrium up to $\sim$30 Myr: the gas will become fully H_2 unless the formed molecular clouds are destructed by stellar feedback. This is in sharp contrast with the PDR models, which explicitly assume chemical equilibrium for H_2 formation. In addition, gas in the MHD simulations is highly inhomogeneous and this results in a large scatter in the spatial distributions of H_2 and CO.

1.3 Thesis Overview

This thesis aims at providing physical insights into the formation of molecular clouds by conducting high-resolution, multi-wavlength studies of interstellar clouds in the Galaxy and the SMC. In Chapter 2, I present the first component of the thesis, which is a study of the high-extinction regions in the SMC. The SMC is a nearby dwarf irregular galaxy with an exceptionally low metallicity. As briefly described in Section 1.1.4, the traditional way to study molecular clouds is challenging in low-metallicity galaxies because of the strong dependence of CO formation on the amount of dust that provides shielding against dissociating photons. To study the physical properties of the dense interstellar medium in the SMC, I instead apply the unsharp-masking technique to the 24 μm image obtained with the *Spitzer Space Telescope* to systematically search for high-extinction regions and perform follow-up observations of multiple molecular

line transitions toward one of the selected high-extinction regions. Considering that CO-emitting clumps in low metallicity galaxies are much smaller than those in the Galaxy and therefore difficult to be located, this unsharp-masking technique can facilitate the studies of molecular gas in high-redshift galaxies by revealing regions of interest for follow-up observations with new interferometric telescopes such as the Atacama Large Millimeter Array (ALMA).

In Chapters 3 and 4, I present two studies of H_2 and CO formation in the Perseus molecular cloud. Perseus is a nearby, low-mass molecular cloud with an intermediate level of star formation and a wealth of multi-wavelength observations. Here I describe my investigation of the transition from HI to H_2 and spatial variations of $X_{\rm CO}$ across Perseus. One important observational advance in these studies comes from the HI data from the Galactic Arecibo L-band Feed Array HI (GALFA-HI) Survey. The high resolution, excellent sensitivity, and large sky coverage provided by the GALFA-HI survey allow me to probe the extended HI envelope surrounding Perseus on sub-parsec scales (which turn out to be essential for H_2 and CO formation). The observed transition from HI to H_2 and spatial variations of $X_{\rm CO}$ are then compared with predictions from the latest analytical and numerical models of H_2 and CO formation. As discussed in Section 1.2, the two conceptual frameworks for molecular clouds predict different chemical properties of the clouds. By testing the two different chemical models in detail, my studies provide constraints on the formation of molecular clouds. In addition, considering that large-scale simulations of galaxy formation and evolution have recently implemented small-scale models of the interstellar medium as their sub-grid physics, my studies serve as a "zero-point calibration" for the models of gas evolution and star formation in galaxies.

Finally, I summarize the thesis and provide future directions in Chapter 5.

References

Abdo, A. A., Ackermann, M., Ajello, M., et al. 2010, ApJ, 710, 133

Allen, R. J. 2001. Gas and Galaxy Evolution, ASP Conf. Proc., Vol. 240, ed. JE Hibbard, M Rupen, JH van Gorkom, p. 331. San Francisco: Astron. Soc. Pac.

Audit, E., & Hennebelle, P. 2005, A&A, 433, 1

Ballesteros-Paredes, J., Hartmann, L., & Vázquez-Semadeni, E. 1999, ApJ, 527, 285

Barriault, L., Joncas, G., Falgarone, E., et al. 2010a, MNRAS, 406, 2713

Barriault, L., Joncas, G., Lockman, F. J., & Martin, P. G. 2010b, MNRAS, 407, 2645

Basu, S., Mouschovias, T. Ch., & Paleologou, E. V. 1997, ApJL, 480, 55

Bell, T. A., Roueff, E., Viti, S., & Williams, D. A. 2006, MNRAS, 371, 1865

Bensch, F., Leuenhagen, U., Stutzki, J., & Shieder, R. 2003, ApJ, 591, 1913

Bergin, E. A., Hartmann, L. W., Raymond, J.C., & Ballesteros-Paredes, J. 2004, ApJ, 612, 921

Bigiel, F., Leroy, A. K., Walter, F., et al. 2008, AJ, 136, 2846

Black, J. H., & Dalgarno, A. 1977, ApJS, 34, 405

Black, J. H., & van Dishoeck, E. F. 1987, ApJ, 322, 412

Blitz, L., & Shu, F. H. 1980, ApJ, 238, 148

Blitz, L., & Rosolowsky, E. 2004, ApJ, 612, 29

Blitz, L., & Rosolowsky, E. 2006, ApJ, 650, 933

Bohlin, R. C., Savage, B. D., & Drake, J. F. 1978, ApJ, 224, 132

Bolatto, A. D., Leroy, A. K., Rosolowsky, E., Walter, F., & Blitz, L. 2008, ApJ, 686, 948

Bot, C., Boulanger, F., Lagache, G., Cambrésy, L., & Egret, D. 2004, A&A, 423, 567

Carilli, C. L., & Walter, F. 2013, arXiv:1301.0371

Chernin, A. D., Efremovm Y. N., & Voinovich, P. A. 1995, MNRAS, 275, 313

Cohen, R. S., & Thaddeus, P. 1977, ApJL, 217, 155

Dame, T. M., Hartmann, D., & Thaddeus, P. 2001, ApJ, 547, 792

Dobbs, C., Burkert, A., & Pringle, J. E. 2011, MNRAS, 413, 2935

Donovan Meyer, J., Koda, J., Momose, R., et al. 2012, ApJ, 744, 42

Douglas, K. A., & Taylor, R. A. 2007, ApJ, 659, 426

Engargiola, G., Plambeck, R. L., Rosolowsky, E., & Blitz, L. 2003, ApJS, 149, 343

Federrath, C., Klessen, R., & Schmidt, W. 2008, ApJ, 688, 79

Ferland, G. J., Korista, K. T., Verner, D. A., et al. 1998, PASP, 110, 761

Frerking, M. A., Langer, W. D., & Wilson, R. W. 1982, ApJ, 262, 590

Fukui, Y., Kawamura, A., Minamidani, T., et al. 2008, ApJS, 178, 56

Fukui, Y., & Kawamura, A. 2010, ARA&A, 48, 547

Garcia-Burillo, S., Combes, F., & Gerin, M. 1993, A&A, 274, 148

Gillmon, K., Shull, M. J., Tumlinson, J., & Danforth, C. 2006, ApJ, 636, 891

Gir, B.-Y., Blitz, L., & Magnani, L. 1994, ApJ, 434, 162

Glover, S. C. O., & Mac Low, M.-M. 2007, ApJ, 659, 1317

Glover, S. C. O., Federrath, C., Mac Low, M.-M., & Klessen, R. S. 2010, MNRAS, 404, 2

Glover, S. C. O., & Clark, P. C. 2012, MNRAS, 426, 377

Gordon, M. A., & Burton, W. B. 1976, ApJ, 208, 346

Gratier, P., Braine, J., Rodriguez-Fernandez, N. J., et al. 2010, A&A, 512, 68

Hartmann, L., Ballesteros-Paredes, J., & Bergin, E. A. 2001, ApJ, 562, 852

Heiderman, A., Evans, N. J. II., Allen, L. E., Huard, T., & Heyer, M. H. 2010, ApJ, 723, 1019

Heiner, J. S., Allen, R. J., & van der Kruit, P. C. 2009, ApJ, 700, 545

Heiner, J. S., Allen, R. J., & van der Kruit, P. C. 2011, MNRAS, 416, 2

Heitsch, F., Burkert, A., Hartmann, L., Slyz, A. D., & Devriendt, J. E. G. 2005, ApJL, 633, 113

Heyer, M. H., Carpenter, J. M., & Snell, R. L. 2001, ApJ, 551, 852

Heyer, M. H., & Brunt, C. M. 2004, ApJ, 615, 45

Heyer, M. H., Krawczyk, C., Duval, J., & Jackson, J. M. 2009, ApJ, 699, 1092

Hollenbach, D. J., Werner, M. W., & Salpeter, E. E. 1971, ApJ, 163, 165

Israel, F. P. 1997a, A&A, 317, 65

Israel, F. P. 1997b, A&A, 328, 471

Israel, F. P., Tilanus, R. P. J., Baas, F. 2006, A&A, 445, 907

Israel, F. P. 2009, A&A, 506, 689

Jenkins, E. B., & Savage, B. D. 1974, ApJ, 187, 243

Jura, M. 1975, ApJ, 197, 575

Kainulainen, J., Beuther, H., Henning, T., & Plume, R. 2009, A&A, 2009, 508L, 35

Kainulainen, J., Beuther, H., Banerjee, R., Federrath, C., & Henning, T. 2011, A&A, 530, 64

Kaufman, M. J., Wolfire, M. G., Hollenbach, D. J., & Luhman, M. L. 1999, ApJ, 527, 795

Kim, J., & Hong, S. S. 1998, ApJ, 507, 254

Kim, W.-T., Ostriker, E. C., & Stone, J. M. 2002, ApJ, 581, 1080

Kim, W.-T., & Ostriker, E. C. 2006, ApJ, 646, 213

Knapp, G. R. 1974, AJ, 79, 527

Lada, C. J., Lombardi, M., & Alves J. 2010, ApJ, 724, 687

Larson, R. B. 1981, MNRAS, 194, 809

Leroy, A. K., Bolatto, A. D., Walter, F., & Blitz, L. 2006, ApJ, 643, 825

Leroy, A. K., Bolatto, A., Stanimirović, S., et al. 2007, ApJ, 658, 1027

Leroy, A. K., Bolatto, A., Bot, C., et al. 2009, ApJ, 702, 352

Leroy, A. K., Bolatto, A., Gordon, K., et al. 2011, ApJ, 737, 12

Le Petit, F., Nehmé, C., Le Bourlot, J., & Roueff, E. 2006, ApJS, 164, 506

Lombardi, M., Alves, J., & Lada, C. J. 2006, A&A, 454, 781

Lombardi, M., Lada, C. J., & Alves, J. 2008, A&A, 489, 143

Lombardi, M., Lada, C. J., & Alves, J. 2010, A&A, 512, 67

McKee, C. F., & Ostriker, E. C. 2007, ARA&A, 45, 565

Maloney, P. 1990, ApJ, 348, 9

Martin, C. L., & Kennicutt, R. C. Jr. 2001, ApJ, 555, 301

Mathis, J. S. 1990, ARA&A, 28, 37

Mouschovias, T. Ch. 1974, ApJ, 192, 37

Mouschovias, T. Ch., Shu, F. H., & Woodward, P. R. 1974, A&A, 33, 73

Ostriker, E. C., Gammie, C. F., & Stone, J. M. 1999, 513, 259

Palla, F., & Stahler, S. W. 2000, ApJ, 540, 255

Paradis, D., Dobashi, K., Shimoikura, T., et al. 2012, A&A, 543, 103

Pineda, J. L., Ott, J., Klein, U., et al. 2009, ApJ, 703, 736

Pineda, J. L., Goldsmith, P. F., Chapman, N., et al. 2010, ApJ, 721, 68

Rachford, B. L., Snow, T. P., Tumlinson, J., et al. 2002, ApJ, 577, 221

Reach, W. T., Koo, B.-C., & Heiles, C. 1994, ApJ, 429, 672

Rosolowsky, E. 2007, ApJ, 654, 240

Sancisi, R., Goss, W. M., Anderson, C., Johansson, L. E. B., & Winnberg, A. 1974, A&A, 35, 445

Sandstrom, K. M., Leroy, A. K., Walter, F., et al. 2013, arXiv:1212.1208

Savage, B. D., Bohlin, R. C., Drake, J. F., & Budich, W. 1977, ApJ, 216, 291

Schneider, N., Csengeri, T., Hennemann, M., et al. 2012, A&A, 540L, 11

Schruba, A., Leroy, A. K., Walter, F., et al. 2011, AJ, 142, 37

Scoville, N. Z., & Solomon, P. M. 1975, ApJL, 199, 105

Shetty, R., Collins, D. C., Kauffmann, J., et al. 2010, ApJ, 712, 1049

Shibata, K., & Matsumoto, R. 1991, Natur, 353, 633

Smith, P. A., Brand, P. W. J. L., Mountain, C. M., Puxley, P. J., & Nakai, N. 1991, MNRAS, 252, 6

Solomon, P. M., Rivolo, A. R., Barrett, J., & Yahil, A. 1987, ApJ, 319, 730

Spitzer, L. Jr., & Jenkins, E. B. 1975, ARA&A, 13, 133

Sternberg, A., & Dalgarno, A. 1989, ApJ, 338, 197

Tan, J. C., Krumholz, M. R., & McKee, C. F. 2006, ApJL, 641, 121

Tassis, K., Christie, D. A., Urban, A., et al. 2010, MNRAS, 408, 1089

Taylor, S. D., Hartquist, T. W., & Williams, D. A. 1993, MNRAS, 264, 929

Tielens, A. G. G. M., & Hollenbach, D. 1985, ApJ, 291, 722

van Dishoeck, E. F., & Black, J. H. 1988, ApJ, 334, 771

Vázquez-Semadeni, E. 1994, ApJ, 423, 681

Vázquez-Semadeni, E., Gómez, G. C., Jappsen, A. K., et al. 2007, ApJ, 657, 870

Watanabe, Y., Sorai, K., Kuno, N., & Habe, A. 2011, MNRAS, 411, 1409

Williams, J. P., & Maddalena, R. J. 1996, ApJ, 464, 247

Williams, J. P., & McKee, C. F. 1997, ApJ, 476, 166

Wolfire, M. G., Hollenbach, D., & McKee, C. 2010, ApJ, 716, 1191

Wong, T., & Blitz, L. 2002, ApJ, 569, 157

Wong, T., Hughes, A., Fukui, Y., et al. 2009, ApJ, 696, 370

Wong, T., Hughes, A., Ott, J., et al. 2011, ApJS, 197, 16

Chapter 2

Infrared Dark Clouds in the Small Magellanic Cloud?

This chapter has previously appeared in The Astronomical Journal

Lee, M.-Y., Stanimirović, S., Ott, J., et al. 2009, vol. 138, p. 1101

Abstract

We have applied the unsharp-masking technique to the 24 μm image of the Small Magellanic Cloud (SMC), obtained with the *Spitzer Space Telescope*, to search for high-extinction regions. This technique has been used to locate very dense and cold interstellar clouds in the Galaxy, particularly infrared dark clouds (IRDCs). Fifty five candidate regions of high-extinction, namely high-contrast regions (HCRs), have been identified from the generated decremental contrast image of the SMC. Most HCRs are located in the southern bar region and mainly distributed in the outskirts of CO clouds, but most likely contain a significant amount of H_2. HCRs have a peak-contrast at 24 μm of 2–2.5% and a size of 8–14 pc. This corresponds to the size of typical and large Galactic IRDCs, but Galactic IRDCs are 2–3 times darker at 24 μm than our HCRs. To constrain the physical properties of the HCRs, we have performed NH_3, N_2H^+, HNC, HCO^+, and HCN observations toward one of the HCRs, HCR LIRS36–east, using the Australia Telescope Compact Array and the Mopra single-dish radio telescope. We did not detect any molecular line emission, however, our upper limits to the column densities of molecular species suggest that HCRs are most likely moderately dense with $n \sim 10^3$ cm^{-3}. This volume density is in agreement with predictions for the cool atomic phase in low metallicity environments. We suggest that HCRs may be tracing clouds at the transition from atomic to molecule-dominated medium, and could be a powerful way to study early stages of gas condensation in low metallicity galaxies. Alternatively, if made up of dense molecular clumps < 0.5 pc in size, HCRs could be counterparts of Galactic IRDCs, and/or regions with highly unusual abundance of very small dust grains.

2.1 Introduction

The discovery of infrared dark clouds (IRDCs) through the *Infrared Space Observatory (ISO)* and the *Midcourse Space Experiment (MSX)* surveys of the Galactic plane (Pérault et al. 1996; Carey et al. 1998; Egan et al. 1998) opened a new window for studies of the dense and cold interstellar medium (ISM). IRDCs, a new class of interstellar clouds, are seen as dark extinction features against the bright Galactic background at mid-infrared (mid-IR) wavelengths. In-depth studies with images obtained by the *Infrared Astronomical Satellite (IRAS)* and the *MSX* showed that IRDCs are opaque at wavelengths from 7 μm to 100 μm (Egan et al. 1998). Millimeter and submillimeter observations confirmed that IRDCs are dense ($n > 10^5$ cm^{-3}) and cold ($T_{\rm gas} < 20$ K), and have high H_2 column densities (10^{23-25} cm^{-2}) (Carey et al. 1998, 2000; Rathborne et al. 2005).

A new approach for studying the dense and cold ISM, based on the unsharp-masking technique, may be particularly useful for low metallicity environments where, due to a low shielding ability, molecules can survive only in dense cores (Elmegreen 1989) and thus it is extremely difficult to find them with blind searches. High-sensitivity and high-resolution IR images, obtained with the *Spitzer Space Telescope* (*Spitzer* throughout this chapter; Werner et al. 2004), are suitable for searching for dark clouds at mid-IR wavelengths to locate potential dense molecular clouds. Motivated by the recent *Spitzer* observations of the Small Magellanic Cloud (SMC) (Bolatto et al. 2007), we undertook the first search for IR dark clouds in the SMC.

One of the closest neighbors of the Galaxy, the SMC is a low mass ($M_{\rm dyn} \sim 2.4 \times 10^9$ M$_\odot$; Stanimirović et al. 2004), gas-rich (Staveley-Smith et al. 1998), dwarf irregular galaxy at a distance of approximately 60 kpc[1] from Earth (Westerlund 1991). Like its companion galaxy, the Large Magellanic Cloud (LMC), the SMC has a number of active star-forming regions. Most of the star formation activity in the SMC is concentrated in the feature known as the bar. The SMC bar contains most of the dense gas as well. Rubio et al. (1991) pointed out the difference in the star-formation activity along the bar, with the south-west (SW) region being more active and containing a large number of young objects which correlate well with CO clouds, while the north-east (NE) region containing only smaller CO clouds with almost no association with young stellar objects. The second prominent large-scale feature in the SMC, the wing, is

[1]Throughout this chapter we assume a distance to the SMC of 60 kpc.

located to the south-east (SE) of the SMC and contains young stellar components (e.g., N83/N84 region) which imply recent star formation (Westerlund & Glaspey 1971; Kunkel 1980).

The interstellar environment in the SMC is very different from that in the Galaxy. The SMC has a much lower heavy element abundance ($Z \sim 0.2$ $Z_{\odot}$; Dufour 1975) and an interstellar UV radiation field (ISRF) 4–10 times higher than that in the Solar neighborhood (Lequeux 1979; Vangioni-Flam et al. 1980; Azzopardi et al. 1988). Hence, the SMC provides a unique laboratory to study how different galactic interstellar environments affect properties and evolution of the ISM. In addition, the SMC is the closest local example of a relatively primitive ISM and provides a stepping stone in our understanding of the ISM in high-redshift galaxies.

While many authors have investigated properties of molecular gas in the SMC based on CO observations, only a few measurements of molecular species other than CO exist (Chin et al. 1998; Heikkilä et al. 1999). Rubio et al. (1993) and Lequeux et al. (1994) analyzed CO data obtained by the Swedish-ESO Submillimeter Telescope (SEST) and found that CO($J = 1 \rightarrow 0$) emission is deficient in the SMC by a factor of 10–20 relative to the Galaxy. Their results also showed that CO clouds in the SMC are clumpy with a surface filling factor lower than for Galactic clouds. In addition, several studies suggested that the CO emission is found only in dense cores, and that molecular hydrogen (H_2) may have a more extended distribution. Mizuno et al. (2001) compared CO luminosities for clouds observed by both NANTEN (angular resolution $\sim 2.6'$) and SEST (angular resolution $\sim 45''$) and concluded that the CO emission is highly clumped, with no diffuse CO emission in the inter-cloud medium. Rubio et al. (2000) performed observations of the v=(1–0)S(1) line of H_2 toward N66 and found that CO molecules only exist in regions with A_V larger than 1 mag, compared to 0.1 mag or less for the the v=(1–0)S(1) line of H_2. Using the *Spitzer* 24 μm, 70 μm, and 160 μm images, Leroy et al. (2007) constructed the H_2 surface density map under the assumption that all excess of far-IR emission, relative to the observed HI emission (corrected for self-absorption), comes from the H_2 component. They estimated $M_{\rm H2} = 3.2 \times 10^7$ $M_{\odot}$ and suggested that H_2 is on average 1–3 times more extended than CO[2].

Several studies have used IR emission to explore properties of dust in the SMC. Sauvage et al. (1990) studied the effects of stellar age and metallicity on the IR emission in the Magellanic Clouds and

[2]It is important to point out that the excess far-IR emission could result from an increased far-IR emissivity, possibly due to growth of icy mantles on the surface of dust grains, and/or spatial variations of the dust-to-gas ratio.

found that there is a decrease of the 12 μm flux as a function of metallicity, which indicates a relative under-abundance of the polycyclic aromatic hydrocarbons (PAHs) compared to the large grain population. Similarly, Stanimirović et al. (2000) suggested that PAH molecules and very small grains (VSGs) contribute little to the dust emission at wavelengths longer than 45 μm, based on *IRAS* images of the SMC. On the other hand, the recent LMC study with the Surveying the Agents of a Galaxy's Evolution (SAGE) data suggested that the 70 μm excess observed in the spectral energy distributions (SEDs) of both the LMC and SMC could be due to the abundant large VSGs produced through erosion of larger grains in the diffuse medium (Bernard et al. 2008).

The main goal of this study is to search for high-extinction regions at mid-IR wavelengths in the SMC by applying the unsharp-masking technique. By obtaining further molecular line observations, we aim at constraining physical properties of these regions. The *Spitzer* 24 μm image used for this study was obtained as part of the S^{3}MC survey (Bolatto et al. 2007) and has an excellent spatial resolution (1.7 pc) high enough to disentangle individual molecular clouds.

This chapter is organized as follows. In Section 2.2 we use the *Spitzer* 24 μm image of the SMC to generate the decremental contrast image and search for high-extinction regions (high-contrast regions; HCRs throughout this chapter). In Section 2.3 overall properties of identified HCRs are investigated. In Section 2.4 we examine characteristics of several selected HCRs using the available multi-wavelength data. In Section 2.5 we present our observations of NH_3, N_2H^+, HNC, HCO^+, and HCN toward one HCR (named as HCR LIRS36–east) and derive upper limits to the column densities of observed molecular species. Constraints on the physical properties and potential origins of HCRs are discussed in Section 2.6. We summarize our main findings in Section 2.7.

2.2 Search for High-Extinction Regions in the SMC: The 24 μm Contrast Image

In the Galaxy, high-extinction regions (like IRDCs) are identified as silhouettes against the diffuse Galactic background at mid-IR wavelengths that easily stand out when an unsharp-masking technique is applied (e.g., Simon et al. 2006a). Assuming that similar reasoning will apply in the SMC, we have searched for fractional decrements in the *Spitzer* 24 μm image. We followed the method of Simon et al. (2006a) who identified and cataloged 10,931 Galactic IRDC candidates by searching for contiguous regions of high-

contrast with respect to the background of the *MSX* 8.3 μm image. Since the small dust grains, especially PAHs are less abundant in the SMC than in the Galaxy (Sauvage et al. 1990; Stanimirović et al. 2000), the 8 μm image of the SMC obtained with the *Spitzer* (Bolatto et al. 2007) does not show significant diffuse emission. In addition, the diffuse 8 μm emission is mainly concentrated around HII regions, providing very little diffuse IR background for unsharp-masking. The diffuse IR emission at 24 μm is more pronounced, providing the opportunity to look for local spatial variations. In addition, at least one sharp silhouette is noticeable by eye in the southern bar region, giving us confidence that this method may reveal some interesting structures.

The *Spitzer* 24 μm image has an angular resolution of 6″ and this corresponds to a linear size of 1.7 pc at a distance of 60 kpc. The 24 μm wave band is sensitive to continuum emission from PAHs and VSGs ($a \lesssim 0.005$ μm) but much of the 24 μm emission in the SMC is expected to come from stochastically heated ($\sim$150 K) VSGs. For example, Madden et al. (2006) showed that the mid-IR emission from N66 is dominated by VSGs. These authors used one of ISOCAM bands, covering the wavelength range from 12 μm to 18 μm, and estimated that 85–95% of the IR flux comes from VSGs. To search for high-extinction regions, we first determined the diffuse IR background at 24 μm and then derived the decremental contrasts against this background.

2.2.1 Determining the Diffuse 24 μm Background

We assumed that the *Spitzer* 24 μm image, apart from bright emission from star-forming regions and point sources, consists of the diffuse IR background against which high-extinction clouds are superposed. To determine the background, we smoothed the *Spitzer* 24 μm image using the technique of spatial median filtering. The median filtering size must be larger than the typical size of high-extinction regions, but small enough to follow the spatial distribution of the background. Typical IRDCs in the Galaxy are smaller than 10 pc (or 0.6′, which is $\sim$10 pixels in the 24 μm image; one pixel corresponds to 1×10^{-3} deg), and we used this as the absolute minimal size for our smoothing kernel. On the other hand, as the spatial variation of the background at 24 μm is typically larger than 100 pc (or 6′, which is $\sim$95 pixels in the 24 μm image), the median filtering size must be smaller than 95 pixels. We examined the spatial variation of the background at 24 μm by obtaining profiles across the *Spitzer* image at various positions. We varied the median filtering size from about 33 pixels to 95 pixels and selected the kernel with 63 pixels (or 66 pc) as providing the best estimate of the IR background.

Figure 2.1 shows the estimated 24 μm background image (top) and a profile along the x-axis of the background image superposed on the original 24 μm data (bottom). For the median-kernel with 63 pixels, the diffuse background emission contributes only 27% of the total 24 μm emission. Most of the 24 μm emission comes from HII regions, in particular, those in the southern bar region. The ratio of diffuse to total 24 μm emission varies from 23% in the NE portion of the bar, to 31% in the SW portion of the bar.

2.2.2 The Contrast Image

After determining the background, we generated the contrast image by subtracting the *Spitzer* 24 μm image from the estimated background and then dividing the residual image by the background image, contrast = (background − original image)/background. By this definition, regions having lower surface brightness against the background will have positive contrasts. The HII regions have negative contrasts as their IR emission is higher than the IR background and we exclude them from further analysis. Our detection method is therefore limited to positive contrasts and we are essentially blind to high-extinction regions that may be present within the boundaries of HII regions.

The (positive) contrasts are typically very small and range from 0% to 4%. To estimate the significance of contrasts, we derived the signal-to-noise ratio image. The signal-to-noise ratio here is defined by the ratio of the contrast to its error ($c/\Delta c$). The contrast error (Δc) for a particular pixel was calculated by dividing the average 1σ noise level in the 24 μm image by the pixel value in the background image. We have assumed a constant value for the 1σ noise level of 0.06 MJy sr^{-1} by considering several emission-free regions in the image. The derived signal-to-noise ratio image is shown in Figure 2.2.

Figure 2.3 shows a histogram of pixel values from the signal-to-noise ratio image for the SMC SW bar. For small values ($< 3\sigma$), this distribution can be well fit with a Gaussian function, suggesting that a majority of pixels have low significance and are purely due to Gaussian noise. However, the distribution has a significant tail, peaking around 4σ, and suggesting that a certain fraction of pixels with high-significance deviate from the Gaussian statistics and could represent real features.

2.2.3 Selection of High-Contrast Regions (HCRs)

Figure 2.2 shows many small and large features with significant fractional decrements of the 24 μm intensity relative to the IR background. Figure 2.3 shows a significant fraction of pixels with $c > 3\sigma$. To select reliable HCRs, we take a conservative approach and search for contiguous regions with contrasts

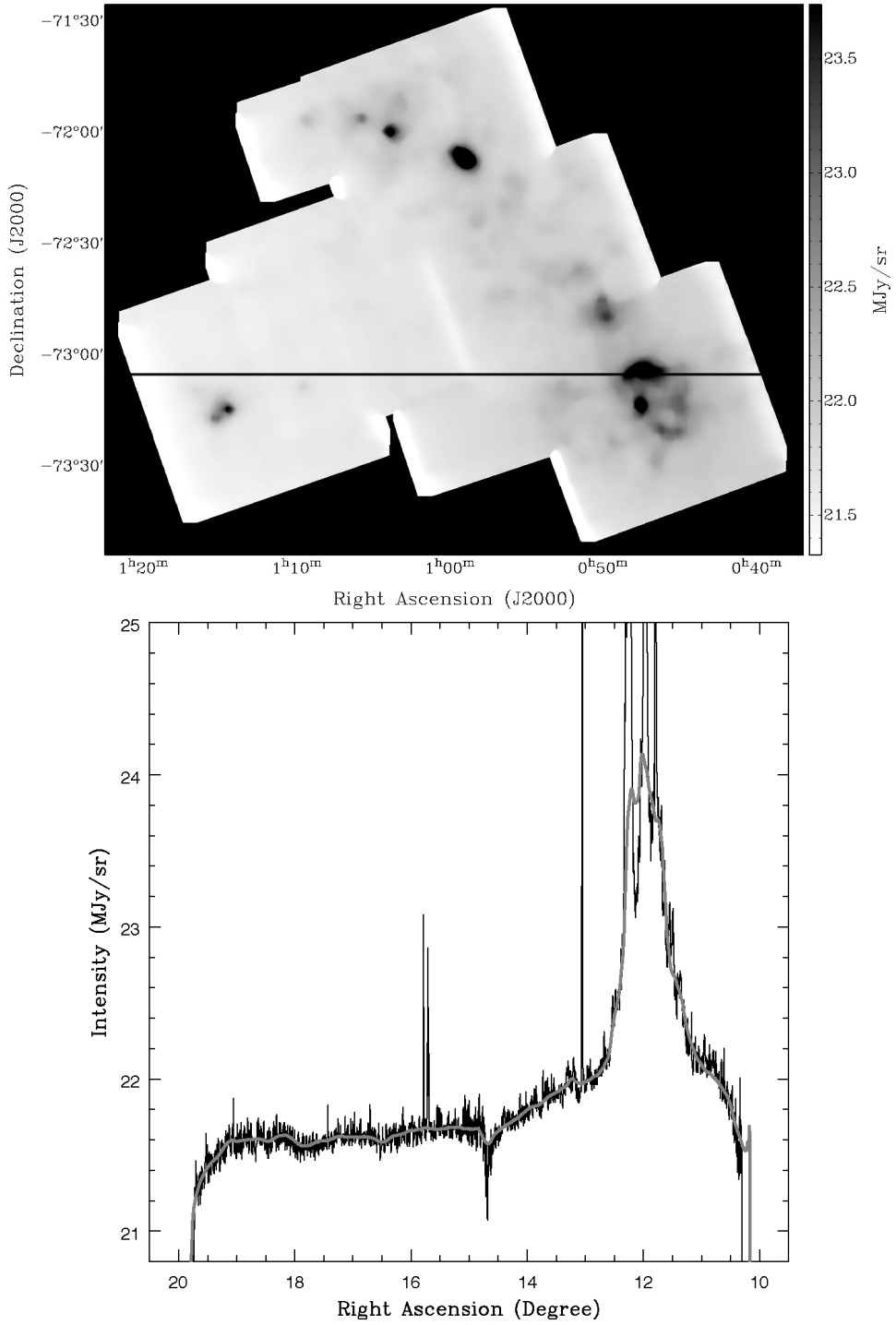

Fig. 2.1. — (Top) The IR background obtained using the median filtering with 63 pixels. The horizontal line shows the location of the profile shown in the bottom panel. (Bottom) The profile of the IR background (grey) superposed on the original *Spitzer* image data (black). Foreground emission (a sum of zodiacal light, Galactic dust emission, and small cosmic IR background, ∼21.6 MJy/sr) is not subtracted. The gap at RA = 15° is due to a small gap between different mosaic pieces of the *Spitzer* 24 μm image.

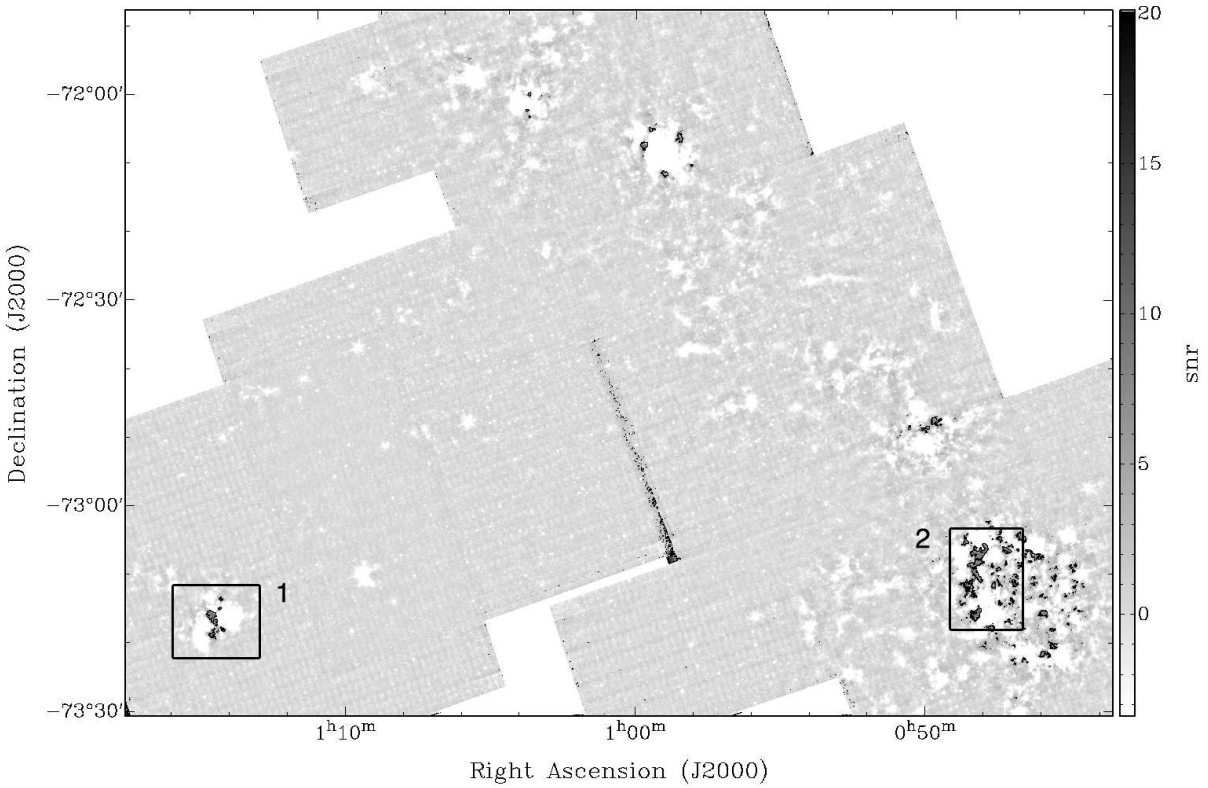

Fig. 2.2. — Signal-to-noise ratio image derived from the *Spitzer* 24 μm image. The black contours are at 5σ level. HII regions and stars have values higher than the IR background and appear as negative (white) pixels in this image. Regions with intensity lower than the IR background (HCRs) appear as positive (dark) features in this image. Boxes 1 and 2 show selected sub-regions for Figures 2.5 and 2.6 (Box 1: Figure 2.5; Box 2: Figure 2.6).

higher than 5σ. This is mainly motivated by a high likelihood of spurious detections at low contrasts (discussed below). In addition, we require HCRs to be extended and contain at least 9–10 pixels. This corresponds to twice the full width half maximum (FWHM) beam solid angle of the *Spitzer* at 24 μm (2Ω = 2.26 × $(6'')^2$ = 81 arcsec^2 ∼ 3 × 3 pixels). Therefore, the smallest clouds we are sensitive to have a size of ∼3 pc. This is similar to the typical size of Galactic IRDCs, ∼4 pc (Simon et al. 2006b), although Galactic IRDCs can range in size from 0.4 pc to 10 pc (Pillai et al. 2006; Frieswijk et al. 2007). We are therefore sensitive to the counterparts of typical and large Galactic IRDCs. By these criteria, 55 candidate HCRs (39 from the southern bar, 6 from the eastern wing, and 10 from the northern bar) were identified.

However, it is possible that some HCRs are spurious and do not trace regions of high-extinction due to the following limitations of our method.

(1) The HCRs have peak-contrasts up to 4%, which is lower than what is found for Galactic IR

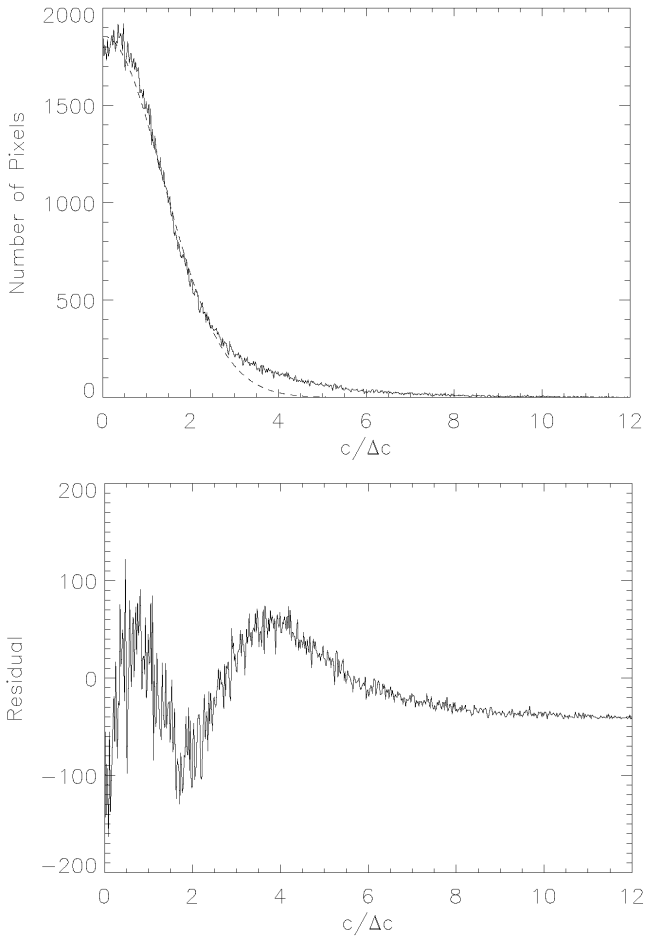

Fig. 2.3. — (Top) The histogram of the signal-to-noise ratio image for the SMC SW bar region. The fitted Gaussian function is shown with the dashed line. (Bottom) The residuals after removing the Gaussian fit. From about 3σ there is a certain fraction of pixels with significant deviation from the Gaussian statistics.

images (Section 2.3 for details). For the Galactic HCRs, Simon et al. (2006a) and Jackson et al. (2008) showed that higher contrast candidates have high CS($J = 2 \rightarrow 1$) line ($n_{\rm crit} = 7 \times 10^5$ cm^{-3}) detection rates and are therefore prime regions for being real IRDCs. For contrasts of $c_8 = 20$–40% at 8 μm, which corresponds to $c_{24} = 4$–10% at 24 μm (assuming the relation $A_\lambda \propto \lambda^{-1.7}$ in the near-IR regime; Mathis 1990), their detection rate of CS($J = 2 \rightarrow 1$) emission was 50%, while for $c_8 > 60\%$, which corresponds to $c_{24} > 20\%$, the detection rate increased to nearly 100%. Based on these studies, HCRs with $c_{24} < 4\%$ are expected to have high likelihood of being spurious detections in terms of being tracers of regions with the highest extinction.

(2) To be detected, HCRs need to lie in front of the bulk of diffuse IR emission. The SMC has been

postulated to have a significant line-of-sight depth (e.g., Mathewson et al. 1986; Welch et al. 1987), which complicates the detection of HCRs. HCRs in the parts of the SMC with lower line-of-sight depth (NW) and at a near distance will be easier to find, while HCRs in regions with a larger depth (SW) will tend to be filled by the foreground emission and hard to detect (Section 2.3 for details).

(3) The uncertainty and fluctuations in the IR background, especially close to complex HII regions, affect the reliability of HCRs. It has been pointed out by several studies that the unsharp-masking technique cannot distinguish voids in regions of complex emission from actual extinction features. This results in false detections and the exact reliability of the method is best constrained through observations of molecular lines (Jackson et al. 2008).

After taking into consideration all selection effects, we stress that our detection method is blind to high-extinction regions within the boundaries of HII regions and is biased towards the outskirts of HII regions where the diffuse IR emission is stronger than in outer parts of the SMC. Considering that HCRs with very high-contrasts in the Galaxy show a high detection rate in molecular line observations, we focus in this chapter primarily on several selected regions with the highest contrasts, and therefore the highest likelihood of being real. The best approach for checking the reliability of HCRs is through a detection and morphological matching of molecular line emission/continuum data which we attempt in Sections 2.4 and 2.5.

2.3 Overall Properties of HCRs

Figure 2.2 shows the spatial distribution of HCRs, with most of them (39 out of 55) being in the SW portion of the SMC bar. Other SMC regions contain only a few HCRs. While the exact line-of-sight depth of the SMC is uncertain, most studies agree that the depth is higher in the SW portion of the bar than in the NE region (Mathewson et al. 1986; Groenewegen 2000; Subramanian & Subramaniam 2009). Based on our selection bias discussed in Section 2.2.3, this effect would result in a smaller number of HCRs in the SW region, yet we see an opposite trend. The distribution of HII regions seen in Figure 2.2 (as negative, white pixels) is relatively uniform along the bar; no strong north-south asymmetry is observed. In addition, the fraction of IR background emission relative to the total emission is not very different between the NE and the SW, 23% versus 31% respectively. This all suggests that the highly inhomogeneous spatial distribution of HCRs, with a large abundance of HCRs in the SW, is not a selection bias but is an intrinsic property.

It is interesting to note that the large disproportion in the spatial distribution of HCRs is qualitatively similar to the spatial distribution of CO clouds by Mizuno et al. (2001). Most of the CO clouds (ranging in size from 50 pc to 160 pc) are located in the SW bar, with only a few sporadic clouds being found elsewhere. The total area of CO clouds corresponds to ∼5% for the NE and ∼11% for the SW (Mizuno et al. 2001). Young emission objects (e.g., HII regions with embedded OB associations and star clusters) tracing star formation in the range < 5–6 Myrs were found to be well correlated with CO clouds, while emissionless objects (e.g., emissionless OB associations and star clusters of ages ∼6–100 Myrs) do not show any particular association with CO clouds. This suggests that HCRs are intimately connected with CO clouds and active (more recent) sites of star formation.

In Figure 2.4 we present two histograms showing the peak-contrast and size distribution of selected 55 HCRs. The peak-contrast of HCRs ranges from 1.7% to 3.5% and peaks at 2–2.5%. The distribution of peak-contrasts of Galactic IRDCs at 8 μm is approximately a power-law, with a peak around 15–20% (full range 10–60%, Simon et al. 2006a). After converting this to the expected extinction at 24 μm (using the relation $A_\lambda \propto \lambda^{-1.7}$ in the near-IR regime; Mathis 1990), HCRs in the SMC have a peak-contrast a factor of 2–3 lower than Galactic IRDCs.

The size distribution in Figure 2.4 (bottom) shows that 80% of the selected HCRs have a size in the range from 3 pc to 18 pc (to estimate cloud size we counted the number of pixels within the HCRs and then assumed simply spherically symmetric clouds). The lower limit of this size distribution is set by our selection criteria and resolution. There is a strong peak at 8–14 pc and a tail going all the way to ∼50 pc. Galactic IRDCs have diameters of 0.4–10 pc (Pillai et al. 2006; Frieswijk et al. 2007), with a typical size of ∼4 pc (Simon et al. 2006b). This is much smaller than the average diameter of giant molecular clouds (GMCs) in the Galaxy, which is about 50 pc. HCRs in the SMC therefore, size wise, are significantly smaller than the GMCs in either the Galaxy or the SMC and similar to counterparts of typical and large Galactic IRDCs.

Under the assumption that HCRs are entirely due to the extinction of IR background emission at 24 μm, we can use the following simple radiative transfer equation to estimate their optical depth

$$c = \beta(1 - e^{-\tau}), \tag{2.1}$$

where c is the peak-contrast, $\beta = I_{\rm bh}/I_{\rm bg}$ is the fraction of IR emission behind the HCR relative to the total IR background emission along the line-of-sight, and τ is the optical depth at 24 μm. By definition

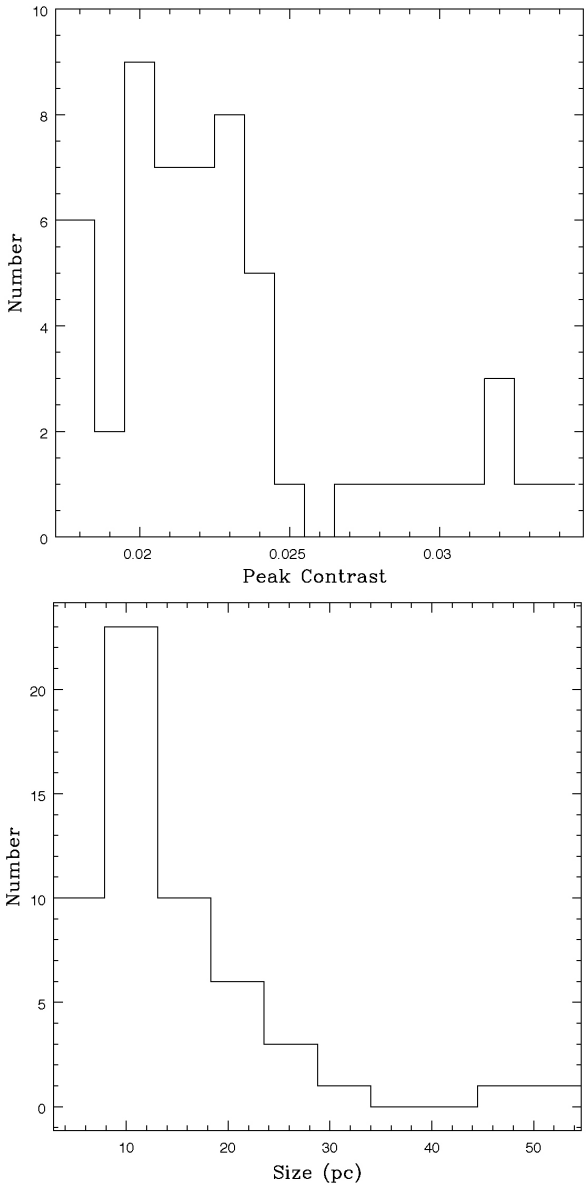

Fig. 2.4. — (Top) The histogram of peak-contrasts of selected 55 HCRs. Signal-to-noise ratio > 5 was used for the selection. (Bottom) The histogram of sizes of selected 55 HCRs. Regions larger than 3 pc were identified as HCRs.

$\beta \leq 1$, $\beta = 1$ if HCRs are at the front of the SMC and $\beta = 0.5$ if HCRs are in the middle of the SMC. By assuming $\beta = 0.5$ and using the relation $A_V = A_{24}/0.045$ (based on Figures 1 and 4 of Draine et al. 2003), we obtained $A_V = 1$–1.2 mag for HCRs with $c_{24} = 0.02$-0.025. This is moderately high for the SMC, considering that molecular peaks in the SMC have $A_V = 1$–2 mag (Leroy et al. 2007).

We have considered possible variations in A_V when β varies from 0.1 to 1. For $\beta = 0.1$, the estimated

A_V is significantly higher, 5–7 mag. However, it would be very hard to detect HCRs from the far side of the SMC as they would not have much IR background emission to absorb. In addition, even if a HCR at a far distance has a suitable IR background against which to absorb, the dark extinction feature will tend to be filled by the foreground IR emission along the line-of-sight. It is therefore highly unlikely to observe HCRs with such low β values. On the other hand, if HCRs are at the front of the SMC with $\beta = 1$, the estimated A_V would be slightly lower, 0.5–0.6 mag. However, using the HI surface density map (Stanimirović et al. 1999), which has a linear resolution of 30 pc, and applying the relation $N(\mathrm{HI})/A_V = (13.18 \pm 1.02) \times 10^{21}$ cm^{-2} mag^{-1} established for the SMC bar region (Gordon et al. 2003), we estimate the expected extinction of $A_V = 0.8$–1 mag in the direction of HCRs. This is a lower limit as denser regions are most likely smaller than 30 pc. This suggests that $\beta = 1$ assumption most likely underestimates the amount of extinction, and therefore we assume $\beta = 0.5$ and $A_V \sim 1$ mag throughout the chapter.

Using the H_2 surface density map of Leroy et al. (2007), we estimated H_2 surface densities of the HCRs, $\Sigma_{\mathrm{H2}} = 60$–$180$ M$_\odot$ pc^{-2}. Molecular peaks in the SMC are typically found to have only slightly higher surface densities, $\Sigma_{\mathrm{H2}} = 100$–$200$ M$_\odot$ pc^{-2} (Leroy et al. 2007), suggesting that HCRs contain a significant amount of H_2. Interestingly, contributions from HI and H_2 to the total hydrogen column density are roughly similar, which was also noted for the SMC as a whole by Oliveira (2009).

We conclude that the global properties of the HCRs suggest they are related to recent sites of star formation, and have sizes similar or larger than those of Galactic IRDCs. The peak-contrasts of HCRs, $A_V \sim 1$ mag, and the estimated H_2 surface density suggest regions of moderately high-density.

2.4 Selected HCRs

In this section we focus on several of the most prominent HCRs and examine their properties based on the available multi-wavelength observations.

2.4.1 HCRs in the N83/N84 Region

N83 and N84 are isolated, relatively active star-forming regions in the SMC wing. The top panel of Figure 2.5 shows the CO($J = 2 \rightarrow 1$) integrated intensity map from Bolatto et al. (2003) overlaid on the Digitized Sky Survey (DSS) R band image of the N83/N84 region. In the bottom panel of Figure 2.5 selected HCRs are shown as black contours on the background of CO($J = 2 \rightarrow 1$) intensity map. Four large features with the highest contrasts are labeled. The low abundance of stars between N83 and N84 is

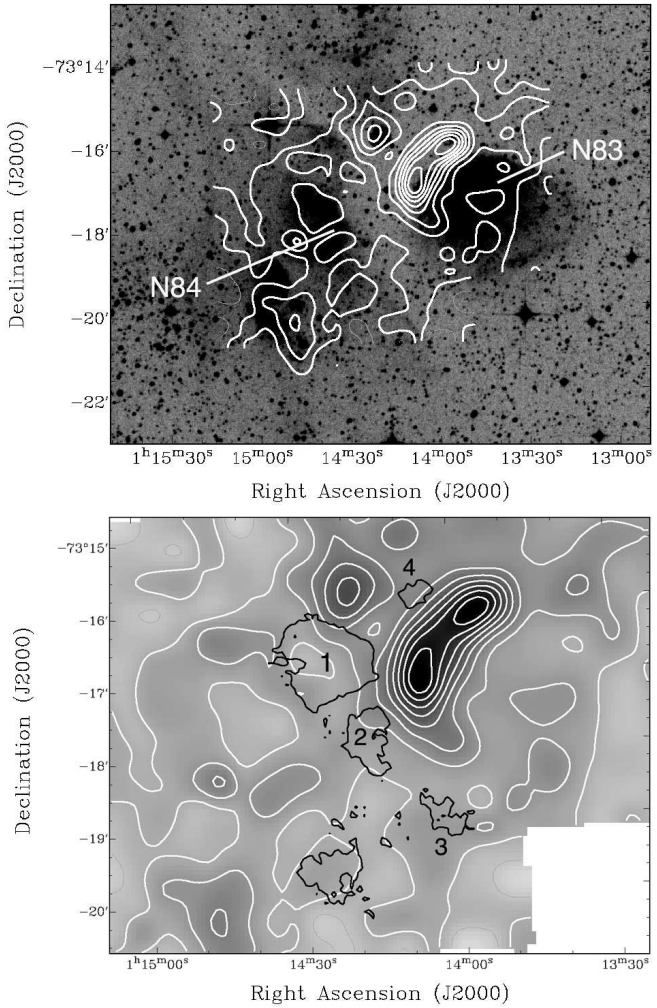

Fig. 2.5. — (Top) The CO($J = 2 \rightarrow 1$) integrated intensity map (Bolatto et al. 2003) overlaid on the DSS R band image of the N83/N84 region. The CO contour levels are from 10% to 90% of the peak (0.0045 K km s^{-1}), with a 10% step. (Bottom) The 4 highest contrast features (from 1 to 4 in order of size) are overlaid in black contours on the CO($J = 2 \rightarrow 1$) integrated intensity map.

clearly seen in the DSS R band image, which suggests the existence of high-extinction gas. Interestingly, 4 HCRs (size range 6–21 pc), weakly traced by CO($J = 2 \rightarrow 1$) emission, are identified exactly in this region.

Bolatto et al. (2003) found two distinct regions with anomalously high ratios of CO($J = 2 \rightarrow 1$)/CO($J = 1 \rightarrow 0$) (N83 and N84D in Figure 1 of Bolatto et al. 2003). They suggested that this CO emission arises from an ensemble of small ($R \sim 0.1$ pc), moderately dense ($n \sim 10^4$ cm^{-3}), and fairly warm ($T \sim 40$ K) clumps. The 4 HCRs are located between the two regions with high ratios of CO($J = 2 \rightarrow 1$)/CO($J = 1 \rightarrow 0$). This suggests that HCRs may trace gas compressed between N83 and N84. As N83 is an expanding molecular shell, this would give a mechanism for warm CO gas to be swept

up and compressed.

Leroy et al. (2009) investigates the relationship between the integrated CO($J = 1 \rightarrow 0$) and CO($J = 2 \rightarrow 1$) emission ($I_{\rm CO}$) and $\Sigma_{\rm H2}$ in the N83/N84 region at 10 pc resolution. They find that $I_{\rm CO(1-0)} = 0$ K km s^{-1} corresponds to roughly $\Sigma_{\rm H2} = 50$–150 M$_\odot$ pc^{-2} and interpret this as the presence of an envelope of H_2 with little or no associated CO. Regions with enough high dust shielding ($A_V > 2$ mag; A_V is estimated from the *Spitzer* 160 μm image assuming optically thin dust grains) are found to have $I_{\rm CO(1-0)} > 0$ K km s^{-1}. The threshold of $A_V > 2$ mag required for CO survival in the presence of an intense radiation field is in agreement with Lequeux et al. (1994)'s modeling. The 4 HCRs in this region have $\Sigma_{\rm H2} = 100$–150 M$_\odot$ pc^{-2}, very little CO, and $A_V = 0.6$–1.5 mag. This is in agreement with properties of CO-weak, H_2-dominated envelopes.

In summary, from the studies of Bolatto et al. (2003) and Leroy et al. (2009), we suggest that HCRs in the N83/N84 region most likely trace moderately dense gas ($n \sim 10^4$ cm^{-3} as the critical density for CO($J = 2 \rightarrow 1$) is $\sim 10^4$ cm^{-3}) in the extended H_2-dominated molecular cloud envelope, on spatial scales of 6–20 pc.

2.4.2 HCRs in the SMC–B2 Region

The SMC–B2 region is located in the southern bar at $(\alpha, \delta)_{\rm J2000} = (00^{\rm h}{:}48^{\rm m}{:}01.96^{\rm s}, -73^\circ{:}15'{:}38.5'')$. This region contains many HCRs, whose sizes range from 4 pc to 48 pc. The top panel of Figure 2.6 shows the CO($J = 1 \rightarrow 0$) integrated intensity map overlaid on the DSS R band image. In the bottom panel of Figure 2.6 selected HCRs are shown in black contours with the background of CO($J = 1 \rightarrow 0$) intensity map. Two large features with the highest contrasts are labeled. HCR LIRS36–east, which will be discussed in the next subsection, is also shown in Figure 2.6.

The most striking feature in Figure 2.6 is that HCRs are mainly distributed along the edges of CO($J = 1 \rightarrow 0$) contours. The fact that no HCR is found close to the CO($J = 1 \rightarrow 0$) peaks is mainly due to our selection effect as CO($J = 1 \rightarrow 0$) peaks often coincide with HII regions. However, the distribution of HCRs is clearly more extended than the CO($J = 1 \rightarrow 0$) distribution. The HCR B2–1 is especially interesting. Its morphology follows the CO distribution between molecular clouds SMC–B2 and LIRS49, but along the periphery of the CO peaks. While no obvious decrease in the stellar distribution is seen in the DSS R band image, there is a sharp edge of N27 right where B2–1 starts.

The extended HCR distribution around CO($J = 1 \rightarrow 0$) peaks is reminiscent of the H_2 distribution

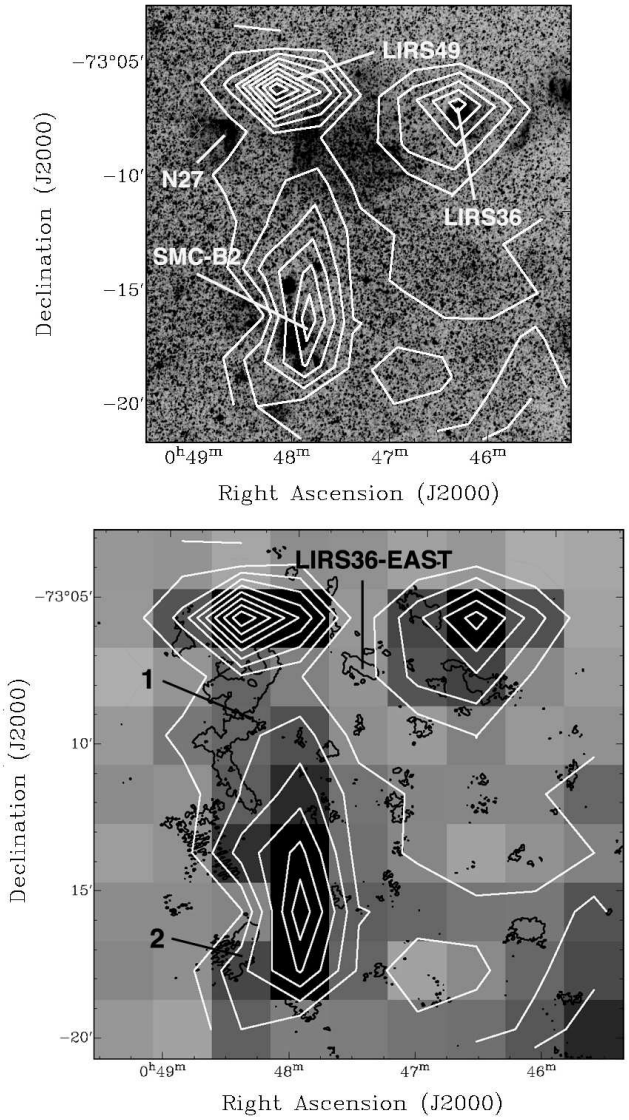

Fig. 2.6. — (Top) The CO($J = 1 \rightarrow 0$) integrated intensity map (Mizuno et al. 2001) overlaid on the DSS R band image of the SMC–B2 region. The CO contour levels are from 10% to 90% of the peak (2.49 K km s^{-1}), with a 10% step. Molecular clouds, LIRS36, LIRS49, SMC–B2, and the star-forming region N27 are labeled. (Bottom) HCR LIRS36–east and the 2 highest contrast HCRs (from 1 to 2 in order of size) overlaid in black contours on the CO($J = 1 \rightarrow 0$) integrated intensity map.

derived by Leroy et al. (2007). While CO($J = 1 \rightarrow 0$) and H_2 (spatial resolution of 46 pc) were found to have similar structure in the SW bar region, the H_2 distribution was found to be extended by 30% in the outer parts of SMC molecular clouds. One possible reason for this is the selective photodissociation of CO by the intense radiation field while H_2 survives due to its high self-shielding (e.g., Rubio et al. 1993). We show the selected HCRs overlaid on the H_2 surface density map of Leroy et al. (2007) in Figure 2.7.

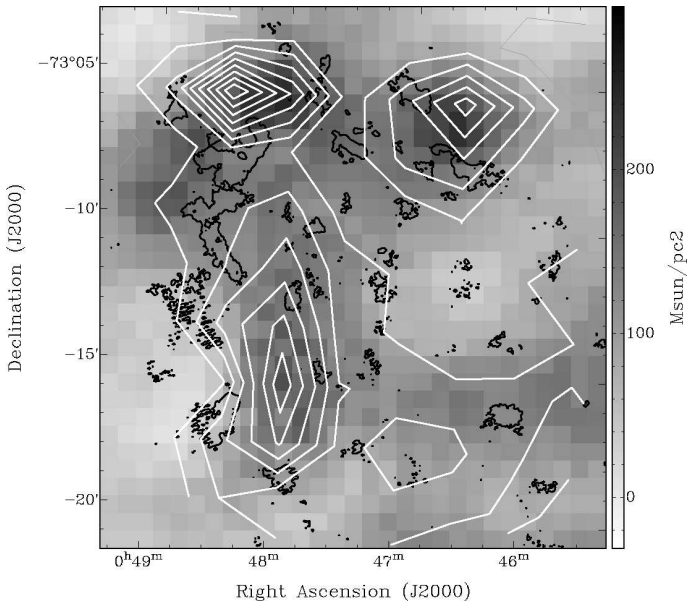

Fig. 2.7. — Selected HCRs in the SMC–B2 region overlaid in black contours on the H_2 surface density map of Leroy et al. (2007). CO($J = 1 \rightarrow 0$) emission from the NANTEN survey (Mizuno et al. 2001) is also overlaid in white contours. The CO contours are from 10% to 90% of the peak (2.49 K km s^{-1}), with a 10% step.

The extended HCR distribution is clearly seen in the figure. HCRs avoid the H_2 peaks, which mostly coincide with the CO($J = 1 \rightarrow 0$) peaks, but are still distributed in regions with Σ_{H2} = 60–180 $M_\odot$ pc^{-2}.

Bolatto et al. (2005) analyzed multiple CO line ratios of star-forming regions in the SMC bar and found that high-temperature molecular gas traced by CO($J = 4 \rightarrow 3$) (T_{kin} = 100–300 K and n_{H2} = 10^{2-3} cm^{-3}) is frequently associated with colder (T_{kin} = 10–60 K) but much denser ($n_{H2} = 10^{4-5}$ cm^{-3}) molecular gas. This suggests that a multi-phase (cold and warm) molecular medium exists in this region. Therefore, the HCR B2–1 may be tracing a moderately dense and warm envelope of the cool SMC–B2 molecular cloud.

The emerging picture from the above two regions is that HCRs most likely trace a moderately dense gas in the outskirts of CO($J = 1 \rightarrow 0$) clouds, abundant in H_2, but generally weak in CO($J = 1 \rightarrow 0$) in regions with strong radiation field, and most likely reasonably warm ($T > 10$ K). Since our IR observations have a high angular resolution of 6″ (or 3 pc), significantly higher than what has been achieved for CO or H_2, HCRs (ranging in size from a few pc to 50 pc) demonstrate that H_2 gas traced by weak CO emission is clumpy on scales of a few pc in the SMC.

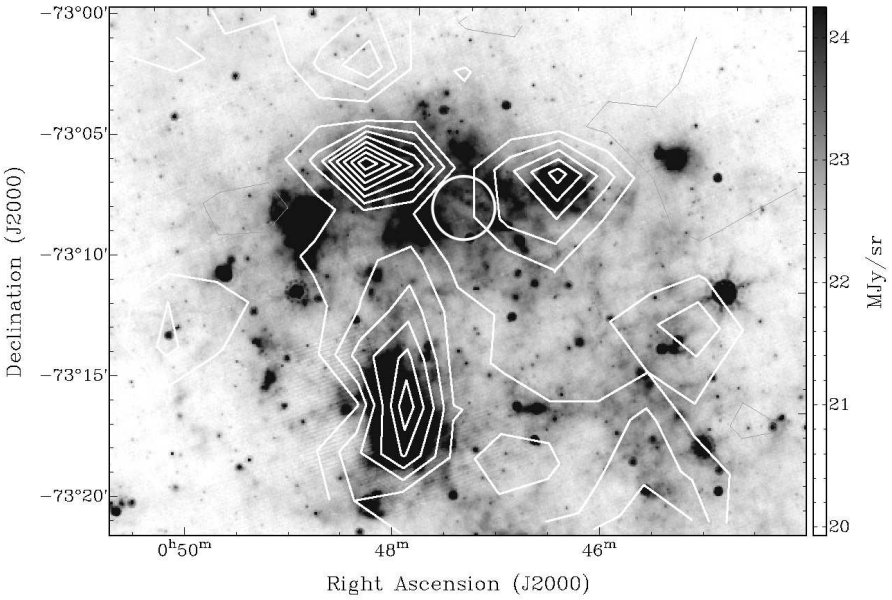

Fig. 2.8. — *Spitzer* 24 μm image of the SMC SW bar region. The intensity scale of the image was stretched to emphasize the location of HCR LIRS36-east between molecular clouds LIRS36 and LIRS49. The white contours are from the NANTEN CO($J = 1 \rightarrow 0$) survey (Mizuno et al. 2001). The contour levels are from 10% to 90% of the peak (2.49 K km s^{-1}), with a 10% step. The primary beam of the ATCA (2.4′ at 23 GHz) is centered on HCR LIRS36–east, $(\alpha,\ \delta)_{\rm J2000} = (00^{\rm h}{:}47^{\rm m}{:}30^{\rm s},\ -73^{\circ}{:}07'{:}30'')$, and is shown as a white circle.

2.4.3 HCR LIRS36–EAST

This particular HCR is the only one visible by eye as a dark silhouette in the *Spitzer* 24 μm image and has largely motivated our study. The HCR LIRS36–east is located at the east edge of molecular cloud LIRS36 $(\alpha,\ \delta)_{\rm J2000} = (00^{\rm h}{:}47^{\rm m}{:}30^{\rm s},\ -73^{\circ}{:}07'{:}30'')$ and near SMC–B2. Figure 2.8 shows the HCR LIRS36–east seen as a white, finger-like silhouette in the *Spitzer* 24 μm image. White contours are from the NANTEN CO($J = 1 \rightarrow 0$) survey (Mizuno et al. 2001).

In Figure 2.9 we show H_2 (28.2 μm; red), SIII (33.5 μm; blue), and 1.2 cm radio continuum (white) emission overlaid on the *Spitzer* 24 μm image. Observations of H_2 and SIII were obtained with the Infrared Spectrograph (IRS) on board the *Spitzer* (Sandstrom et al. 2012), while the radio continuum source at 1.2 cm is a detection of SNR J0047.2–7308 from our study (Section 2.5.3). SNR J0047.2–7308 is visible in the radio continuum emission, while SNR B0045–7322 (Ye & Turtle 1993) is traced by SIII north of HCR LIRS36–east. It is interesting to note the compressed morphology of SIII and H_2 contours on both north

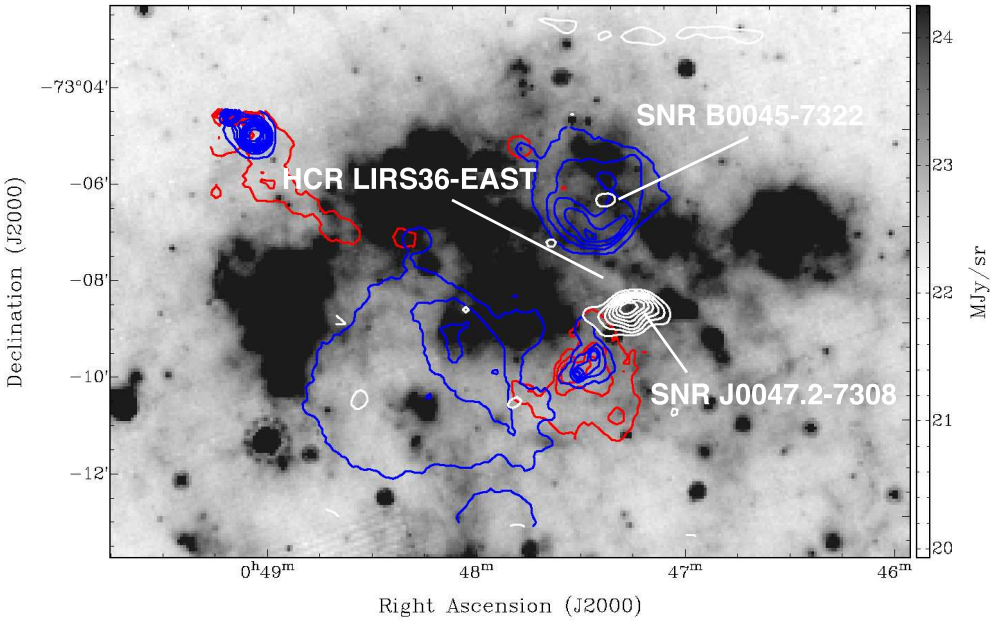

Fig. 2.9. — Emission of H_2 at 28.2 μm (red), SIII at 33.5 μm (blue), and 1.2 cm radio continuum (white) overlaid on the *Spitzer* 24 μm image of the SMC SW bar region. H_2 and SIII data were obtained with the IRS (Sandstrom et al. 2012). The contour levels range from 20% to 90% of the peak (0.16 erg s^{-1} cm^{-2}) for H_2, from 10% to 90% of the peak (2.52 erg s^{-1} cm^{-2}) for SIII, and from 30% to 90% of the peak (0.0023 mJy Beam^{-1}) for 1.2 cm emission. All contours have a step of 10%.

and south side of HCR LIRS36–east. This morphology is suggestive of the existence of a dense medium associated with HCR LIRS36–east, in agreement with findings for several other HCRs discussed earlier.

In addition, Scalise & Braz (1982) detected $6_{16} - 5_{23}$ transition of the water molecule (ν = 22.235 GHz) at a position very close to HCR LIRS36–east (α, δ)$_{J2000}$ = (00^h:47^m:31^s, $-73°$:$08'$:$20''$) with the 14-m Itapetinga Radio Telescope (IRT). While the existence of water molecule in this region will clearly signify dense molecular gas, it is possible that the water maser is associated with one of nearby HII regions since the positional accuracy of the IRT is quite poor (beam size $\sim 3'$). In addition, Oliveira et al. (2006) performed 22 GHz observations toward the pointing of Scalise & Braz (1982) with the 64-m Parkes telescope but failed to confirm the water maser detection.

2.5 Search for Molecules in HCR LIRS36–EAST

Based on the estimated properties of HCRs (Section 2.3), as well as their comparison with observations at other wavelengths, HCRs likely trace reasonably dense molecular gas. To investigate physical

properties of this medium, we have undertaken a search for several molecular species in the direction of HCR LIRS36–east. This particular HCR was chosen because of its obvious dark silhouette in the *Spitzer* 24 μm image. In addition, other multi-wavelength data strongly suggest the existence of dense gas in this region. Surprisingly, no spectral lines were detected. In this section we summarize our observations and estimate upper limits to the column densities of several molecular species. We did detect a radio continuum source at 1.2 cm, corresponding to SNR J0047.2–7308. This finding is discussed in Section 2.5.3.

2.5.1 Observations of NH_3 with the ATCA

Observations of (1,1) and (2,2) inversion transitions of ammonia (NH_3) were made on 2007 September 26–29 using the Australia Telescope Compact Array (ATCA)[3]. Six (effectively five; the sixth antenna is down-weighted due to its long baseline) antennas in the H75 configuration were used during the observations. The primary beam of the ATCA in the H75 configuration at 1.2 cm is $2.4'$. The synthesized beam size is $24.6'' \times 22.4''$. Two intermediate frequencies (IFs) were used to measure both transitions simultaneously. The first IF ($\Delta\nu$ = 8 MHz; 102 km s^{-1}) was tuned to the frequency of 23.694 GHz with 512 channels ($\Delta\nu$ = 16 kHz; 0.2 km s^{-1}) to sample emission from the (1,1) transition. The second IF ($\Delta\nu$ = 16 MHz; 205 km s^{-1}) was set at the rest frequency of 23.723 GHz with 256 channels ($\Delta\nu$ = 63 kHz; 0.8 km s^{-1}) to sample the emission from the (2,2) transition. As shown in Figure 2.8, HCR LIRS36-east is well enclosed by the ATCA primary beam and we have used only a single-pointing for our observations. The total integration time on the source was 32 hours. PKS 2353–686 was observed every 30 minutes to calibrate the phase and gain. The flux calibration source was PKS 1934–638. Observations of PKS 1921–293 were made to calibrate the bandpass.

The data reduction including flagging, calibration of antenna amplitude and phase was made by using the radio interferometry reduction package, MIRIAD (Sault et al. 1995). We followed the procedure outlined in the MIRIAD manual for 1.2 cm ATCA observations[4]. We achieved a sensitivity of $\sim$1 mJy per synthesized beam per channel for both transitions.

---

[3]The Australia Telescope Compact Array is part of the Australia Telescope which is funded by the Commonwealth of Australia for operation as a National Facility managed by CSIRO.

[4]http://www.atnf.csiro.au/computing/software/miriad/userguide/node186.html

2.5.1.1 Upper Limits to the Column Density of NH_3

We did not detect emission from the either (1,1) or (2,2) transitions. Three-channel Hanning smoothing to reduce the noise per spectral resolution element was also unsuccessful in yielding any detection of emission. Table 2.1 shows 3σ noise levels in the non-smoothed image.

With 3σ values, we can set upper limits to the optical depths of the (1,1) and (2,2) transitions. The upper limits can be determined from the basic radiative transfer equation

$$T_{\rm mb} = T_{\rm bg} e^{-\tau} + T_{\rm ex}(1 - e^{-\tau}) \tag{2.2}$$

where $T_{\rm mb}$ is the main beam brightness temperature of each transition, $T_{\rm bg}$ is the background temperature, $T_{\rm ex}$ is the excitation temperature of the observed transition, and τ is its optical depth. Since we have to subtract the continuum emission to be able to detect any line emission over the continuum, an observable quantity $T_{\rm mb}^{'}$ can be defined as $T_{\rm mb}^{'} = T_{\rm mb} - T_{\rm c}$ where $T_{\rm c}$ is the brightness temperature of the continuum emission. Furthermore, we assumed that $T_{\rm c} = T_{\rm cmb} = 2.73$ K. Hence, Equation (2.2) can be written as

$$T_{\rm mb}^{'} = (T_{\rm ex} - T_{\rm cmb})(1 - e^{-\tau}) \tag{2.3}$$

To obtain upper limits, we assumed the excitation temperature for the (1,1) and (2,2) transitions, $T_{\rm ex} =$ 20 K (Frieswijk et al. 2007). The column densities of the (1,1) and (2,2) transitions were derived by using the following equations (Mangum, Wootten, & Mundy 1992)

$$\begin{aligned} N(1,1) &= 6.60 \times 10^{14}\ \frac{T_{\rm ex}(2,2;1,1)}{\nu(1,1)}\ \tau(1,1)\Delta v\ {\rm cm}^{-2} \\ N(2,2) &= 3.11 \times 10^{14}\ \frac{T_{\rm ex}(2,2;1,1)}{\nu(2,2)}\ \tau(2,2)\Delta v\ {\rm cm}^{-2} \end{aligned} \tag{2.4}$$

Table 2.1. Summary of ATCA Observations

Molecule	Transition	Rest Frequency (MHz)	3σ Level[a] (mJy Beam^{-1})	NH_3 Column Density[b] (cm^{-2})
NH_3	(1,1)	23694.506	3.2	$< 2.7 \times 10^{12}$
NH_3	(2,2)	23722.634	1.7	$< 6.5 \times 10^{11}$

[a]Noise levels at central channels for frequency resolutions of 16 kHz and 63 kHz, respectively for (1,1) and (2,2) transitions.

[b]When (A15) of Ungerechts et al. (1986) is used, total ammonia column density, N(NH_3) is estimated as 6.2×10^{12} cm^{-2}.

where $\nu(1,1)$ and $\nu(2,2)$ are the transition frequencies in GHz, $\tau(1,1)$ and $\tau(2,2)$ are the optical depths of the main hyperfine components of the (1,1) and (2,2) transitions, and Δv is the velocity width in km s^{-1}. From the recent detection of NH_3 in the LMC (Henkel & Ott 2009), we adopted $\Delta v = 5$ km s^{-1}. Table 2.1 shows the derived upper limits to the column densities of the two transitions.

2.5.2 Observations of N_2H^+, HNC, HCO^+ and HCN with the Mopra Telescope

Observations of $N_2H^+(J = 1 \rightarrow 0)$, HNC$(J = 1 \rightarrow 0)$, $HCO^+(J = 1 \rightarrow 0)$, and HCN$(J = 1 \rightarrow 0)$ lines were made on 2008 May 5–7 using the 22-m Mopra single-dish radio telescope[5]. All 4 lines are good tracers of dense and cold gas ($n_{\rm crit} = 10^{5-6}$ cm^{-3}). The zoom mode of the Mopra Spectrometer (MOPS) was used for these observations. The bandwidth and resolution of the zoom mode at 90 GHz are 456 km s^{-1} and 0.11 km s^{-1} (137 MHz and 33 kHz) respectively. The beam size of the Mopra telescope at 90 GHz is $\sim$36″ (Ladd et al. 2005). Observations of two positions with the highest contrasts were performed. The positions of these two pointings are $(\alpha,\ \delta)_{\rm J2000} = (00^{\rm h}{:}47^{\rm m}{:}24.6^{\rm s},\ -73^\circ{:}07'{:}34'')$ and $(00^{\rm h}{:}47^{\rm m}{:}30.4^{\rm s},\ -73^\circ{:}07'{:}28'')$. The first and second pointings were integrated for 2.6 hours and 2.4 hours, on source, respectively. The system temperature varied from 170 K to 260 K during the observations.

The initial data reduction of correcting the spectra for the off-source bandpass, and averaging, was done with the ATNF Spectral line Analysis Package, ASAP[6]. Further data reduction including summing spectra, fitting and subtracting of baseline ripples, and smoothing spectra was done by using generic IDL routines and MPFITFUN (Markwardt 2009). We achieved a sensitivity of $\sim$15 mK in the main beam brightness temperature scale per channel for 4 lines.

2.5.2.1 Upper Limits to the Column Densities of N_2H^+, HNC, HCO^+ and HCN

We did not detect emission from any of the 4 lines. Smoothing spectra with 20 channels also failed to yield emission. Table 2.2 shows 3σ upper limits to the column densities of all transitions. These values were calculated in the Rayleigh-Jeans and optically thin approximation, using the following equation

$$N = \frac{8\pi W}{\lambda^3 A} \times \frac{g_{\rm l}}{g_{\rm u}} \times \frac{1}{J_\nu(T_{\rm ex}) - J_\nu(T_{\rm bg})} \times \frac{1}{1 - \exp(-h\nu/kT_{\rm ex})} \times \frac{Q_{\rm rot}}{g_{\rm l}\ \exp(-E_{\rm l}/kT_{\rm ex})} \qquad (2.5)$$

[5]The Mopra radio telescope is part of the Australia Telescope which is funded by the Common- wealth of Australia for operation as a National Facility managed by CSIRO. The University of New South Wales Digital Filterbank used for the observations with the Mopra Telescope was provided with support from the Australian Research Council.

[6]http://www.atnf.csiro.au/computing/software/asap/

where W is the integrated intensity of the line ($W = \pi^{1/2}\Delta v T_{\rm mb}/2\sqrt{ln2}$ for a Gaussian line), λ is the rest wavelength of the transition, A is the Einstein coefficient, $g_{\rm l}$ and $g_{\rm u}$ are the statistical weights of the lower and upper levels, $J_\nu(T_{\rm ex})$ and $J_\nu(T_{\rm bg})$ are the equivalent Rayleigh-Jeans excitation and background temperatures, $Q_{\rm rot}$ is the partition function, and $E_{\rm l}$ is the energy of the lower level from the ground rotational level.

Throughout our calculation, we adopted A and $Q_{\rm rot}$ values from molecular spectroscopy data of the Jet Propulsion Laboratory[7]. $T_{\rm ex} = 20$ K and $T_{\rm bg} = 2.73$ K were assumed for the calculation. $\Delta v = 4$ km s^{-1} was adopted based on observations by Chin et al. (1998) of the nearby molecular cloud LIRS36. Table 2.2 shows the calculated upper limits to the column densities.

2.5.3 Detection of Continuum Emission from SNR J0047.2–7308

The only detection in our observations is a radio continuum source at 1.2 cm. The location of the source coincides with the well-known supernova remnant in the SMC, SNR J0047.2–7308 (Dickel et al. 2001), centered at $(\alpha, \delta)_{\rm J2000} = (00^{\rm h}{:}47^{\rm m}{:}17^{\rm s}, -73^\circ{:}08'{:}43'')$. While a wealth of data at other wavelengths exists for this SNR, this is the first detection at 1.2 cm. The 1.2 cm continuum image shown in Figure 2.9 was obtained by summing over all channels in the two ATCA data cubes for the (1,1) and (2,2) transitions. The estimated flux density of the SNR at 1.2 cm is 7.4 ± 0.5 mJy.

SNR J0047.2–7308 has been observed at several different radio frequencies (408 MHz: Clarke et al. 1976; 843 MHz: Ye 1988; 1 GHz, 1.34 GHz, and 2.4 GHz: Dickel et al. 2001; 1.42 GHz, 2.37 GHz, 4.8 GHz, and 8.64 GHz: Payne et al. 2004). Figure 2.10 shows 23 GHz (1.2 cm) and 4.8 GHz radio continuum emission, in white and thick-grey contours respectively, overlaid on the 1.34 GHz image. The 1.2 cm continuum source coincides with most of the northern rim of the SNR. On the NE side of the rim, the 1.2 cm contours follow well the morphology of the rim, however the peak of the 1.2 cm emission is off-set slightly ($\sim$30″) from the peak of the northern rim.

Figure 2.11 shows the radio spectrum of the SNR. Error bars show available flux measurements from the literature at several frequencies. Our flux density measurements at 1.34 GHz, 4.8 GHz, and 23 GHz, obtained only for the area enclosed by the 23 GHz radio emission (which covers most of the northern rim of the SNR), are shown as circles in the same figure. These measurements are very similar to the values

[7] http://spec.jpl.nasa.gov/

Table 2.2. Summary of Mopra Observations

Molecule	Transition	Rest Frequency (MHz)	3σ Level (mK)[a]		Column Density (cm^{-2})	
			Pointing 1[b]	Pointing 2[c]	Pointing 1	Pointing 2
N_2H^+	$J = 1 \rightarrow 0$	93173.809	47	42	$< 2.7 \times 10^{12}$	$< 2.4 \times 10^{12}$
HNC	$J = 1 \rightarrow 0$	90663.574	35	31	$< 2.9 \times 10^{11}$	$< 2.5 \times 10^{11}$
HCO^+	$J = 1 \rightarrow 0$	89188.518	48	47	$< 3.5 \times 10^{11}$	$< 3.4 \times 10^{11}$
HCN	$J = 1 \rightarrow 0$	88631.847	45	36	$< 1.2 \times 10^{12}$	$< 9.6 \times 10^{11}$

[a]Noise levels for an individual channel in the main beam brightness temperature scale.

[b]The position is $(\alpha, \delta)_{J2000} = (00^h{:}47^m{:}24.6^s, -73^\circ{:}07'{:}34'')$.

[c]The position is $(\alpha, \delta)_{J2000} = (00^h{:}47^m{:}30.4^s, -73^\circ{:}07'{:}28'')$.

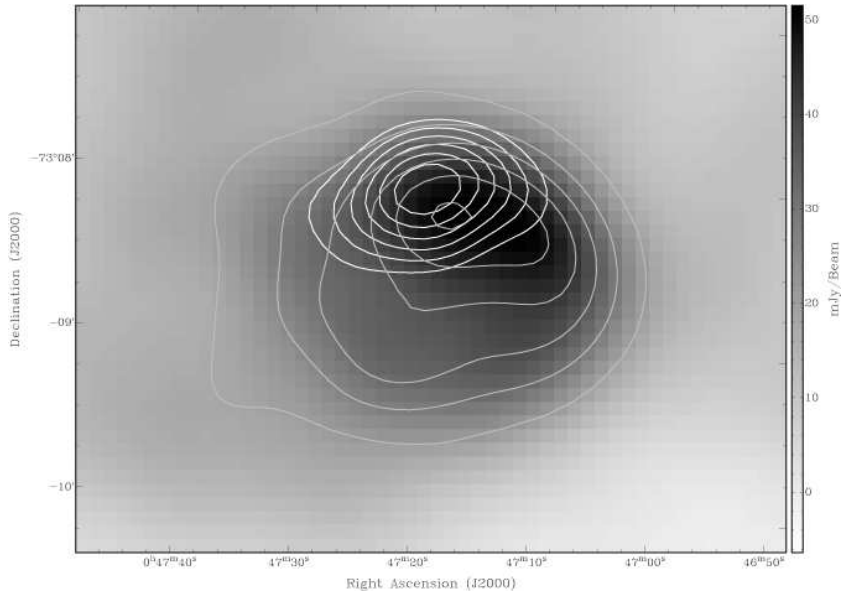

Fig. 2.10. — 1.34 GHz image of SNR J0047.2–7308. 4.8 GHz (thick-grey) and 1.2 cm (white) emission are overlaid on the image. Images at 1.34 GHz and 4.8 GHz were kindly provided by John Dickel. The contours range from 5% and 90% of the peak (0.2 mJy Beam^{-1}) with a step of 2% for the 4.8 GHz emission, and from 40% to 90% of the peak (0.0023 mJy Beam^{-1}) with a step of 10% for the 1.2 cm emission. The contours of the 23 GHz (1.2 cm) source follow well the morphology of the SNR at 1.34 GHz and 4.8 GHz, however its center is off-set slightly from the center of the northern rim of the SNR.

from the literature derived for the extent of the whole SNR, suggesting that most of the SNR flux is in its northern rim, as also evident from Figure 2.10. The solid line in Figure 2.11 corresponds to the spectral index of -0.6 ± 0.2 and was derived using the measurements from the literature. This spectral index agrees with Payne et al. (2004), and falls within the range expected for SNRs ($-0.8 < \alpha < -0.2$; McGee & Newton 1972).

Curiously, our flux density at 23 GHz is at least a factor of 5 lower than what would be expected for the SNR based on its spectral index. As the largest angular scale we are sensitive to in our observations corresponds to $1'$ and is smaller than the SNR itself (diameter $\sim 2'$), it is possible that some flux is missing in our observations, resulting in the underestimated flux density at 23 GHz. In addition, the SNR is located at the south edge of our field-of-view where we are 5 times less sensitive than in the image center. We therefore conclude that both missing short-spacings and low sensitivity are the most likely reasons for this large departure of the radio spectrum at 23 GHz. An alternative/additional source for this departure could be a spatial variation of the spectral index across the SNR. Dickel et al. (2001) used images at 1.34 GHz and 2.4 GHz to derive the spectral index image of the SNR. Across the SNR, a significant variation can be

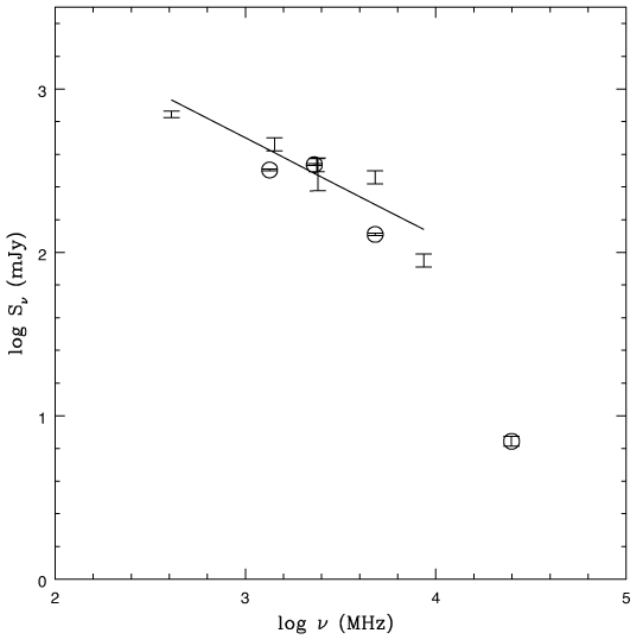

Fig. 2.11. — Radio spectrum of SNR J0047.2–7308: S_ν (flux density) in mJy versus ν (frequency) in MHz. The flux densities at 408 MHz, 1.42 GHz, 2.37 GHz, 2.4 GHz, 4.8 GHz, and 8.64 GHz of the SNR were collected from the literature and are shown with 1σ error bars. Our measurements at 1.34 GHz, 4.8 GHz, and 23 GHz are shown as circles, and encompassed only the portion of the SNR seen at 23 GHz. The spectral index at the lower frequencies (solid line) $\alpha = -0.6 \pm 0.2$ was estimated using the data from literature.

seen in their Figure 4, with the spectral index steepening from $\alpha = -0.4$ close to the center of the SNR, to $\alpha \sim -1$ in several small knots in the northern rim.

2.6 Discussion

2.6.1 Comparison with Other Studies of Dark Clouds in the SMC

Dobashi et al. (2009) recently constructed an extinction map of the SMC using the color excess at near-IR wavelengths ($E(J-H)$). They selected ten dark clouds from the $E(J-H)$ map (6 in the southern bar, 2 in the eastern wing, and 2 in a region just below the northern bar). Similarly to our results, their distribution of dark clouds is similar to that of CO clouds, based on the NANTEN CO($J = 1 \rightarrow 0$) map. However, their dark clouds, in particular those in the southern bar, frequently coincide with CO peaks, whereas our HCRs are distributed along the peripheries of CO peaks. This difference mainly arises from the fact that our method is blind to high-extinction regions within HII regions, which mostly correspond

to strong CO clouds (Section 2.2.3). While the two methods are complementary, we emphasize that our spatial resolution is much higher; angular resolution of the $E(J-H)$ map is $2.6'$ and thus even the largest HCRs in our study ($\sim$50 pc or $\sim 2.9'$) can hardly be identified.

Dobashi et al. (2009) also provides independent evidence for the nature of the largest HCR found in the N83/N84 region (labeled as 1 in the lower panel of Figure 2.5; HCR N83/N84–1). This HCR corresponds to their Cloud I. It has $E(J-H) = 0.23 \sim 0.29$ mag or $A_V = 2.51 \sim 3.16$ mag. This is 2 times higher than our estimate. The most likely cause for this discrepancy is the uncertainty in the position of the HCR/Cloud I along the line-of-sight. As we discussed in Section 2.3, we have assumed that all HCRs are located in the middle of the SMC, while Dobashi et al. (2009) inferred this quantity from a comparison of the $E(J-H)$ map with a simple model.

2.6.2 Abundances of Molecular Species

As shown in Table 2.1, our upper limit to $N(NH_3)$ of HCR LIRS36–east is about 6×10^{12} cm^{-2}. This column density is similar to the only detection of NH_3 in the LMC, accomplished very recently with the upgraded ATCA (Henkel & Ott 2009) in the direction of N159–W, one of the most active star-forming regions in the LMC. They found two velocity components in the spectrum and obtained $N(NH_3)$ of $(4.7 \pm 0.5) \times 10^{12}$ cm^{-2} and $(1.1 \pm 0.3) \times 10^{12}$ cm^{-2}, with rotational temperatures of 17 ± 2 K and 15 ± 5 K, respectively. Obviously, our ATCA observations achieved a sensitivity comparable to the NH_3 detection in the LMC. However, considering that the SMC has metallicity a few times lower than the LMC, its molecular abundance is expected to be lower in general (e.g., Israel et al. 1993). Future, more sensitive observations are required to probe and constrain the NH_3 abundance in the SMC. Up to present, NH_3 has not been detected in the SMC.

Our upper limit to $N(NH_3)$ could be significantly underestimated due to the beam dilution if dense molecular clouds are significantly smaller than the ATCA synthesized beam, an effect first pointed out by Osterberg et al. (1997) in their unsuccessful search for NH_3 in the Magellanic Clouds. The ATCA beam at 1.2 cm (synthesized beam size $\sim 24''$) corresponds to 7 pc at the distance of the SMC, but dense molecular clumps are likely to be much smaller than the beam. If this is the case, our upper limit to $N(NH_3)$ may be significantly underestimated. If we assume that molecular clumps within our ATCA beam have a size of 1 pc (for example, a dense clump $\sim$2 pc in size was observed in the LMC by Wong et al. 2006), then the upper limit to $N(NH_3)$ increases to a few $\times 10^{14}$ cm^{-2}.

Our upper limits for other molecular transitions are shown in Table 2.2. For HCO^+ we have achieved an excellent sensitivity. The upper limit to $N(HCO^+)$ is 2–6 times lower than previous measurements obtained in the SMC (Chin et al. 1998; Heikkilä et al. 1999) and at least 10 times lower than any detection of the same molecule in the LMC. Several of earlier SMC and LMC measurements are summarized in Table 2.3 for a comparison with our results. Similarly to $N(NH_3)$, the upper limit to $N(HCO^+)$ is about 1000 times lower than what is found typically for Galactic IRDCs, but is similar to $N(HCO^+)$ for Galactic diffuse clouds. If we correct for the beam dilution effect (assuming again a cloud size of 1 pc), the upper limit to $N(HCO^+)$ reaches a few $\times\ 10^{13}$ cm^{-2}.

Our upper limits for HCN and HNC are significantly lower than any detections of these molecules in the LMC, but worse (higher) than the two previous detections in the SMC (Chin et al. 1998; Heikkilä et al. 1999). N_2H^+ was never detected in the SMC and the only detection of this molecule in the LMC has a column density that is 3 times lower than our upper limit. Our upper limit to $N(HNC)$ is 3 times higher than the SMC detection in the quiescent molecular cloud LIRS36, but 4–6 times lower than several detections in the LMC. For HCN, the existent SMC detections show large variations in column density, from 1.4×10^{12} cm^{-2} in the star-forming region N27 to 2×10^{10} cm^{-2} in LIRS36. Our upper limit, $< 10^{12}$ cm^{-2}, is significantly lower than any of the LMC detections. Clearly, our upper limits for HNC and HCN are lower than the column densities detected in N27, but higher than detections in LIRS36 and require future, more sensitive observations.

Our upper limits for HCN, HNC and HCO^+, which are better than typical LMC detections, confirm that molecular abundances in the SMC are generally lower than in the LMC. In addition, the abundance in both the LMC and SMC can vary spatially by a factor of 10–100. For example, the molecular abundance of the quiescent molecular cloud LIRS36 is significantly lower than the abundance of the star-forming molecular cloud N27. This effect has been reported previously (Heikkilä et al. 1999) and was considered to be due to either metallicity variation and/or ISRF variation. However, it is important to emphasize that molecular multi-line studies of the Magellanic Clouds are still rare and only a handful of measurements exists.

Four molecular species in our study (all except HCO^+) contain nitrogen (N). NH_3 and N_2H^+ were never detected in the SMC, while HCN and HNC were detected only in two molecular clouds. Several authors have noticed a low abundance of N-containing species in the SMC and LMC and have suspected

Table 2.3. N_2H^+, HNC, HCO^+, and HCN Column Densities
(Comparison with Other Magellanic Clouds Studies)

Quantities	Our Work	LMC			SMC	
		N159–W[a]	30Dor–10[a]	N113[b]	N27[a]	LIRS36[c]
$N(N_2H^+)$ (cm^{-2})	$< 2 \times 10^{12}$	-	-	6.3×10^{11}	-	-
N(HNC) (cm^{-2})	$< 3 \times 10^{11}$	4.7×10^{12}	1.3×10^{12}	2.5×10^{12}	$< 3.7 \times 10^{11}$	9×10^{10}
$N(HCO^+)$ (cm^{-2})	$< 3 \times 10^{11}$	1.4×10^{13}	6.6×10^{12}	4.0×10^{12}	1.9×10^{12}	7×10^{11}
N(HCN) (cm^{-2})	$< 10^{12}$	1.2×10^{13}	4.8×10^{12}	6.3×10^{12}	1.4×10^{12}	2×10^{10}

[a]Heikkilä et al. (1999); Column densities are obtained from LTE analysis.

[b]Wang et al. (2008).

[c]Chin et al. (1999); Column densities are obtained from LTE analysis. $T_{\rm kin} = T_{\rm ex} = 20$ K is assumed.

that this is due to a very small nitrogen abundance in these galaxies (e.g., Chin et al. 1998; Wang et al. 2009). It was not clear though whether nitrogen abundance is exceptionally low in the handful of observed molecular clouds, or this is due to chemical processes which operate in all molecular clouds. Future, deeper observations will be required to constrain molecular abundance in HCR LIRS36–east, however based on our current non-detections its conditions are more similar, or even more extreme, to those of the quiescent molecular cloud LIRS36 than the star-forming cloud N27. The exceptionally low abundance of nitrogen makes the detection of any N-containing molecular species in the SMC extremely hard.

2.6.3 Constrainst on the Physical Properties of HCRs

What can we learn from our non-detections? Observed molecular species probe gas with a range of physical properties. CO is considered as a good tracer for low-density molecular gas with a density of $n \sim 10^3$ cm^{-3}, while NH_3 is a good tracer for moderately dense gas with a density of $n \sim 10^{3-4}$ cm^{-3}. N_2H^+, HNC, HCO^+, and HCN trace dense and cold gas with $n \sim 10^{5-6}$ cm^{-3}. Our strong upper limit to $N(HCO^+)$, as well as the presence of weak CO($J = 1 \rightarrow 0$) emission, suggest that the density in HCR LIRS36–east is likely to be $n \sim 10^3$ cm^{-3}. This agrees with the morphological hints in Section 2.4. Hence, at least one of our HCRs is most likely moderately dense with $n \sim 10^3$ cm^{-3}. This also agrees with the estimated density of $n \sim$ (0.5–2) $\times 10^3$ cm^{-3} based on the H_2 image of Leroy et al. (2007), the HI surface density map of Stanimirović et al. (1999), and assuming a cloud size of ∼10 pc.

The hydrogen volume density (∼10^3 cm^{-3}) of HCRs agrees with the expectation for the cool atomic medium in a low metallicity environment. For example, Wolfire et al. (1995) estimated, based on the heating and cooling equilibrium, that for a dust-to-gas ratio ∼30 times lower than in the Galaxy, the cold neutral medium (CNM) and the warm neutral medium (WNM) can co-exist only at a significantly high-pressure (∼10^4 K cm^{-3}). This results in the CNM temperature being as low as 25 K and a volume density being as high as 1.2×10^3 cm^{-3}. Dickey et al. (2000) measured the CNM temperature of 40 K or less in the SMC, in agreement with the Wolfire et al. (1995) prediction. Much of the cold gas in the SMC comes from regions deep inside interstellar clouds, at cold temperatures but high-densities, which in the Galaxy would be totally dominated by H_2.

In addition, HCRs appear to have roughly an equal column density of HI and H_2, a few $\times 10^{21}$ cm^{-2} (Section 2.3). This is consistent with what Dickey et al. (2000) predicted for the transition between HI-dominated and molecule-dominated clouds in the SMC. In the Galaxy, molecular clouds achieve enough

self-shielding from the interstellar radiation field at a much lower hydrogen column density, $\sim 4 \times 10^{20}$ cm^{-2} (Draine & Bertoldi 1996 and references therein). As atomic clouds are converted into molecular clouds, which consequently become fuel for star formation, properties of such transition clouds are important for constraining the process of gas condensation and collapse. We suggest that HCRs are good candidates for future observations with the *Herschel Space Observatory* of species such as neutral carbon (C), which are good tracers of translucent gas.

2.6.4 Are HCRs Counterparts of Galactic IRDCs?

As pointed out in Section 2.6.1, our non-detections of various molecular species could be due to significant clumping of molecular gas inside HCRs. In addition, if HCRs are located at the back of the SMC, our extinction values are significantly underestimated. Therefore, we cannot exclude the possibility of HCRs being counterparts of IRDCs found in the Galaxy.

What are the expected molecular abundances for dark clouds in the SMC? The only chemical model that investigated molecular abundances of dark clouds (with $A_V \sim 10$ mag) in the SMC is by Millar & Herbst (1990). This work showed that the abundance of various molecular species does not simply scale with the metal abundance. While the abundance of the N-containing species is often more directly related to the total nitrogen abundance, the abundance of hydrocarbons (like HCO^+) has a more complex dependance on metallicity. In steady state, the abundance of NH_3 is expected to scale roughly with the abundance of nitrogen, while the abundance of HCO^+ is expected to be roughly similar to that in dark clouds in the Galaxy. While the direct model predictions depend heavily on the exact input parameters, we expect that these trends will hold as direct consequences of interstellar chemical reactions. We hence expect the abundance of NH_3 to be at least 10 times lower in the SMC than in the Galaxy (based on the nitrogen abundance from Millar & Herbst 1990), while the abundance of HCO^+ should be roughly similar in the SMC and the Galaxy.

Galactic IRDCs have $N(NH_3) \sim 10^{15}$ cm^{-2} (Pillai et al. 2006; Frieswijk et al. 2007) and $N(HCO^+)$ $\sim$ a few $\times 10^{14}$ cm^{-2} (Purcell et al. 2006). In the case of the SMC, after accounting for the beam dilution effect (due to molecular clumps $\sim$1 pc in size), we arrived at the upper limits on $N(NH_3) \sim$ a few $\times 10^{14}$ cm^{-2} and $N(HCO^+) \sim$ a few $\times 10^{13}$ cm^{-2}. Our upper limit on $N(HCO^+)$ is especially stringent. While our upper limit on the abundance of NH_3 in HCRs is in agreement with what would be expected for IRDCs in the SMC (after accounting for metallicity), the abundance of HCO^+ is at least a factor of 10 lower.

We conclude that HCRs are not counterparts of Galactic IRDCs, unless HCO^+ emitting gas contains tiny clumps, $\sim$0.5 pc or smaller in size, and/or there are significant spatial variations in metallicity across the SMC. Only future high-resolution observations (e.g., with the Atacama Large Millimeter Array) will be able to investigate this possibility.

2.6.5 Alternative Explanation for HCRs

An alternative possibility which may be able to explain properties of HCRs involves an anomalous dust abundance yielding an unusually low intensity of 24 μm emission. This would happen if for example there are significant spatial variations in the abundance of various dust species. The 24 μm emission in both the SMC and the LMC is dominated by emission from VSGs. In the LMC, the recent *Spitzer* observations have shown regions of 70 μm excess relative to the 24 μm emission (Bernard et al. 2008). The most likely interpretation of this excess is an increased abundance of large VSGs relative to smaller VSGs, which could be caused by erosion of even larger grains by shocks. This illustrates just one of several possible physical processes that could result in an anomalous VSG abundance. Interestingly, the 70 μm excess sources in the LMC do not correlate well with molecular clouds. This is different from HCRs in the SMC where the largest number of objects is found around CO clouds.

To examine the possible anomalous dust abundance in HCRs, we measured flux densities at IR wavelengths provided by the *IRAS* images (Stanimirović et al. 2000) and the *Spitzer* images (Bolatto et al. 2007) for several selected HCRs, including HCR LIRS36–east, HCR B2–1, and HCR N83/N84–1. We examined various flux density ratios; an anusually low value of the 24–to–160 μm flux density ratio would be an especially good indicator for the deficiency of VSGs relative to the large dust grains. However, we found that the 24–to–160 μm flux density ratio of several HCRs is similar to the average SMC ratio, suggesting that VSGs are not unusually deficient in HCRs. It is important to emphasize that more detailed measurements of flux ratios are hampered by coarse resolution of IR images at long wavelengths (100 μm and 160 μm) relative to the 24 μm image. In addition, the proximity of HCRs to bright HII regions makes the background subtraction highly uncertain. Further analysis of the SED of HCRs at long IR wavelengths with higher-angular resolution will be possible with the *Herschel Space Observatory* and would allow us to investigate further this possibility.

2.7 Summary and Conclusions

We have searched for dense ISM in the SMC by applying the unsharp-masking technique to the *Spitzer* 24 μm image. When applied to Galactic IR images, the unsharp-masking technique reveals the highest extinction regions, IRDCs, which are very dense ($n > 10^5$ cm^{-3}) and cold ($T < 25$ K) interstellar clouds. The unsharp-masking technique is limited to regions with diffuse IR background and is blind to dense gas within boundaries of HII regions. As HII regions are often associated with CO peaks, we are not sensitive to molecular gas with substantial CO emission but are mainly tracing a population of interstellar clouds located in the outskirst of CO/HII regions. We call these clouds high-contrast regions (HCRs) and our main results are as follows.

1. We have identified a population of 55 HCRs from the decremental contrast image. HCRs have a highly inhomogeneous spatial distribution, 39 are located in the southern bar, 10 in the northern bar, and 6 in the eastern wing. This distribution is qualitatively similar to the distribution of CO clouds and is suggestive of a possible physical connection between the two populations of clouds. While HCRs with low contrast values may be spourious detections, this correlation with CO clouds gives us confidence that most HCRs are distinct physical entities.

2. Most identified HCRs have a size of 3–18 pc, which is similar to typical or large Galactic IRDCs. The distribution of peak-contrasts (at 24 μm) of HCRs has a peak at 2–2.5% and this is a factor of 2–3 lower than that of Galactic IRDCs, suggesting only moderately dense environments ($A_V \sim 1$ mag). HCRs in the SMC are less dark than Galactic IRDCs.

3. In the southern bar region, HCRs are mainly distributed in the outskirts of CO clouds and have integrated CO($J = 1 \rightarrow 0$) intensity of 0.1–0.5 K km s^{-1}. The H_2 surface density map (Leroy et al. 2007), however, suggests they are abundant in H_2 (Σ_{H2} = 60–180 M$_\odot$ pc^{-2}).

4. To constrain the physical properties of HCRs, we have performed NH_3 (with the ATCA), N_2H^+, HNC, HCO^+, and HCN observations (with the Mopra telescope) toward one of HCRs, HCR LIRS36–east. While we did not detect any molecular emission, we achieved excellent sensitivities for NH_3 and HCO^+. Our upper limits to the column density of various molecular species highlight the need for future, more sensitive molecular line observations, especially for N-containing molecules. Our upper

limits also place a constraint on the density of HCRs, $n \sim 10^3$ cm^{-3}, suggesting that they are lower density environments than Galactic IRDCs.

5. HCRs appear to trace regions where about half the hydrogen is molecular. Due to the low metal abundance, typical CNM in the SMC (usually traced through 21-cm absorption lines) has temperature similar to what is found for Galactic molecular clouds but much higher density as the multi-phase medium can exist only at a higher pressure (Wolfire et al. 1995). The estimated volume density ($\sim 10^3$ cm^{-3}) of HCRs is in agreement with the theoretical expectation for the CNM in an environment with a dust-to-gas ratio about 30 times lower than in the Galaxy. The HI column density, a few $\times$ 10^{21} cm^{-2}, suggests that HCRs trace clouds where H_2 is enough shielded against photodissociation. As such clouds are an essential stage for star formation, searching for HCRs in IR images may be a significant way to study early phases of gas condensation in low metallicity galaxies.

6. Two alternative explanations may account for the observed properties of HCRs. Firstly, HCRs could be counterparts of Galactic IRDCs consisting of very small molecular clumps (size $\sim$ 0.5 pc). If only a tiny portion of the cloud surface area produces emission, severe beam dilution may be causing our non-detections of several molecular species. Secondly, an unusual abundance of dust grains, may result in the absence of emission at 24 μm and appearance of HCRs.

7. We have detected a radio continuum source at 1.2 cm, at a position that corresponds to the northern portion of SNR J0047.2–7308. The measured flux density of the continuum source is 7.4 $\pm$ 0.5 mJy. Using the available literature data for frequencies below 10 GHz, we estimated the spectral index of -0.6 ± 0.2. Based on this estimation, the flux density at 23 GHz is at least a factor of 5 lower than what would be expected from an extrapolation of the low frequency spectral index to 1.2 cm. Some missing short-spacings, and poor sensitivity at the position of the SNR, and the possible spatial variation of the spectral index across the SNR can be responsible for the underestimated flux density at 23 GHz.

This work is based (in part) on observations made with the *Spitzer Space Telescope*, which is operated by the Jet Propulsion Laboratory, California Institute of Technology under NASA contract 1407. Support for this work was provided by NASA through contract 1289519 issued by JPL/Caltech. We also wish to

thank Jay Gallagher, Tony Wong, Monica Rubio, Francois Boulanger for useful discussions, John Dickel for his kind offer of multi-frequency radio data of SNR J0047.2–7308, and Adam Leroy for his gracious offer of the SMC H_2 surface density map and comments that improved the manuscript.

References

Azzopardi, M., Lequeux, J., & Maeder, A. 1988, A&A, 189, 34

Bernard, J.-P., Reach, W. T., Paradis, D., et al. 2008, AJ, 136, 919

Bolatto, A. D., Leroy, A. K., Israel, F. P., & Jackson, J. M. 2003, ApJ, 595, 167

Bolatto, A. D., Israel, F. P., & Martin, C. L. 2005, ApJ, 633, 210

Bolatto, A. D., Simon, J. D., Stanimirović, S., et al. 2007, ApJ, 655, 212

Carey, S. J., Clark, F. O., Egan, M. P., et al. 1998, ApJ, 508, 721

Carey, S. J., Feldman, P. A., Redman, R. O., et al. 2000, ApJ, 543, L157

Chin, Y. N., Henkel, C., Millar, T. J., Whiteoak, J. B., & Marx-Zimmer, M. 1998, A&A, 330, 901

Clarke, J. N., Little, A. G., & Mills, B. Y. 1976, Australian J. Phys. Astrophys. Suppl., 40, 1

Dickey, J. M., Mebold, U., Stanimirović, S., & Staveley-Smith, L. 2000, ApJ, 536, 756

Dickel, J. R., Williams, R. M., Carter, L. M., et al. 2001, AJ, 122, 849

Dobashi, K., Bernard, J.-P., Kawamura, A., et al. 2009, AJ, 137, 5099

Draine, B. T., & Bertoldi, F. 1996, ApJ, 468, 269

Draine, B. T. 2003, ARA&A, 41, 241

Dufour, R. J. 1975, ApJ, 195, 315

Egan, M. P., Shipman, R. F., Price, S. D., et al. 1998, ApJ, 494, L199

Elemgreen, B. G. 1989, ApJ, 338, 178

Frieswijk, W. W. F., Spaans, M., Shipman, R. F., Teyssier, D., & Hily-Blant, P. 2007, A&A, 475, 263

Groenewegen, M. A. T. 2000, A&A, 363, 901

Gordon, K. D., Clayton, G. C., Misselt, K. A., Landolt, A. U., & Wolff, M. J. 2003, ApJ, 594, 279

Heikkilä, A., Johansson, L. E. B., & Olofsson, H. 1999, A&A, 344, 817

Henkel, C., & Ott, J. 2009, in IAU Symp. 256, The Magellanic System: Stars, Gas, and Galaxies, eds. J. Th. van Loon & J. M. Oliveira (Cambridge: CUP), 256, PDF–14

Israel, F. P., Johansson, L. E. B., Lequeux, J., et al. 1993, A&A, 276, 25

Jackson, J. M., Finn, S. C., Rathborne, J. M., Chambers, E. T., & Simon, R. 2008, ApJ, 680, 349

Kunkel, W. E. 1980, in IAU Symp. 85, Star Clusters, eds. J. E. Hesser (Dordrecht: Reidel), P353

Ladd, N., Purcell, C., Wong, T., & Robertson, S. 2005, Publ. Astron. Soc. Australia, 22, 62

Leroy, A. K., Bolatto, A. D., Stanimirović, S., et al. 2007, ApJ, 658, 1027

Leroy, A. K., Bolatto, A. D., Bot, C., et al. 2009, ApJ, 702, 352

Lequeux, J. 1979, A&A, 71, 1

Lequeux, J., Le Bourlot, J., Des Forêts, G. P., et al. 1994, A&A, 292, 371

Madden, S. C., Galliano, F., Jones, A. P., & Sauvage, M. 2006, A&A, 446, 877

Markwardt, C. B. 2009, Astronomical Data Analysis Software and Systems XVIII (ASP Conf. Ser. 411), ed. D. A. Bohlender, D. Durand, & P. Dowler (San Francisco, CA: ASP), 25

Mathewson, D. S., Ford, V. L., & Visvanathan, N. 1986, ApJ, 301, 664

Mangum, J. G., Wootten, A., & Mundy, L. G. 1992, ApJ, 388, 467

Mathis, J. S. 1990, ARA&A, 28, 37

McGee R. X., & Newton L. M., 1972, Australian J. Phys., 25, 619

Millar, T. J., & Herbst, E. 1990, A&A, 231, 466

Mizuno, N., Rubio, M., Mizuno, A., et al. 2001, PASJ, 53, L45

Oliveira, J. M., van Loon, J. Th., Stanimirović, S., & Zijlstra, A. A. 2006, MNRAS, 372, 1509

Oliveira, J. M. 2009, in IAU Symp. 256, The Magellanic System: Stars, Gas, and Galaxies, eds. J. Th. van Loon & J. M. Oliveria (Cambridge: CUP), 256, 191

Osterberg, J., Staveley-Smith, L., Weisberg, J. M., Dickey, J. M., & Mebold, U. 1997, PASA, 14, 246O

Payne, J. L., Filipović, M. D., Reid, W., et al. 2004, MNRAS, 355, 44

Pérault, M., Omont, A., Simon, G., et al. 1996, A&A, 315, L165

Pillai, T., Wyrowski, F., Carey, S. J., & Menten, K. M. 2006, A&A, 450, 569

Purcell, C. R., Balasubramanyam, R., Burton, M. G., et al. 2006, MNRAS, 367, 553

Rathborne, J. M., Jackson, J. M., Chambers, E. T., et al. 2005, ApJ, 630, L181

Rubio, M., Garay, G., Montani, J., & Thaddeus, P. 1991, ApJ, 368, 173

Rubio, M., Lequeux, J., & Boulanger, F. 1993, A&A, 271, 9

Rubio, M., Contursi, A., Lequeux, J., et al. 2000, A&A, 359, 1139

Sandstrom, K. M., Bolatto, A. D., Bot, C., et al. 2012, ApJ, 744, 20

Sault, R. J., Teuben, P. J., & Wright, M. C. H. 1995, Astronomical Data Analysis Software and Systems IV (ASP Conf. Ser. 77), ed. R. Shaw, H. E. Payne, & J. J. E. Hayes (San Francisco, CA: ASP), 433

Sauvage, M., Vigroux, L., & Thuan, T. X. 1990, A&A, 237, 296

Scalise, E., & Braz, M. A. 1982, AJ, 87, 528

Simon, R., Jackson, J. M., Rathborne, J. M., & Chambers, E. T. 2006a, ApJ, 639, 227

Simon, R., Rathborne, J. M., Shah, R. Y., Jackson, J. M., & Chambers, E. T. 2006b, ApJ, 653, 1325

Stanimirović, S., Staveley-Smith, L., Dickey, J. M., Sault, R. J., & Snowden, S. L. 1999, MNRAS, 302, 417

Stanimirović, S., Staveley-Smith, L., van der Hulst, J. M., et al. 2000, MNRAS, 315, 791

Stanimirović, S., Staveley-Smith, L., & Jones, P. A. 2004, ApJ, 604, 176

Staveley-Smith, L., Kim, S., Putman, M., & Stanimirović, S. 1998, Rev. of Modern Astronomy, 11, 117

Subramanian, S., & Subramaniam, A. 2009, A&A, 496, 399

Vangioni-Flam, E., Lequeux, J., Maucherat-Joubert, M., & Rocca-Volmerange, B. 1980, A&A, 90, 73

Wang, Y., Zhang, Q., Pillai, T., Wyrowski, F., & Wu, Y. 2008, ApJ, 672, L33

Wang, M., Chin, Y.-N., Henkel, C., Whiteoak, J. B., & Cunningham, M. 2009, ApJ, 690, 580

Welch, D. L., McLaren, R. A., Madore, B. F., & McAlary, C. W. 1987, ApJ, 321, 162

Werner, M. W., Roelling, T. L., Low, F. J., et al. 2004, ApJS, 154, 1

Westerlund, B. E. 1991, in The Magellanic Clouds, IAU Symp., 148, 15

Westerlund, B. E., & Glaspey, J. 1971, A&A, 10, 1

Wolfire, M. G., Hollenbach, D., McKee, C. F., Tielens, A. G. G. M., & Bakes, E. L. O. 1995, ApJ, 443, 152

Wong, T., Whiteoak, J. B., Ott, J., Chin, Y.-N., & Cunningham, M. R. 2006, ApJ, 649, 224

Ye, T. 1988, PhD thesis, Sydney Univ.

Ye, T., & Turtle, A. J. 1993, in Lecture Notes in Physics 416: New Aspects of Magellanic Cloud Research, eds. B. Baschek, G. Klare, & J. Lequeux (Berlin: Springer-Verlag), P167

Chapter 3

A High-Resolution Study of the Atomic-to-Molecular Transition across the Perseus Molecular Cloud

This chapter has previously appeared in The Astrophysical Journal

Lee, M.-Y., Stanimirović, S., Douglas, K. A., et al. 2012, vol. 748, p. 75

Abstract

To investigate the fundamental principles of H_2 formation in a giant molecular cloud, we derive the HI and H_2 surface density ($\Sigma_{\rm HI}$ and $\Sigma_{\rm H2}$) images of the Perseus molecular cloud on sub-pc scales ($\sim$0.4 pc). We use the far-infrared data from the Improved Reprocessing of the *IRAS* Survey and the V-band extinction image provided by the COMPLETE Survey to estimate the dust column density image of Perseus. In combination with the HI data from the Galactic Arecibo L-band Feed Array HI Survey and an estimate of the local dust-to-gas ratio, we then derive the $\Sigma_{\rm H2}$ distribution across Perseus. We find a relatively uniform $\Sigma_{\rm HI} \sim$ 6–8 $M_\odot$ pc^{-2} for both dark and star-forming regions, suggesting a minimum HI surface density required to shield H_2 against photodissociation. As a result, a remarkably tight and consistent relation is found between $\Sigma_{\rm H2}/\Sigma_{\rm HI}$ and $\Sigma_{\rm HI}+\Sigma_{\rm H2}$. The transition between the HI- and H_2-dominated regions occurs at $N({\rm HI})+2N(H_2) \sim$ (8–14) $\times$ 10^{20} cm^{-2}. Our findings are consistent with predictions for H_2 formation in equilibrium, suggesting that turbulence may not be of primary importance for H_2 formation. However, the importance of warm neutral medium for H_2 shielding, internal radiation field, and the timescale of H_2 formation still remain as open questions. We also compare H_2 and CO distributions and estimate the fraction of "CO-dark" gas, $f_{\rm DG} \sim 0.3$. While significant spatial variations of $f_{\rm DG}$ are found, we do not find a clear correlation with the mean V-band extinction.

3.1 Introduction

Most of the dense molecular gas in galaxies is assembled into giant molecular clouds (GMCs) with masses from 10^4 $M_\odot$ to 10^7 $M_\odot$ and radii from 50 pc to a few hundred pc (e.g., Fukui & Kawamura 2010). As stars, the "atoms" of galaxies, are exclusively formed in these GMCs, physical processes that govern the conversion of HI into H_2 clearly play an important role in determining the properties of GMCs and consequently the initial conditions for star formation. Therefore, understanding the properties of the interstellar regions where gas transitions from HI-dominated to H_2-dominated (HI-H_2 transition hereafter) is an important step toward a complete theory of star formation.

From an observational point of view, the HI-H_2 transition has been investigated in the Galaxy mainly via ultraviolet (UV) absorption measurements toward background sources. For example, Savage et al. (1977) and Gillmon et al. (2006) measured H_2 column densities, $N(H_2)$, along the lines of sight to early-type stars and AGNs using the *Copernicus* and *FUSE* satellites and combined them with HI column densities, N(HI), to estimate H_2 fraction, $f = 2N(H_2)/(N(HI) + 2N(H_2))$. They found that f sharply rises at $N(H) = N(HI) + 2N(H_2) \sim$ (3–5) $\times$ 10^{20} cm^{-2}. Several far-infrared (FIR) studies of interstellar clouds have revealed the presence of H_2 based on the comparison between dust and atomic gas contents (e.g., Reach et al. 1994; Meyerdierks & Heithausen 1996; Douglas & Taylor 2007). Reach et al. (1994) found a significant positive deviation from a linear relation between IR intensity at 100 μm and N(HI) for cirrus clouds, indicating a substantial amount of H_2. The threshold N(HI) at which $N(H_2)$ implied by the FIR data becomes significant was found to be $\sim$4 $\times$ 10^{20} cm^{-2}, consistent with the results from Savage et al. (1977) and Gillmon et al. (2006).

More recently, the HI-H_2 transition has been observationally inferred by an absence of high N(HI). For example, Barriault et al. (2010) observed two high Galactic latitude clouds in the OH and HI transitions and found that N(HI) saturates at $\sim$5 $\times$ 10^{20} cm^{-2} for high values of N(OH), suggesting that there is molecular gas not traced by HI. Extragalactic studies have found this saturation as well. Wong & Blitz (2002), Blitz & Rosolowsky (2004, 2006), Bigiel et al. (2008), and Wong et al. (2009) observed nearby galaxies in the CO and HI transitions and found that HI surface density, Σ_{HI}, saturates at $\sim$10 $M_\odot$ pc^{-2}. Most extragalactic studies have a spatial resolution of $\sim$700 pc at best, where most GMCs are unresolved

and several are likely to be blended along a line of sight. In addition, at this resolution it is impossible to compare H_2 with the corresponding HI associated with the cloud envelopes.

From a theoretical point of view, the HI-H_2 transition has been studied in the context of the structure of photodissociation regions (PDRs). As UV photons filling up the bulk of the interstellar medium (ISM) photodissociate H_2, predominantly molecular gas is only found in the dense regions where high enough shielding is achieved by both dust grains and H_2 self-shielding. These molecular regions are bounded by PDRs where the gas predominantly exists in the atomic phase (e.g., Hollenbach & Tielens 1997). The structure of PDRs has been mainly investigated for 1D geometries that include uni-directional or bi-directional beams of radiation propagating into semi-infinite slabs or purely radial radiation fields hitting the surfaces of spherical clouds (e.g., van Dishoeck & Black 1986; Draine & Bertoldi 1996; Browning et al. 2003). However, this 1D approximation is not appropriate for GMCs that are embedded in a radiation field produced by the combination of many single stars and star clusters. In addition, when GMCs are surrounded by large HI envelopes, which have been frequently observed in the Galaxy (e.g., Wannier et al. 1983, 1991), the curvature of the PDRs and the finite size of the molecular regions are no longer negligible. A higher dimensional approach is required in this case, but as it requires a treatment of the angular dependence of the radiation field, all previous studies have been purely numerical (e.g., Spaans & Neufeld 1997; Liszt & Lucas 2000; Liszt 2002). These numerical studies do not provide a simple analytic estimate of the structure of PDRs that allows us to extrapolate the models over a wide range of ISM environments and to easily compare with observations.

Recently, Krumholz et al. (2008, 2009; KMT08 and KMT09 hereafter) performed analytic studies on a PDR in a spherical cloud that is bathed in a uniform and isotropic interstellar radiation field (ISRF). They investigated the steady-state equilibrium formation and photodissociation of H_2 and approximated the HI-H_2 transition as being infinitely sharp. Their calculation of where exactly inside a molecular cloud this transition happens resulted in two important analytic predictions. First, they found that a certain amount of $\Sigma_{\rm HI}$ is required to provide enough shielding for H_2 formation. For GMCs with solar metallicity, this is $\Sigma_{\rm HI} \sim 10$ $M_\odot$ pc^{-2}. Once the minimum $\Sigma_{\rm HI}$ is achieved to shield H_2 against photodissociation, all excess HI is converted into H_2 and the H_2 abundance increases. Second, they derived an analytic function for H_2-to-HI ratio, $R_{\rm H2} = \Sigma_{\rm H2}/\Sigma_{\rm HI}$, and showed that $R_{\rm H2}$ depends on the total gas surface density and metallicity but is interestingly almost independent of the strength of the ISRF. This is a very powerful

prediction, suggesting that for a given ISM environment, the total gas surface density determines the H_2-to-HI ratio. If confirmed by observations, this "easy" prescription of H_2 formation will be invaluable for numerical simulations of galaxy formation and evolution. From a purely practical perspective, as the above predictions are functions of direct observables (total gas surface density and metallicity), they are much easier to test observationally. Most of the previous models of H_2 formation (e.g., van Dishoeck & Black 1986; Draine & Bertoldi 1996; Browning et al. 2003) require the intensity of the UV radiation field and the number density of H nuclei as input parameters, which cannot be easily determined by observations.

KMT09's predictions specifically focus on the properties of GMCs on galactic scales (∼kpc). Several recent studies investigated the HI and H_2 properties of nearby spiral and dwarf galaxies on kpc scales and found reasonable agreement with KMT09's prediction of $R_{\rm H2}$ as a function of total gas surface density and metallicity (e.g., KMT09; Fumagalli et al. 2009, 2010). On the other hand, KMT09's simplified treatment of the thermal and chemical processes in PDRs may be less suited for studies of individual PDRs. For example, KMT09's model does not consider the temperature dependence of H_2 formation rate coefficients, H_2 dissociation by cosmic rays, or absorption of Lyman-Werner (LW) photons by molecules other than H_2. Nevertheless, KMT09's model provides strong physical insights into the fundamental principles of H_2 formation.

In this chapter, we test KMT09's predictions on the Perseus molecular cloud (Perseus hereafter) on sub-pc scales (∼0.4 pc) for the first time in an attempt to understand the fundamental principles of H_2 formation in GMCs. Perseus is a nearby molecular cloud located at a distance ranging from 200 pc to 350 pc (Herbig & Jones 1983; Černis 1990) and has roughly a projected angular size of 6° by 3° on the sky (based on CO emission[1]). We adopt the distance to Perseus of 300 pc throughout this chapter. Perseus is part of the large Taurus–Auriga–Perseus molecular cloud complex and lies below the Galactic plane ($b \sim -20°$), resulting in slightly less confused HI spectra compared to other Galactic GMCs. With $M \sim 10^4$ $M_\odot$ (Sancisi et al. 1974; Ungerechts & Thaddeus 1987), this is a low mass cloud with an intermediate level of star formation (Bally et al. 2008). Figure 3.1 shows the V-band extinction image of Perseus with CO contours to emphasize the locations of several prominent dark and star-forming regions. IC348 (age = 0.7–12 Myr; Herbig 1998) and NGC 1333 (age < 1 Myr; Lada et al. 1996) are active star-forming regions, while B5, B1E, B1, L1455, L1448, and L1451 are dark regions with low levels of star formation.

[1]In this chapter, all ^{12}CO($J = 1 \rightarrow 0$) data are quoted as CO.

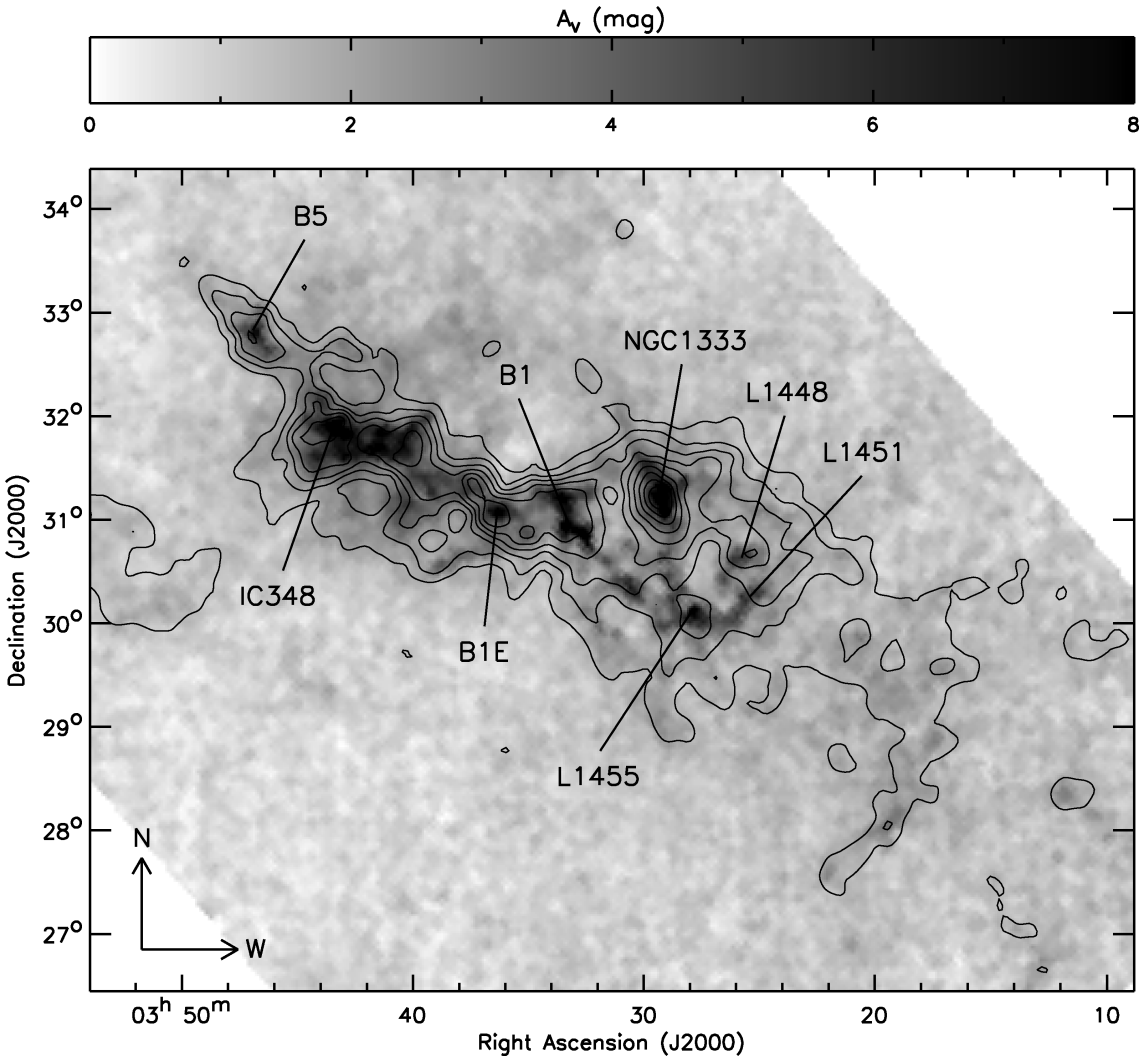

Fig. 3.1. — 2MASS A_V image of Perseus. The contours of CfA $I_{\rm CO}$ are overlaid in black. The contour levels range from 10% to 90% of the peak (69 K km s^{-1}) with 10% steps. The angular resolution of the 2MASS A_V and CfA $I_{\rm CO}$ images is $5'$ and $8.4'$, respectively. Several prominent dark and star-forming regions are labeled.

A wealth of multi-wavelength observations exist for Perseus; we provide details in Section 3.2. One of the recent observational advances is the high-resolution HI data set of Perseus and its outskirts provided by the GALFA-HI survey (Peek et al. 2011). This data set nicely matches the angular resolution of FIR images, $\sim 4'$, allowing us to estimate $R_{\rm H2}$ across and around Perseus and to compare the results to KMT09's predictions.

This chapter is organized in the following way. We start with a description of the data sets used in this study (Section 3.2). We then describe details of our methodology to derive N(HI) and $N(\rm H_2)$ images

(Sections 3.3 and 3.4). In Section 3.5, we examine the dust temperature image closely and discuss the implications for the strength of the radiation field across Perseus. In Section 3.6, we summarize KMT09's model and predictions. In Section 3.7, we compare our $\Sigma_{\rm HI}$ and $R_{\rm H2}$ images with KMT09's predictions. We then compare the derived H_2 distribution with the existing CO observations and investigate the existence of the "CO-dark" H_2 gas (Section 3.8). Finally, we discuss and summarize our conclusions (Sections 3.9 and 3.10).

3.2 Data

3.2.1 HI

We use HI data from the Galactic Arecibo L-band Feed Array HI Survey (GALFA-HI). GALFA-HI uses ALFA, a seven-beam array of receivers mounted at the focal plane of the 305-m Arecibo telescope, to map HI emission in the Galaxy. Each of seven dual polarization beams has an effective beamsize of $3.9'$ $\times$ $4.1'$ and a gain of 8.5–11 Jy K^{-1} (Peek et al. 2011). The GALFA-HI spectrometer, GALSPECT, has a velocity resolution of 0.184 km s^{-1} (872 Hz) and covers -700 km s^{-1} $< v <$ $+700$ km s^{-1} (7 MHz) in the Local Standard of Rest (LSR) frame[2].

GALFA-HI adopts two different scanning modes, the drift and basketweaving modes. In the drift mode, the telescope is fixed at azimuth of 0° or 180° and the sky is allowed to drift by. In the basketweaving mode, on the other hand, the telescope is fixed at the meridian and is driven up and down in zenith angle over the chosen declination (Dec) range. For each day of observations, the starting point of the telescope is shifted in right ascension (RA) by $\sim 12'$ such that the entire proposed region is covered. ALFALFA (Giovanelli et al. 2005) and GALFACTS (Guram & Taylor 2009), two large area surveys with which GALFA-HI commensally observes, use the drift and basketweaving mode, respectively.

GALFA-HI combines HI data from many individual projects, both in solo and commensal modes. Reduction of HI data is performed with the GALFA-HI Standard Reduction (GSR) pipeline. Full details of GSR are presented in Peek et al. (2011), but here we briefly describe its most important steps. First, HI spectra are corrected for the intermediate frequency (IF) gain by dividing them by a reference spectrum. This reference spectrum is obtained via the least-squares frequency switching (LSFS) technique (Heiles 2005). The LSFS observation is performed at the beginning of each observing period and the obtained IF

[2]In this chapter, all velocities are quoted in the LSR frame.

gain spectrum is used for the whole period's data. Second, the HI spectra are searched for baseline ripples produced by reflections in the signal chain, the primary reflector, and the Gregorian dome. This initial calibration is done by examining the HI data in the Fourier space and removing the Fourier components that correspond to the reflection patterns. Third, the gain calibration is applied to the HI spectra. The relative gains of each beam over each day of observations are determined by finding the points where beam tracks intersect and comparing the HI spectra of each beam. This gain calibration is most effective for the scans obtained in the basketweaving mode, where a large number of intersection points are produced. Lastly, the fully calibrated HI spectra are gridded onto the image plane in Cartesian coordinates. The gridded HI data are then calibrated for the first sidelobe and the final brightness temperature scale. The lower angular resolution HI data from the Leiden-Argentine-Bonn (LAB) Survey (Kalberla et al. 2005) are used for the final brightness temperature calibration.

The GALFA-HI first data release (DR1) has been presented by Peek et al. (2011). The DR1 data cover 7520 deg^2 of sky and have been produced using 3046 hours of data obtained from 12 individual projects. RMS noise in a 1 km s^{-1} channel ranges from 140 mK to 60 mK with a median of 80 mK. The DR1 data can be downloaded at https://purcell.ssl.berkeley.edu/. The HI data used in this chapter are part of DR1 and have been obtained from TOGS2 (Turn-On GALFA Spectrometer2; PI: C. Heiles & S. Stanimirović), a2004 (HI Survey of the Taurus Molecular Cloud; PI: P. Goldsmith), and a2174 (HI Survey of the Perseus Molecular Cloud; PI: L. Knee). We combined the scans from these three projects and produced an HI cube centered at (RA,Dec) = ($03^{\rm h}29^{\rm m}52^{\rm s}$,$+30°34'1''$) in J2000[3] with a size of $14.8° \times 9°$.

3.2.2 Infrared

We use 60 μm and 100 μm images from the Improved Reprocessing of the *IRAS* Survey (IRIS) (Miville-Deschênes & Lagache 2005). IRIS provides an improved zero point calibration and correction for the zodiacal light and striping in the images, as well as increased angular resolution compared to the original *IRAS* images. The angular resolution at 60 μm and 100 μm is $4'$ and $4.3'$, respectively, comparable to that of the GALFA-HI data. The noise level in the IRIS images is approximately 0.07 MJy sr^{-1} and 0.48 MJy sr^{-1} at 60 μm and 100 μm, respectively.

[3]In this chapter, all coordinates are quoted in J2000.

3.2.3 CO

We use the CO integrated intensity image provided by Dame et al. (2001). Dame et al. (2001) combined CO surveys of the Galactic plane and local molecular clouds and produced a composite survey of the entire Galaxy at an angular resolution of $8.4'$. The CO data were obtained by the 1.2-m telescope at the Harvard-Smithsonian Center for Astrophysics (CfA). The spectra were sampled with an angular spacing of $7.5'$ and the final data cube has a uniform RMS noise of 0.25 K per a 0.65 km s^{-1} channel. To estimate CO integrated intensity, $I_{\rm CO}$, Dame et al. (2001) integrated CO emission from $v = -15$ km s^{-1} to $+15$ km s^{-1}. See Section 2 of Dame et al. (2001) for details of the observations and analysis.

While we use the CfA CO data for the most of our analysis, ^{13}CO($J = 1 \rightarrow 0$) data provided by the COMPLETE survey (Ridge et al. 2006a) are used in Section 3.7. As ^{13}CO($J = 1 \rightarrow 0$) is a better tracer of dense molecular gas than CO, we use the $I_{^{13}\rm CO}$ image with a size of $6.25^\circ \times 3^\circ$ to set the boundaries of the dark and star-forming regions in Perseus. The ^{13}CO($J = 1 \rightarrow 0$) data were obtained by the 14-m Five College Radio Astronomy Observatory (FCRAO) telescope at an angular resolution of $44''$. To study Perseus, Ridge et al. (2006a) integrated ^{13}CO($J = 1 \rightarrow 0$) emission from $v = 0$ km s^{-1} to $+20$ km s^{-1} with a velocity resolution of 0.07 km s^{-1} and estimated an average RMS noise per channel of 0.17 K.

3.2.4 A_V

We use the A_V image provided by the COMPLETE survey. This image was constructed from the Two Micron All Sky Survey (2MASS) Point Source Catalog using the NICER algorithm (Lombardi & Alves 2001) at an angular resolution of $5'$. The NICER algorithm estimates reddening along a line of sight by comparing the observed colors of background stars to the intrinsic colors (measured in a nearby control field, where the extinction is negligible). Note that this method does not assume a grain-size distribution or dust emissivity and therefore provides the most reliable estimate of the total gas column density in a molecular cloud (e.g., Goodman et al. 2009; GPS09 hereafter). In this chapter, however, we do not directly use the 2MASS A_V image to derive the total gas column density because it only covers the central region of Perseus, while we are mainly interested in the cloud outskirts. Instead, we use the 2MASS A_V image to calibrate our τ_{100} image derived from the IRIS data (Section 3.4.4).

3.2.5 Treatment of Angular Resolution

In this chapter, we combine the data sets described above in several ways. In each case, we first bring all input data sets to common angular resolution determined by the lowest angular resolution data set. This is done by performing convolution with an appropriate Gaussian kernel. For example, to determine the velocity range of HI emission based on the correlation between N(HI) and the dust column density, we smooth the HI data to the angular resolution of the 2MASS A_V image, $5'$ (Section 3.3.2). To derive $N(\mathrm{H_2})$, the IRIS and HI data are convolved with a Gaussian kernel to have an angular resolution of $4.3'$. Consequently, our final Σ_{HI}, Σ_{H2}, and R_{H2} images have an angular resolution of $4.3'$ (Sections 3.4.5 and 3.7).

3.3 Methodology: Steps in Deriving N(HI)

3.3.1 General Properties of HI Spectra

The main component of the HI emission in Perseus is centered at $v = +4 \sim +8$ km s^{-1}. Compared to the molecular gas traced by CO, the peak of the HI emission is offset by 2–3 km s^{-1}. As an example, we compare the HI and CO spectra at the position of IC348 in Figure 3.2. There are (at least) two components in the HI spectrum and the stronger one peaks at $v \sim +5$ km s^{-1}. Interestingly, the location of the dip between the two HI components corresponds to the CO peak at $v \sim +8$ km s^{-1}. This dip is likely from HI self-absorption (HISA) and indicates the presence of very cold neutral medium (spin temperature $T_{\mathrm{s}} < 50$ K; e.g., Gibson 2010). The correction for HISA requires a knowledge of the relative contributions from cold and warm gas to the HI emission, which can be obtained via HI absorption measurements. However, only two HI absorption measurements exist for Perseus (e.g., Heiles & Troland 2003a). This is clearly too sparse to interpolate the relative contributions from cold and warm gas throughout the whole molecular cloud. Therefore, we do not apply the correction for HISA to N(HI) but we investigate the optical depth effect in Section 3.7.1.1 by applying the first order opacity correction.

3.3.2 Determining the Velocity Range

To determine the velocity range of HI emission associated with Perseus, we investigate the correlation between N(HI) and the dust column density. The correlation between HI emission and FIR emission has been well-established for high Galactic latitudes (e.g., Boulanger et al. 1996). We use the 2MASS A_V

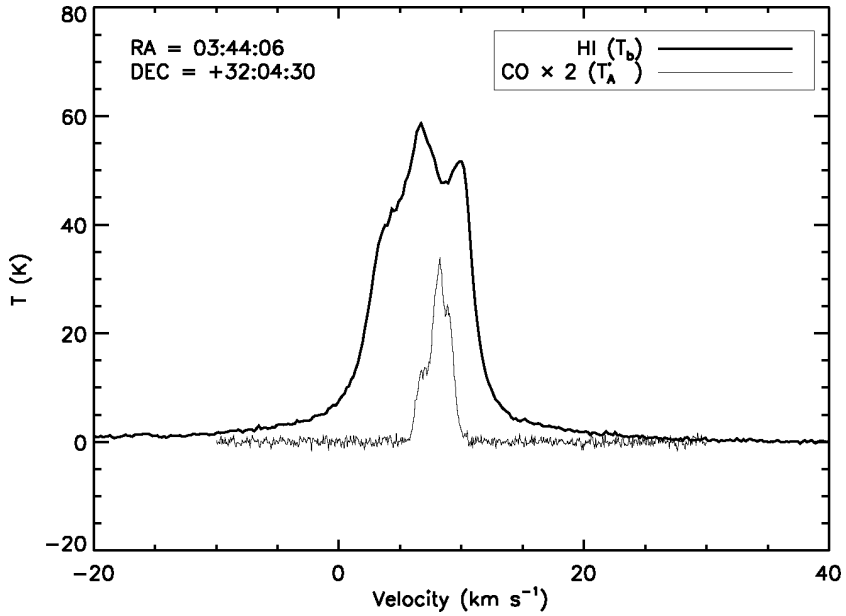

Fig. 3.2. — HI (thick) and CO (thin) spectra at the position of IC348. For comparison, CO is amplified twice. The main component of HI peaks at $v \sim +5$ km s^{-1} and is offset by 2–3 km s^{-1} from the peak of CO.

image as a tracer of the dust column density and smooth the HI data to the angular resolution of the 2MASS A_V image. We fix the central velocity of HI emission at $v = +5$ km s^{-1} based on Section 3.3.1 and integrate HI emission using a velocity width Δv increasing from 2 km s^{-1} to 80 km s^{-1} with 2 km s^{-1} intervals. For each derived N(HI) image, we calculate the correlation coefficient between N(HI) and 2MASS A_V. Only data points with signal-to-noise ratio (S/N) > 5 in the 2MASS A_V image are used for this calculation. Figure 3.3 shows the correlation coefficient as a function of Δv. Although the correlation coefficient is never very high, there is a clear peak at $\Delta v \sim 10$ km s^{-1}. The lack of strong correlation between A_V and N(HI) has been noticed before and is mostly ascribed to the presence of molecular gas (e.g., Reach et al. 1994; Dame et al. 2001; Leroy et al. 2009). We take the correlation coefficient of 0.15 (half of the maximum) as a threshold and use the corresponding Δv of 20 km s^{-1} to derive N(HI) under the assumption of optically thin HI gas[4]. The derived N(HI) ranges from 3.5×10^{20} cm^{-2} to 1.3×10^{21} cm^{-2} with a median of 7.9×10^{20} cm^{-2}. We present the N(HI) image in Figure 3.4.

Sancisi et al. (1974) and Imara & Blitz (2011) estimated N(HI) for Perseus independently and their results are essentially consistent with ours. Sancisi et al. (1974) obtained HI data for Perseus using the 25-m Dwingeloo telescope and estimated N(HI) by integrating HI emission from $v = -10$ km s^{-1} to +20

[4]For optically thin HI gas, N(HI) is calculated by $N(\mathrm{HI}) = 1.823 \times \int T_\mathrm{b} dv$ (cm^{-2}), where T_b is the brightness temperature.

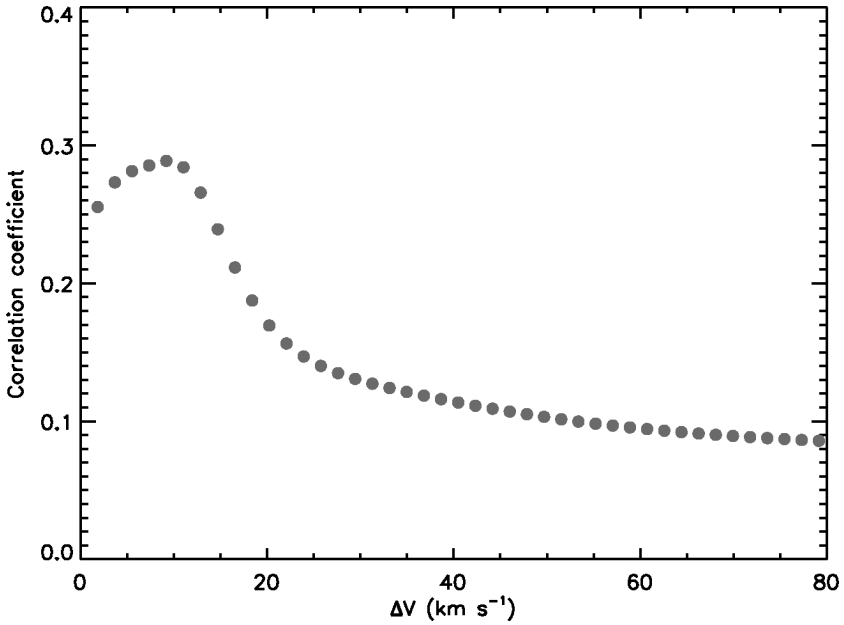

Fig. 3.3. — Correlation coefficient between N(HI) and 2MASS A_V as a function of velocity width Δv. Data points with S/N > 5 in the 2MASS A_V image are used to calculate the correlation coefficient.

km s^{-1}. In addition, they attempted to subtract the foreground and background N(HI) by comparing the HI emission in the direction of Perseus to the HI emission measured in a nearby field spatially offset by a few degrees. They found an average N(HI) associated with Perseus $\sim 5 \times 10^{20}$ cm^{-2}. This is close to our median N(HI). On the other hand, Imara & Blitz (2011) used HI data from the LAB survey and estimated N(HI) by integrating HI emission from $v = -8$ km s^{-1} to $+14$ km s^{-1}. To determine the velocity range for N(HI), they assumed that HI spectra can be approximated with Gaussian functions and set Δv to be equal to four times the standard deviation of the Gaussian component associated with Perseus. In summary, both Sancisi et al. (1974) and Imara & Blitz (2011) derived N(HI) under the assumption of optically thin HI gas and their velocity ranges for N(HI) are consistent with ours.

3.4 Methodology: Steps in Deriving $N(H_2)$

3.4.1 Removal of Point Sources from the IRIS Data

Before further processing, we remove point sources from the 60 μm and 100 μm images. We identify compact point sources from the *IRAS* Point Source Catalog that have $I_{60} > 1$ MJy sr^{-1} and remove them by applying a circular mask with a radius equal to twice the angular resolution of the 100 μm image. These

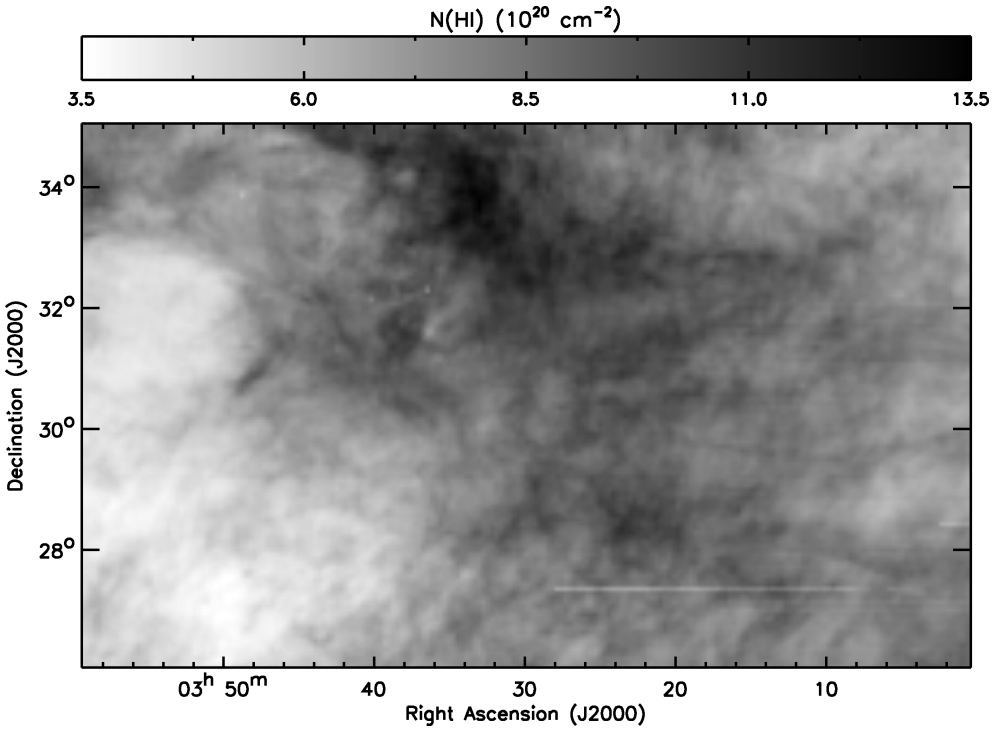

Fig. 3.4. — N(HI) image at an angular resolution of 4.3′. HI emission is integrated from $v = -5$ km s^{-1} to +15 km s^{-1} and N(HI) is derived under the assumption of optically thin HI gas.

masks are shown as blank pixels in Figures 3.6, 3.7, 3.10, and 3.14.

3.4.2 Exclusion of Possible Contaminations

As Perseus belongs to the Taurus-Auriga-Perseus molecular cloud complex and our data cover a large area on the sky ($\sim 15^\circ \times 9^\circ$), there is a concern of including molecular gas not associated with Perseus in our analysis. To investigate this, we plot I_{60} and I_{100} as a function of N(HI) in Figure 3.5. As I_{60}/N(HI) and I_{100}/N(HI) are approximations of dust-to-gas ratio (DGR), an overall linear relation, implying a single DGR, is a reasonable expectation for a single molecular cloud. Figure 3.5 shows that the data points are segregated into two possible distinct features at N(HI) $\sim 6 \times 10^{20}$ cm^{-2}. The majority of the data points shows a global linear relation between N(HI) and FIR emission. These data points are shown in gray and we assume that they mostly trace Perseus. However, the data points in black have a slightly different slope. We selected the black data points as having N(HI) $< 6 \times 10^{20}$ cm^{-2}. In Figure 3.6, we show the spatial distribution of the black data points by overlaying them on the 100 μm image. Clearly, they are all found at the southeast edge of the image in the direction of Taurus. Taurus is centered at (α,δ) = (04^h30^m,+28°)

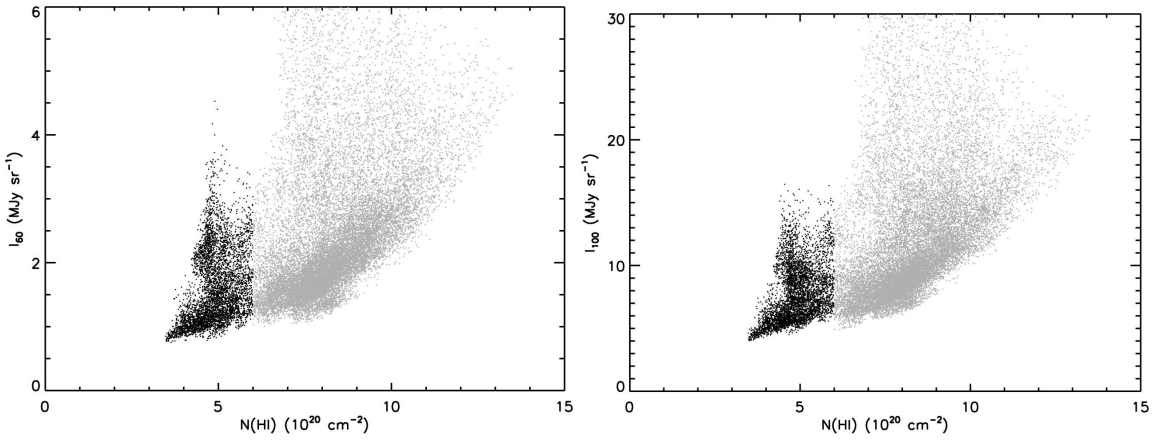

Fig. 3.5. — (Left) I_{60} as a function of N(HI). (Right) I_{100} as a function of N(HI). The gray data points are assumed to mostly trace Perseus and the black data points are likely from the Taurus molecular cloud. See Section 3.4.2.

and has $v_{\rm CO} = 0 \sim +12$ km s^{-1} (e.g., Narayanan et al. 2008). As a distinct molecular cloud, Taurus would have a different DGR. To avoid any possible contamination, we exclude (blank) the black data points from the IRIS images and further analysis.

In addition to the above consideration, the warm dust ring that stands out in the dust temperature image (Section 3.4.3) is an additional source of contamination and we exclude it from further analysis.

3.4.3 $T_{\rm dust}$ and τ_{100}

For optically thin dust grains at an equilibrium temperature $T_{\rm dust}$, the optical depth at 100 μm, τ_{100}, is determined by:

$$\tau_{100} = \frac{I_{100}}{B(T_{\rm dust}, \lambda_{100})}, \tag{3.1}$$

where I_{100} is the measured intensity at 100 μm and $B(T_{\rm dust}, \lambda_{100})$ is the intensity of a blackbody of temperature $T_{\rm dust}$ at 100 μm. To estimate τ_{100}, we first estimate $T_{\rm dust}$ using the ratio I_{60}/I_{100}. Under the assumption that the mass absorption coefficient, κ_λ, has a wavelength dependence such as $\kappa_\lambda \propto \lambda^{-\beta}$, $T_{\rm dust}$ can be estimated from:

$$\frac{I_{60}}{I_{100}} = \left(\frac{\lambda_{60}}{\lambda_{100}}\right)^{-(3+\beta)} \frac{\exp(hc/\lambda_{100}kT_{\rm dust}) - 1}{\exp(hc/\lambda_{60}kT_{\rm dust}) - 1}, \tag{3.2}$$

where h is the Planck constant and k is the Boltzmann constant. The emissivity spectral index, β, can vary between 1 (for amorphous carbon) and 2 (for metallic and crystalline dielectric material), depending on the grain composition and size. Throughout this chapter, we adopt $\beta = 2$ based on the discussions in Schnee et al. (2005; S05 hereafter). To estimate $T_{\rm dust}$, we smooth the 60 μm image to the angular resolution of

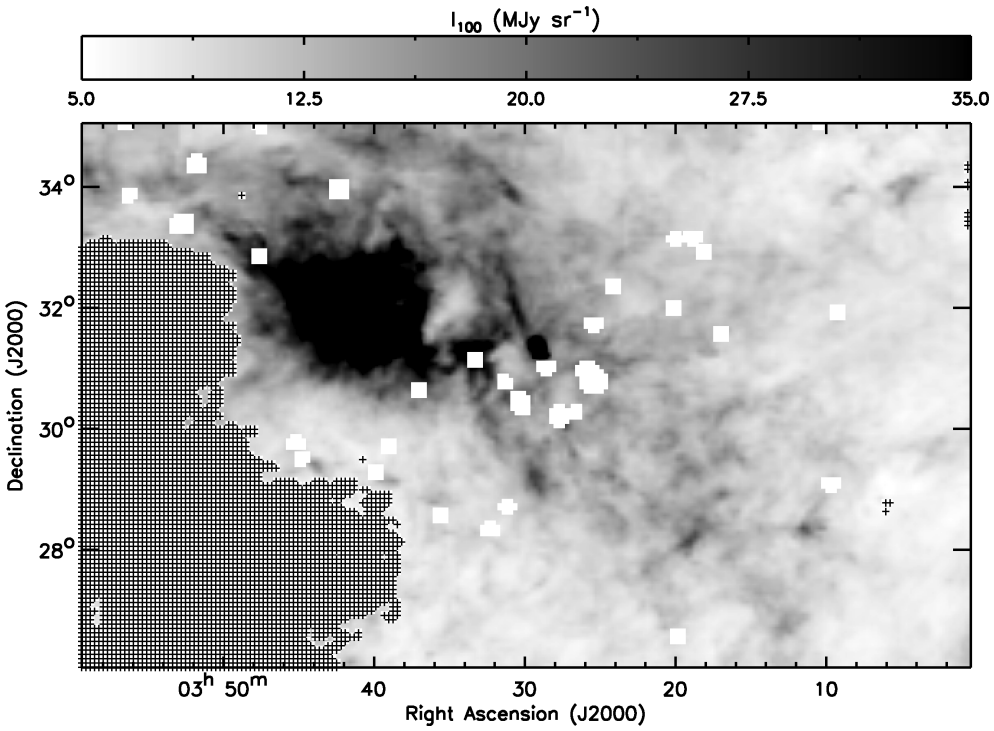

Fig. 3.6. — IRIS 100 μm image with the black data points from Figure 3.5.

the 100 μm image.

I_{60} may include a significant contribution from stochastically heated very small grains (VSGs) that must be accounted for. To do this, we adopt the method used by S05. First, we smooth the 60 μm and 100 μm images to the angular resolution of the $T_{\rm dust}$ map derived by Schlegel et al. (1998; SFD98 hereafter). SFD98 used the low resolution DIRBE 100 μm and 240 μm data to derive $T_{\rm dust}$; the contribution from VSGs is expected to be negligible at these wavelengths (e.g., Li & Draine 2001). Second, we calculate $T_{\rm dust}$ based on 100% of I_{100} and a lesser percentage of I_{60}, assuming $\beta = 2$. The fraction of I_{60} is chosen to minimize the average difference between our $T_{\rm dust}$ and SFD98's $T_{\rm dust}$. We find that the best matching fraction is 22%, meaning that 78% of I_{60} is due to VSGs. This result is consistent with S05, who found 26%, but lower than the prediction of interstellar dust model for the solar neighborhood ($\sim$40%; Désert et al. 1990).

We present the $T_{\rm dust}$ image in Figure 3.7. Our $T_{\rm dust}$ image is generally consistent with the $T_{\rm dust}$ image derived by S05, but shows systematically slightly lower $T_{\rm dust}$. The difference between our $T_{\rm dust}$ and S05's $T_{\rm dust}$, $T_{\rm dust} - T_{\rm dust,S05}$, has a median of -1 K. This discrepancy likely arises from the fact that S05 adopted a $T_{\rm dust}$-dependent formula for β and used a different fitting algorithm. Their $T_{\rm dust}$-dependent formula for

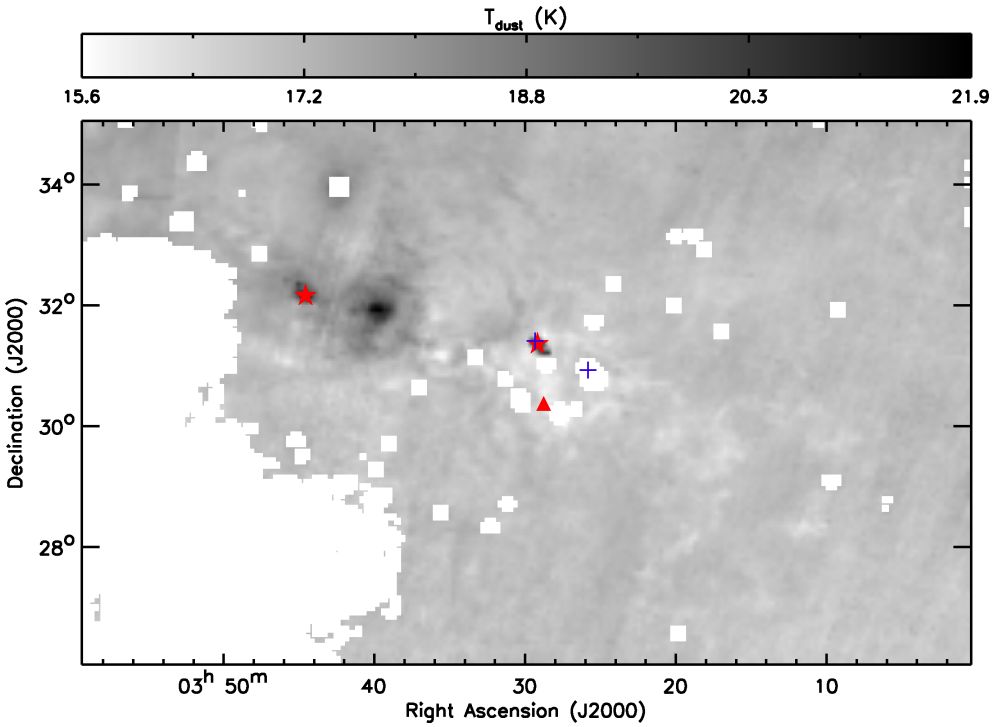

Fig. 3.7. — $T_{\rm dust}$ image derived from the IRIS 60 μm and 100 μm images after accounting for the contribution from VSGs. Several B-type stars as potential dust heating sources are marked; B8 V-type stars (BD+30°540 and BD+30°549) are shown as blue crosses (Černis 1990); B5 V-type stars (BD+31°643 and SVS3) are shown as red stars (Černis 1990; Luhman et al. 2003); B4 IV–V-type star (BD+29°566) is shown as a red triangle (Černis 1990).

β considered the observed inverse relation between $T_{\rm dust}$ and β and had two free parameters (Equation 2 of S05). To simultaneously fit these two free parameters, S05 used the IDL routine AMOEBA, which adopts the downhill method of Nelder & Meade (1965), while we estimated the best matching parameter using the least-squares method.

$T_{\rm dust}$ across Perseus ranges from ∼16 K to ∼22 K. The lowest $T_{\rm dust}$ regions spatially correlate with the highest A_V, in agreement with the expectation for dense and cold molecular gas. Several localized regions with high $T_{\rm dust}$ stand out; two are the star-forming regions, IC348 and NGC1333, while the third is a ring-like feature located at $(\alpha,\delta) = (03^{\rm h}39^{\rm m}30^{\rm s},+32°)$ with a radius of ∼56′. Ridge et al. (2006b) investigated this ring in detail using *IRAS*, *MSX*, 2MASS A_V, and CO data and concluded that the ring, the product of an HII region driven by the B-type star HD 278942, is likely located behind IC348. However, they also argued that the ring is interacting with Perseus, based on the spatial correlation between 8 μm emission and 2MASS A_V. The ring is visible in the 2MASS A_V image but at a much lower contrast,

implying that the ring is not as significant column density feature as one might infer from the IRIS data. Therefore, we exclude it from further analysis by applying a circular mask of radius of $56'$. This mask size is consistent with what Ridge et al. (2006b) used to separate the ring from the Perseus cloud component, $\sim 50'$.

At this point, we refined the zero point of the τ_{100} image by assuming that the dust column density traced by τ_{100} is proportional to $N(\mathrm{HI})$ for the regions dominated by diffuse atomic gas. Under this assumption, τ_{100} would approach zero as $N(\mathrm{HI})$ approaches zero and any offset from this relation is likely due to the uncertainties in the zero points of the IRIS images. As a result of this exercise, we added 1.8×10^{-4} to the τ_{100} image. The observed offset in τ_{100} implies a small additional uncertainty in T_{dust}, which is of order of 0.03–0.6 K.

3.4.4 A_V

Once we estimate τ_{100} using the VSG-corrected T_{dust}, we convert τ_{100} to A_V by:

$$A_V = X\tau_{100}, \tag{3.3}$$

where X is the conversion factor that relates the dust column density to the extinction in the V-band. The conversion factor $X = 720$ is estimated by finding the best agreement between our derived A_V image and the 2MASS A_V image for the region where the two images overlap. Our A_V and 2MASS A_V have a 1:1 relation but with an average scatter of $\sim$0.5 mag. This scatter around the 1:1 relation is mostly attributed to the variation in T_{dust} along a line of sight (e.g., GPS09).

We note that the bootstrapping of our A_V image derived from the IRIS data with the A_V image derived from the 2MASS extinction data is motivated by GPS09. For Perseus, GPS09 inter-compared three methods for measuring total gas column density; extinction mapping at near-infrared (NIR) wavelengths, thermal emission mapping at FIR wavelengths, and CO emission mapping. They found that the dust-based measures (NIR extinction and FIR emission) are superior to the gas-based measure (CO emission) and particularly suggested the NIR extinction as the best probe of total gas column density. Any molecular transition, such as CO emission, traces a limited range of volume densities due to the critical density for excitation, opacity, and depletion. The dust-based measures have a wider dynamic range, but the NIR extinction measure saturates at high extinctions where background sources cannot be observed and the FIR emission measure is limited at low extinction values. In addition, the FIR emission measure suffers

from its intrisic uncertainty, the variation of $T_{\rm dust}$ along a line of sight. Overall, the NIR extinction measure is the best probe up to its saturation level. Therefore, our calibration of τ_{100} to the 2MASS A_V image would provide a better estimate of the total gas column density, compared to the total gas column density derived solely from the IRIS data.

3.4.5 Dust-to-Gas Ratio and $N(\mathrm{H_2})$

Finally, we calculate $N(\mathrm{H_2})$ by:

$$N(\mathrm{H_2}) = \frac{1}{2}\left(\frac{A_V}{\mathrm{DGR}} - N(\mathrm{HI})\right), \tag{3.4}$$

where DGR is defined by DGR $= A_V/N(\mathrm{H})$ and $N(\mathrm{H}) = N(\mathrm{HI}) + 2\mathrm{N}(\mathrm{H_2})$.

To measure DGR in Perseus, we plot A_V as a function of $N(\mathrm{HI})$ over the whole cloud in Figure 3.8. As we expect $N(\mathrm{H}) \sim N(\mathrm{HI})$ for the regions dominated by diffuse atomic gas (which correspond to the majority of data points in Figure 3.8), the fitted slope $A_V/N(\mathrm{HI}) = 1.1 \times 10^{-21}$ mag cm^2 is a good measure of DGR. Our estimate is $\sim$2 times higher than the typical Galactic DGR, 5.3×10^{-22} mag cm^2 (e.g., Bohlin et al. 1978). This is not concerning as notable variations have been found for the Galactic DGR. For example, Kim & Martin (1996) compiled $A_V/N(\mathrm{H})$ values for the Galaxy derived from UV absorption measurements from literature and found that $A_V/N(\mathrm{H})$ can be higher than the typical Galactic value by a factor of three (their Figure 4).

We also compare our DGR estimate with values obtained from two independent methods.

1. *Copernicus/FUSE absorption measurements.* Toward HD 22951, HD 23180, and BD+31°643, *Copernicus/FUSE* measured $\mathrm{H_2}$ directly in absorption (Savage et al. 1977; Rachford et al. 2002). HD 22951 and HD 23180 are B1 stars and BD+31°643 is a B5 star. Towards BD+31°643, Snow et al. (1994) measured A_V= 2.68 mag and combined this with the observed $N(\mathrm{HI})$ and $N(\mathrm{H_2})$ resulting in $A_V/N(\mathrm{H}) = 5.5 \times 10^{-22}$ mag cm^2. However, extinction parameters are not known for HD 22951 and HD 23180. Considering that HD 22951, HD 23180, and BD+31°643 are close to each other on the sky, if we apply $R_V = 3.19$ measured for BD+31°643 to both HD 22951 and HD 23180, we obtain $A_V/N(\mathrm{H}) = (4.6\text{–}6) \times 10^{-22}$ mag cm^2. While these estimates are close to the typical Galactic DGR, we note that they are likely lower limits on the DGR of Perseus, considering that most of the lines of sight surveyed by the *Copernicus/FUSE* are composed of two or more diffuse clouds (e.g., Rachford et al. 2002, 2009). Rachford et al. (2002) compared the observed high rotational transition column

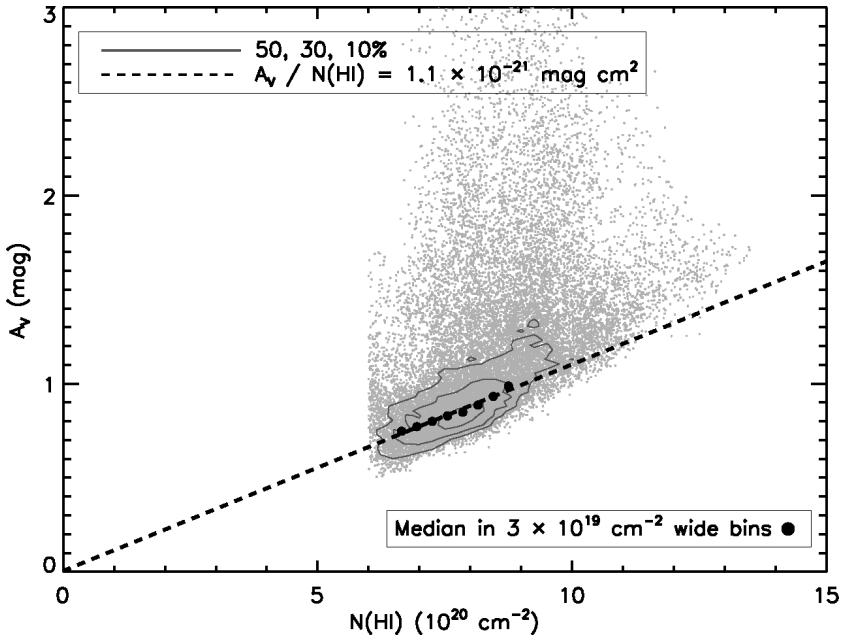

Fig. 3.8. — A_V as a function of N(HI). The contour levels correspond to 50%, 30%, and 10% of the total data points. The black circles are median A_V values in 3×10^{19} cm^{-2} wide bins. The linear least-squares fit for the median A_V values is shown as a black dashed line.

densities of H_2 to the model of H_2 formation, destruction, and ro-vibrational excitation developed by Browning et al. (2003) and found that it is impossible to reproduce the observed column densities under a single cloud assumption. Instead, models with multiple clouds along the line of sight, and/or multiple pathways of incident UV radiation, match much better the observed column densities. Stars preferentially form in regions with high DGR, where dust grains provide both high shielding against photodissociation and sites for H_2 formation. Therefore, if several diffuse clouds exist along the line of sight toward Perseus, the component associated with Perseus likely has a higher DGR. In this case, the DGR measured along the whole line of sight is lower than the actual DGR of Perseus.

2. *Upper limit on the DGR.* Equation (3.4) itself provides an upper limit on the DGR. If the DGR is too high, a large number of data points will have a negative value of $N(H_2)$. For example, if DGR $> 1.5 \times 10^{-21}$ mag cm^2, more than 50% of the pixels with $A_V > 1$ mag will have a negative value of $N(H_2)$. Therefore, it is most likely that the DGR in Perseus is less than 1.5×10^{-21} mag cm^2.

3. *Conclusion.* Based on two independent constraints on the DGR, we conclude that our estimate of $A_V/N(\mathrm{HI}) = 1.1 \times 10^{-21}$ mag cm^2 is midway between the lower and upper limits and therefore represents a very reasonable estimate.

3.4.6 Uncertainty in $N(H_2)$

We estimate the uncertainty in $N(H_2)$ for each pixel by performing a series of Monte Carlo simulations. In these simulations, we take into account the uncertainties in N(HI) and A_V and how they propagate into $N(H_2)$.

For the uncertainty in N(HI), we generate 1000 N(HI) images by using 1000 velocity widths randomly drawn from a Gaussian distribution that peaks at 20 km s^{-1} with 1σ of 4 km s^{-1} (based on Section 3.3.2). The median 1σ of N(HI) due to the systematic uncertainty in using a particular velocity width is 5.6 $\times$ 10^{19} cm^{-2}.

For the uncertainty in A_V, we assess the range of A_V by varying the input parameters and deriving A_V each time. We add/subtract 1σ noise to/from the 60 μm and 100 μm images (0.07 MJy sr^{-1} at 60 μm and 0.48 MJy sr^{-1} at 100 μm) and use $\beta = 1$ or 2. Therefore, we derive the A_V images with 8 different combinations of the input parameters and for each case the contribution from VSGs to I_{60} and X for $A_V = X\tau_{100}$ are determined by finding the best matching parameters. To include the uncertainties of the zero point, we also derive the τ_{100} images with and without the zero point calibration. We find that the contribution from VSGs to I_{60} varies from 0.12 to 0.24 with a median of 0.17, while X varies from 630 to 810 with a median of 728. Finally, we compare the 16 A_V images and find the maximum and minimum estimates of A_V for each pixel.

The uncertainty in N(HI) and the maximum/minimum estimates of A_V are incorporated in a Monte Carlo simulation to produce 1000 $N(H_2)$ images. We use the distribution of the simulated $N(H_2)$ to estimate the uncertainty in $N(H_2)$ on a pixel-by-pixel basis. The median 1σ of $N(H_2)$ is 3.6 $\times$ 10^{19} cm^{-2}.

In addition to the above considerations, several systematic effects are also likely to affect $N(H_2)$: (1) the assumption of a single dust population and temperature along a line of sight, (2) the assumption of a single DGR, and (3) the assumption that H_2 is the dominant source of excess dust emission. As it is difficult to estimate the magnitude of these effects, we do not include them in our Monte Carlo simulations.

3.5 General Results

3.5.1 $T_{\rm dust}$

$T_{\rm dust}$ across Perseus ranges from ∼16 K to ∼22 K with a median of 17 K. This is in agreement with SFD98 who found $T_{\rm dust} \sim 17$ K for the same region and S05 who found a slightly higher $T_{\rm dust} \sim 18$ K for the main body of Perseus. Similarly, Stepnik et al. (2003) derived $T_{\rm dust} \sim 17$ K for the outskirts of Taurus using the DIRBE data at 140 μm and 240 μm.

As shown in Figure 3.7, the lowest $T_{\rm dust}$ regions spatially correlate with the A_V and CO images, in agreement with the expectation for dense and cold clouds. The prominent minima in $T_{\rm dust}$ correspond to B5, B1E, B1, L1448, L1451, and L1455. These dark regions contain a number of IR sources and Herbig-Haro objects that are considered to be associated with pre-main sequence stars (e.g., Bally et al. 2008), but the luminosities of these objects are so low that their influence on the overall energy budget of the clouds would be negligible. Therefore, $T_{\rm dust}$ within these dark regions is determined by the external ISRF and dust grain properties. Low $T_{\rm dust}$ in B5, B1E, B1, L1448, L1451, and L1455 compared to the surrounding regions suggests that the inside of these regions gas is dense enough to have sufficient shielding against the external ISRF, leading to efficient cooling. For example, B5 has limb-brightening in CO, indicating a cold cloud interior surrounded by a photo-heated exterior (e.g., Beichman et al. 1988).

Figure 3.7 also shows several localized regions with high $T_{\rm dust}$. One of the prominent features is the warm dust ring at $(\alpha,\delta) = (03^{\rm h}39^{\rm m}30^{\rm s},+32^{\circ})$, already discussed in Section 3.4.3. The other high $T_{\rm dust}$ features include IC348 and NGC1333. To quantify how much hotter these star-forming regions are, we plot the histograms of $T_{\rm dust}$ in Figure 3.9. For the histograms, we use the data points in the rectangular boxes shown in Figure 3.10. Each box has either a dark or a star-forming region and extends up to the edge of the image. The width of each box is set based on the COMPLETE $^{13}{\rm CO}(J = 1 \rightarrow 0)$ data to include the whole region of interest. While all regions have a similar median $T_{\rm dust}$ of 17 K, the star-forming regions have data points with higher $T_{\rm dust}$. For example, for IC348 and NGC1333, 11% and 2% of data points have $T_{\rm dust} > 18$ K, while for B5, B1E, and B1, all data points have $T_{\rm dust} < 18$ K. The data points with $T_{\rm dust} > 18$ K are found in the central parts of IC348 and NGC1333, where B-type stars are located (blue crosses and red stars in Figure 3.7), and this implies that the internal radiation field may play a significant role in heating dust grains inside IC348 and NGC1333. This possibility is discussed further in the next section.

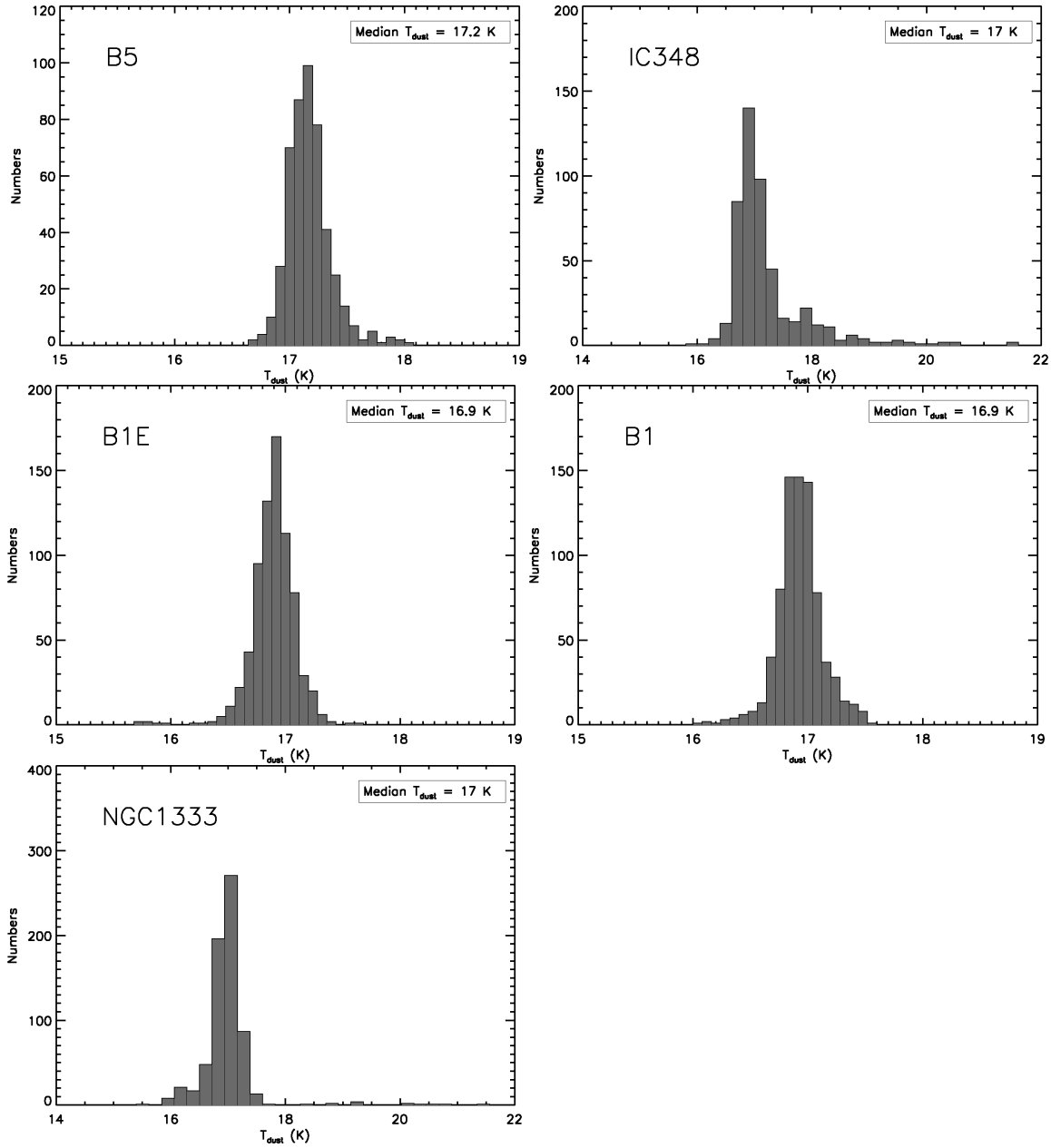

Fig. 3.9. — Histograms of $T_{\rm dust}$. The median $T_{\rm dust}$ is given in the top right corner of each plot.

3.5.2 ISRF: External or Internal?

We now investigate possible heating sources that can result in the measured $T_{\rm dust}$. As we mentioned in Section 3.1, KMT09's model assumes a uniform external ISRF. Understanding the origin of ISRF is therefore important for comparison between observations and the model. There are two possible sources of ISRF that are responsible for the measured $T_{\rm dust}$ across Perseus: (1) the UV flux from the B-type stars in

Perseus (local) and (2) the UV radiation field determined by the overall stellar distribution in the Galaxy (global).

1. We consider two B5 V-type stars in Perseus (red stars in Figure 3.7) as possible sources of the local ISRF. All other stars have spectral types later than B5[5]. We assume that the spectral energy distribution of a B-type star is approximately a black body curve (e.g., Spaans et al. 1994) and adopt $T_{\rm eff}$ = 15600 K for a B5 V-type star (Morton & Adams 1968). For λ = 912–2066 Å, two B5 V-type stars emit 2.12 $\times$ 10^{12} erg cm^{-2} s^{-1}. If a distance of 15 pc from each star, which corresponds to $\sim$1/3 of the longitudinal size of our sky coverage, is assumed, the UV flux from the two B5 V-type stars is reduced to 3.04 $\times$ 10^{-5} erg cm^{-2} s^{-1} ($1/r^2$ geometrical dilution). For dust grains in thermal equilibrium, $T_{\rm dust}$ is determined by (Lequeux 2005):

$$G = 4.6 \times 10^{-11} \left(\frac{a}{0.1\ \mu{\rm m}} \right) T_{\rm dust}^6 \ {\rm erg\ cm^{-2}\ s^{-1}}, \tag{3.5}$$

where G is the UV flux and a is the size of dust grains. An absorption efficiency $Q_{\rm a}$ = 1, appropriate for large dust grains that dominate the FIR emission and have a size comparable to UV wavelengths, and a dust emissivity spectral index β = 2 are assumed for Equation (3.5). Therefore, dust grains with a radius a = 0.1 μm in the UV radiation field of 3.04 $\times$ 10^{-5} erg cm^{-2} s^{-1} would have $T_{\rm dust}$ $\sim$ 9.3 K. Note that we do not consider the decrement of UV flux by dust attenuation. Therefore, if the B-type stars are the only sources of the ISRF, we would expect $T_{\rm dust} \lesssim$ 9.3 K in the outskirts of Perseus.

2. We consider the global Galactic ISRF of Porter & Strong (2005). Porter & Strong (2005) adopted the Galactic stellar and dust distribution models and calculated the radiation field from stars at λ = 0.1–1000 μm. The ISRF was found to be the most intense in the inner Galaxy, to decrease toward the Galactic poles, but to remain steady up to $\sim$5 kpc from the Galactic plane. For $R_{\rm gal}$ (Galactocentric radius) = 0 and z (Galactocentric height) = 0, the radiation field at 0.1 μm is $\sim$0.08 eV cm^{-3} and for $R_{\rm gal}$ = 0 and z = 5 kpc, the radiation field at 0.1 μm is $\sim$0.01 eV cm^{-3} (Figure 2 of Porter & Strong 2005). If we assume that this $\sim$87.5% decrement of the UV radiation field at $R_{\rm gal}$ = 0 from

[5]Two B8 V-type stars in NGC1333 (blue crosses in Figure 3.7) contribute negligibly to the UV flux. We do not consider the B4 IV–V-type star (red triangle in Figure 3.7) due to its uncertain stellar classification (e.g., Lesh 1969; Klochkova & Kopylov 1985; Černis 1990). Nevertheless, inclusion of this star does not change our result.

$z = 0$ to 5 kpc would be applicable for $R_{\rm gal} \sim 8$ kpc, the UV radiation field at $z \sim -100$ pc (the location of Perseus; $R_{\rm gal} \sim 8$ kpc and $z \sim -100$ pc) would be between 2.7×10^{-3} (the UV radiation field in the solar neighborhood at $\lambda = 912$–2066 Å; G_0) and 3.4×10^{-4} erg cm^{-2} s^{-1} (12.5% of G_0). Applying Equation (3.5), this corresponds to 14 K $< T_{\rm dust} <$ 20 K. As our median $T_{\rm dust} \sim 17$ K is indeed in this range, the UV ISRF determined by the overall stellar distribution in the Galaxy could be the dominant heating source for dust grains across Perseus.

Therefore, we conclude that Perseus is embedded in the uniform Galactic ISRF that heats dust grains up to $T_{\rm dust} \sim 17$ K, except for the central parts of IC348 and NGC1333 where the radiation from the B-type stars is dominant.

3.6 The HI-H_2 Transition in Perseus: Theoretical Perspective

KMT08 modeled H_2 formation and photodissociation for a spherical cloud that is bathed in a uniform ISRF. They assumed that the HI-H_2 transition is infinitely sharp and found that the location of the transition inside an atomic-molecular complex is solely determined by two dimensionless numbers:

$$\chi = \frac{f_{\rm diss}\sigma_{\rm d} c E_0^*}{n_{\rm CNM}\mathcal{R}} \tag{3.6}$$

$$\tau_{\rm R} = n_{\rm CNM}\sigma_{\rm d} R. \tag{3.7}$$

Here $f_{\rm diss} \sim 0.1$ is the fraction of absorptions of LW photons that produce H_2 dissociation rather than decay back to a bound state, $\sigma_{\rm d}$ is the dust absorption cross section per H nucleus in the LW band, E_0^* is the number density of LW photons, $n_{\rm CNM}$ is the number density of CNM in the HI shielding layer, $\mathcal{R}$ is the H_2 formation rate coefficient on dust grains, and R is the cloud radius. χ is the ratio of the rate at which LW photons are absorbed by dust grains to the rate at which they are absorbed by H_2. We can consider χ as a dimensionless measure of the strength of the ISRF. For example, in strong radiation fields, H_2 molecules are easily photodissociated and therefore the absorption of LW photons is dominated by dust grains (large χ). On the contrary, in weak radiation fields, H_2 molecules survive and due to their large resonant cross section the absorption of LW photons is dominated by H_2 molecules (small χ). $\tau_{\rm R}$ is simply the dust optical depth that the cloud would have if its density is equal to $n_{\rm CNM}$.

Using χ and $\tau_{\rm R}$, KMT08 derived $x_{\rm H2}$, the fraction of the cloud radius where the HI-H_2 transition

occurs:

$$\begin{aligned} x_{\rm H2} &= \left[1 - \frac{3\psi}{4(\tau_{\rm R} + 0.2\psi)}\right]^{1/3} \\ &\approx 1 - \frac{\psi}{4\tau_{\rm R} - 0.7\psi} \end{aligned} \tag{3.8}$$

where

$$\psi = \chi \frac{2.5 + \chi}{2.5 + \chi e}.$$

Then, the dust optical depth through the HI shielding layer, $\tau_{\rm HI}$, can be determined by:

$$\begin{aligned} \tau_{\rm HI} &= n_{\rm CNM} \sigma_{\rm d} R (1 - x_{\rm H2}) \\ &\approx \frac{\tau_{\rm R} \psi}{4\tau_{\rm R} - 0.7\psi}. \end{aligned} \tag{3.9}$$

The HI shielding surface density for H_2 formation, $\Sigma_{\rm HI,s}$, is simply:

$$\Sigma_{\rm HI,s} = \tau_{\rm HI} \left(\frac{\mu_{\rm H}}{\sigma_{\rm d}}\right), \tag{3.10}$$

where $\mu_{\rm H}$ is the mass per H nucleus.

To investigate what fraction of the gas in an atomic-molecular complex is molecular, KMT09 simplified the above equations as follows. First, as both $\sigma_{\rm d}$ and $\mathcal{R}$ are the measures of dust surface area, their ratio is nearly unity and drops out of Equation (3.6). Second, $n_{\rm CNM}$ is determined from the condition of pressure balance between the cold neutral medium (CNM) and warm neutral medium (WNM) phases:

$$\begin{aligned} n_{\rm CNM} &= \phi_{\rm CNM} n_{\rm min} \\ &= \phi_{\rm CNM} \frac{31 G_0'}{1 + 3.1 Z'^{0.365}}. \end{aligned} \tag{3.11}$$

Here G_0' is the incident UV radiation field and Z' is the metallicity. The primes indicate that quantities are normalized to the values in the solar neighborhood. There is a maximum temperature at which CNM can be in pressure balance with WNM and the corresponding density is the minimum CNM density, $n_{\rm min}$ (Wolfire et al. 2003). Typically, $\phi_{\rm CNM} \sim$ 1–10. As $n_{\rm CNM} \propto G_0' \propto E_0^*$, G_0' and E_0^* drop out of Equation (3.6) and χ becomes purely a function of Z' and $\phi_{\rm CNM}$:

$$\chi = 2.3 \ \frac{1 + 3.1 Z'^{0.365}}{\phi_{\rm CNM}}. \tag{3.12}$$

To estimate $\tau_{\rm R}$, KMT09 started from the mean column density, $\Sigma_{\rm comp}$, of a spherical cloud that consists of a molecular core of number density $n_{\rm mol}$ and a HI shielding layer of number density $n_{\rm CNM}$:

$$\Sigma_{\rm comp} = \frac{4}{3} \mu_{\rm H} n_{\rm CNM} R \left[1 + (\phi_{\rm mol} - 1) x_{\rm H2}^3\right]. \tag{3.13}$$

Here $\phi_{\rm mol}$ is the ratio of $n_{\rm mol}$ to $n_{\rm CNM}$. Once $\tau_{\rm c}$, the dust optical depth that the cloud would have if its HI and H_2 are uniformly mixed, is defined by:

$$\tau_{\rm c} = \frac{3}{4}\left(\frac{\Sigma_{\rm comp}\sigma_{\rm d}}{\mu_{\rm H}}\right), \tag{3.14}$$

$\tau_{\rm R}$ can be expressed as a function of $\tau_{\rm c}$, $\phi_{\rm mol}$, and $x_{\rm H2}$:

$$\begin{aligned}\tau_{\rm R} &= \frac{3}{4}\left(\frac{\Sigma_{\rm comp}\sigma_{\rm d}}{\mu_{\rm H}}\right)\frac{1}{[1+(\phi_{\rm mol}-1)x_{\rm H2}^3]} \\ &= \tau_{\rm c}\frac{1}{[1+(\phi_{\rm mol}-1)x_{\rm H2}^3]}.\end{aligned} \tag{3.15}$$

As a consequence of these simplified functions, the H_2 mass fraction, $f_{\rm H2}$, can be expressed with the following analytic function:

$$\begin{aligned}f_{\rm H2} &= \frac{M_{\rm H2}}{M} \\ &= 1 - \frac{3\psi}{4\tau_{\rm c}}\left[1+\frac{0.8\psi\phi_{\rm mol}}{4\tau_{\rm c}+3(\phi_{\rm mol}-1)\psi}\right]^{-1},\end{aligned} \tag{3.16}$$

where $M_{\rm H2}$ is the H_2 mass and M is the total cloud mass. Finally, the H_2-to-HI ratio, $R_{\rm H2}$, can be expressed as:

$$\begin{aligned}R_{\rm H2} &= f_{\rm H2}/f_{\rm HI} \\ &= f_{\rm H2}/(1-f_{\rm H2}) \\ &= \frac{4\tau_{\rm c}}{3\psi}\left[1+\frac{0.8\psi\phi_{\rm mol}}{4\tau_{\rm c}+3(\phi_{\rm mol}-1)\psi}\right]-1.\end{aligned} \tag{3.17}$$

With ψ being a function of Z' and $\phi_{\rm CNM}$, and $\tau_{\rm c}$ being a function of the cloud gas column density, $R_{\rm H2}$ is determined by the total gas column density, Z', $\phi_{\rm CNM}$, and $\phi_{\rm mol}$, and is independent of the strength of the ISRF. While the total gas column density and Z' are direct observables, $\phi_{\rm CNM}$ and $\phi_{\rm mol}$ are not. KMT09 adopted $\phi_{\rm CNM} = 3$ and $\phi_{\rm mol} = 10$ as fiducial values. Note that the H_2-to-HI ratio can observationally be expressed as $R_{\rm H2} = \Sigma_{\rm H2}/\Sigma_{\rm HI}$.

Another important model prediction is that $\Sigma_{\rm HI,s}$ has a dependence on Z' and is almost independent of the strength of the ISRF. Based on Equation (3.9) and (3.10), $\tau_{\rm HI}$ slightly increases with Z' via $\tau_{\rm R}$ and ψ and $\sigma_{\rm d}$ increases with Z' via $\sigma_{\rm d} = \sigma'_d Z'$. Therefore, $\Sigma_{\rm HI,s}$ decreases with Z' to a power less than unity as $\Sigma_{\rm HI,s} \propto \tau_{\rm HI}/\sigma_{\rm d}$. For solar metallicity, KMT09 predict $\Sigma_{\rm HI,s} \sim 10\ {\rm M}_\odot\ {\rm pc}^{-2}$.

3.7 The HI-H_2 Transition in Perseus: Observational Perspective

From our derived N(HI) and $N(H_2)$ images, we calculate $\Sigma_{\rm HI}$ and $\Sigma_{\rm H2}$ by:

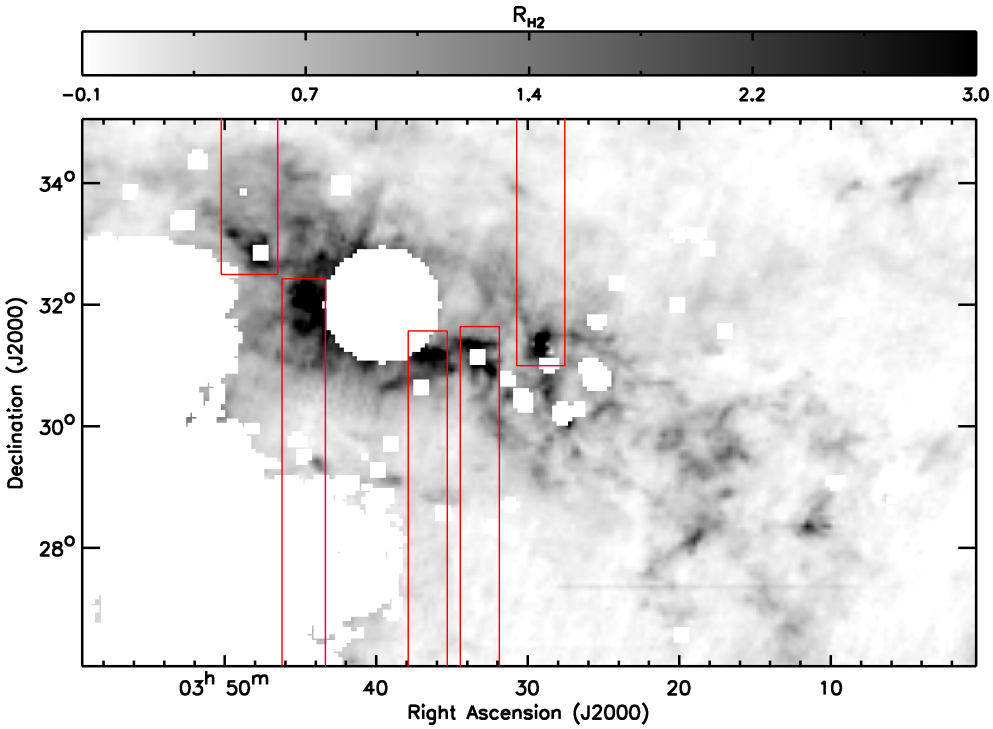

Fig. 3.10. — $R_{\rm H2}$ image. The red rectangular boxes show the boundaries of each dark and star-forming region set by the COMPLETE ^{13}CO($J = 1 \rightarrow 0$) data.

$$\Sigma_{\rm HI}\ ({\rm M}_\odot\ {\rm pc}^{-2}) = \frac{N({\rm HI})}{1.25 \times 10^{20}\ ({\rm cm}^{-2})}$$
$$\Sigma_{\rm H2}\ ({\rm M}_\odot\ {\rm pc}^{-2}) = \frac{N({\rm H_2})}{6.25 \times 10^{19}\ ({\rm cm}^{-2})}. \quad (3.18)$$

We find that $\Sigma_{\rm HI}$ is relatively constant across Perseus with a range of 5–11 M$_\odot$ pc^{-2}, while $\Sigma_{\rm H2}$ has a wider range of 0–73 M$_\odot$ pc^{-2}. This results in a small dynamic range of $\Sigma_{\rm HI} + \Sigma_{\rm H2}$, from 8 M$_\odot$ pc^{-2} to 30 M$_\odot$ pc^{-2} across most of the Perseus cloud.

We then derive $R_{\rm H2} = \Sigma_{\rm H2}/\Sigma_{\rm HI}$, which allows us to directly test KMT09's predictions. The $R_{\rm H2}$ image is presented in Figure 3.10. We find that the derived $R_{\rm H2}$ ranges from 0 to 10 with a median of 0.1. This suggests that diffuse molecular gas is pervasive in Perseus. For example, the data points with $R_{\rm H2} > 1$, which can be considered to be molecular-dominated, comprise only 9% of the total data points. We note that spatial variations in the $R_{\rm H2}$ distribution are mainly determined by the $\Sigma_{\rm H2}$ distribution, due to the small dynamic range of $\Sigma_{\rm HI}$. The high $R_{\rm H2}$ features spatially correlate with the A_V and CO images and correspond to the dark and star-forming regions in Perseus.

3.7.1 $\Sigma_{\rm HI}$ vs $\Sigma_{\rm HI}+\Sigma_{\rm H2}$ for the Dark and Star-forming Regions

To investigate KMT09's predictions, we focus on several dark and star-forming regions in Perseus and measure $R_{\rm H2}$ radially to probe the cloud envelopes with the lowest $R_{\rm H2}$. In Figure 3.11, we plot $\Sigma_{\rm HI}$ as a function of $\Sigma_{\rm HI}+\Sigma_{\rm H2}$ for B5, IC348, B1E, B1, and NGC1333. For each plot we use the data points in the rectangular boxes shown in Figure 3.10. The overlaid curves are KMT09's predictions for particular combinations of input parameters, Z', $\phi_{\rm CNM}$, and $\phi_{\rm mol}$. These parameters will be determined and discussed in Section 3.7.2.1.

We find an almost constant $\Sigma_{\rm HI} \sim 6$–8 M$_\odot$ pc^{-2} for each region. This is consistent with the small range of $\Sigma_{\rm HI}$ found across the whole Perseus cloud. However, the median value of $\Sigma_{\rm HI}$ slightly changes between the regions. For example, B5 has the lowest median $\Sigma_{\rm HI} \sim 5.8$ M$_\odot$ pc^{-2} and NGC1333 has the highest median $\Sigma_{\rm HI} \sim 8.2$ M$_\odot$ pc^{-2}. A similar result for Perseus was pointed out by Sancisi et al. (1974) who found that $\Sigma_{\rm HI}$ remains approximately constant at $\sim$8 M$_\odot$ pc^{-2} for a wide range of interstellar extinction. Several extragalactic studies have also noticed that $\Sigma_{\rm HI}$ does not exceed $\sim$10 M$_\odot$ pc^{-2} for nearby galaxies (e.g., Wong & Blitz 2002; Blitz & Rosolowsky 2004, 2006; Bigiel et al. 2008; Wong et al. 2009).

In KMT09's model, H_2 formation requires a certain amount of $\Sigma_{\rm HI,s}$ to shield H_2 against photodissociation. Once this minimum $\Sigma_{\rm HI}$ is achieved, H_2 forms out of HI and $\Sigma_{\rm HI}$ remains constant. KMT09's model predicts $\Sigma_{\rm HI,s} \sim 10$ M$_\odot$ pc^{-2} for solar metallicity and this is indeed consistent with what we find in Figure 3.11. For all five regions, we find saturation of $\Sigma_{\rm HI} \sim 6$–8 M$_\odot$ pc^{-2}. However, in the case of B5 and NGC1333, we do not probe the regions of purely atomic gas, which correspond to the linear portion of the model curves in Figure 3.11. For IC348, B1E, and B1, we see hints of a possible turnover between atomic- and molecular-dominated zones at $\Sigma_{\rm HI}+\Sigma_{\rm H2} = 5$–$8$ M$_\odot$ pc^{-2}, yet our observations do not sample well the purely atomic zones. This inability to probe purely atomic regions is not due to the sensitivity of our $\Sigma_{\rm HI}$ and $\Sigma_{\rm H2}$ images. In Figure 3.11, we show the median 3σ values of $\Sigma_{\rm HI}$ and $\Sigma_{\rm HI}+\Sigma_{\rm H2}$ for the whole Perseus cloud as the black dashed lines. All data points are clearly above the 3σ values and this suggests that the lack of turnover detection is due to the highly extended atomic envelopes. For example, in the case of B5 and NGC1333, we are probing radial profiles up to $\sim$15–20 pc from the centers of the regions. Therefore, the purely atomic envelopes are likely located more than $\sim$20 pc from the molecular peaks.

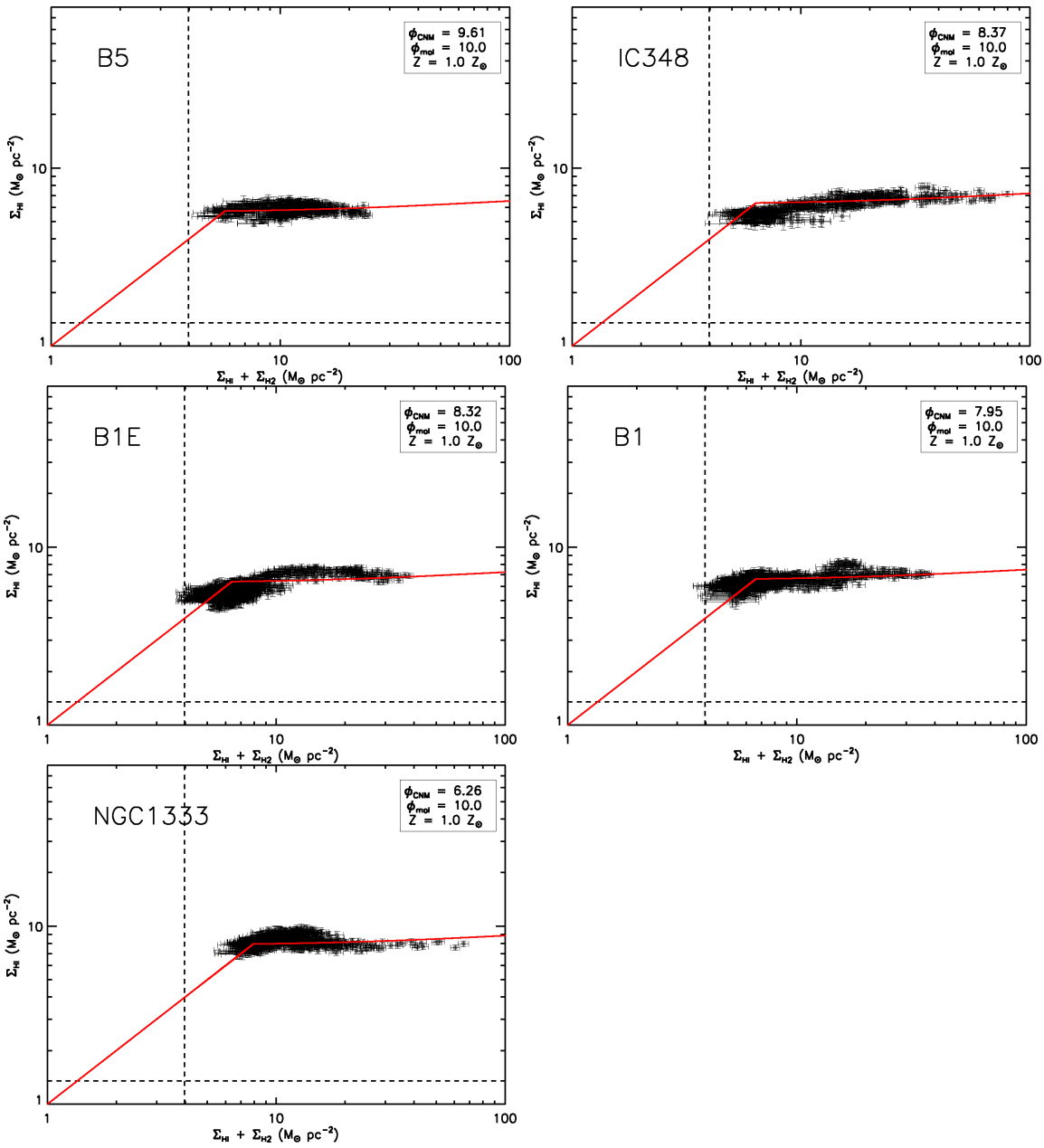

Fig. 3.11. — $\Sigma_{\rm HI}$ as a function of $\Sigma_{\rm HI} + \Sigma_{\rm H2}$. All data points in the rectangular boxes (Figure 3.10) are used for plotting. The median 3σ values of $\Sigma_{\rm HI}$ and $\Sigma_{\rm HI} + \Sigma_{\rm H2}$ for the whole Perseus cloud are shown as the black dashed lines. The red curves are the best-fit model curves determined in Section 3.7.2.1. The best-fit parameters are summarized in the top right corner of each plot.

3.7.1.1 Effect of High Optical Depth

An alternative or additional explanation for the relatively constant $\Sigma_{\rm HI}$ we measured could be a high optical depth of HI in Perseus. If HI gas is optically thick, the measured brightness temperature $T_{\rm b}$ levels off at a temperature close to the kinetic temperature $T_{\rm k}$. Therefore, under the assumption of optically thin HI gas (which we used to calculate our $\Sigma_{\rm HI}$), $\Sigma_{\rm HI}$ would saturate as $\Sigma_{\rm HI} \propto T_{\rm b} \sim T_{\rm k}$ and therefore be underestimated. There are a few lines of evidence that indicate the presence of cold, optically thick CNM in Perseus. For example, HISA features were found toward the centers of several dark and star-forming regions (e.g., Ridge et al. 2006a). In addition, Heiles & Troland (2003b) analyzed the HI emission/absorption spectra obtained toward two radio sources behind Perseus, 3C93.1 and NRAO140, and found CNM components in Perseus (based on radial velocity information) that have optical depths $\tau \sim 1$ and $\sim$7.

The best way to estimate the effect of optical depth is to measure CNM in absorption in the direction of many background radio sources behind Perseus. This provides the total column density of atomic hydrogen gas (CNM + WNM) along each line of sight, which can be compared with the column density we measured in Section 3.3.2 to derive the optical depth corrections for the whole cloud. As only two such measurements exist so far, we are in the process of obtaining additional HI absorption measurements (Stanimirović et al. in prep). Here we investigate only the magnitude of the optical depth effect.

If we assume $T_{\rm s} = 70$ K as measured by Heiles & Troland (2003b), the corrected N(HI) will need to be calculated using the following equation:

$$N({\rm HI})\ ({\rm cm}^{-2}) = 1.823 \times 10^{18}\ T_{\rm s} \int \ln\left(\frac{T_{\rm s}}{T_{\rm s} - T_{\rm b}}\right) dv. \tag{3.19}$$

If we apply this equation to our N(HI) image, we find that $\Sigma_{\rm HI}$ changes by a factor of 1.2–2. Another approach involves using the statistics of CNM and WNM from Heiles & Troland (2003b). Their Table 1 summarizes the CNM and WNM column densities for all sources in their survey. We can then estimate the fraction of CNM column density (relative to the total column density) as a function of WNM column density. Using only the table entries for a region centered on Perseus and $\sim$1200 deg^2 in size, we find that the CNM fraction is close to 50% for WNM column density less than 1.2×10^{21} cm^{-2}. This again suggests that our N(HI) or $\Sigma_{\rm HI}$ could be underestimated by a factor of two.

Our excercise shows that a high optical depth along each line of sight could result in a factor of two

spread in $\Sigma_{\rm HI}$ for Perseus. This is not substantial and therefore the almost constant $\Sigma_{\rm HI}$ we measured is likely a real physical feature, possibly driven by the conversion of HI into H_2. However, the magnitude of the optical depth effect we estimated is approximate and measuring the true $\Sigma_{\rm HI}$ distribution across Perseus needs a more sophisticated investigation.

3.7.2 $R_{\rm H2}$ vs $\Sigma_{\rm HI} + \Sigma_{\rm H2}$ for the Dark and Star-forming Regions

We now investigate KMT09's prediction of $R_{\rm H2}$ vs $\Sigma_{\rm HI} + \Sigma_{\rm H2}$ for the dark and star-forming regions in Perseus. In Figure 3.12, we plot $R_{\rm H2}$ as a function of $\Sigma_{\rm HI} + \Sigma_{\rm H2}$ for B5, IC348, B1E, B1, and NGC1333. For each plot we use the data points in the rectangular boxes shown in Figure 3.10.

We find that the relation between $R_{\rm H2}$ and $\Sigma_{\rm HI} + \Sigma_{\rm H2}$ is remarkably consistent for all dark and star-forming regions. Each plot in Figure 3.12 shows a very sharp rise of $R_{\rm H2}$ at low $\Sigma_{\rm HI} + \Sigma_{\rm H2}$, a turnover around $R_{\rm H2} \sim 1$, and a slow increase toward higher $R_{\rm H2}$. For the two star-forming regions, $R_{\rm H2}$ reaches a value of $\sim$10, while for the three dark regions, $R_{\rm H2}$ is less than 5.

3.7.2.1 Best-fit Curves

In Figure 3.12, we overlay KMT09's predictions as red solid curves and find excellent agreement. The overlaid curves were derived using Equation (3.17) with the assumption of $\phi_{\rm mol} = 10$ and $Z' = 1$ for all dark and star-forming regions. The fiducial value $\phi_{\rm mol} = 10$ was adopted following the discussion in KMT09. We note that $\phi_{\rm mol}$ does not make a significant change in $R_{\rm H2}$. For example, between $\phi_{\rm mol} =$ 10 and 50, $R_{\rm H2}$ at $\Sigma_{\rm HI} + \Sigma_{\rm H2} = 100$ $M_\odot$ pc^{-2} only varies by a factor of 1.1. Our assumption of a single $Z' = 1$ is based on the result of González Hernández et al. (2009) and our DGR investigation in Section 3.4.5. González Hernández et al. (2009) studied the chemical composition of Černis 52, an A3 V-type star in the direction of Perseus and derived a metallicity of [Fe/H] $= -0.01 \pm 0.15$ (corresponding to 0.7–1.4 $Z_\odot$). They determined a distance to Černis 52 of 231^{+135}_{-85} pc and in conjuction with the radial velocity information concluded that Černis 52 is likely a member of IC348. As a single DGR fits most of the diffuse regions in Perseus, there is probably no significant variation of Z' across the cloud. Therefore, we adopt $Z' = 1$ for all dark and star-forming regions in Perseus throughout this chapter and constrain only $\phi_{\rm CNM}$ from our fitting[6].

[6]We have attempted to determine the best-fit curve for $R_{\rm H2}$ vs $\Sigma_{\rm HI} + \Sigma_{\rm H2}$ by using both Z and $\phi_{\rm CNM}$ as free parameters but have found that the results are consistent with the case of $Z' = 1$ and varying $\phi_{\rm CNM}$ within 1σ.

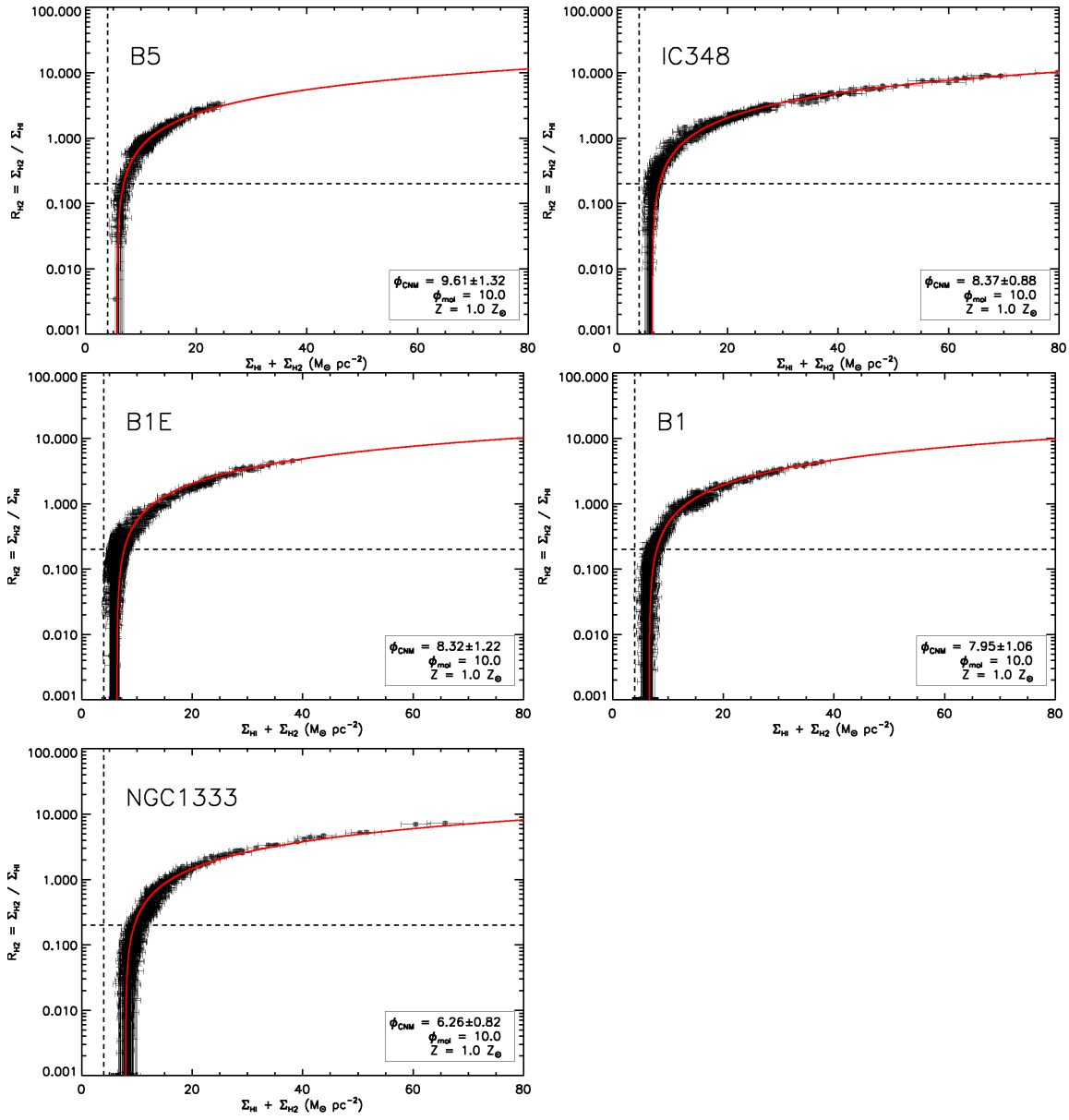

Fig. 3.12. — $R_{\rm H2}$ as a function of $\Sigma_{\rm HI} + \Sigma_{\rm H2}$. All data points in the rectangular boxes (Figure 3.10) are used for plotting. The median 3σ values of $R_{\rm H2}$ and $\Sigma_{\rm HI} + \Sigma_{\rm H2}$ for the whole Perseus cloud are shown as the black dashed lines. The best-fit model curves determined in Section 3.7.2.1. are shown in red. The best-fit parameters are summarized in the lower right corner of each plot.

We performed Monte Carlo simulations to determine the best-fit curves with consideration of uncertainties in both $R_{\rm H2}$ and $\Sigma_{\rm HI}+\Sigma_{\rm H2}$. We added random offsets to $R_{\rm H2}$ and $\Sigma_{\rm HI}+\Sigma_{\rm H2}$ and repeated this process 1000 times. For each variable, offsets were drawn from a Gaussian distribution with the standard deviation equal to the measured noise. For each realization, we determined the best-fit curve by assuming $\phi_{\rm mol}=10$ and $Z'=1$ and finding $\phi_{\rm CNM}$ that minimizes the sum of the squares of the residuals. IDL routine MPFITFUN (Markwardt 2009) was used for the fitting. Finally, we estimate the median $\phi_{\rm CNM}$ among the simulated 1000 $\phi_{\rm CNM}$ and use it as the best-fit parameter. We summarize this best-fit $\phi_{\rm CNM}$ for each region in Table 3.1.

3.7.2.2 Fitting Results

We find that $\phi_{\rm CNM}$ ranges from $\sim$6 to $\sim$10. As $\phi_{\rm CNM}$ determines the typical CNM number density via $n_{\rm CNM}=\phi_{\rm CNM}n_{\rm min}$, $\phi_{\rm CNM}=6$–10 translates into $T_{\rm CNM}=60$–75 K under the assumption of thermal pressure allowing the coexistence of CNM and WNM (Equation (19) of KMT09). This temperature range is indeed consistent with typical CNM properties in the solar neighborhood. Heiles & Troland (2003b) examined HI emission/absorption spectra obtained toward 79 radio sources and found a median $T_{\rm s}$ of $\sim$70 K for CNM.

While $\phi_{\rm CNM}$ appears to systematically decrease toward the west of Perseus, we find no significant difference in $\phi_{\rm CNM}$ between the dark and star-forming regions. This implies that HI envelopes surrounding these regions have similar $n_{\rm CNM}$. We estimate $n_{\rm CNM}=20$–30 cm^{-3} using $G_0'=G/G_0=0.4$ derived from Equation (3.5) with $T_{\rm dust}=17$ K. The similar $n_{\rm CNM}$ further suggests a similar normalized radiation field

Table 3.1. Fitting Results for $R_{\rm H2}$ vs $\Sigma_{\rm HI}+\Sigma_{\rm H2}$

Region	$\phi_{\rm CNM}$[a]
B5	9.61 ± 1.32
IC348	8.37 ± 0.88
B1E	8.32 ± 1.22
B1	7.95 ± 1.06
NGC1333	6.26 ± 0.82

[a]Uncertainties in $\phi_{\rm CNM}$ are estimated from the distribution of simulated 1000 $\phi_{\rm CNM}$.

χ of 1–1.5. As χ measures the relative importance of dust shielding and H_2 self-shielding, $\chi \sim 1$ implies that dust shielding and H_2 self-shielding are equally important for H_2 formation in Perseus.

3.7.2.3 Column Density at The HI-H_2 Transition

KMT09 assume an infinitely sharp HI-H_2 transition and in this case R_{H2} would be zero at the HI shielding column density. However, in reality, the transition cannot be infinitely sharp and KMT09 estimate $R_{H2} \sim 0.25$ at the HI shielding column density by comparing the theoretical HI shielding column densities with the detailed numerical radiative transfer calculations. For solar metallicity, KMT09 predict (as shown with the red solid curves) that $R_{H2} \sim 0.25$ occurs at $\Sigma_{HI} + \Sigma_{H2} = 7$–$10$ $M_\odot$ pc^{-2}. This is indeed consistent with what we see in Figure 3.12: $R_{H2} \sim 0.25$ at $\Sigma_{HI} + \Sigma_{H2} = 6$–$12$ $M_\odot$ pc^{-2} or $N(HI) + 2N(H_2) = (8$–$14) \times 10^{20}$ cm^{-2}. This transition column density is a factor of 2–3 larger than what previous studies found in the Galaxy via UV absorption measurements (e.g., Savage et al. 1977; Gillmon et al. 2006). However, considering that the previous studies defined the transition column density at $R_{H2} \sim 0.1$ and Σ_{H2} linearly increases with $\Sigma_{HI} + \Sigma_{H2}$, our result is consistent with the previous studies.

3.7.3 R_{H2} Radial Profiles

To investigate how R_{H2} radially changes from a molecular peak, we plot R_{H2} as a function of distance from the center of each dark and star-forming region in Figure 3.13. We use the data points in the rectangular boxes (Figure 3.10) and calculate the mean R_{H2} in three-pixel size bins (bin size = $12.9'$, corresponding to 1.1 pc at the distance of 300 pc) to remove small-scale fluctuations.

For all five regions, we find two power-law functions ($R_{H2} \propto r^{-\alpha}$) in their radial profiles up to $r \sim 150'$. Beyond $r \sim 150'$, the radial profiles show slight fluctuations due to the presence of small-scale structure in the R_{H2} image and/or become flat. We perform a linear least-squares fit to each radial profile up to $r \sim 150'$ and summarize the results in Table 3.2 with other properties of the radial profiles. We list the slopes of power-law functions (α_1 and α_2), the radius where the transition from the shallow to steep power-law functions occurs (r_b), R_{H2} at r_b ($R_{b,H2}$), the radius where the HI-H_2 transition occurs (r_t), the radius where hydrogen is predominantly in the form of HI (r_{HI}), and the thickness of the HI-H_2 transition region (d_t). We define r_t as a radius at $R_{H2} \sim 0.25$, r_{HI} as a radius at $R_{H2} \sim 0.1$, and d_t as $r_t - r_b$.

We find no significant difference between the dark and star-forming regions in terms of their R_{H2}

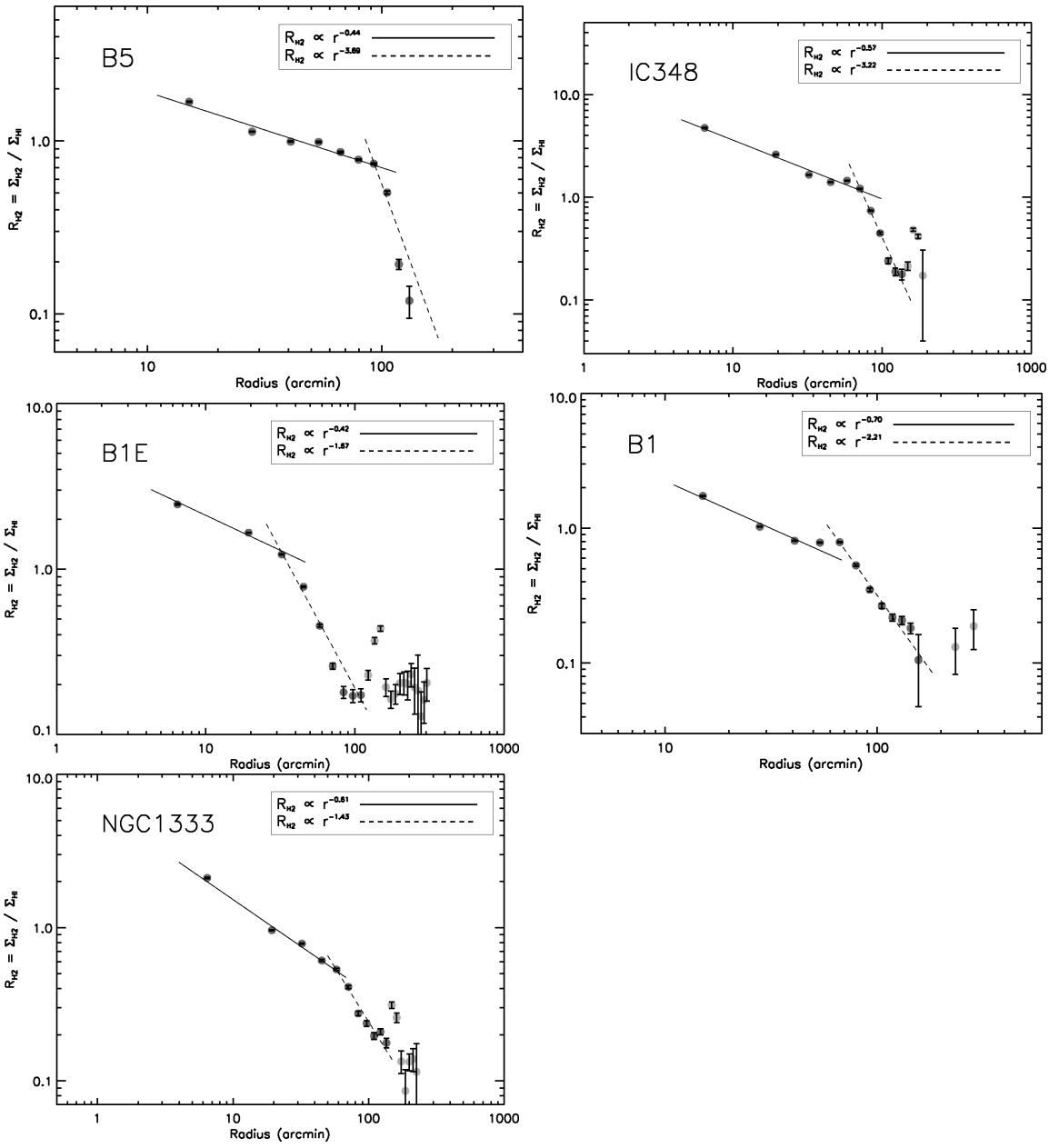

Fig. 3.13. — $R_{\rm H2}$ radial profiles. The data points with S/N of $R_{\rm H2} > 1$ are selected from the rectangular boxes (Figure 3.10) and the mean $R_{\rm H2}$ values in three-pixel size bins are calculated. The results from the power-law fitting are summarized in the top right corner of each plot. The light gray data points are excluded from the power-law fitting. $1'$ corresponds to 0.09 pc at the distance of 300 pc.

Table 3.2. Properties of $R_{\rm H2}$ Radial Profiles

Region	α[a] (J2000)	δ[a] (J2000)	$\alpha 1$	$\alpha 2$	$r_{\rm b}$[b] ($'$)	$R_{\rm b,H2}$[c]	$r_{\rm t}$[d] ($'$)	$r_{\rm HI}$[e] ($'$)	$d_{\rm t}$[f] ($'$)
B5	03 47 39	+32 51 28	3.69 ± 0.15	0.44 ± 0.01	$\sim$90	$\sim$0.7	$\sim$120	$\sim$160	$\sim$30 (< 0.19)
IC348	03 44 13	+32 04 13	3.22 ± 0.06	0.57 ± 0.01	$\sim$70	$\sim$1.2	$\sim$120	$\sim$150	$\sim$50 (< 0.33)
B1E	03 36 45	+31 12 40	1.67 ± 0.02	0.42 ± 0.01	$\sim$30	$\sim$1.2	$\sim$90	$\sim$150	$\sim$60 (< 0.40)
B1	03 33 18	+31 08 23	2.21 ± 0.05	0.70 ± 0.01	$\sim$60	$\sim$0.8	$\sim$110	$\sim$170	$\sim$50 (< 0.29)
NGC1333	03 29 17	+31 21 16	1.43 ± 0.04	0.61 ± 0.01	$\sim$60	$\sim$0.5	$\sim$100	$\sim$190	$\sim$40 (< 0.21)

[a]Central position of each region. For B5 and B1, the centers correspond to the $I_{^{13}\rm CO}$ peaks as their $R_{\rm H2}$ peaks are masked. For IC348, B1E, and NGC1333, the centers correspond to the $R_{\rm H2}$ peaks.

[b]Radius where the transition from the steep to shallow power-law functions occurs.

[c]$R_{\rm H2}$ at $r_{\rm b}$.

[d]Radius where the HI-H_2 transition occurs. This radius is defined at $R_{\rm H2} \sim 0.25$.

[e]Radius where gas is mainly in HI. This radius is defined at $R_{\rm H2} \sim 0.1$.

[f]Thickness of the HI-H_2 transition region. This is measured as $r_{\rm t} - r_{\rm b}$. The values in parantheses are $d_{\rm t}/r_{\rm HI}$.

[b,c,d,e]Estimated by eye.

[b,d,e,f]$1'$ corresponds to 0.09 pc at the distance of 300 pc.

radial distribution. The shallow portion of the radial profiles has a slope of $\alpha_2 = 0.4$–0.7, while the steep portion has a slope of $\alpha_1 = 1.4$–3.7. The transition from the shallow to the steep power-law function occurs at $r_{\rm b} \sim 30$–$90'$ or $\sim$3–8 pc. At this $r_{\rm b}$, $R_{\rm H2}$ ranges from 0.5 to 1.2. In addition, we find that H_2 extends up to $r \sim 200'$ or $\sim$17 pc from the centers of the dark and star-forming regions. This suggests that molecular clouds are much more extended than what is suggested by molecular tracers such as CO. The HI-H_2 transition, however, seems to be relatively sharp. We estimate $d_{\rm t} = r_{\rm t} - r_{\rm b}$, which measures the size of diffuse H_2 layer and therefore could be considered as the thickness of the transition region, and find $d_{\rm t} \sim 30$–$60'$, corresponding to $\sim$3–5 pc. We then estimate the ratio of the thickness of the HI-H_2 transition region to the region size, $d_{\rm t}/R < d_{\rm t}/r_{\rm HI} = 0.2$–$0.4$. As we do not know the exact size of the dark and star-forming regions, $d_{\rm t}/r_{\rm HI}$ provides only an upper limit on $d_{\rm t}/R$.

The other interesting thing to note is that the $R_{\rm H2}$ radial distribution becomes smoother toward the west of Perseus. Namely, $\Delta\alpha = |\alpha_1 - \alpha_2|$ becomes smaller from B5 to NGC1333. This may be related to $n_{\rm CNM}$ decreasing from B5 to NGC1333 (inferred from $\phi_{\rm CNM}$ decreasing from B5 to NGC1333 with the same $n_{\rm min}$: Section 3.7.2.1), even though it is not clear how $n_{\rm CNM}$ affects the smoothness of $R_{\rm H2}$ radial distribution. In KMT09's model, $n_{\rm CNM}$ determines the location of the HI-H_2 transition and due to the assumption of the infinitely sharp transition, there is no such relation between $n_{\rm CNM}$ and the smoothness of the $R_{\rm H2}$ radial distribution. This systematic variation of $\Delta\alpha$ across Perseus could be resulted from the change of internal density structure and/or the complicated viewing geometry.

3.8 Comparison of H_2 and CO Distributions

In Figure 3.14, we compare the H_2 and CO distributions. The black and gray contours show the CfA $I_{\rm CO}$ data and our $\Sigma_{\rm H2}$ data, respectively. To ease the comparison, we plot only 3σ contours for both data sets. Figure 3.14 shows that H_2 is found wherever significant CO exists. However, the reverse is not true: a considerable amount of H_2 exists beyond the 3σ contour of $I_{\rm CO}$. While H_2 is generally more extended than CO, there are significant spatial variations. For example, CO and H_2 trace each other remarkably well in the southwest part of Perseus, while H_2 is significantly more extended elsewhere (particularly around B5, B1E, B1, IC348, and NGC1333).

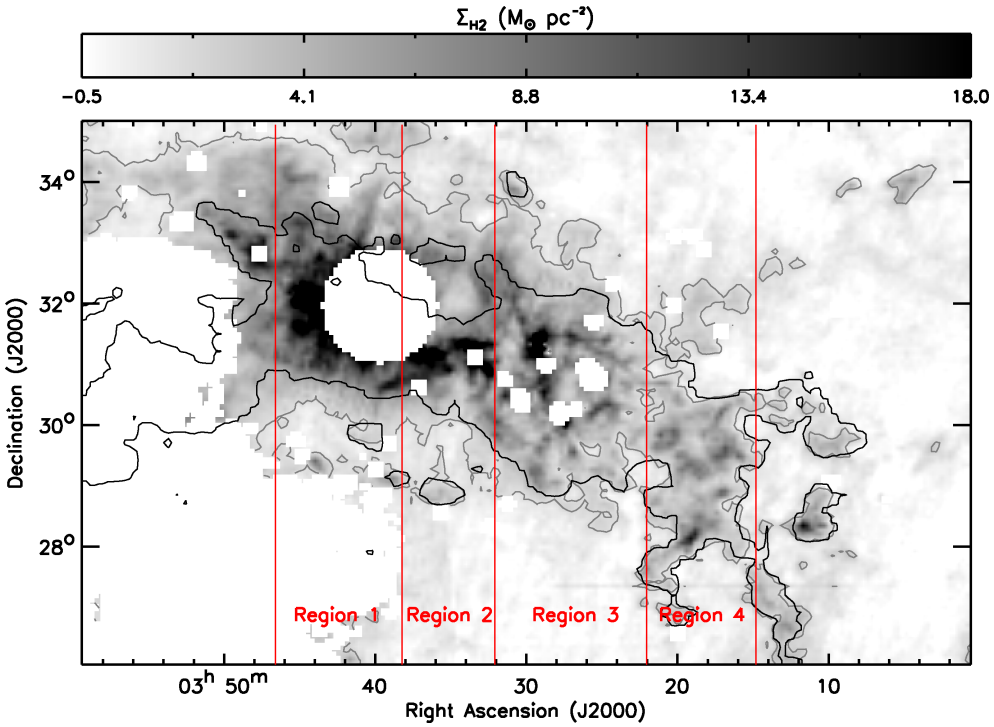

Fig. 3.14. — Σ_{H2} image. The contour for S/N of $\Sigma_{H2} = 3$ is overlaid in gray. The contour for S/N of CfA $I_{CO} = 3$ is also overlaid in black. The angular resolution of the Σ_{H2} and CfA I_{CO} images is 4.3′ and 8.4′, respectively. The Σ_{H2} image is divided into four regions and each region has either a dark or a star-forming region.

3.8.1 Relative Distribution of H_2 and CO

To quantify the relative distribution of H_2 and CO, we plot Σ_{H2} and I_{CO} as a function of distance from the center of each dark and star-forming region in Figure 3.15. We first smooth the Σ_{H2} image to the angular resolution of the CfA I_{CO} image and use the data points in the rectangular boxes shown in Figure 3.10. We then calculate the mean Σ_{H2} and I_{CO} in two-pixel size bins (bin size = 16.8′, corresponding to 1.5 pc at the distance of 300 pc). Finally, each radial profile is normalized by its peak value and therefore Figure 3.15 shows the relative distribution of H_2 and CO. As spatial averaging improves S/N, the radial profiles of Σ_{H2} and I_{CO} allow us to investigate the relative distribution of H_2 and CO more reliably than the visual comparison of 3σ contours.

We find that all five regions have extended H_2 compared to CO at all radii. For IC348, B1E, and NGC1333, H_2 radial profiles show slight fluctuations and/or become flat at $r > 150'$, which has been seen in Figure 3.13. We measure the radius where each H_2 and CO radial profile drops off to 1/4 of its peak value (r_{H2} and r_{CO}) and calculate the ratio of r_{H2} to r_{CO}. We find that the ratio, r_{H2}/r_{CO}, ranges from

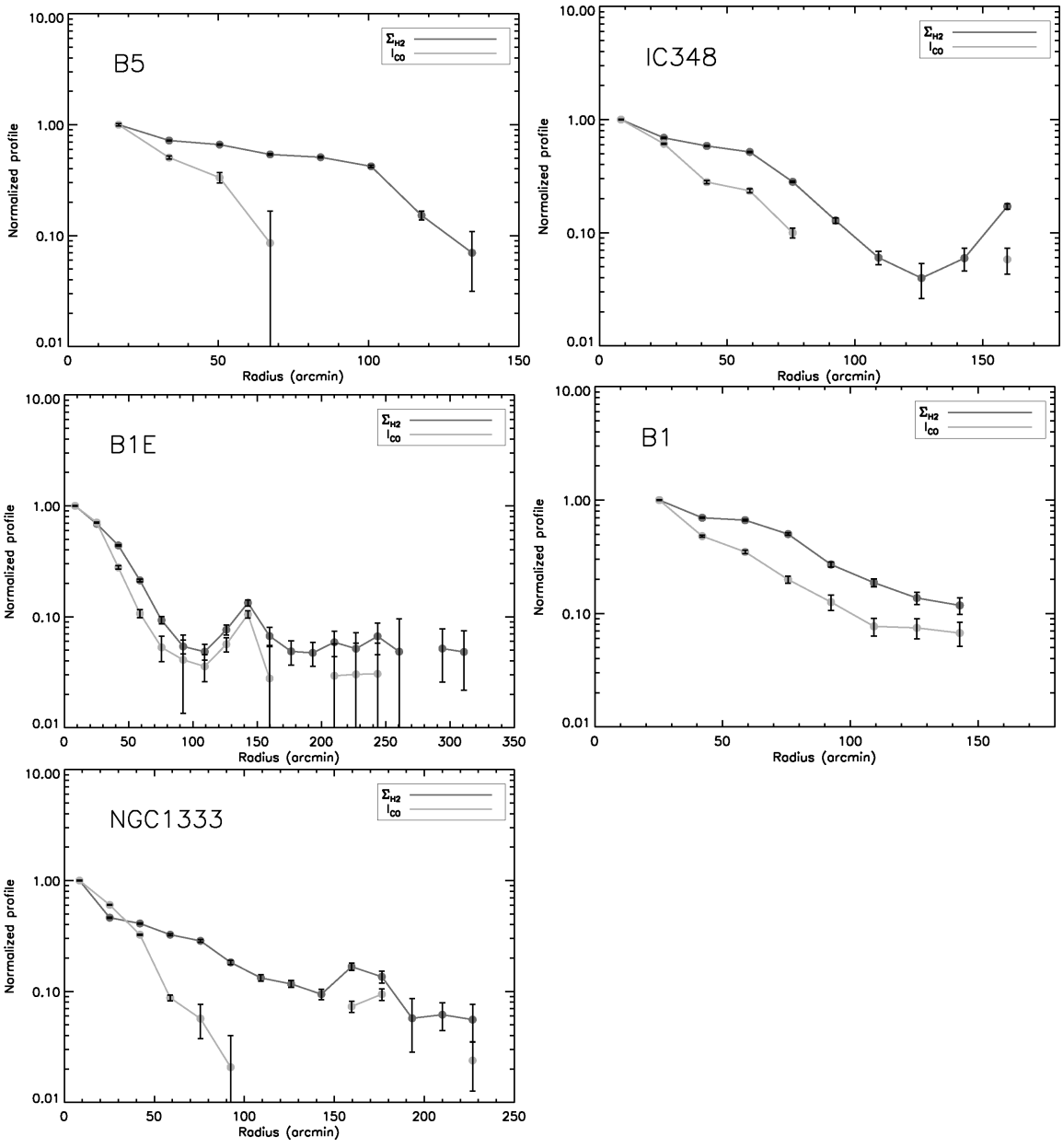

Fig. 3.15. — $\Sigma_{\rm H2}$ (gray) and CfA $I_{\rm CO}$ (light gray) normalized radial profiles. For each radial profile, the data points with S/N > 1 are selected from the rectangular boxes (Figure 3.10) and the mean $\Sigma_{\rm H2}$ and $I_{\rm CO}$ values in two-pixel size bins are calculated.

1.2 to 2 with a median of 1.4. This suggests that on average H_2 is ∼1.4 times more extended than CO in Perseus, implying the existence of a substantial amount of "CO-dark" gas.

3.8.2 Comparison to Wolfire et al. (2010): "CO-dark" Gas

The "CO-dark" gas refers to interstellar gas that exists in the form of H_2 along with CI and CII, but little or no CO. Such gas has been predicted from theoretical models of PDRs, which showed that the CII-CO transition occurs deeper into an interstellar cloud than the HI-H_2 transition due to the more effective self-shielding for H_2 than CO (e.g., van Dishoeck & Black 1988; Tielens & Hollenbach 1985).

Recently, Wolfire et al. (2010; WHM10 hereafter) modeled the "CO-dark" gas and explored how the fraction of H_2 gas mass in this "CO-dark" component depends on the mass of a cloud (M), the UV radiation field (G_0'), the metallicity (Z'), and the mean V-band extinction ($\overline{A}_V$). They used a PDR code to calculate the H_2, CI, and CII abundances in a spherical cloud and found that the fraction of "CO-dark" gas, $f_{\rm DG}$, is ∼0.3 for solar metallicity over a wide range of M and G_0'. Here $f_{\rm DG}$ is defined as $f_{\rm DG} = (M(r'_{\rm H2}) - M(r'_{\rm CO}))/M(r'_{\rm H2})$, where $r'_{\rm H2}$ and $r'_{\rm CO}$ is the radius of the H_2 and CO part of the cloud, respectively. Formally, $r'_{\rm H2}$ is defined as the radius where $2n_{\rm H2} = n_{\rm HI}$ and $r'_{\rm CO}$ is defined as the radius where the optical depth from the cloud surface to $r'_{\rm CO}$ is 1. More simply, when expressed in terms of $\Delta A_{V,\rm DG} = A_V(r'_{\rm CO}) - A_V(r'_{\rm H2})$, $f_{\rm DG}$ depends only on the ratio $\Delta A_{V,\rm DG}/\overline{A}_{\rm V}$. This is because $\Delta A_{V,\rm DG}$ is a measure of the "CO-dark" gas mass and $\overline{A}_{\rm V}$ is a measure of the H_2 gas mass. Interestingly, WHM10 found that $\Delta A_{V,\rm DG}$ is a weak function of G_0' and is almost constant. Therefore, $f_{\rm DG}$ is strongly dependent only on $\overline{A}_{\rm V}$. For example, for a cloud with CO mass of 10^6 $M_\odot$ and solar metallicity, $f_{\rm DG} \sim 0.8$ is expected at $\overline{A}_V = 2$ mag, while $f_{\rm DG} \sim 0.2$ is expected at $\overline{A}_V = 20$ mag.

To compare our observations to WHM10's prediction, we calculate the H_2 mass within the 3σ boundary of $I_{\rm CO}$ ($M(r_{3\sigma,\rm CO})$) and compare it with the H_2 mass within the 3σ boundary of $\Sigma_{\rm H2}$ ($M(r_{3\sigma,\rm H2})$). We find $f_{\rm DG} = (M(r_{3\sigma,\rm H2}) - M(r_{3\sigma,\rm CO}))/M(r_{3\sigma,\rm H2}) \sim 0.3$. Note that our definition of $f_{\rm DG}$ is different from that of WHM10. This is because $r'_{\rm CO}$ cannot be directly measured from observations. Nevertheless, $M(r'_{\rm H2})$ and $M(r'_{\rm CO})$ of WHM10 represent the total H_2 and CO masses and therefore our $f_{\rm DG}$ is conceptually similar with what WHM10 used. We estimate $\overline{A}_V \sim 1.5$ mag for the data points within $r_{3\sigma,\rm H2}$. As WHM10 do not provide a prediction of $f_{\rm DG}$ at $\overline{A}_V < 2$ mag, we extrapolate it from their Figure 11: $f_{\rm DG} \sim 0.8$ is expected at $\overline{A}_V \sim 1.5$ mag. Note that the expected $f_{\rm DG} \sim 0.8$ at $\overline{A}_V \sim 1.5$ mag is for a cloud that has a much higher mass ($M \sim 10^6$ $M_\odot$) and a stronger radiation field ($G_0' \sim 10$) than Perseus. Considering the predicted

insensitivity of $f_{\rm DG}$ to the cloud mass and the strength of radiation field, however, we measure a factor of three lower value, $f_{\rm DG} \sim 0.3$.

To investigate this discrepancy between our $f_{\rm DG}$ and WHM10's prediction, we first examine the dependence of $f_{\rm DG}$ on the DGR. As shown in Section 3.4.5, our estimate of $\Sigma_{\rm H2}$ and consequently $f_{\rm DG}$ depends on the DGR via Equation (3.4). In the same section, we discussed the lower and upper limits on the DGR. If we use the lower limit on the DGR instead of our adopted DGR, $\overline{A}_V$ decreases to 1.1 mag and $f_{\rm DG}$ increases to 0.6. Our estimate is a factor of two lower than WHM10's prediction at $\overline{A}_V \sim 1.1$ mag, $f_{\rm DG} \sim 0.9$. Similarly, if we use the upper limit on the DGR, $\overline{A}_V$ increases to 1.9 mag and $f_{\rm DG}$ decreases to 0.2. Our estimate is now a factor of four lower than WHM10's prediction at $\overline{A}_V \sim 1.9$ mag, $f_{\rm DG} \sim 0.8$. Note that "CO-dark" gas exists in Perseus even for these extreme cases and the discrepancy with the model persists.

Second, we test if $f_{\rm DG}$ is a strong function of $\overline{A}_V$ as WHM10 predicted. For this purpose, we divide the $\Sigma_{\rm H2}$ image into four regions (Figure 3.14) and estimate $f_{\rm DG}$ and $\overline{A}_V$ for each region. We use the $\Sigma_{\rm H2}$ image derived from our adopted DGR, 1.1×10^{-21} mag cm^2. In Table 3.3, we list the estimated $f_{\rm DG}$ and $\overline{A}_V$ for the four regions. We find $f_{\rm DG} \sim 0.3$ for regions 1 and 2 and $f_{\rm DG} = 0.1$–0.2 for regions 3 and 4. All regions have similar mean extinction, $\overline{A}_V = 1.4$–1.7 mag. While we have only four data points covering a small range of $\overline{A}_V$, we measure a relatively large range of $f_{\rm DG}$, from $\sim$0.1 to $\sim$0.3. The large variation we find in $f_{\rm DG}$ is not consistent with WHM10, but echos the observations of other diffuse clouds in the Galaxy. For example, the Polaris cloud has $\overline{A}_V \sim 0.3$ mag (Heithausen & Thaddeus 1990) and $f_{\rm DG} \sim 0.36$ (Abdo et al. 2010). On the other hand, the Pegasus cloud has $\overline{A}_V \sim 0.6$ mag (Yamamoto et al. 2006) and $f_{\rm DG} \sim 0.6$ (Grenier et al. 2005).

Table 3.3. $f_{\rm DG}$ and $\overline{A}_V$ for Perseus

Region	$f_{\rm DG}$[a]	$\overline{A}_V$ (mag)[a]
1	0.32	1.71
2	0.31	1.73
3	0.18	1.58
4	0.10	1.43

[a] 1σ uncertainty is less than 1% of each quantity.

This region-to-region variation we find in $f_{\rm DG}$ could be due to the DGR systematically changing across Perseus. For example, a factor of two lower DGR would allow regions 3 and 4 to have similar $f_{\rm DG}$ as regions 1 and 2. However, we do not find any evidence for such systematic change of the DGR when examining the correlation between N(HI) and FIR emission (Section 3.4.2). As an alternative, the complicated viewing geometry of the H_2 and CO distributions could result in the regional variation in $f_{\rm DG}$.

3.9 Discussion

The excellent agreement between our data and KMT09's predictions (Sections 3.7.1 and 3.7.2) suggests that KMT09's model captures the fundamental physics of H_2 formation reasonably well even on sub-pc scales. This is certainly encouraging, but slightly surprising considering how simple KMT09's model is. Essentially, for a spherical cloud bathed in a uniform and isotropic ISRF, the most important factor for H_2 formation is the HI shielding surface density $\Sigma_{\rm HI,s}$. Once enough shielding against photodissociation is achieved by $\Sigma_{\rm HI,s}$, all additional $\Sigma_{\rm HI}$ is fully converted into $\Sigma_{\rm H2}$, resulting in a uniform $\Sigma_{\rm HI}$ distribution and therefore a linear increase of $\Sigma_{\rm H2}$ with $\Sigma_{\rm HI} + \Sigma_{\rm H2}$.

Before going into a more detailed discussion of several important aspects of KMT09's model, we would like to remind the reader that two main predictions summarized in Section 3.6 are not independent. The predicted behavior of $R_{\rm H2}$ as a function of $\Sigma_{\rm HI} + \Sigma_{\rm H2}$ is a consequence of saturation of $\Sigma_{\rm HI}$. Therefore, the excellent agreement between our data and KMT09's predictions in Figure 3.12 is entirely driven by the constant $\Sigma_{\rm HI}$. While we are not able to probe the purely atomic envelope of Perseus, the constant $\Sigma_{\rm HI}$ of 6–8 $M_\odot$ pc^{-2} we find is in agreement with KMT09's prediction of $\Sigma_{\rm HI,s}$ for solar metallicity.

In addition, we caution that our data do not allow us to fully test the dependence of $R_{\rm H2}$ on metallicity and ISRF. KMT09's model predicts that $R_{\rm H2}$ depends on metallicity, while being almost insensitive to the strength of ISRF. While our findings are in agreement with KMT09's predictions for solar metallicity and $\sim$2/5 of the Galactic ISRF, the lack of metallicity and ISRF variations across Perseus does not permit more detailed model testing. Future studies of high-latitude molecular clouds and GMCs in external galaxies with sub-solar metallicity will provide crucial tests of KMT09's model. We now turn to several crucial model assumptions and discuss their possible limitations.

3.9.1 Equilibrium vs Non-equilibrium H_2 Formation

The most fundamental principle underlying KMT09's model is H_2 formation in equilibrium. In equilibrium, H_2 formation and photodissociation are balanced and H_2 abundance is locally constant. Several authors have investigated the time evolution of H_2 and found a typical timescale of H_2 formation in equilibrium, τ_{H2} = 10–30 Myr (e.g., Goldsmith et al. 2007; Liszt 2007).

As τ_{H2} is comparable to or longer than the estimated lifetime of GMCs, $\tau_{life} \sim 10$ Myr (McKee & Ostriker 2007 and references therein), the role of interstellar turbulence in accelerating H_2 formation has received significant attention in recent years (e.g., Hartmann et al. 2001; Bergin et al. 2004; Glover & Mac Low 2007; Glover et al. 2010). The main idea behind the models of H_2 formation in turbulent media is that shocks induced by cloud-cloud collisions, spiral density waves, supernovae explosions, etc., compress diffuse atomic gas, allowing H_2 to form in the postshock gas where high enough shielding is achieved against photodissociation. While earlier studies have been limited to 1D, Glover & Mac Low (2007) and Glover et al. (2010) performed 3D magnetohydrodynamical (MHD) simulations of turbulence with detailed chemical modeling. They showed that a significant amount of H_2 could form within 1–2 Myr, due to the turbulence-driven clumping that accelerates H_2 formation. However, the H_2 abundance keeps increasing over time and never reaches equilibrium by 20–30 Myr. Eventually, the gas will become fully molecular unless the H_2 formation is terminated by destruction of GMCs via stellar feedback, e.g., photoevaporation by HII regions and protostellar outflows. This sharply contrasts with KMT09's model.

Our results are consistent with the model of H_2 formation in equilibrium and suggest that turbulence may play a secondary role in the H_2 formation. Clearly, further studies are needed to compare abundances of H_2 and other molecular species with the predictions from both stationary and turbulent models.

3.9.2 The Importance of WNM in the Envelopes of GMCs

We find that Σ_{HI} is uniform across Perseus with a range of 6–8 $M_\odot$ pc^{-2}, consistent with KMT09's prediction of $\Sigma_{HI,s}$ for solar metallicity. However, as CNM is far more effective at shielding against photodissociation than WNM, the predicted $\Sigma_{HI,s}$ comes purely from CNM, while our measured Σ_{HI} includes the contributions from both CNM and WNM. As we discussed in Section 3.7.1.1, our measured Σ_{HI} could be underestimated by a factor of two for high optical depth gas (CNM). While Σ_{HI} corrected for high optical depth would likely still be comparable to KMT09's prediction, the importance of WNM in the envelopes of

atomic-molecular complexes clearly needs to be taken into account in the models of H_2 formation. This is also supported by Bolatto et al. (2011) who found a relatively good agreement between KMT09's prediction and the observed R_{H2} vs $\Sigma_{HI} + \Sigma_{H2}$ in the Small Magellanic Cloud, where WNM dominates the total HI (Dickey et al. 2000). At the same time, it is essential to observationally constrain the relative contribution from CNM and WNM to Σ_{HI}. We are in the process of obtaining HI absorption measurements for Perseus, which will allow us to separate the contributions from cold and warm gas (Stanimirović et al. in prep).

3.9.3 The Importance of Internal Radiation

As we showed in Section 3.5.2, in the case of IC348 and NGC1333, the embedded B-type stars are the dominant sources of the radiation field. KMT09's model does not take into account the role of internal radiation in determining R_{H2}, with the assumption that massive stars producing significant amounts of dissociating photons do not stay inside their parent molecular clouds for a long time. While we clearly see the importance of the B-type stars for dust heating, we find no significant difference in our analysis of R_{H2} for the dark and star-forming regions. This supports the idea that the internal radiation is not important for H_2 formation. However, as we show below, this is valid for Perseus because it does not contain any stars earlier than the B5 V-type.

When O- or B-type stars suddenly turn on in a molecular cloud, UV photons from the stars photodissociate H_2 and create HI dissociation regions around HII regions. This variation of the UV radiation field has a much shorter timescale ($\sim 10^3$ yr) than H_2 formation ($\sim 10^7$ yr) and therefore totally changes the thermal and chemical structures of the molecular cloud (e.g., Hollenbach & Natta 1995; Bertoldi & Draine 1996). However, the sphere of photodissociation influence depends greatly on the stellar type.

Roger & Dewdney (1992) studied the properties of HI dissociation regions around O- and B-type main sequence stars. Their source list includes SVS3, the B5 V-type star in NGC1333 (red star in Figure 3.7). An HI region associated with SVS3 was measured to have $M_{HI} = 0.017$ $M_\odot$ and $R_{HI} = 0.03$ pc (Rodríguez et al. 1990). This is consistent with an HI dissociation region created by a star of $T_{eff} \sim 16{,}600$ K in a dense medium of $n_{HI} \sim 6{,}000$ cm^{-3}. The size of the HI dissociation region around this particular B5 star is only $\sim$1/10 of our spatial resolution. Therefore, the HI dissociation regions around the individual B-type stars in Perseus are below our spatial resolution and therefore are negligible for our consideration of R_{H2}.

However, the internal radiation is still important for dust heating inside IC348 and NGC1333. This

can be understood by the fact that not every UV photon produces photodissociation of H_2. While UV and visible photons heat dust grains, only the UV photons in the narrower LW band (912–1120 Å) photodissociate H_2. In addition, only ∼10% of the LW photons actually photodissociate H_2 ($f_{\rm diss} \sim 0.1$). Therefore, the UV photons from the B-type stars in IC348 and NGC1333 could be dominant for dust heating, while relatively ineffective for photodissociation of H_2.

If any stars earlier than B3 V resided in Perseus, on the other hand, the role of the internal radiation in determining $R_{\rm H2}$ would be no longer negligible. For example, Roger & Dewdney (1992) found that an HI region associated with IRAS 23545+6508 has $M_{\rm HI} = 1.4$ M$_\odot$ and $R_{\rm HI} = 0.4$ pc and these properties are consistent with an HI dissociation region created by a B3 V-type star in a medium of $n_{\rm HI} \sim 100$ cm^{-3}. The size of the HI dissociation region is now comparable to our spatial resolution and therefore $R_{\rm H2}$ around the stars earlier than B3 V would be significantly modified. Therefore, depending on the stellar type of stars residing inside GMCs, the internal radiation should not be ignored.

3.10 Summary

In this paper, we study the HI-H_2 transition across the Perseus molecular cloud on sub-pc scales (∼0.4 pc). We use the highest resolution HI data for Perseus from the GALFA-HI survey, which allow us to probe the outskirts as well as the main body of the cloud. The velocity range of the HI emission associated with Perseus is determined based on the correlation between N(HI) and the dust column density traced by the 2MASS A_V image. We then derive the N(HI) image under the assumption of optically thin HI gas. The dust column density is estimated using the IRIS 60 μm and 100 μm images and is calibrated with the 2MASS A_V image. In combination with the N(HI) image and the derived DGR, we use the dust column density to derive the $N(H_2)$ image.

The N(HI) and $N(H_2)$ images and the existing CO data for Perseus allow us to test two recent models of H_2 and CO formation in equilibrium. For several dark and star-forming regions (B5, B1E, B1, IC348, and NGC1333), we investigate $\Sigma_{\rm HI}$ and $R_{\rm H2}$ as a function of $\Sigma_{\rm HI} + \Sigma_{\rm H2}$ and compare the results to KMT09's predictions. We also compare the H_2 and CO distributions and estimate the fraction of H_2 mass in the "CO-dark" component, $f_{\rm DG}$. We investigate $f_{\rm DG}$ as a function of $\overline{A}_V$ and compare the result to WHM10's prediction. Several of the main results can be summarized as follows.

1. For both dark and star-forming regions in Perseus, we find an almost uniform $\Sigma_{\rm HI} \sim$ 6–8 M$_\odot$ pc^{-2}.

This is consistent with KMT09's prediction of the HI shielding surface density for solar metallicity, $\Sigma_{\rm HI,s} \sim 10$ M$_\odot$ pc^{-2}.

2. The purely atomic envelopes are located more than ∼20 pc from the centers of the dark and star-forming regions. We probe the $\Sigma_{\rm HI}$ and $\Sigma_{\rm HI} + \Sigma_{\rm H2}$ distributions up to ∼20–30 pc from the centers of the regions and barely detect the turnover between atomic- and molecular-dominated zones for IC348, B1E, and B1.

3. The relation between $R_{\rm H2}$ and $\Sigma_{\rm HI} + \Sigma_{\rm H2}$ on a log-linear scale is remarkably consistent for all dark and star-forming regions, having a very sharp rise of $R_{\rm H2}$ at low $\Sigma_{\rm HI} + \Sigma_{\rm H2}$, a turnover around $R_{\rm H2} \sim 1$, and a slow increase toward higher $R_{\rm H2}$.

4. The dark and star-forming regions have similar $\phi_{\rm CNM} = 6$–10, which implies that these regions are embedded in the atomic envelopes with $n_{\rm CNM} = 20$–30 cm^{-3}. In addition, $\phi_{\rm CNM} = 6$–10 indicates a similar normalized radiation field $\chi \sim 1$, suggesting that dust shielding and H_2 self-shielding are equally important for H_2 formation.

5. We measure the HI-H_2 transition gas column density of $N({\rm HI}) + 2N(H_2) = (8$–$14) \times 10^{20}$ cm^{-2} or $\Sigma_{\rm HI} + \Sigma_{\rm H2} = 6$–12 M$_\odot$ pc^{-2} at $R_{\rm H2} \sim 0.25$. This is consistent with the previous estimates for the Galaxy.

6. We estimate the fraction of "CO-dark" gas, $f_{\rm DG} \sim 0.3$, for Perseus, a factor of three lower than WHM10's prediction. This implies that a significant amount of H_2 gas is not traced by Galactic CO surveys.

7. We investigate the dependence of $f_{\rm DG}$ on $\overline{A}_V$ and find a relatively large variation of $f_{\rm DG} \sim 0.1$–0.3 for similar $\overline{A}_V \sim 2$ mag. This is not consistent with WHM10's prediction that $f_{\rm DG}$ is a strong function of $\overline{A}_V$.

While we generally find good agreement with KMT09's predictions, several outstanding questions remain. Our estimated $\Sigma_{\rm HI} \sim 6$–8 M$_\odot$ pc^{-2} is likely dominated by WNM, while KMT09's model predicts shielding by CNM alone. Clearly, the WNM in the atomic envelopes of GMCs needs to be considered in the models of H_2 formation as a source of shielding against photodissociation. The importance of gravitationally bound vs diffuse gas is another important aspect, as explored in Ostriker et al. (2010). In

addition, KMT09's model does not take into account the role of internal radiation for H_2 formation. This is valid for Perseus as it does not contain early-type stars to photodissociate a significant amount of H_2 that could be detected at our spatial resolution. However, if GMCs are young enough to harbor early-type stars that are able to change the thermal and chemical structures of the GMCs, the internal radiation cannot be ignored. Most importantly, our Perseus data on sub-pc scales are consistent with KMT09's model for H_2 formation in equilibrium and suggest that turbulence may not be of primary importance for H_2 formation. Yet, the timescale for equilibrium H_2 formation is longer than the estimated lifetime of most GMCs. This problem remains to be resolved. Future detailed comparisons of observations with non-equilibrium, turbulence-driven H_2 formation models will be important to investigate the role of turbulence for formation of H_2 and various molecular species.

We thank Ron Allen, Joss Bland-Hawthorn, Alberto Bolatto, Bruce Elmegreen, Fabian Heitsch, Mordecai Mac Low, Chris McKee, Eve Ostriker, Rene Plume, and Mark Wolfire for stimulating discussions. M.-Y.L., S.S., M.E.P., C.H., E.J.K., J.E.G.P., A.B., J.G., N.P., and D.S. acknowledge support from NSF grants AST-0707597, 0917810, 0707679, and 0709347. M.-Y.L. and S.S. thank the Research Corporation for Science Advancement for their support. K.A.D. acknowledges funding from the European Community's Seventh Framework Program under grant agreement no PIIF-GA-2008-221289. J.E.G.P. was supported by HST-HF-51295.01A, provided by NASA through a Hubble Fellowship grant from STScI, which is operated by AURA under NASA contract NAS5-26555. The Arecibo Observatory is part of the National Astronomy and Ionosphere Center, which is operated by Cornell University under a cooperative agreement with the National Science Foundation. The National Radio Astronomy Observatory is a facility of the National Science Foundation operated under cooperative agreement by Associated Universities, Inc. We credit the use of the KARMA visualization software (Gooch 1996).

References

Abdo, A. A., Ackermann, M., Ajello, M., et al. 2010, ApJ, 710, 133

Bally, J., Walawender, J., Johnstone, D., Kirk, H., & Goodman, A. A. 2008, Handbook of Star Forming Regions, Volume I: The Northern Sky, ed. B. Reipurth (ASP Monograph Publications, Vol. 4; San Francisco, CA: ASP), 308

Barriault, L., Joncas, G., Lockman, F. J., & Martin P. G. 2010, MNRAS, 407, 2645

Beichman, C. A., Wilson, R. W., Langer, W. D., & Goldsmith, P. F., et al. 1988, ApJ, 332, L81

Bergin, E. A., Hartmann, L. W., Raymond, J. C., & Ballesteros-Paredes, J. 2004, ApJ, 612, 921

Bertoldi, F., & Draine, B. T. 1996, ApJ, 458, 222

Bigiel, F., Leroy, A. K., Walter, F., et al. 2008, AJ, 136, 2846

Blitz, L., & Rosolowsky, E. 2004, ApJ, 612, 29

Blitz, L., & Rosolowsky, E. 2006, ApJ, 650, 933

Bolatto, A., Leroy, A. K., Jameson, K., et al. 2011, ApJ, 741, 12

Browning, M. K., Tumlinson, J., & Shull, J. M. 2003, ApJ, 582, 810

Bohlin, R. C., Savage, B. D., & Drake, J. F. 1978, ApJ, 224, 132

Boulanger, F., Abergel, A., Bernard, J.-P., et al. 1996, A&A, 312, 256

Černis, K. 1990, Ap&SS, 166, 315

Dame, T. M., Hartmann, D., & Thaddeus, P. 2001, ApJ, 547, 792

Désert, F.-X., Boulanger, F., & Puget, J. L. 1990, A&A, 237, 215

Dickey, J. M., Mebold, U., Stanimirović, S., Staveley-Smith, L. 2000, ApJ, 536, 756

Douglas, K. A., & Taylor, A. R. 2007, ApJ, 659, 426

Draine, B. T., & Bertoldi, F. 1996, 468, 269

Fukui, Y., & Kawamura, A. ARA&A, 2010, 48, 547

Fumagalli, M., Krumholz, M. R., Prochaska, J. X., Gavazzi, G., & Boselli, A. 2009, ApJ, 697, 1811

Fumagalli, M., Krumholz, M. R., & Hunt, L. K. 2010, ApJ, 722, 919

Gibson, S. J. 2010, ASPC, 438, 111

Gillmon, K., Shull, J. M., Tumlinson, J., & Danforth, C. 2006, ApJ, 636, 891

Giovanelli, R., Haynes, M. P., Kent, B. R., et al. 2005, AJ, 130, 2598

Glover, S. O. C., & Mac Low, M.-M. 2007, ApJ, 659, 1317

Glover, S. O. C., Federrath, C., Mac Low, M.-M., & Klessen, R. S. 2010, MNRAS, 404, 2

Goldsmith, P. F., Li, D., & Krčo, M. 2007, ApJ, 654, 273

González Hernández, J., Iglesias-Groth, S., Rebolo, R., et al. 2009, ApJ, 706, 866

Gooch, R. 1996, Astronomical Data Analysis Software and Systems V (ASP Conf. Ser. 101), ed. G. H. Jacoby & J. Barnes (San Francisco, CA: ASP), 80

Goodman, A. A., Pineda, J. E., & Schnee, S. L. 2009, ApJ, 692, 91

Grenier, I. A., Casandjian, J.-M., & Terrier, R. 2005, Science, 307, 1291

Guram, S. S., & Taylor, A. R. 2009, The Low-Frequency Radio Universe (ASP Conf. Ser. 407), ed. D. J. Saikia et al. (San Francisco, CA: ASP), 282

Hartmann, L. W., Ballesteros-Paredes, J., & Bergin, E. A. 2001, 562, 852

Heithausen, A., & Thaddeus, P. 1990, ApJ, 353, L49

Heiles, C. 2005, Obtaining the IF Bandpass Using Least-Squares Frequency Switching (LSFS), http://www.naic.edu/ astro/aotms/performance/lsfs.ps

Heiles, C., & Troland, T. H. 2003a, ApJS, 145, 329

Heiles, C., & Troland, T. H. 2003b, ApJ, 586, 1067

Herbig, G. H., & Jones, B. F. 1983, AJ, 88, 1040

Herbig, G. H. 1998, ApJ, 497, 736

Hollenbach, D., & Natta, A. 1995, ApJ, 455, 133

Hollenbach, D., & Tielens, A. G. G. M. 1997, ARA&A, 35, 179

Imara, N., & Blitz, L. 2011, ApJ, 732, 78

Kalberla, P. M. W., Burton, W. B., & Hartmann, D., et al. 2005, A&A, 440, 775

Klochkova, V. G., & Kopylov, I. M. 1985, Astrofiz. Issled. Izv. Spets. Astrofiz. Obs., 20, 3

Kim, S.-H., & Martin, P. G. 1996, ApJ, 462, 296

Krumholz, M. R., McKee, C. F., & Tumlinson, J. 2008, ApJ, 689, 865

Krumholz, M. R., McKee, C. F., & Tumlinson, J. 2009, ApJ, 693, 216

Lada, C. J., Alves, J., & Lada, E. A. 1996, AJ, 111, 1964

Lequeux, J. 2005, The Interstellar Medium (Berlin: Springer)

Leroy, A. K., Bolatto, A. D., Bot, C., et al. 2009, ApJ, 702, 352

Lesh, J. R. 1969, AJ, 74, 891

Li, A. & Draine, B. T. 2001, ApJ, 554, 778

Liszt, H. S., & Lucas, R. 2000, A&A, 355, 333

Liszt, H. S. 2002, A&A, 389, 393

Liszt, H. S. 2007, A&A, 461, 205

Lombardi, M. & Alves, J. 2001, A&A, 377, 1023

Luhman, K. L., Stauffer, J. R., Muench, A. A., et al. 2003, ApJ, 593, 1093

Markwardt, C. B. 2009, ASP Conf. Ser. 411, Astronomical Data Analysis Software and Systems XVIII, ed. D. A. Bohlender, D. Durand, & P. Dowler (San Francisco, CA: ASP), 251

McKee, C. F., & Ostriker, E. C. 2007, ARA&A, 45, 565

Meyerdierks, H. & Heithausen, A. 1996, A&A, 313, 929

Miville-Deschênes, M.-A. & Lagache, G. 2005, ApJS, 157, 302

Morton, D. C., & Adams, T. F. 1968, ApJ, 151, 611

Nelder, J., & Meade, R. 1965, Comput. J., 7, 308

Narayanan, G., Heyer, M. H., Brunt, C., et al. 2008, ApJS, 177, 341

Ostriker, E. C., McKee, C. F., & Leroy, A. K. 2010, ApJ, 721, 9750

Peek, J. E. G., Heiles, C., Douglas, K. A., et al. 2011, ApJS, 194, 20

Porter, T. A. & Strong, A. W. 2005, ICRC (Pune), arXiv:astro-ph/0507119

Rachford, B. L., Snow, T. P., Tumlinson, J., et al. 2002, ApJ, 577, 221

Rachford, B. L., Snow, T. P., Destree, J. D., et al. 2009, ApJS, 180, 125

Reach, W. T., Koo, B.-C., & Heiles, C. 1994, ApJ, 429, 672

Ridge, N. A., Di Francesco, J., Kirk, H., et al. 2006a, AJ, 131, 2921

Ridge, N. A., Schnne, S. L., Goodman, A. A., & Foster, J. B. 2006b, ApJ, 643, 932

Rodríguez, L. F., Escalante, V., Lizano, S., Canto, J., & Mirabel, I. F. 1990, 365, 261

Roger, R. S., & Dewdney, P. E. 1992, ApJ, 385, 536

Sancisi, R. Goss, W. M., Anderson, C., Johansson, L. E. B., & Winnberg, A. 1974, A&A, 35, 445

Savage, B. D., Bohlin, R. C., Drake, J. F., & Budich, W. 1977, ApJ, 216, 291

Schlegel, D. J., Finkbeiner, D. P., & Davis, M. 1998, ApJ, 500, 525

Schnee, S. L., Ridge, N. A., Goodman, A. A., & Li, J. G. 2005, ApJ, 634, 442

Snow, T. P., Hanson, M. M., Seab, G. C., & Saken, J. M. 1994, ApJ, 420, 632

Spaans, M., Tielens, A. G. G. M., van Dishoeck, E. F., & Bakes, E. L. O. 1994, ApJ, 437, 270

Spaans, M., & Neufeld, D. A. 1997, ApJ, 484, 785

Stepnik, B., Abergel, A., Bernard, J.-P., et al. 2003, A&A, 398, 551

Tielens, A. G. G. M., & Hollenbach, D. 1985, ApJ, 291, 772

Ungerechts, H., & Thaddeus, P. 1987, ApJS, 63, 645

van Dishoeck, E. F., & Black, J. H. 1986, ApJS, 62, 109

van Dishoeck, E. F., & Black, J. H. 1988, ApJ, 334, 771

Wannier, P. G., Lichten, S. M., & Morris, M. 1983, ApJ, 268, 727

Wannier, P. G., Lichten, S. M., Andersson, B.-G., & Morris, M. 1991, ApJS, 75, 987

Wolfire, M. G., McKee, C. F., Hollenbach, D., & Tielens, A. G. G. M. 2003, ApJ, 587, 278

Wolfire, M. G., Hollenbach, D., & McKee, C. F. 2010, ApJ, 716, 1191

Wong, T., & Blitz, L. 2002, ApJ, 569, 157

Wong, T., Hughes, A., Fukui, Y., et al. 2009, ApJ, 696, 370

Yamamoto, H., Kawamura, A., Tachihara, K., et al. 2006, ApJ, 642, 307

Chapter 4

The *X*-factor across the Perseus Molecular Cloud

Lee, M.-Y., Stanimirović, S., Wolfire, M. G., Shetty, R., Glover, S. C. O.,
Molina, F. Z., & Klessen, R. S. 2013, ApJ, *submitted*

Abstract

We estimate the conversion factor relating CO integrated intensity to H_2 column density, $X_{CO} = N(H_2)/I_{CO}$, for the Perseus molecular cloud. We combine the dust-based $N(H_2)$ data with the I_{CO} data from the COMPLETE and CfA Survey to derive X_{CO} on sub-parsec scales. The X_{CO} distribution across Perseus has a median of $\sim 2.8 \times 10^{19}$ cm^{-2} K^{-1} km^{-1} s and shows a factor of $\sim$3 large-scale spatial variations. In combination with the dust temperature and CO velocity dispersion image, we find that a factor of $\sim$3 larger X_{CO} in the northeastern part of Perseus can result from the stronger radiation field and/or the smaller non-thermal gas motion. Within individual dark and star-forming regions in Perseus, X_{CO} varies up to a factor of $\sim$100. We investigate X_{CO} as a function of A_V and find that X_{CO} sharply decreases at $A_V \lesssim 3$ mag but gradually increases at $A_V \gtrsim 3$ mag. The transition from decreasing to increasing X_{CO} occurs where I_{CO} becomes optically thick and saturates to $\sim$50–80 K km s^{-1}. We compare the N(HI), $N(H_2)$, I_{CO}, and X_{CO} data with two theoretical models of the formation of molecular gas, a one-dimensional model of photodissociation regions (PDRs) and a three-dimensional magnetohydrodynamic (MHD) simulation tracking both the dynamical and chemical evolution of gas, with a goal to understand H_2 and CO formation in molecular clouds. The PDR model based on the steady state and equilibrium chemistry reproduces our data very well but requires a density distribution with a diffuse HI halo component to provide dust shielding against H_2 and CO dissociation. The MHD model generally matches our data as well, suggesting that time-depedent effects are not significant for low-mass, old molecular clouds such as Perseus. However, there are a number of systematic discrepancies, including the broader range of N(HI), smaller I_{CO}, and more gradual increase of I_{CO} with A_V along with a large scatter. These discrepancies likely result from the complex spatial and kinematic structure of the gas in the MHD model.

4.1 Introduction

Stars form exclusively in giant molecular clouds (GMCs), although the question whether molecular gas is a prerequisite to star formation or not is under debate (e.g., Glover & Clark 2012; Kennicutt & Evans 2012; Krumholz 2012). In either case, accurate measuruments of the physical properties of GMCs are critical to constrain the initial conditions for star and molecular gas formation. However, obtaining such measurements is hampered by the fact that molecular hydrogen (H_2), the most abundant molecular species in the interstellar medium (ISM), is not directly observed under the typical conditions in GMCs. As a homonuclear diatomic molecule, H_2 does not have a permanent electric dipole moment and its ro-vibrational states change only via weak quadrupole transitions. Therefore, alternative tracers have been employed to infer the abundance and distribution of H_2.

Carbon monoxide (CO) is one of the most commonly used tracers of H_2 due to its large abundance and low rotational transitions that are readily excited in GMCs through collisions with H_2. In particular, the ^{12}CO($J = 1 \rightarrow 0$) integrated intensity[4], $I_{\rm CO}$, is often used to estimate the H_2 column density, $N(H_2)$, via the so-called "X-factor"[5], which is defined by

$$X_{\rm CO} = \frac{N(H_2)}{I_{\rm CO}} \quad {\rm cm^{-2}\ K^{-1}\ km^{-1}\ s}. \tag{4.1}$$

Accurate knowledge of $X_{\rm CO}$ is crucial to address some of the fundamental questions in astrophysics. For example, one of the most intriguing properties of galaxies is a strong power-law relation between the surface density of star formation rate, $\Sigma_{\rm SFR}$, and the surface density of H_2, $\Sigma_{\rm H2}$, generally known as the "Kennicutt-Schmidt relation" (e.g., Schmidt 1959; Kennicutt 1989; Bigiel et al. 2008; Schruba et al. 2011; Rahman et al. 2012; Shetty et al. 2013). While this empirical relation provides important insights into the physical process of star formation (e.g., a close connection between the chemical or thermal state of the ISM and star formation), its precise form has been a subject of debate and strongly depends on $X_{\rm CO}$.

From an observational perspective, $X_{\rm CO}$ is usually adopted as a conversion factor. Its estimate relies on the derivation of $N(H_2)$ using observational methods independent of CO (Bolatto et al. 2013 for a review). One of the methods to derive $N(H_2)$ utilizes dust as a tracer of total gas column density. Dust

[4]Hereafter ^{12}CO($J = 1 \rightarrow 0$) is quoted as CO.

[5]Hereafter $X_{\rm CO}$ is quoted without its unit.

has been observed to be well mixed with gas (e.g., Boulanger et al. 1996) and can be mapped through its emission at far-infrared (FIR) wavelengths or its absorption at near-infrared (NIR) wavelengths. The procedure is to estimate the dust column density or the V-band extinction, A_V, from FIR emission or NIR absorption and assume a dust-to-gas ratio (DGR) that linearly relates A_V with the total gas column density $N(\mathrm{H}) = N(\mathrm{HI}) + 2N(\mathrm{H_2})$. The atomic gas column density, $N(\mathrm{HI})$, is then measured from the 21 cm emission and removed from $N(\mathrm{H})$ for an estimate of $N(\mathrm{H_2})$ (e.g., Israel 1997a,b; Dame et al. 2001; Leroy et al. 2007, 2009, 2011; Lee et al. 2012; Sandstrom et al. 2013). The derived $N(\mathrm{H_2})$ is finally combined with I_{CO} to estimate X_{CO}.

This procedure has been applied to the Milky Way and a number of nearby galaxies. For the Milky Way, Dame et al. (2001) showed that X_{CO} does not significantly change for $|b| \gtrsim 5^\circ$ from its mean of 1.8×10^{20}. Several studies of individual GMCs estimated similar X_{CO} values (e.g., Frerking et al. 1982 for Ophiuchus; Lombardi et al. 2006 for Pipe; Pineda et al. 2010 for Taurus; Paradis et al. 2012 for Aquila-Ophiuchus, Cepheus-Polaris, Taurus, and Orion). At the same time, X_{CO} values different from the Galactic mean value have been occasionally found: e.g., $X_{\mathrm{CO}} = 0.5 \times 10^{20}$ for high-latitude clouds in Ursa Major (de Vries et al. 1987) and $X_{\mathrm{CO}} = 1.2 \times 10^{21}$ for the outskirts of Taurus (Pineda et al. 2010). In studies of nearby galaxies on kpc scales, X_{CO} shows a greater range of $\sim$(0.4–130) $\times 10^{20}$ (e.g., Smith et al. 1991; Israel 1997a,b; Leroy et al. 2007, 2009; Gratier et al. 2010; Leroy et al. 2011; Sandstrom et al. 2013). For example, Leroy et al. (2011) estimated $X_{\mathrm{CO}} \sim$ (1–3) $\times 10^{21}$ for two low metallicity galaxies, NGC 6822 and the Small Magellanic Cloud (SMC), and suggested that X_{CO} strongly increases for metallicities smaller than $12 + \log(\mathrm{O/H}) \sim 8.2$–$8.4$.

From a theoretical perspective, X_{CO} has been primarily studied using photodissociation region (PDR) models because the majority of CO emission originates from the outskirts of molecular clouds, where the interstellar radiation field (ISRF) is incident upon (e.g., Taylor et al. 1993; Le Bourlot et al. 1993; Wolfire et al. 1993; Kaufman et al. 1999; Bell et al. 2006; Wolfire et al. 2010). For example, Bell et al. (2006) used the UCL_PDR code (Papadopoulos et al. 2002) to calculate chemical abundances and emission strengths for a wide range of physical parameters and found that X_{CO} can vary by over an order of magnitude, particularly with changes in density, metallicity, and cloud age. While PDR models are limited to simple geometries and density distributions, three-dimensional magnetohydrodynamic (MHD) simulations have been recently performed to investigate X_{CO} in turbulent molecular clouds (e.g., Glover

& Mac Low 2011; Shetty et al. 2011a,b). These simulations model time-dependent chemistry for simple molecules such as H_2 and CO and show that X_{CO} is not constant within individual clouds and can vary by up to four orders of magnitude in the case of low density, low metallicity, and strong radiation field. Such variability in X_{CO} has been rarely probed or found in observations, largely due to the lack of high resolution observations.

In this chapter, we derive X_{CO} for the Perseus molecular cloud on sub-pc scales and test two theoretical models of the formation of molecular gas, in an attempt to understand the origins of the variations in X_{CO} and the physical processes of H_2 and CO formation. One model is the one-dimensional PDR model initially developed by Tielens & Hollenbach (1985) and updated by Kaufman et al. (2006), Wolfire et al. (2010), and Hollenbach et al. (2012). Here we use a modified version that has two-sided illumination and either a constant density or a simple prescription for the density distribution (hereafter the modified W10 model). The other model is the three-dimensional MHD model by Shetty et al. (2011a) that is based on the modified ZEUS–MP code described in Glover et al. (2010) (hereafter the S11 model). These models are different from each other mainly in two apsects. First, the S11 model simulates H_2 and CO formation in turbulent molecular clouds by coupling the chemical and dynamical evolution of gas, while the modified W10 model takes into account the impact of turbulence only via a constant supersonic linewidth for spectral line formation and cooling. Second, the S11 model follows the non-equilibrium evolution of a number of chemical species, including H_2 and CO, while the modified W10 model uses a detailed chemical network that explicitly assumes chemical equilibrium for every atomic and molecular species. Hence, we consider the modified W10 model and the S11 model as a representative "microturbulent equilibrium model" and "macroturbulent non-equilibrium model", respectively. Our study is one of the first attempts to test the MHD model tracking both the chemical and dynamical evolution of the ISM and compare it with a more traditional view of the formation of molecular gas (i.e., PDR model). In addition, considering that small-scale ISM models are starting to be implemented in large-scale galaxy formation simulations (e.g., Feldmann et al. 2012a,b; Lagos et al. 2012; Narayanan et al. 2012), our study will serve as a "zero point test" for the models of gas contents in galaxies.

We focus on the Perseus molecular cloud because of its proximity and a wealth of multi-wavelength data. Located at a distance of ∼200–350 pc (Herbig & Jones 1983; Černis 1990), Perseus has a projected angular size of $\sim 6^\circ \times 3^\circ$ on the sky. In this chapter, we adopt the distance to Perseus of 300 pc. With a

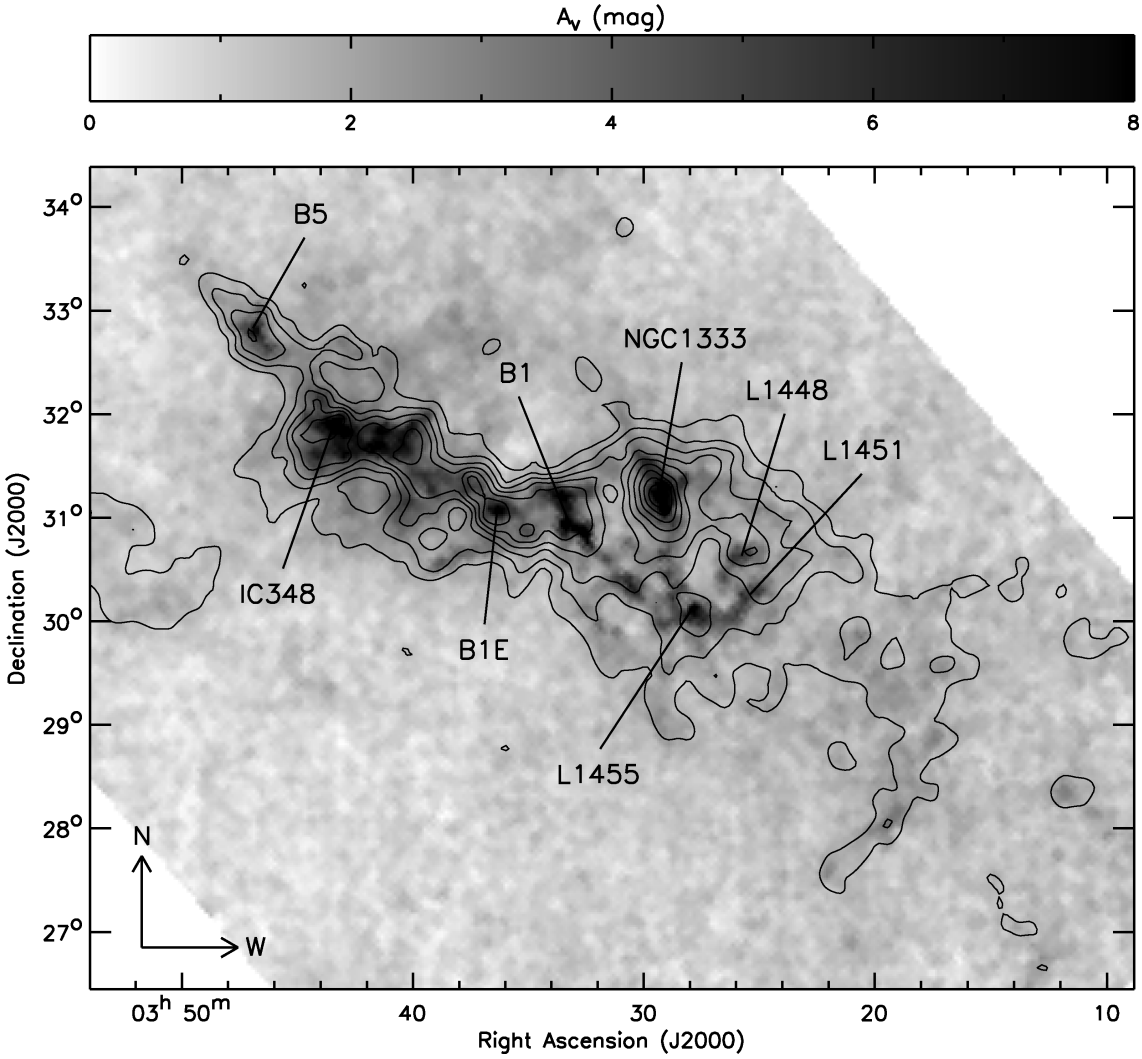

Fig. 4.1. — COMPLETE A_V image of Perseus. The CfA $I_{\rm CO}$ contours are overlaid in black. The contour levels range from 10% to 90% of the peak (69 K km s^{-1}) with 10% steps. The angular resolution of the COMPLETE A_V and CfA $I_{\rm CO}$ image is $5'$ and $8.4'$, respectively. A number of prominent dark and star-forming regions are labelled.

mass of $\sim 2 \times 10^4$ M$_\odot$ (Sancisi et al. 1974; Lada et al. 2010), Perseus is considered as a low-mass molecular cloud with an intermediate level of star formation (Bally et al. 2008). The cloud contains a number of dark (B5, B1E, B1, L1455, L1448, and L1451) and star-forming regions (IC348 and NGC1333) shown in Figure 4.1.

This chapter is organized as follows. In Section 4.2, we summarize the results from previous studies highly relevant to our investigation and provide constraints on important physical parameters of Perseus. In Section 4.3, we describe the multi-wavelength data used in this study. In Section 4.4, we divide Perseus

into a number of regions and select data points for each region. We then derive the $X_{\rm CO}$ image of Perseus (Section 4.5) and investigate the large-scale spatial variation of $X_{\rm CO}$ and its correlation with physical parameters such as the strength of the radiation field and the CO velocity dispersion (Section 4.6). In addition, we examine how $I_{\rm CO}$ and $X_{\rm CO}$ change with A_V in Perseus. In Sections 4.7 and 4.8, we summarize the details of the modified W10 and S11 model and compare our data with model predictions. Finally, we discuss and summarize our conclusions (Sections 4.8 and 4.9).

4.2 Background

4.2.1 Previous Studies

Pineda et al. (2008) used the $I_{\rm CO}$ and A_V data from the COMPLETE Survey of Star Forming Regions (COMPLETE; Ridge et al. 2006) to investigate $X_{\rm CO}$ in Perseus. They assumed that all hydrogen traced by A_V is in H_2 and fitted a linear function to $I_{\rm CO}$ vs A_V to estimate $X_{\rm CO}$. They found $X_{\rm CO} \sim 1.4 \times 10^{20}$ for the whole Perseus cloud and a range of $X_{\rm CO} \sim$ (0.9–1.6) $\times 10^{20}$ for six sub-regions in Perseus, suggesting that spatial variations of $X_{\rm CO}$ are caused by different ISM conditions. In addition, they noticed that $X_{\rm CO}$ is heavily affected by the saturation of $I_{\rm CO}$ at $A_V \gtrsim 4$ mag and re-estimated $X_{\rm CO} \sim 0.7 \times 10^{20}$ from the linear fit only to the unsaturated CO emission. Pineda et al. (2008) also compared the observed CO and ^{13}CO($J = 1 \rightarrow 0$) integrated intensity with the theoretical predictions from the Meudon PDR code (Le Petit et al. 2006) and found that the PDR models reproduce the CO and ^{13}CO observations reasonably well and that the variations among the six sub-regions can be explained by the variations in physical parameters, in particular density and non-thermal gas motions.

In our recent study, we derived the $\Sigma_{\rm HI}$ and $\Sigma_{\rm H2}$ image of Perseus on $\sim$0.4 pc scales and investigated how the H_2-to-HI ratio, $R_{\rm H2} = \Sigma_{\rm H2}/\Sigma_{\rm HI} = 2N({\rm H_2})/{\rm N(HI)}$, varies across the cloud (Lee et al. 2012). We found that $\Sigma_{\rm HI}$ is relatively uniform with $\sim$6–8 $M_\odot$ pc^{-2} (corresponding to N(HI) $\sim$ (8–10) $\times 10^{20}$ cm^{-2}), while $\Sigma_{\rm H2}$ significantly varies from $\sim$0 $M_\odot$ pc^{-2} to $\sim$73 $M_\odot$ pc^{-2}, resulting in $R_{\rm H2} \sim$ 0–10 with a median of $\sim$0.1. Due to the nearly constant $\Sigma_{\rm HI}$, a strong linear relation between $R_{\rm H2}$ and $\Sigma_{\rm HI} + \Sigma_{\rm H2}$ was found. Interestingly, these results are consistent with the equilibrium H_2 formation model by Krumholz et al. (2009; hereafter the K09 model). In the K09 model, a spherical cloud is bathed in a uniform and isotropic radiation field and the abundance of H_2 is estimated based on the balance between H_2 formation on dust grains and photodissociation by Lyman-Werner photons. The most important prediction by the K09 model

is the minimum $\Sigma_{\rm HI}$ required to shield H_2 against photodissociation. This minimum $\Sigma_{\rm HI}$ for H_2 formation depends on metallicity (e.g., $\Sigma_{\rm HI} \sim 10$ $M_\odot$ pc^{-2} for solar metallicity) but only weakly on the strength of the radiation field. Once the minimum $\Sigma_{\rm HI}$ is achieved, additional $\Sigma_{\rm HI}$ is converted into $\Sigma_{\rm H2}$, resulting in a uniform $\Sigma_{\rm HI}$ distribution and a linear increase of $R_{\rm H2}$ with $\Sigma_{\rm HI}$+$\Sigma_{\rm H2}$.

4.2.2 Constraints on Physical Parameters

We summarize estimates of several important physical parameters of Perseus obtained from previous studies. We will use these parameters in later sections of this chapter.

Density $n \sim 10^{3-4}$ cm^{-3}: Young et al. (1982) estimated $n \sim$ (1.7–5) $\times 10^3$ cm^{-3} for B5 based on the large velocity gradient (LVG) model applied to CO and CO($J = 2 \rightarrow 1$) observations. Bensch (2006) derived larger $n \sim$ (3–30) $\times 10^3$ cm^{-3} for the same cloud by comparing PDR models with CO, ^{13}CO, and [CI] observations. Similarly, Pineda et al. (2008) found that PDR models with $n \sim$ a few $\times 10^{3-4}$ cm^{-3} can reproduce CO and ^{13}CO($J = 1 \rightarrow 0$) observations of Perseus. In summary, gas traced by CO emission in Perseus is likely to have $n \sim 10^{3-4}$ cm^{-3}.

ISRF $G \sim 0.4$ G_0': Lee et al. (2012) investigated the dust temperature, $T_{\rm dust}$, across Perseus and potential heating sources and concluded that Perseus is embedded in the uniform Galactic ISRF heating dust grains to ∼17 K, except for the central parts of IC348 and NGC1333, where the radiation from internal B-type stars likely dominates. Under the assumption that dust grains are in thermal equilibrium, we can use $T_{\rm dust} \sim 17$ K to estimate the strength of the uniform Galactic ISRF by

$$G = 4.6 \times 10^{-11} \left(\frac{a}{0.1\ \mu{\rm m}} \right) T_{\rm dust}^6 \ {\rm erg\ cm^{-2}\ s^{-1}}, \tag{4.2}$$

where G is the flux at ultraviolet (UV) wavelengths and a is the size of dust grains (Lequeux 2005). Equation (4.2) assumes the absorption efficiency $Q_{\rm a} = 1$ and the dust emissivity index $\beta = 2$. For dust grains with $a \sim 0.1$ μm, whose size is comparable to UV wavelengths therefore $Q_{\rm a} \simeq 1$, we estimate $G \sim 1.1 \times 10^{-3}$ erg cm^{-2} s^{-1} ~ 0.4 G_0' (G_0' = the local Galactic field estimated by Draine (1978) = 2.7×10^{-3} erg cm^{-2} s^{-1}) for the uniform ISRF where Perseus is embedded. The exceptions are the central regions of IC348 and NGC1333, where the radiation from the B-type stars is dominant.

Cosmic-ray ionization rate $\zeta \gtrsim 10^{-17}$ s^{-1}: There is emerging evidence that ζ likely lies between ∼10^{-17} s^{-1} to ∼10^{-15} s^{-1} with lower values in dense molecular clouds and ∼10^{-16} s^{-1} to ∼10^{-15} s^{-1} in the diffuse ISM (e.g., Dalgarno 2006; Indriolo & McCall 2012; Hollenbach et al. 2012). This suggests that

ζ could be larger than the canonical $\zeta \sim 10^{-17}$ s^{-1} by a factor of $\sim$10–100 in the regions where the CO emission arises.

Metallicity $Z \sim 1$ Z$_\odot$: González Hernández et al. (2009) performed a chemical abundance analysis for Černis 52, a member of IC348 whose spectral type is A3 V, and derived [Fe/H] = -0.01 ± 0.15 (corresponding to $Z \sim 0.7$–1.4 Z$_\odot$). In addition, Lee et al. (2012) compared the intensity at 100 μm, I_{100}, with N(HI) for Perseus and found an overall linear relation (Figure 5 of Lee et al. 2012). As I_{100}/N(HI) is an approximation of DGR, the fact that a single I_{100}/N(HI) fits most of the diffuse regions suggests no significant variation of DGR or Z across the cloud. Therefore, $Z \sim 1$ Z$_\odot$ would be a reasonable estimate for Perseus. Note that Lee et al. (2012) derived DGR = A_V/N(H) $\sim 1.1 \times 10^{-21}$ mag cm^2, which is $\sim$2 times larger than the typical Galactic DGR $\sim 5.3 \times 10^{-22}$ mag cm^2 (Bohlin et al. 1978).

Turbulent linewidth $v_{\rm turb} \lesssim 2$–5 km s^{-1}: Pineda et al. (2008) compared CO excitation temperature, $T_{\rm ex}$, with COMPLETE A_V and found that $T_{\rm ex}$ increases from $\sim$5 K at $A_V \sim 2$ mag to $\sim$20 K at $A_V \gtrsim 4$ mag. If $n > n_{\rm crit}$ where $n_{\rm crit}$ is the critical density, the case likely for the regions with $A_V \gtrsim 4$ mag, we expect that CO emission is in local thermodynamic equilibrium (LTE) and $T_{\rm ex} \sim T_{\rm k}$ where $T_{\rm k}$ is the kinetic temperature. When we assume $T_{\rm ex} \sim T_{\rm k} \sim 20$ K for Perseus, the mean thermal velocity of gas would be $\langle v_{\rm th} \rangle = \sqrt{2k_{\rm B}T_{\rm k}/\mu m_{\rm H}} \sim 0.1$ km s^{-1} ($k_{\rm B}$ = the Boltzmann constant, μ = the mass of a molecule in amu ~ 28 for CO, $m_{\rm H}$ = the mass of a hydrogen atom). This $\langle v_{\rm th} \rangle \sim 0.1$ km s^{-1} is an order of magnitude smaller than the CO velocity dispersion $\sigma_{\rm CO} \sim 0.9$–2 km s^{-1} (corresponding to FWHM = $(8{\rm ln}2)^{1/2}$ $\sigma_{\rm CO}$ ~ 2.1–4.7 km s^{-1}) measured across Perseus (Pineda et al. 2008). This suggests that $\sigma_{\rm CO}$ is dominated by turbulent motions for $A_V \gtrsim 4$ mag and/or multiple components along a line of sight. Therefore, $v_{\rm turb} \sim$ 2–5 km s^{-1} is an upper limit on the average turbulent linewidth for the whole Perseus cloud.

Age $t_{\rm age} \sim 10$ Myr: For IC348, Muench et al. (2003) derived a mean age of $\sim$2 Myr with a spread of $\sim$3 Myr using published spectroscopic observations. However, there are some indications for the existence of older stars in IC348. For example, Herbig (1998) found that Hα emission line stars in IC348 have an age spread from $\sim$0.7 Myr to $\sim$12 Myr. A similar spread in stellar ages, from $\sim$0.5 Myr to $\sim$10 Myr, has been found by Luhman et al. (1998) from their infrared and optical spectroscopic observations. Considering this duration of star formation in IC348, $t_{\rm age} \sim 10$ Myr would be a reasonable age estimate for Perseus.

4.3 Data

4.3.1 Derived H_2 Distribution

We use the $N(H_2)$ image derived in our recent study, Lee et al. (2012). We used the 60 μm and 100 μm data from the Improved Reprocessing of the *IRAS* Survey (IRIS; Miville-Deschênes & Lagache 2005) to derive the dust optical depth at 100 μm, τ_{100}. Dust grains were assumed to be in thermal equilibrium and the contribution from very small grains to the intensity at 60 μm was accounted for by calibrating the derived $T_{\rm dust}$ image with $T_{\rm dust}$ data from Schlegel et al. (1998). The τ_{100} image was then converted into the A_V image by finding the conversion factor X for $A_V = X\tau_{100}$ that results in the best agreement between the derived A_V and COMPLETE A_V. This calibration of τ_{100} to COMPLETE A_V was motivated by Goodman et al. (2009), who found that dust extinction at NIR wavelengths is the best probe of total gas column density. Finally, Lee et al. (2012) estimated a local DGR for Perseus and derived the $N(H_2)$ image in combination with the HI data from the Galactic Arecibo L-band Feed Array HI Survey (GALFA-HI; Peek et al. 2011). The HI emission was integrated from -5 km s^{-1} to $+15$ km s^{-1}, the range that maximizes the spatial correlation between the HI integrated intensity and the dust column density, and N(HI) was calculated under the assumption of optically thin HI. The derived $N(H_2)$ ranges from $\sim$0 cm^{-2} to $\sim 4.5 \times 10^{21}$ cm^{-2} with a median of $\sim 1 \times 10^{20}$ cm^{-2} (calculated for the data points with $N(H_2) > 0$ cm^{-2}). Its median 1σ uncertainty is $\sim 3.6 \times 10^{19}$ cm^{-2}. See Section 4 of Lee et al. (2012) for details on the derivation of the $N(H_2)$ image and its 1σ uncertainty.

The $T_{\rm dust}$, A_V, N(HI), and $N(H_2)$ image derived by Lee et al. (2012) are all at 4.3$'$ angular resolution, corresponding to $\sim$0.4 pc at the distance of 300 pc. In this chapter, we use them in combination with the CO data from two surveys, COMPLETE and CfA (Section 4.3.2). When we work with the COMPLETE CO data, we smooth the CO data to obtain the same 4.3$'$ angular resolution. On the other hand, when we use the CfA CO data, we bring all relevant images to the common 8.4$'$ angular resolution. All smoothing is done by performing convolution with an appropriate Gaussian kernel. At 8.4$'$ angular resolution, $N(H_2)$ varies from $\sim$0 cm^{-2} to $\sim 3.6 \times 10^{21}$ cm^{-2} with a median of $\sim 1 \times 10^{20}$ cm^{-2} (calculated for the data points with $N(H_2) > 0$ cm^{-2}). The median 1σ uncertainty is almost identical at 4.3$'$ angular resolution.

We present the $N(H_2)$ image at 4.3$'$ angular resolution in Figure 4.2. The blank data points correspond to point sources and regions with possible contamination (i.e., the Taurus molecular cloud and a

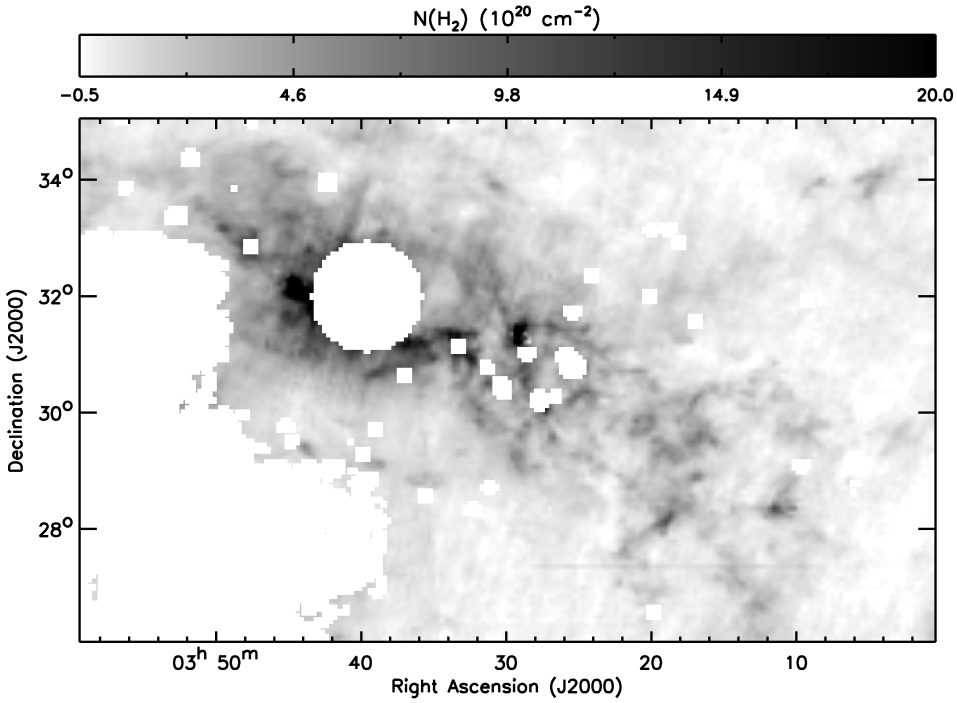

Fig. 4.2. — $N(H_2)$ image at 4.3′ angular resolution derived by Lee et al. (2012). The blank data points correspond to point sources and regions with possible contamination (i.e., the Taurus molecular cloud and a background HII region). See Sections 4.2 and 4.3 of Lee et al. (2012) for details.

background HII region). See Sections 4.2 and 4.3 of Lee et al. (2012) for details.

4.3.2 Observed CO Distributions

We use the COMPLETE CO data cube obtained with the 14 m FCRAO telescope (Ridge et al. 2006). This cube covers the main body of Perseus with a spatial area of $\sim 6^\circ \times 3^\circ$ at $46''$ angular resolution. We correct the CO data for the main-beam efficiency of 0.45, following Ridge et al. (2006) and Pineda et al. (2008). The rms noise per channel[6] ranges from $\sim$0.3 K to $\sim$3.5 K with a median of $\sim$0.7 K. To derive $I_{\rm CO}$, we integrate the CO emission from -5 km s^{-1} to $+15$ km s^{-1}, the range where Lee et al. (2012) found the HI emission associated with Perseus, with a spectral resolution of 0.064 km s^{-1}. The average CO spectrum for Perseus is shown in Figure 4.3. To produce this spectrum, we average spectra of all data points where the ratio of the peak main-beam brightness temperature to the rms noise is greater than 3. The CO emission is clearly contained between -5 km s^{-1} and $+15$ km s^{-1} and shows multiple velocity

[6]In this chapter, all temperatures are in main-beam brightness unit and all velocities are quoted in the local standard of rest (LSR) frame.

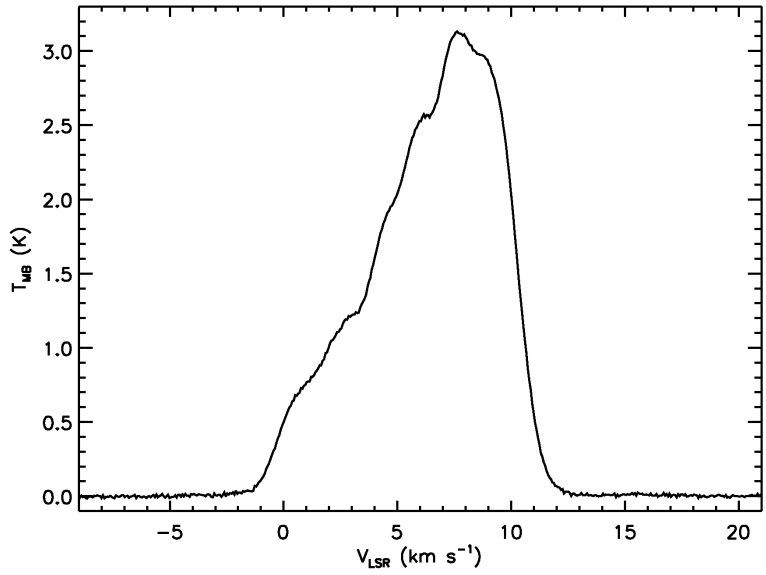

Fig. 4.3. — Average CO spectrum obtained by averaging spectra of all data points where the ratio of the peak main-beam brightness temperature to the rms noise is greater than 3. Note that the CO emission shows multiple velocity components.

components.

In addition, we use the $I_{\rm CO}$ image derived by Dame et al. (2001). This study combined the CO data of the Galactic plane and local molecular clouds obtained with the 1.2 m telescope at the Harvard Smithsonian Center for Astrophysics (CfA) and produced a composite survey of the Galaxy at 8.4′ angular resolution. To derive $I_{\rm CO}$ for Perseus, Dame et al. (2001) integrated the CO emission from -15 km s^{-1} to $+15$ km s^{-1} with a spectral resolution of 0.65 km s^{-1}. This range is slightly more extended toward negative velocities than the range of the HI emission. However, this is not concerning because no significant CO emission is found below -5 km s^{-1}. The derived $I_{\rm CO}$ image has a spatial coverage of $\sim 9^\circ \times 6^\circ$ and a uniform 1σ uncertainty of $\sim$1.1 K km s^{-1}. See Section 2 of Dame et al. (2001) for details on the CO data and the derivation of the $I_{\rm CO}$ image. We show the contours of the CfA $I_{\rm CO}$ image in Figure 4.1.

The COMPLETE CO data set offers a higher angular resolution (final angular resolution of 4.3′) and a better sensitivity (median 1σ uncertainty of $\sim$0.1 K km s^{-1} at 4.3′ angular resolution) than the CfA CO data set. However, it lacks a large spatial coverage. Therefore, we utilize the CfA CO data to investigate the large-scale properties across Perseus (Section 4.6.1), while using the COMPLETE CO data for most of our analysis. In comparison of the CfA $I_{\rm CO}$ image with the COMPLETE $I_{\rm CO}$ image smoothed to 8.4′

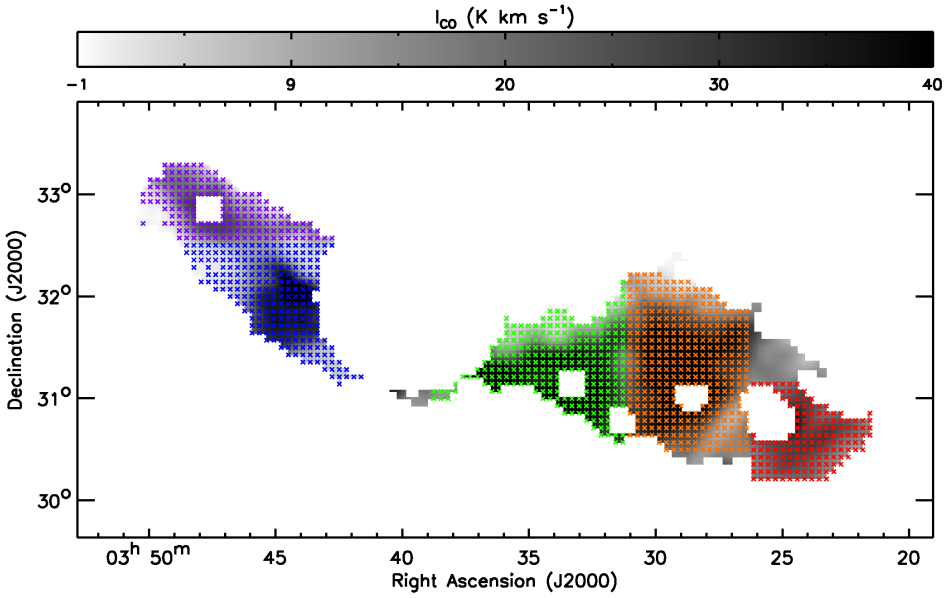

Fig. 4.4. — Each of the five regions is shown on the COMPLETE I_{CO} image with a different color. B5 is purple, IC348 is blue, B1E/B1 is green, NGC1333 is orange, and L1448 is red. See Section 4 for details on how we determined these regions.

angular resolution, we find that ∼80% of data points are consistent within 20%.

4.4 Region Division

As pointed out by Pineda et al. (2008) and Lee et al. (2012), there are considerable region-to-region variations in physical parameters across Perseus. We therefore divide Perseus into five regions and perform analyses mainly on the individual regions. To define the individual regions, we draw the COMPLETE I_{CO} contours from 4 K km s^{-1} (5% of the peak) to 72 K km s^{-1} (90% of the peak) with 4 K km s^{-1} intervals and determine the boundaries of each region. In addition, we select data points that have (1) -5 km s^{-1} < CO velocity centroid < +15 km s^{-1}, (2) $I_{CO} > 0$ K km s^{-1}, and (3) $N(H_2) > 0$ cm^{-2}. These criteria are to select data points that are reliable and kinematically associated with Perseus. Applying these criteria results in 1160 independent data points and all except three data points have S/N > 1 for both I_{CO} and $N(H_2)$. We show the selected data points for each region (dark regions: B5, B1E/B1, L1448 and star-forming regions: IC348, NGC1333) with a different color in Figure 4.4. The individual regions have an average size of ∼5–7 pc at the distance of 300 pc (Table 4.2).

Similarly, we determine seven regions for the CfA I_{CO} image. Compared to the five regions we previously defined, two dark regions (L1455 and Westend) are added in the southwest thanks to the large

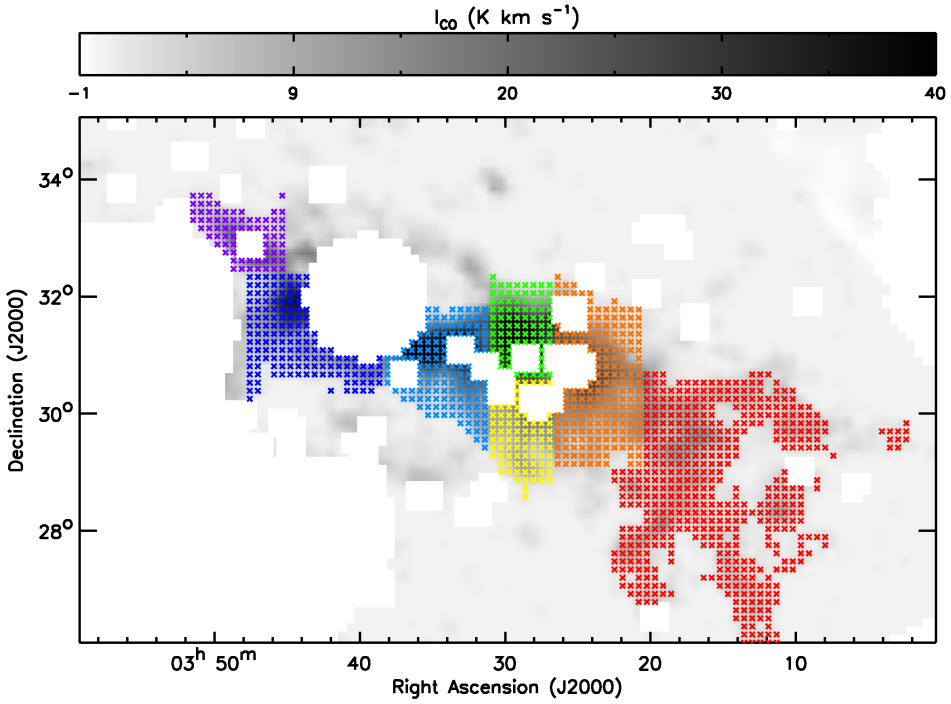

Fig. 4.5. — Each of the seven regions is shown on the CfA I_{CO} image with a different color. B5 is purple, IC348 is blue, B1E/B1 is sky blue, NGC1333 is green, L1455 is yellow, L1448 is orange, and Westend is red. See Section 4 for details on how we determined these regions.

spatial coverage of the CfA I_{CO} data. We base our determination of regional boundaries on the morphology of the CfA I_{CO} contours and select data points that have (1) S/N of $I_{CO} > 1$ and (2) S/N of $N(H_2) > 1$. In addition, we exclude data points that appear to be small-scale fluctuations in the far outskirts of the CfA I_{CO} image and therefore are likely not associated with our dark and star-forming regions. Note that we apply more restricted selection criteria than what we did for the COMPLETE I_{CO} image in an attempt to avoid possible contamination from noisy data points in the outskirts. Finally, 1196 data points remain for our analyses and each region is shown with a different color in Figure 4.5. The average size of the seven regions range from ∼6 pc to ∼16 pc at the distance of 300 pc (Table 4.1).

4.5 Deriving X_{CO}

We derive the X_{CO} image at 4.3′ angular resolution by applying Equation (4.1) to the $N(H_2)$ image and the COMPLETE I_{CO} image on a pixel-by-pixel basis (hereafter COMPLETE X_{CO}). Similarly, the CfA I_{CO} image is used to derive the X_{CO} image at 8.4′ angular resolution (hereafter CfA X_{CO}). We show both X_{CO} images in Figures 4.6 and 4.7.

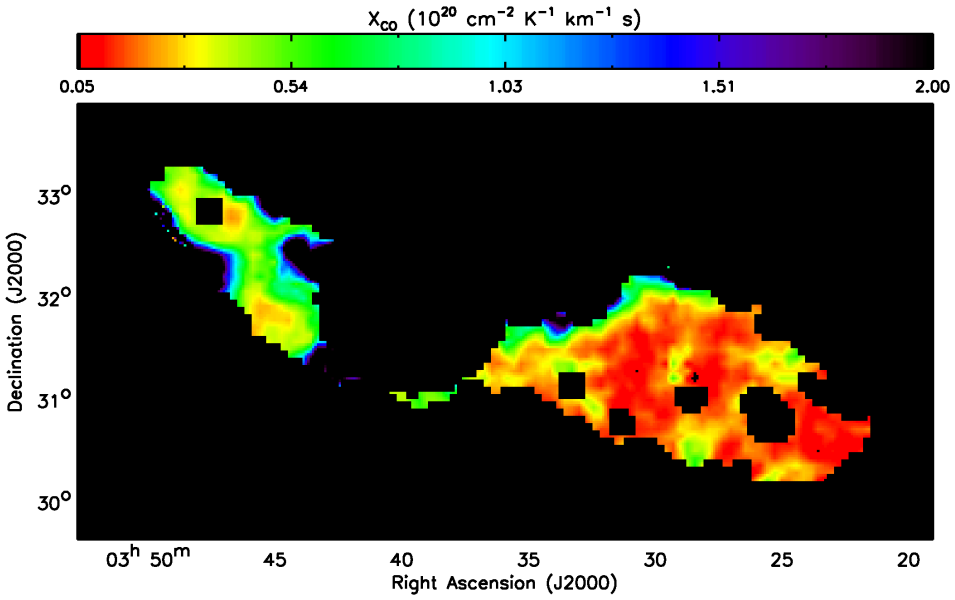

Fig. 4.6. — COMPLETE $X_{\rm CO}$ image at 4.3′ angular resolution.

For the five regions defined in Section 4.4, COMPLETE $X_{\rm CO}$ ranges from $\sim$5.7 $\times$ 10^{15} to $\sim$4.4 $\times$ 10^{21} with a median of $\sim$2.8 $\times$ 10^{19}. While $X_{\rm CO}$ shows a substantial range, most of the data points ($\sim$80%) have $10^{19} < X_{\rm CO} < 10^{20}$. The 1$\sigma$ uncertainty of $X_{\rm CO}$ is derived based on the propagation of errors (Bevington & Robinson 2003) and its median is $\sim$1.4 $\times$ 10^{18}.

4.6 Results

4.6.1 Large-scale Spatial Variations of $X_{\rm CO}$

Figure 4.7 shows interesting spatial variations of $X_{\rm CO}$ across Perseus. To quantify these variations, we estimate the median $X_{\rm CO}$ for each dark and star-forming region (Table 4.1). We find a factor of $\sim$3 decrease in $X_{\rm CO}$ from the northeastern regions (B5 and IC348) where $X_{\rm CO} \sim 7.1 \times 10^{19}$ to the southwestern regions (B1E/B1, NGC1333, L1455, L1448, and Westend) where $X_{\rm CO} \sim 2.8 \times 10^{19}$. Our result is in agreement with Pineda et al. (2008) who found a factor of $\sim$2 variation in $X_{\rm CO}$ for different sub-regions in Perseus. However, while they estimated a single $X_{\rm CO}$ for each sub-region, we have derived the spatial distribution of $X_{\rm CO}$. Based on this distribution, we investigate large-scale trends in several physical parameters and their possible connection with the variations of $X_{\rm CO}$.

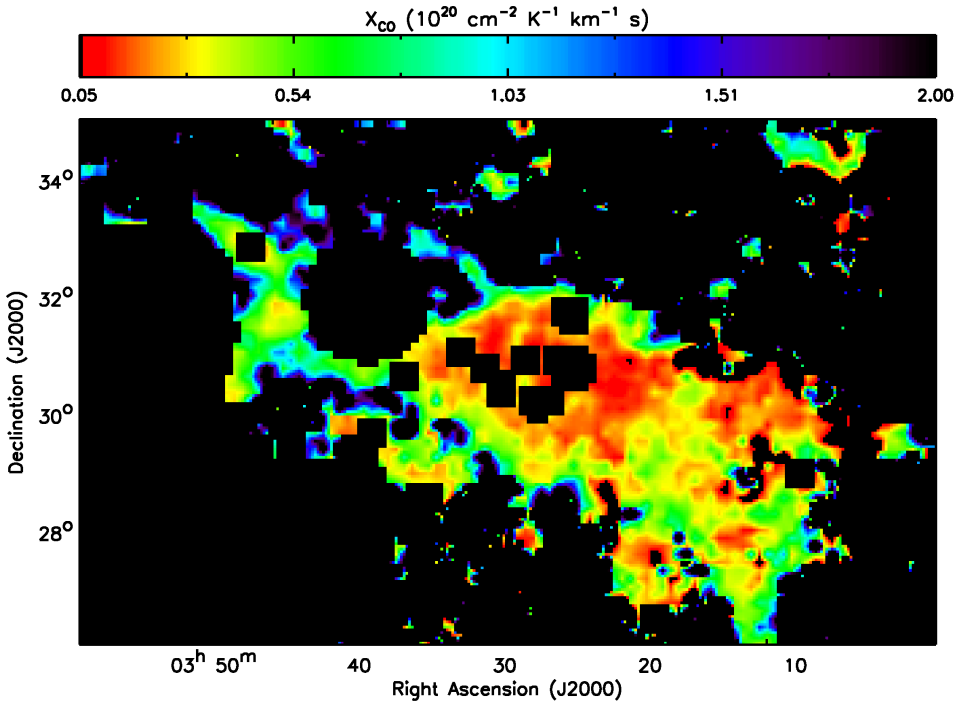

Fig. 4.7. — CfA $X_{\rm CO}$ image at 8.4′ angular resolution.

We first derive the $\sigma_{\rm CO}$ image using the COMPLETE CO data cube (Figure 4.8). For this analysis, we sacrifice the large spatial coverage of the CfA CO data due to the coarse velocity resolution of 0.65 km s^{-1}. Figure 4.8 shows that the southwestern part has systematically larger $\sigma_{\rm CO}$ than the northeastern part. For example, ∼63% of the data points in the southwestern part have 1.5 km s^{-1} $< \sigma_{\rm CO} <$ 3 km s^{-1}, while ∼52% of the data points in the northeastern part have 0.5 km s^{-1} $< \sigma_{\rm CO} <$ 1.5 km s^{-1}. In particular,

Table 4.1. Median $X_{\rm CO}$ for the Dark and Star-forming Regions

Region	Average Size (pc)[a]	Median CfA $X_{\rm CO}$ (cm^{-2} K^{-1} km^{-1} s)
B5	∼6	$\sim 7.3 \times 10^{19}$
IC348	∼9	$\sim 6.9 \times 10^{19}$
B1E/B1	∼8	$\sim 3.3 \times 10^{19}$
NGC1333	∼7	$\sim 2.1 \times 10^{19}$
L1455	∼6	$\sim 3.1 \times 10^{19}$
L1448	∼10	$\sim 2.1 \times 10^{19}$
Westend	∼16	$\sim 3.4 \times 10^{19}$

[a]The characteristic size of each region calculated by (total number of pixels)$^{1/2}$ × 0.73 pc, where 0.73 pc is the physical size of one pixel.

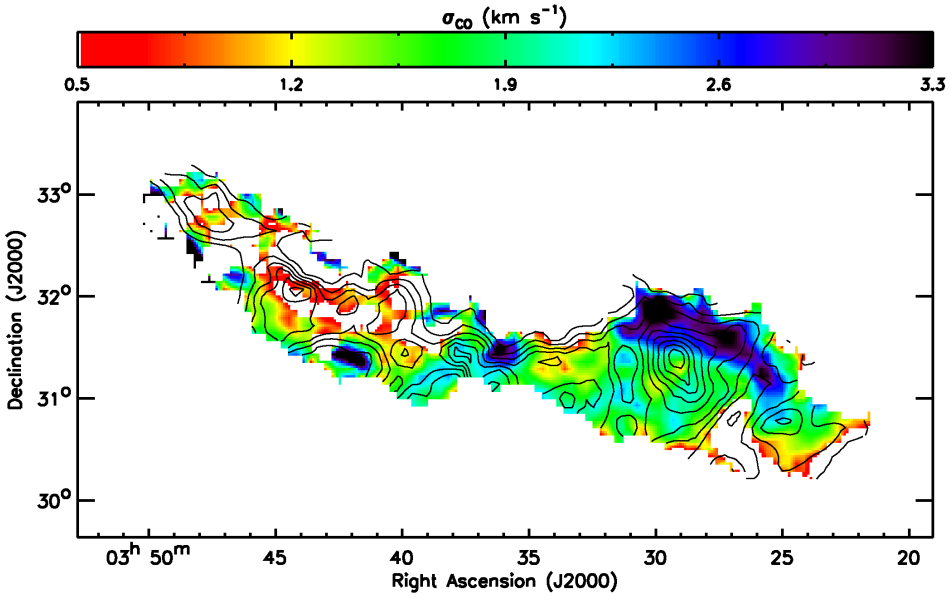

Fig. 4.8. — σ_{CO} image overlaid with the COMPLETE I_{CO} contours. The contour levels range from 10% to 90% of the peak (79 K km s^{-1}) with 10% steps.

B1E/B1 and NGC1333 have the largest median $\sigma_{CO} \sim 2$ km s^{-1} compared to other regions where the median σ_{CO} is $\sim$1.3 km s^{-1} (Table 4.2). The large σ_{CO} in the southwestern part could be caused by more complex velocity structure and/or multiple components along a line of sight. In addition, outflows from embedded protostars could contribute to broad CO spectra. For example, B1 and NGC1333 have a large number of Herbig-Haro (H-H) objects identified from the surveys of Hα and [SII] emission, which trace currently active shocks in outflows (e.g., Figure 6 of Bally et al. 2008).

Table 4.2. Median σ_{CO} for the Dark and Star-forming Regions

Region	Average Size (pc)[a]	Median σ_{CO} (km^{-1} s)
B5	$\sim$5	$\sim$1.3
IC348	$\sim$6	$\sim$1.3
B1E/B1	$\sim$6	$\sim$1.8
NGC1333	$\sim$7	$\sim$2
L1448	$\sim$5	$\sim$1.3

[a]The characteristic size of each region calculated by (total number of pixels)$^{1/2}$ $\times$ 0.38 pc, where 0.38 pc is the physical size of one pixel.

The $T_{\rm dust}$ image derived by Lee et al. (2012) also shows systematic variations across Perseus. Specifically, $T_{\rm dust}$ slightly decreases toward the southwestern part. This is consistent with Pineda et al. (2008) who found $T_{\rm dust} \sim 17$ K for B5/IC348 and $T_{\rm dust} \sim 16$ K for B1E/B1/NGC1333. To investigate the variation of ISRF, we derive G using Equation (4.2) and make histograms for B5/IC348 (*East*), B1E/B1/NGC1333/L1455 (*Middle*), and L1488/Westend (*West*). Figure 4.9 shows the median G of *East* ($\sim 10^{-2.93}$ erg cm^{-2} s^{-1}) as a black dashed line. We find that $\sim$50%, $\sim$10%, and 0% of data points have $G > 10^{-2.93}$ erg cm^{-2} s^{-1} for *East*, *Middle*, and *West*, respectively. This suggests that G systematically decreases toward the southwestern part of Perseus. However, the variation of G is very mild: the median G decreases from *East* to *West* by only a factor of $\sim$1.2. This result does not change even when we examine the median G for each dark and star-forming region.

Finally, Lee et al. (2012) noticed a considerable difference between the northeastern and southwestern part of Perseus with regard to the relative spatial distribution of H_2 and CO. They estimated the amount of "CO-dark" H_2, which refers to interstellar gas in the form of H_2 along with CI and CII but little or no CO, and found a factor of $\sim$3 decrease toward the southwestern part of Perseus. In other words, "CO-free" H_2 envelopes exist in the northeastern part, while CO traces H_2 reasonably well in the southwestern part (Figure 14 of Lee et al. 2012). This suggests that H_2 takes up a larger volume than CO in the northeastern region, which could result in larger $X_{\rm CO}$.

Many theoretical studies of $X_{\rm CO}$ (e.g., Maloney & Black 1988; Taylor et al. 1993; Le Bourlot et al. 1993; Wolfire et al. 1993; Sakamoto 1996, 1999; Kaufman et al. 1999; Bell et al. 2006; Glover & Mac Low 2011; Shetty et al. 2011a,b) have shown that $X_{\rm CO}$ can vary by several orders of magnitude with changes in physical parameters such as density, metallicity, ISRF, microturbulent linewidth, and so on. For example, Bell et al. (2006) predict that a stronger ISRF and a smaller microturbulent linewidth can increase $X_{\rm CO}$. This is qualitatively in agreement with what we found: the northeastern part has on average larger $X_{\rm CO}$ than the southwestern part. In addition, Pineda et al. (2008) modelled the CO and ^{13}CO($J = 1 \rightarrow 0$) integrated intensity of Perseus using the Meudon PDR code (Le Petit et al. 2006) and found that the observed variations among different sub-regions can be explained by variations in density and non-thermal gas motions.

As pointed out by Bell et al. (2006), $X_{\rm CO}$ has high degeneracy and many combinations of input parameters can produce the same value of $X_{\rm CO}$. One therefore has to be cautious when trying to constrain

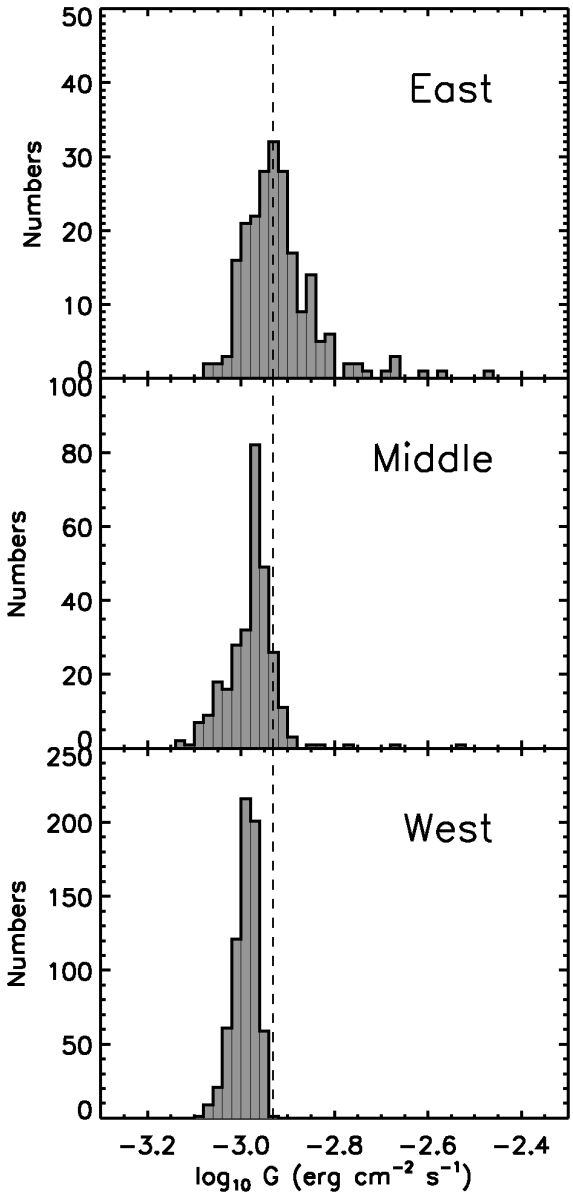

Fig. 4.9. — Histograms of G. B5/IC348, B1E/B1/NGC1333/L1455, and L1448/Westend (determined based on the CfA $I_{\rm CO}$ image) are combined to produce the histograms of *East*, *Middle*, and *West*. The median G of *East* ($\sim 10^{-2.93}$ erg cm^{-2} s^{-1}) is shown as a black dashed line.

physical conditions by matching models to the observed value of $X_{\rm CO}$. However, from a theoretical stand point, $X_{\rm CO}$ has an interesting characteristic dependence on A_V (e.g., Bell et al. 2006; Glover & Mac Low 2011; Shetty et al. 2011a; Feldmann et al. 2012a). We focus on investigating this characteristic dependance of $X_{\rm CO}$ on A_V in comparison with two different theoretical models.

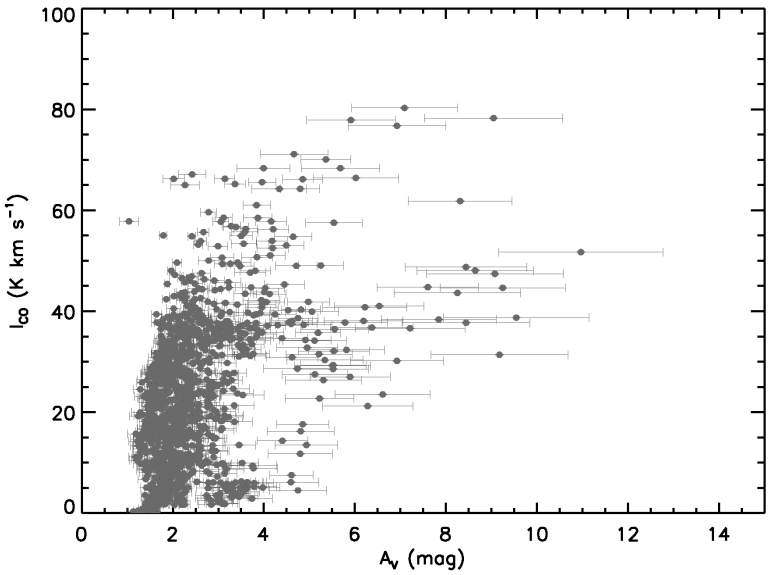

Fig. 4.10. — COMPLETE $I_{\rm CO}$ as a function of A_V for all five regions defined in Section 4.4.

4.6.2 $I_{\rm CO}$ versus A_V

4.6.2.1 Global Properties

To understand how $X_{\rm CO}$ varies with A_V, we begin by plotting COMPLETE $I_{\rm CO}$ as a function of A_V in Figure 4.10 for all five regions defined in Section 4.4. We use the A_V image derived by Lee et al. (2012). Even though there is a large amount of scatter, several important features are noticeable.

First, there is a threshold $A_{V,\rm th} \sim 1$ mag below which no CO emission is detected. A lack of CO detection at $A_V \lesssim 1$ mag is not due to our sensitivity, considering that our median 1σ uncertainty of A_V is $\sim$0.1 mag. Instead, this suggests that CO becomes shielded against photodissociation at $A_V \sim 1$ mag in Perseus. Previous observations of molecular clouds have found a similar value $A_{V,\rm th} \sim 1$ mag (e.g., Lombardi et al. 2006; Pineda et al. 2008; Leroy et al. 2009).

Second, $I_{\rm CO}$ significanly increases from $\sim$0.1 K km s^{-1} to $\sim$70 K km s^{-1} for a narrow range of A_V $\sim$ 1–3 mag. This steep increase of $I_{\rm CO}$ suggests that the transition from CII/CI to CO is sharp once the shielding becomes sufficiently strong to prevent photodissociation.

Third, $I_{\rm CO}$ gradually increases and saturates to $\sim$50–80 K km s^{-1} at $A_{V,\rm sat} \gtrsim 3$ mag. This is consistent with Pineda et al. (2008) who found $A_{V,\rm sat} \sim 4$ mag. Similarly, Lombardi et al. (2006) found the saturation of $I_{\rm CO} \sim 30$ K km s^{-1} for the Pipe nebula at higher $A_{V,\rm sat} \sim 6$ mag (assuming their adopted

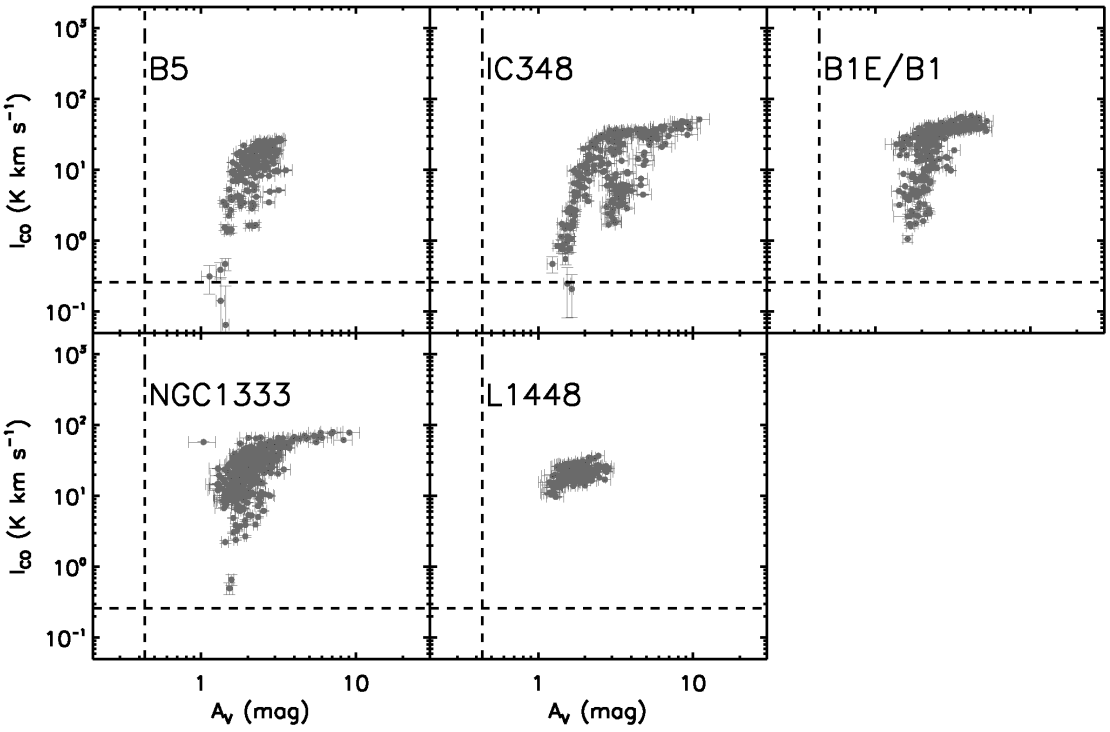

Fig. 4.11. — COMPLETE $I_{\rm CO}$ as a function of A_V for each dark and star-forming region. The median 3σ uncertainties of $I_{\rm CO}$ ($\sim$0.26 K km s^{-1}) and A_V ($\sim$0.43 mag) calculated for the data points with $N(\rm H_2)$ > 0 cm^{-2} and $I_{\rm CO} > 0$ K km s^{-1} are shown as dashed lines.

relation $A_V = A_K/0.112$). We can understand the saturation of $I_{\rm CO}$ by the relation between $I_{\rm CO}$ and τ, $I_{\rm CO} \propto 1 - e^{-\tau}$, where $\tau \propto A_V$. In other words, $I_{\rm CO}$ does not faithfully trace A_V once it becomes optically thick.

4.6.2.2 Individual Regions

In agreement with Pineda et al. (2008), we find that the relation between $I_{\rm CO}$ and A_V has significant region-to-region variations across Perseus, contributing to the large scatter in Figure 4.10. We therefore show COMPLETE $I_{\rm CO}$ vs A_V for each dark and star-forming region in Figure 4.11. To emphasize the steep increase and the saturation of $I_{\rm CO}$, we plot COMPLETE $I_{\rm CO}$ as a function of A_V on a log-log scale.

Among the five regions, B5 and L1448 have the narrowest range of $A_V \sim$ 1–3 mag, simply reflecting their smaller N(H) range on average. Due to this limited range of A_V, we focus on IC348, B1E/B1, and NGC1333 in the rest of this chapter and find the following relation between $I_{\rm CO}$ and A_V:

1. IC348 has the largest ranges of $A_V \sim$ 1–11 mag and $I_{\rm CO} \sim$ 0.2–50 K km s^{-1}. $I_{\rm CO}$ steeply increases

from ∼0.2 K km s^{-1} to ∼35 K km s^{-1} at $A_V \sim$ 1–3 mag and then saturates to ∼50 K km s^{-1} at $A_V \gtrsim$ 3 mag.

2. B1E/B1 appears to have two components. The first component corresponds to the relatively steep increase of $I_{\rm CO}$ from ∼1 K km s^{-1} to ∼20 K km s^{-1} at $A_V \sim$ 1.5–3 mag. The second component corresponds to the gradual increase of $I_{\rm CO}$ from ∼20 K km s^{-1} to ∼60 K km s^{-1} at $A_V \sim$ 1.5–5 mag. Considering the two components together, $I_{\rm CO}$ saturates to ∼60 K km s^{-1} at $A_V \gtrsim$ 3 mag.

3. NGC1333 has the majority of the data points (∼90%) at $A_V \lesssim$ 3 mag. $I_{\rm CO}$ increases from ∼2 K km s^{-1} to ∼70 K km s^{-1} at $A_V \sim$ 1–3 mag. $I_{\rm CO}$ then shows a hint of saturation to ∼80 K km s^{-1} at $A_V \gtrsim$ 3 mag. Note that NGC1333 is the region where $I_{\rm CO}$ saturates to the largest value in Perseus.

In summary, the most important properties we found from the individual regions are the abrupt increase of $I_{\rm CO}$ at $A_V \lesssim$ 3 mag and the saturation of $I_{\rm CO}$ at $A_V \gtrsim$ 3 mag. However, $I_{\rm CO}$ saturates to different values, from ∼50 K km s^{-1} for IC348 to ∼80 K km s^{-1} for NGC1333.

4.6.3 $X_{\rm CO}$ versus A_V

Our derived spatial distribution of $X_{\rm CO}$ allows us to test interesting theoretical predictions such as the dependence of $X_{\rm CO}$ on A_V. For IC348, B1E/B1, and NGC1333, where A_V extends up to ∼5–11 mag, we find the following variations in the shape of the $X_{\rm CO}$ vs A_V profiles (Figure 4.12):

1. IC348 has a clear trend of $X_{\rm CO}$ decreasing at small A_V and increasing at large A_V. $X_{\rm CO}$ decreases by a factor of ∼70 at $A_V \sim$ 1–2.5 mag, while increasing by only a factor of ∼4 at $A_V \sim$ 2.5–11 mag. Overall, $X_{\rm CO}$ varies by a factor of ∼70 within this region (∼9 pc × 7 pc).

2. B1E/B1 appears to have two components. The majority of the data points show a linear increase of $X_{\rm CO}$ from $\sim 7 \times 10^{18}$ to $\sim 5 \times 10^{19}$ for $A_V \sim$ 1.5–5 mag. The additional group of the data points is located at $A_V \sim$ 2–3 mag and $X_{\rm CO} \sim 10^{20}$ with some scatter. Again, we find a factor of ∼35 variations in $X_{\rm CO}$ within this region (∼10 pc × 8 pc).

3. NGC1333 has the majority of the data points (∼83%) at $A_V \lesssim$ 3 mag and $X_{\rm CO} \lesssim 5 \times 10^{19}$ with a large degree of scatter (a factor of ∼10). At $A_V \sim$ 3–10 mag, $X_{\rm CO}$ increases by only a factor of ∼4. On the whole, NGC1333 with a size of ∼6 pc × 9 pc shows a factor of ∼80 variations in $X_{\rm CO}$.

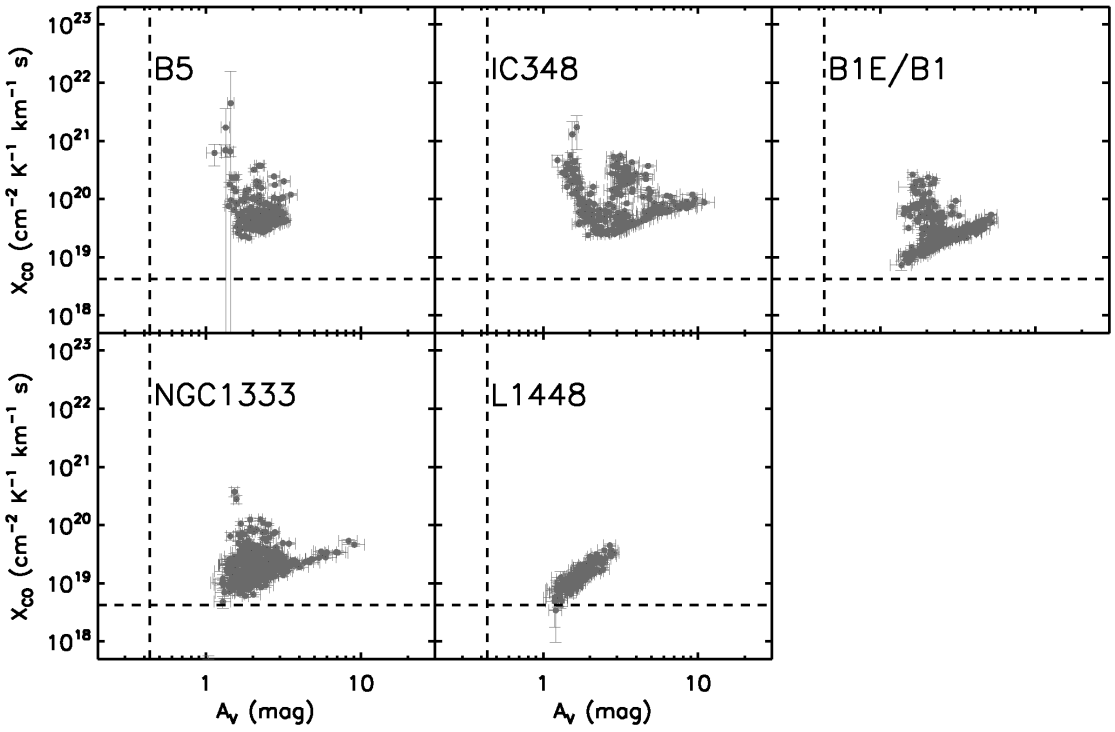

Fig. 4.12. — COMPLETE $X_{\rm CO}$ as a function of A_V for each dark and star-forming region. The median 3σ uncertainties of $X_{\rm CO}$ ($\sim$4.19 $\times$ 10^{18}) and A_V ($\sim$0.43 mag) calculated for the data points with $N(\rm H_2)$ > 0 cm^{-2} and $I_{\rm CO} > 0$ K km s^{-1} are shown as dashed lines.

Clearly, the three regions show a factor of up to $\sim$80 variations in $X_{\rm CO}$ within a spatial area of $\sim$10 pc $\times$ 10 pc. We notice that the shape of the $X_{\rm CO}$ vs A_V profile is primarily driven by how $I_{\rm CO}$ varies with A_V. Specifically, decreasing $X_{\rm CO}$ with A_V results from the steep increase of $I_{\rm CO}$ at small A_V, while increasing $X_{\rm CO}$ with A_V is due to the saturation of $I_{\rm CO}$ at large A_V. $X_{\rm CO}$ decreases because $I_{\rm CO}$ increases more steeply than $N(\rm H_2)$ due to the sharp transition from CII/CI to CO. On the other hand, $X_{\rm CO}$ increases because $I_{\rm CO}$ increases more gradually than $N(\rm H_2)$ due to its saturation. Therefore, the transition from decreasing to increasing $X_{\rm CO}$ occurs in the $X_{\rm CO}$ vs A_V profile where the CO emission becomes optically thick. This is particulary prominent for IC348, where this transition occurs at $A_V \sim 3$ mag. B1E/B1 is relatively similar with IC348, while we do not observe a clear indication of this transition for NGC1333. Several theoretical studies have predicted a similar shape for the $X_{\rm CO}$ vs A_V profile (e.g., Bell et al. 2006; Glover & Mac Low 2011; Shetty et al. 2011a; Feldmann et al. 2012a). In the next sections, we compare our $X_{\rm CO}$ data with predictions from two models.

4.7 $X_{\rm CO}$: Comparison between Observations and Theory

4.7.1 Microturbulent Equilibrium Model

4.7.1.1 Summary of the Modified W10 Model

The modified W10 model describes a one-dimensional plane-parallel slab of gas illuminated by UV photons on two sides. The slab can have either a uniform density or a specified density distribution. The gas temperature and the abundances of atomic/molecular species are calculated as a function of A_V under the assumption of thermal balance and chemical equilibrium. For details on the modified W10 model, we refer to Tielens & Hollenbach (1985), Kaufman et al. (2006), Wolfire et al. (2010), and Hollenbach et al. (2012).

The input parameters for the modified W10 model are n, G, ζ, $v_{\rm turb}$, Z, and DGR. Considering the constraints on the physical parameters of Perseus (Section 4.2.2), we use a set of the modified W10 models with the following inputs: $G = 0.5\ G_0'$, $\zeta = 10^{-16}$ s^{-1}, $v_{\rm turb} = 4$ km s^{-1}, $Z = 1$ Z$_\odot$, and DGR $= 1 \times 10^{-21}$ mag cm^2. For the density distribution, we use both a uniform density distribution with $n = 10^3$, 5×10^3, and 10^4 cm^{-3} and a "core-halo" density distribution. The "halo" consists of HI with a fixed density $n_{\rm halo} = 40$ cm^{-3}, comparable to diffuse cold neutral medium (CNM) clouds (Wolfire et al. 2003) and has $N({\rm HI}) = 4.5 \times 10^{20}$ cm^{-2} on each side of the slab. In the "core", n abruptly increases to a large density $n_{\rm core} = 10^3$, 5×10^3, and 10^4 cm^{-3}. This "core-halo" structure is motivated by observations of molecular clouds that have found HI envelopes with $N({\rm HI}) \sim 10^{21}$ cm^{-2} (e.g., Imara & Blitz 2011; Imara, Bigiel, & Blitz 2011; Lee et al. 2012). The modified W10 model is run for $A_V = 1.25$, 1.3, 1.5, 1.7, 2, 2.8, 4.8, 7.2, 10 mag ("core-halo") and $A_V = 0.6$, 0.8, 1, 1.5, 2, 2.8, 4.8, 7.2, 10 mag (uniform density) and the outputs are $N({\rm HI})$, $N({\rm H_2})$, and $I_{\rm CO}$ for a given A_V. We summarize the outputs from the modified W10 model in Tables 4.3 ("core-halo") and 4.4 (uniform density). The assumed "core" has a typical length of $L_{\rm core} \lesssim 1$ pc, while the "halo" is significantly more extended with $L_{\rm halo} \sim 7$ pc.

4.7.1.2 Comparison with Observations: "Core-halo" Density Distribution

We compare COMPLETE $X_{\rm CO}$ vs A_V with predictions from the modified W10 model ("core-halo") in Figure 4.13. While B5 and L1448 probe too narrow ranges of A_V for significant comparisons, the model

Table 4.3. Predictions from the Modified W10 Model with a "Core-Halo" Density Distribution[a]

	$n_{\rm core} = 10^3$ cm^{-3}	$n_{\rm core} = 5 \times 10^3$ cm^{-3}	$n_{\rm core} = 10^4$ cm^{-3}
N(HI) (cm^{-2})[b]	$9.00 \times 10^{20} \sim 9.60 \times 10^{20}$	$8.98 \times 10^{20} \sim 9.20 \times 10^{20}$	$8.96 \times 10^{20} \sim 9.04 \times 10^{20}$
N(H$_2$) (cm^{-2})[b]	$1.75 \times 10^{20} \sim 4.52 \times 10^{21}$	$1.75 \times 10^{20} \sim 4.54 \times 10^{21}$	$1.75 \times 10^{20} \sim 4.55 \times 10^{21}$
$R_{\rm H2}$[b]	$0.39 \sim 9.42$	$0.39 \sim 9.87$	$0.39 \sim 10.11$
$I_{\rm CO}$ (K km s^{-1})[b]	$0.075 \sim 36.90$	$0.33 \sim 41.40$	$0.39 \sim 33.90$
$L_{\rm halo}$ (pc)[c]	7.28	7.28	7.28
$L_{\rm core}$ (pc)[b,d]	$0.11 \sim 2.94$	$0.022 \sim 0.59$	$0.011 \sim 0.29$
$L_{\rm halo-core}$ (pc)[b,e]	$7.39 \sim 10.23$	$7.30 \sim 7.87$	$7.29 \sim 7.58$
$\langle n \rangle$ (cm^{-3})[b,f]	$54.70 \sim 316.46$	$55.38 \sim 411.18$	$55.47 \sim 427.17$

[a]For all three models, $n_{\rm halo} = 40$ cm^{-3}.

[b]The minimum and maximum values are provided.

[c]The size of the diffuse halo $L_{\rm halo} = 9.00 \times 10^{20}$ cm^{-2}/40 cm^{-3}.

[d]The size of the dense core $L_{\rm core} = (N({\rm H}) - 9.00 \times 10^{20}$ cm^{-2})$/n_{\rm core}$.

[e]The total size of the slab $L_{\rm halo-core} = L_{\rm halo} + L_{\rm core}$.

[f]The average density $\langle n \rangle = N({\rm H})/L_{\rm halo-core}$.

Table 4.4. Predictions from the Modified W10 Model with a Uniform Density Distribution

	$n = 10^3$ cm^{-3}	$n = 5 \times 10^3$ cm^{-3}	$n = 10^4$ cm^{-3}
N(HI) (cm^{-2})[a]	$5.71 \times 10^{19} \sim 1.30 \times 10^{20}$	$1.15 \times 10^{19} \sim 2.66 \times 10^{19}$	$5.59 \times 10^{18} \sim 1.33 \times 10^{19}$
$N(H_2)$ (cm^{-2})[a]	$2.72 \times 10^{20} \sim 4.94 \times 10^{21}$	$2.95 \times 10^{20} \sim 4.99 \times 10^{21}$	$2.98 \times 10^{20} \sim 5.00 \times 10^{21}$
R_{H2}[a]	$9.53 \sim 76.00$	$51.30 \sim 375.19$	$106.62 \sim 751.88$
I_{CO} (K km s^{-1})[a]	$0.84 \sim 46.90$	$9.79 \sim 62.40$	$18.00 \sim 60.20$
$L_{uniform}$(pc)[a,b]	$0.19 \sim 3.24$	$0.039 \sim 0.65$	$0.019 \sim 0.32$

[a]The minimum and maximum values are provided.

[b]The total size of the slab $L_{uniform} = N(H)/n$.

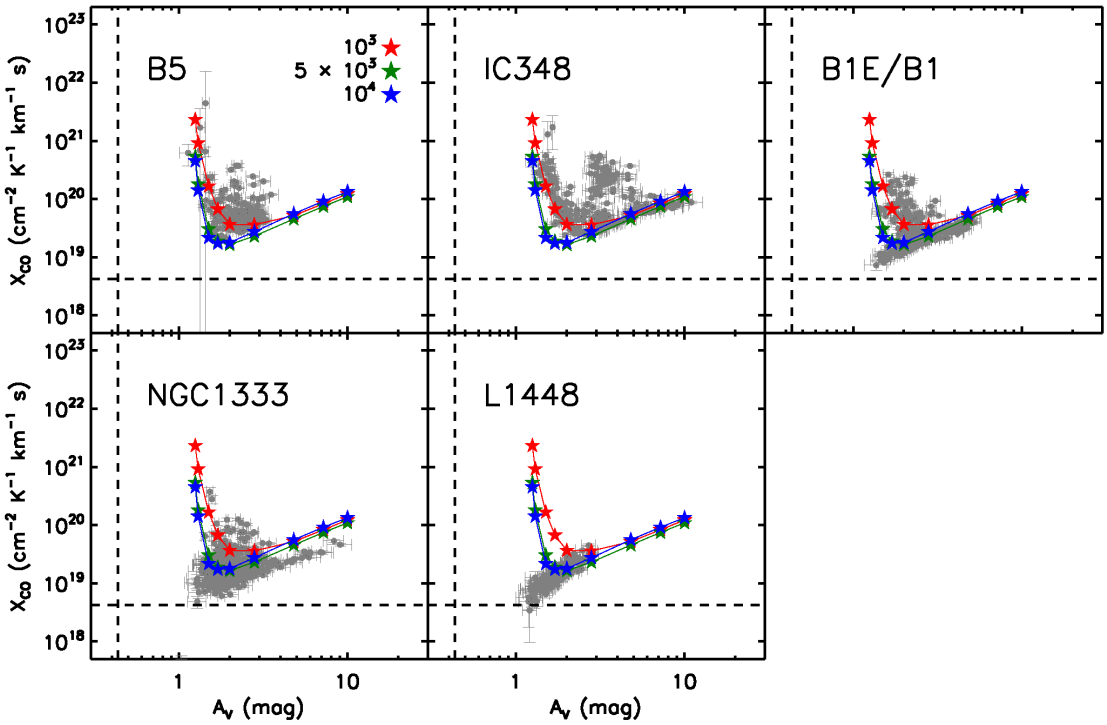

Fig. 4.13. — Comparison with the modified W10 model for $X_{\rm CO}$ vs A_V. The modified W10 model with $n_{\rm core} = 10^3$, 5×10^3, and 10^4 cm^{-3} is shown with red, green, and blue stars, respectively. The median 3σ uncertainties of $X_{\rm CO}$ ($\sim$4.19 $\times$ 10^{18}) and A_V ($\sim$0.43 mag) calculated for the data points with $N(\rm H_2) > 0$ cm^{-2} and $I_{\rm CO} > 0$ K km s^{-1} are shown as dashed lines.

curves with $n_{\rm core} = 10^{3-4}$ cm^{-3} follow the observed trends for IC348 and B1E/B1. The situation is more complicated for NGC1333, where the model matches the observed $X_{\rm CO}$ only for a partial range of A_V and has difficulties in reproducing the observations particularly at $A_V \lesssim 3$ mag and $X_{\rm CO} \lesssim 10^{19}$. In addition, NGC1333 lacks the decreasing portion of the $X_{\rm CO}$ vs A_V profile because of missing data points with small $I_{\rm CO} \lesssim 10$ K km s^{-1}, most likely due to the confined spatial area of the COMPLETE $I_{\rm CO}$ image. Here we provide a description of the detailed comparison between our data and the modified W10 model.

1. For IC348, the modified W10 model with $n_{\rm core} = 10^3$ cm^{-3} reproduces well the observed shape of the $X_{\rm CO}$ vs A_V profile (decreasing $X_{\rm CO}$ at $A_V \lesssim 3$ mag and increasing $X_{\rm CO}$ at $A_V \gtrsim 3$ mag).

2. For B1E/B1, the modified W10 model with $n_{\rm core}$ varying from $\sim 10^3$ cm^{-3} to $\sim 10^4$ cm^{-3} can reproduce the observed shape of the $X_{\rm CO}$ and A_V profile.

3. For NGC1333, the observed scatter at small A_V calls for a range of $n_{\rm core} \sim 10^{3-4}$ cm^{-3}. Considering that the models with $n_{\rm core} = 5 \times 10^3$ cm^{-3} and 10^4 cm^{-3} are essentially identical, however, the

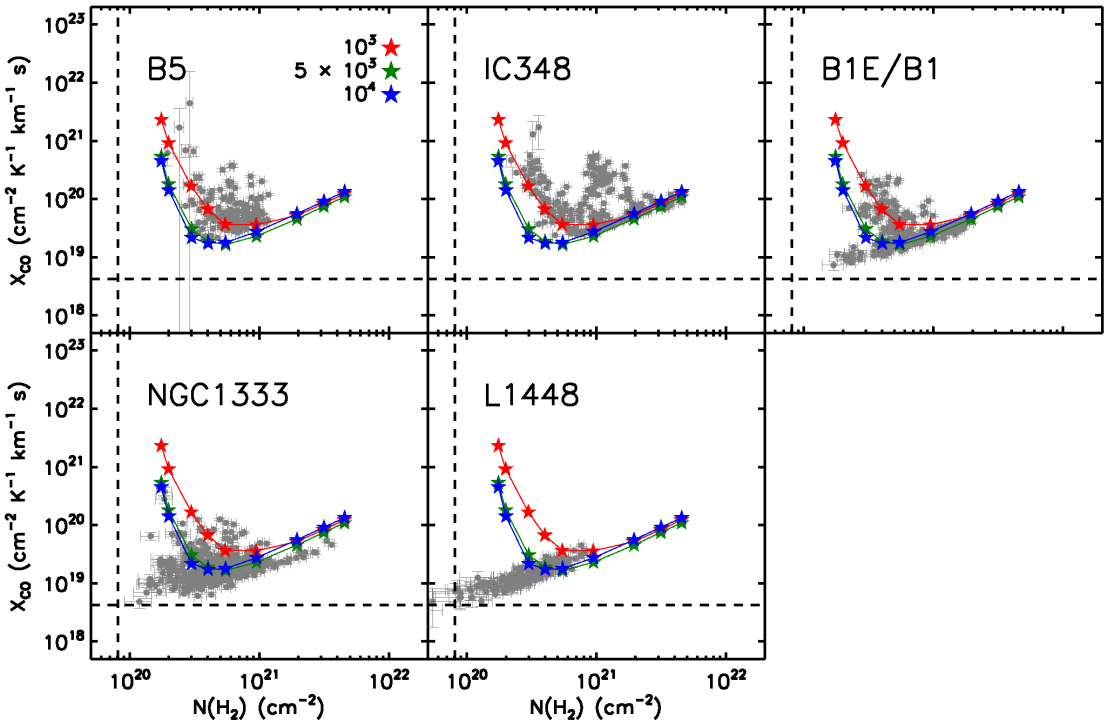

Fig. 4.14. — Comparison with the modified W10 model for $X_{\rm CO}$ vs $N({\rm H_2})$. The modified W10 model with $n_{\rm core} = 10^3$, 5×10^3, and 10^4 cm^{-3} is shown with red, green, and blue stars, respectively. The median 3σ uncertainties of $X_{\rm CO}$ ($\sim$4.19 $\times$ 10^{18}) and $N({\rm H_2})$ ($\sim$8.07 $\times$ 10^{19} cm^{-2}) calculated for the data points with $N({\rm H_2}) > 0$ cm^{-2} and $I_{\rm CO} > 0$ K km s^{-1} are shown as dashed lines.

data points at $A_V \lesssim 3$ mag with $X_{\rm CO} \lesssim 10^{19}$ are likely not reproduced by the model with larger $n_{\rm core}$. In addition, our observational data lack the decreasing portion of the $X_{\rm CO}$ vs A_V profile. We suspect that this is due to the limited spatial coverage of the COMPLETE $I_{\rm CO}$ image, which does not adequately sample low column density regions for NGC1333 (only $\sim$10% of the data points have $I_{\rm CO} < 10$ K km s^{-1}).

In Figure 4.14, we compare the observed $X_{\rm CO}$ vs $N({\rm H_2})$ profiles with the modified W10 model and find similar results. In summary, the modified W10 model with the "core-halo" structure and the input parameters appropriate for Perseus predicts the ranges of $I_{\rm CO}$ and $N({\rm H_2})$ in good agreement with our data. IC348 and B1E/B1 are the best cases where the shape of the $X_{\rm CO}$ vs A_V profile and the location of the minimum $X_{\rm CO}$ are well described by the model. We note that there are some discrepancies at low column densities in NGC1333, where the data points with small $X_{\rm CO} \lesssim 10^{19}$ are not reproduced by the model and at the same time the observed data with $X_{\rm CO} \gtrsim 10^{20}$ are missing due to the limited observational coverage.

Next, we plot N(HI) as a function of N(H) in Figure 4.15 and compare the profiles with the modified W10 model. As summarized in Section 4.2.1, Lee et al. (2012) found a relatively uniform N(HI) distribution across Perseus with $\sim$(8–10) $\times$ 10^{20} cm^{-2}. Here we use the same N(HI) image as in Lee et al. (2012) and apply the same boundaries for the five regions as in Section 4.4. We find that the median N(HI) varies from $\sim$7.4 $\times$ 10^{20} cm^{-2} (B5) to $\sim$9.7 $\times$ 10^{20} cm^{-2} (NGC1333). The model predicts N(HI) $\sim$ (9–9.6) $\times$ 10^{20} cm^{-2}, with essentially no difference between $n_{\rm core} = 10^3$ cm^{-3} and 10^4 cm^{-3} model. The predicted N(HI) distribution with $\sim$9 $\times$ 10^{20} cm^{-2} and its uniformity are consistent with what we observe in Perseus. This agreement will persist even if the N(HI) distribution is corrected for high optical depth HI. Our preliminary work on the effect of high optical depth HI that is missing in the HI emission image of Perseus shows that N(HI) increases by a factor of $\sim$1.4 on average due to the optical depth correction (the corrected N(HI) $\sim$ (8–20) $\times$ 10^{20} cm^{-2}; Stanimirović et al. in prep). The range of the predicted N(HI) and N(H$_2$) distribution is comparable to what we find in Perseus. In Figure 4.16, we plot $R_{\rm H2}$ against N(H) and indeed find that the modified W10 model matches well our observations. In particular, the linearly increasing $R_{\rm H2}$ with N(H) is reproduced well by the model, mainly driven by the uniform N(HI) distribution.

4.7.1.3 Comparison with Observations: Uniform Density Distribution

So far we made comparisons between the observations of Perseus and the modified W10 model with the "core-halo" structure. To investigate the role of the diffuse halo in determining the H$_2$ and CO distribution, we show our data for IC348 and predictions from the modified W10 model both with the "core-halo" structure and the uniform density distribution in Figure 4.17. The uniform density distribution simply assumes a dense "core" with $n = 10^3$, 5×10^3, or 10^4 cm^{-3}. Clearly, the "core-halo" model describes our data better. For example, the uniform density model underestimates the N(HI) distribution compared to the observed one across Perseus. In addition, it predicts the decreasing portion of the $X_{\rm CO}$ vs A_V profile shallower than our data, while reproducing the observed range of $X_{\rm CO}$ reasonably well. We compare the "core-halo" model with the uniform density model in detail as follows.

N(HI) vs N(H): The uniform density model predicts N(HI) significantly smaller than what we measure across Perseus, N(HI) $\sim$ 9 $\times$ 10^{20} cm^{-2}. The discrepancy ranges from a factor of $\sim$10–20 for n = 10^3 cm^{-3} to a factor of $\sim$70–160 for n = 10^4 cm^{-3}. This large discrepancy results from the fact that the H$_2$ self-shielding is so strong that almost all hydrogen is converted into H$_2$. On the other hand, the density of the halo is small enough that the dust shielding is more important than the H$_2$ self-shielding. To

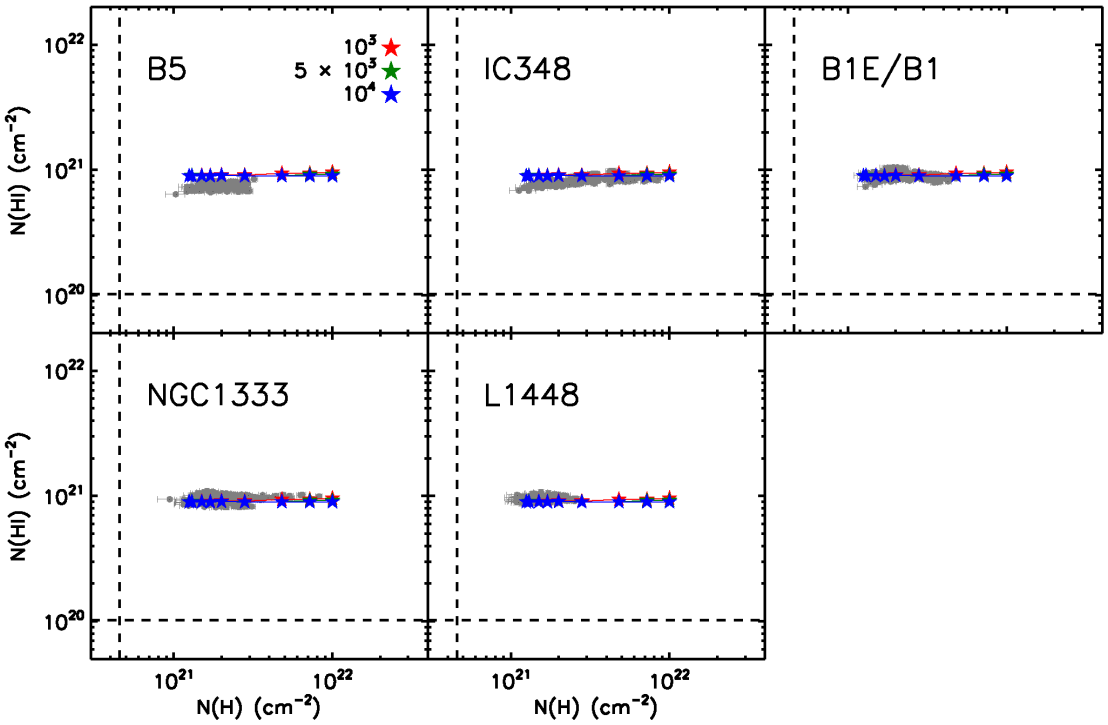

Fig. 4.15. — Comparison with the modified W10 model for N(HI) vs N(H) = N(HI) + 2N(H_2). The modified W10 model with $n_{\rm core}$ = 10^3, 5 × 10^3, and 10^4 cm^{-3} is shown with red, green, and blue stars, respectively. The N(HI) vs N(H) profiles predicted by the models with $n_{\rm core}$ = 5 × 10^3 and 10^4 cm^{-3} are almost identical. The median 3σ uncertainties of N(HI) ($\sim$1.02 × 10^{20} cm^{-2}) and N(H) ($\sim$4.56 × 10^{20} cm^{-2}) calculated for the data points with N(H_2) > 0 cm^{-2} and $I_{\rm CO}$ > 0 K km s^{-1} are shown as dashed lines.

provide the sufficient dust shielding for H_2 formation, the entire halo remains atomic with its initial N(HI) $\sim$ 9 × 10^{20} cm^{-2}, resulting in the uniform N(HI) distribution. We expect that if the density of the halo is significantly larger than the current value of $n_{\rm halo}$ = 40 cm^{-3}, the halo will no longer be purely atomic due to the increased H_2 self-shielding.

N(H_2) vs N(H): All models predict the N(H_2) vs N(H) profile in good agreement with our data, even though the uniform density model slightly overestimates N(H_2) at small N(H). For example, the uniform density model with n = 10^4 cm^{-3} predicts N(H_2) = 9.96 × 10^{20} cm^{-2} at N(H) = 2 × 10^{21} cm^{-2}, larger than our data by less than a factor of 2. However, this discrepancy is significant at such small N(H) and results in the small amount of N(HI) $\lesssim$ 10^{19} cm^{-2}. In addition, models with different densities predict essentially the same N(H_2) for a given N(H). All these results imply that neither the density nor its distribution is critical for the abundance of H_2. Instead, N(H) primarily determines N(H_2).

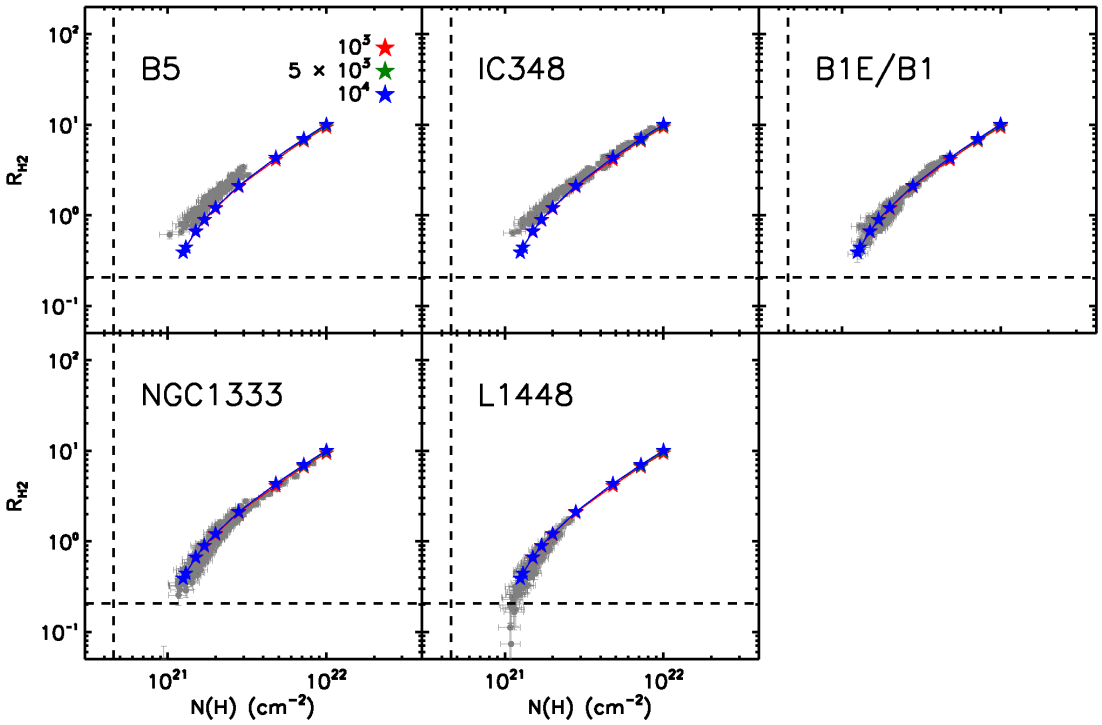

Fig. 4.16. — Comparison with the modified W10 model for $R_{\rm H2} = 2N({\rm H_2})/N({\rm HI})$ vs $N({\rm H}) = N({\rm HI}) + 2N({\rm H_2})$. The modified W10 model with $n_{\rm core} = 10^3$, 5×10^3, and 10^4 cm^{-3} is shown with red, green, and blue stars, respectively. The $R_{\rm H2}$ vs N(H) profiles predicted by the models with $n_{\rm core} = 5 \times 10^3$ and 10^4 cm^{-3} are almost identical. The median 3σ uncertainties of $R_{\rm H2}$ ($\sim$0.21) and N(H) ($\sim 4.56 \times 10^{20}$ cm^{-2}) calculated for the data points with $N({\rm H_2}) > 0$ cm^{-2} and $I_{\rm CO} > 0$ K km s^{-1} are shown as dashed lines.

$R_{\rm H2}$ vs N(H): While the "core-halo" model reproduces both the range of $R_{\rm H2}$ and the linear increase of $R_{\rm H2}$ with N(H), the uniform density model overestimates $R_{\rm H2}$ for a given N(H) by up to a factor of $\sim$700. This discrepancy mainly results from the significantly underestimated N(HI) in the uniform density model.

$I_{\rm CO}$ vs $N({\rm H_2})$: All models reproduce the observed $I_{\rm CO}$ vs $N({\rm H_2})$ profile reasonably well. In particular, both the "core-halo" and uniform density model with the smallest density show an excellent agreement with our data for IC348. While the models with $n \gtrsim 5 \times 10^3$ cm^{-3} and $n_{\rm core} \gtrsim 5 \times 10^3$ cm^{-3} predict the larger $I_{\rm CO}$ at small $N({\rm H_2})$ (up to a factor of $\sim$10), the difference between the models with different densities becomes negligible at $N({\rm H_2}) \gtrsim 1 \times 10^{21}$ cm^{-2}, where $I_{\rm CO}$ saturates to $\sim$45–60 K km s^{-1} for the uniform density model and $\sim$35–40 K km s^{-1} for the "core-halo" model. All these results suggest that $I_{\rm CO}$ depends on the density but only at small $N({\rm H_2})$ and changes in physical parameters other than the density (e.g., $v_{\rm turb}$) will be required to produce larger $I_{\rm CO}$ values once $I_{\rm CO}$ becomes optically thick.

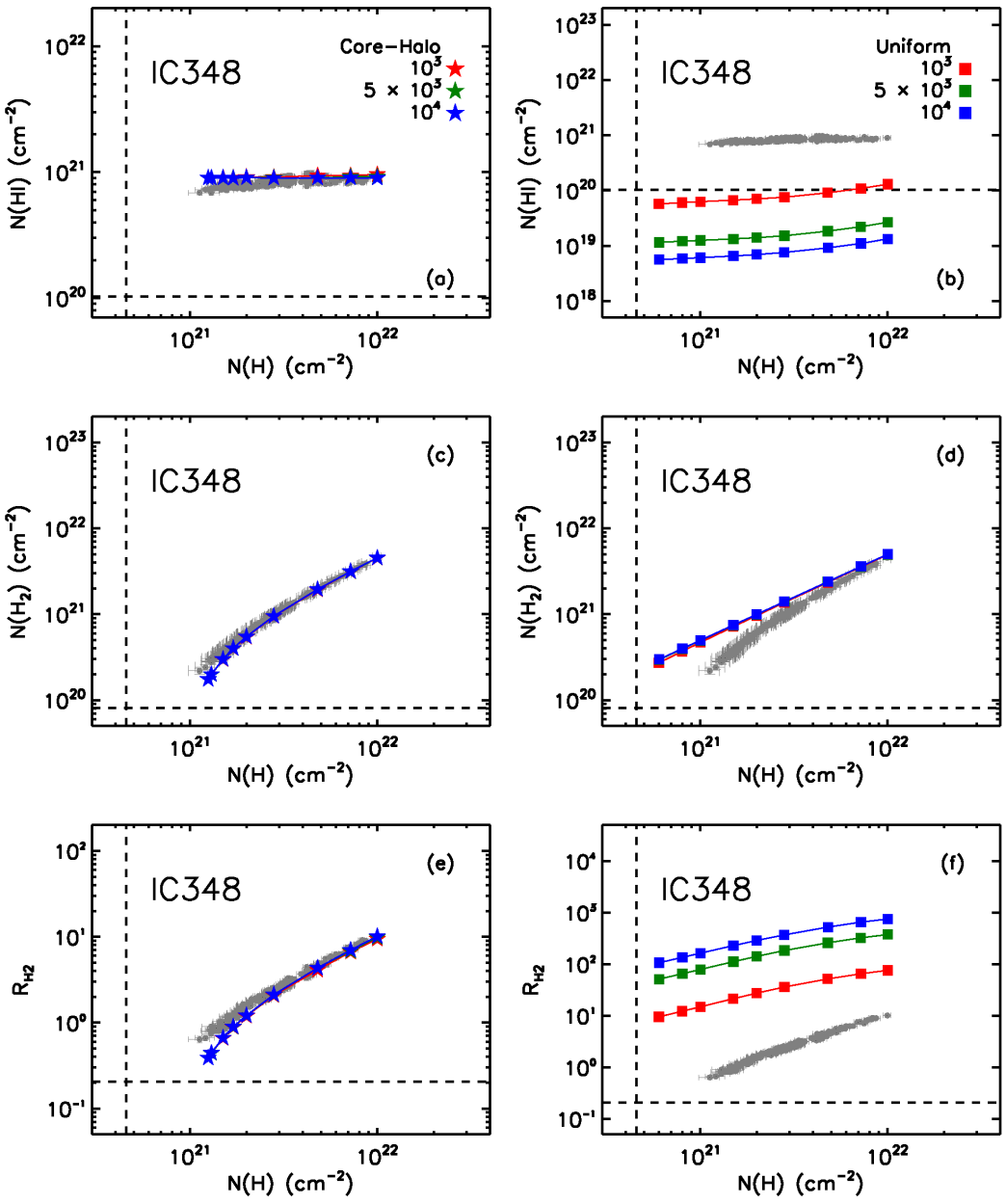

Fig. 4.17. — Comparison with the modified W10 model for IC348. The black dashed line in each panel shows the median 3σ uncertainty of each quantity calculated for the data points with $N(\mathrm{H_2}) > 0$ cm^{-2} and $I_{\mathrm{CO}} > 0$ K km s^{-1}. (Left) The modified W10 model with the "core-halo" structure is shown with red, green, and blue stars ($n_{\mathrm{core}} = 10^3$, 5×10^3, and 10^4 cm^{-3}). (Right) The modified W10 model with the uniform density distribution is shown with red, green, and blue squares ($n = 10^3$, 5×10^3, and 10^4 cm^{-3}).

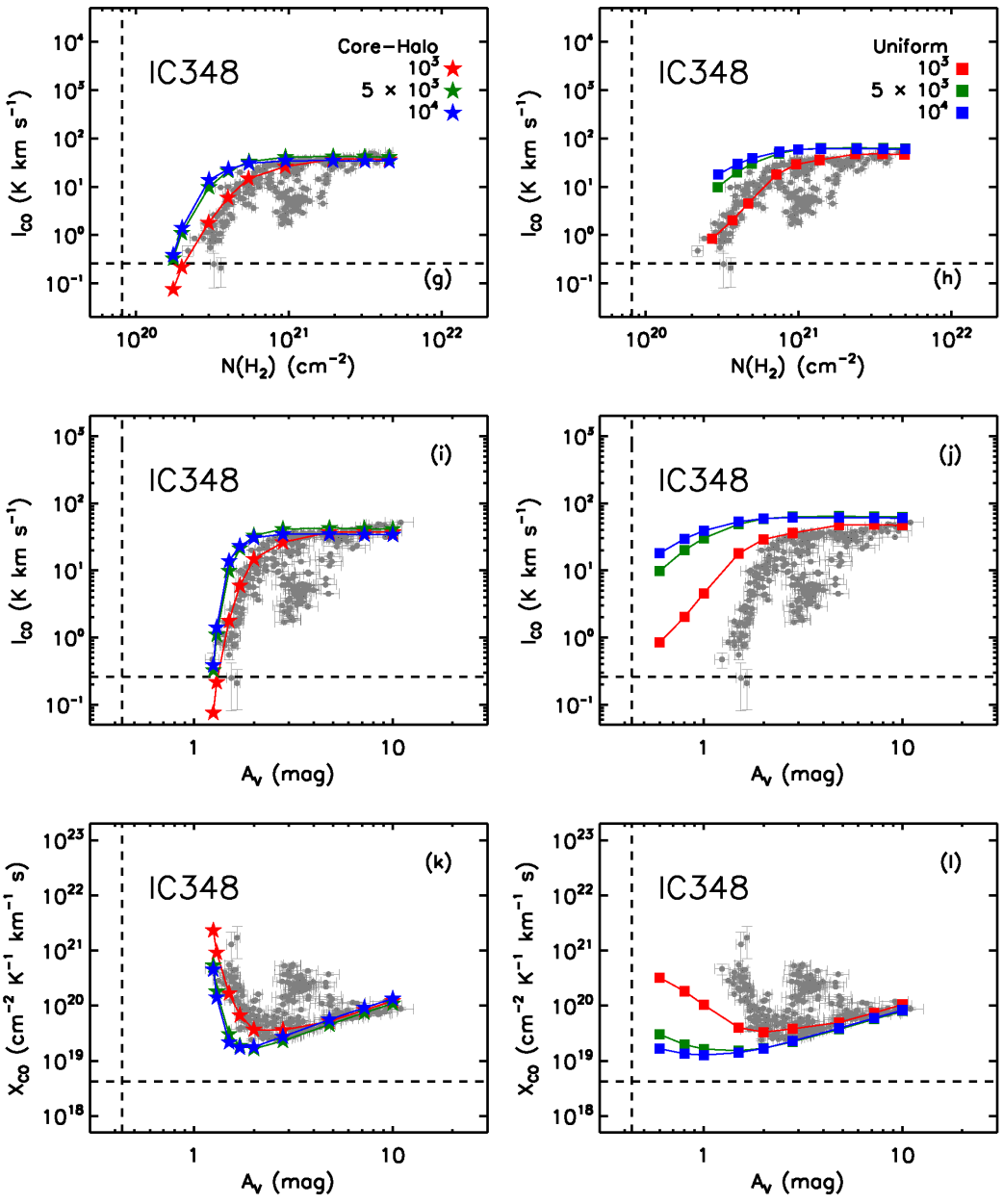

Fig. 4.17. — (Continued)

$I_{\rm CO}$ vs A_V: While the "core-halo" model reproduces the sharp increase of $I_{\rm CO}$ observed at $A_V \gtrsim 1$ mag, the uniform density model predicts the increase of $I_{\rm CO}$ at $A_V \gtrsim 0.6$ mag much more gradually than our data. This difference comes from the fact that the uniform density model has larger density than the "core-halo" model, resulting in the larger $I_{\rm CO}$ for a given $A_V \lesssim 3$ mag ($n \gtrsim 10^3$ cm^{-3} for the uniform density model vs $\langle n \rangle \sim 55$–$125$ cm^{-3} for the "core-halo" model; Table 4.3). On the other hand, all models predict the saturation of $I_{\rm CO}$ to similar values at $A_V \gtrsim 3$ mag, suggesting that the larger density in the uniform density model no longer has a significant impact on $I_{\rm CO}$ due to the high optical depth of $I_{\rm CO}$ ($n \gtrsim 10^3$ cm^{-3} for the uniform density model vs $\langle n \rangle \sim 180$–$430$ cm^{-3} for the "core-halo" model; Table 4.3).

$X_{\rm CO}$ vs A_V: All models reproduce the observed increase of $X_{\rm CO}$ at $A_V \gtrsim 3$ mag because they predict both the range of $N({\rm H_2})$ and the saturation of $I_{\rm CO}$ comparable to our data. On the other hand, the uniform density model shows the decrease of $X_{\rm CO}$ at $A_V \lesssim 3$ mag much shallower than our data. This discrepancy mainly results from the less steep increase of $I_{\rm CO}$ predicted by the model at $A_V \lesssim 3$ mag.

Summary: While we did not perform a full parameter space search, our comparison between the "core-halo" model and the uniform density model is illustrative and demonstrates that the diffuse halo is essential for reproducing the following observed properties: the uniform N(HI) distribution, the H_2-to-HI ratio for a given N(H), the sharp increase of $I_{\rm CO}$ and decrease of $X_{\rm CO}$ at 1 mag $\lesssim A_V \lesssim 3$ mag. Considering that the uniform density model predicts the $I_{\rm CO}$ distribution extended toward smaller A_V, while producing the $N({\rm H_2})$ distribution in reasonably good agreement with our data (Figures 4.17d and j), we expect that the neglect of the diffuse halo will result in the underestimation of the size of the "CO-free" H_2 envelope.

4.7.2 Macroturbulent Non-equilibrium Model

4.7.2.1 Summary of the S11 Model

The S11 model is essentially comprised of two parts. The first part is a modified version of the ZEUS–MP MHD code (Stone & Norman 1992; Norman 2000). Gas in a periodic box is set to have a uniform distribution and driven by a turbulent velocity field with uniform power between wavenumbers $1 \leq k \leq 2$. In addition, the gas is initially magnetized by a magnetic field that has a strength of 1.95 μG and is oriented parallel to the z–axis of the simulation box. To model the chemical evolution of the gas, Glover & Mac Low (2007a,b), Glover et al. (2010), and Glover & Clark (2012) updated the ZEUS-MP MHD code with chemical reactions of several atomic and molecular species. The photodissociation of molecules by a

radiation field is treated by the "six-ray approximation" method developed by Glover & Mac Low (2007a). The effect of self-gravity is not included. We refer to Glover & Mac Low (2007a,b), Glover et al (2010), and Glover & Clark (2012) for details on MHD, thermodynamics, and chemistry included in the S11 model. The second part is a three-dimensional radiative transfer code RADMC–3D (Dullemond et al. in prep)[7]. Once the simulated molecular cloud reaches a statistically steady state, RADMC–3D is executed to model the molecular line emission (e.g., CO). To solve the population levels of atomic and molecular species, RADMC–3D implements the LVG method (Sobolev 1957), which has been shown to be a good approximation for molecular clouds (e.g., Ossenkopf 1997). We refer to Shetty et al. (2011a) for details on RADMC–3D.

The MHD simulation follows the evolution of an initially atomic gas in a $(20\ \mathrm{pc})^3$ box with a numerical resolution of 512^3. In this chapter, we use the S11 model with the following inputs: initial $n = 100\ \mathrm{cm}^{-3}$, $G = 1\ G_0'$, $\zeta = 10^{-17}\ \mathrm{s}^{-1}$, $Z = 1\ \mathrm{Z}_\odot$, and DGR $= 5.3 \times 10^{-22}$ mag cm^2. This simulation is essentially the same as the "dwarf galaxy model" in S11 but has a higher numerical resolution and a simpler CO formation model based on Nelson & Langer (1999). These input parameters are reasonably close to what we expect for Perseus but not exactly the same as what we used in the modified W10 model. As it has been shown in S11 and Glover & Mac Low (2007b) that the simulated H_2 and CO column densities do not depend on small changes in G and ζ, this simulation would be appropriate for the comparison with our observations (Section 4.8.4.1 for details). The final products of the simulation include the $N(H_2)$, $N(H)$, and I_{CO} image obtained at $t > 5$ Myr.

Because the simulation box is larger than our individual regions, the integrated quantities $N(HI)$, $N(H_2)$, and I_{CO} need to be correctly scaled. In the case of $N(HI)$ and $N(H_2)$, the scaling is straight forward under the assumption of isotropic density distributions and we simply need to account for the difference between the box and region size. However, the I_{CO} image was produced by integrating CO brightness temperature, which was estimated by radiative transfer calculations, along a whole radial velocity range. Therefore, estimating a proper scaling for I_{CO} is more complicated. In addition, re-running the simulation with a smaller box does not solve the problem as molecular cores/clouds form out of initially larger environments. We therefore take an approach of determining the optimal line of sight (LoS) depth that minimizes the difference between our observations and the S11 model by investigating the $N(HI)$, $N(H_2)$, and I_{CO} image simultaneously.

[7]See http://www.ita.uni-heidelberg.de/~dullemond/software/radmc-3d/.

To do this, we estimated the difference between the observed median and the simulated median for each of N(HI), $N(H_2)$, and I_{CO} with varying LoS depths. For example, we divided the simulated N(HI), $N(H_2)$, and I_{CO} image by two to calculate the median N(HI), $N(H_2)$, and I_{CO} for the simulation with the LoS depth of 10 pc. We then normalized the difference by the observed median of each quantity and calculated the sum of all three normalized differences in quadrature. The results are shown in Figure 4.18 and we found that the LoS depth that minimizes the difference between our data and the simulation products is ∼6 pc (Figure 4.18e). Given that our linear scaling of I_{CO} for the LoS depth smaller than 20 pc is not very precise, we considered the differences in N(HI) and $N(H_2)$ only and still found the optimal LoS depth of 6 pc (Figure 4.18d). This is because the agreement between our observations and the S11 model is maximum for the initial LoS depth of 20 pc and gets worse as the LoS depth increases (Figure 4.18c). Therefore, the determination of the optimal LoS depth is not heavily affected by how to scale I_{CO}. While the final quantity in Figure 4.18e has a broad minimum, it is encouraging that the estimated scale length is comparable to both the characteristic size of our five regions and the total size of the slab for the "core-halo" model (Tables 4.2 and 4.3). As a double check that this scale length is appropriate, we use Larson's law established for turbulent molecular clouds from both observations and MHD simulations: $\sigma_{CO} = (0.96 \pm 0.17) L_{pc}^{0.59\pm0.07}$ km s^{-1} (Heyer & Brunt 2004). For a region size of 20 pc we expect $\sigma_{CO} \sim$ 6 km s^{-1}, while for a region size of 6 pc we expect $\sigma_{CO} \sim 3$ km s^{-1}. This level of CO velocity dispersion is in agreement with what is shown in Figure 4.8, confirming that scaling the simulation products to the LoS depth of 6 pc is reasonable.

Finally, before comparing the simulated data with our observations, we smooth and regrid the simulated $N(H_2)$, N(H), and I_{CO} image so that they have both a spatial resolution of 0.4 pc and a pixel size of 0.4 pc. In addition, we apply the observational thresholds of 2.7×10^{19} cm^{-2} for $N(H_2)$ and 0.09 K km s^{-1} for I_{CO} (the median 1σ uncertainties calculated for the data points with $N(H_2) > 0$ cm^{-2} and $I_{CO} > 0$ K km s^{-1}).

One of the differences between the modified W10 model and the S11 model is that the S11 model is a non-equilibrium chemical model for H_2 formation. Glover et al. (2010) found from their MHD simulations that the H_2 abundance primarily depends on the time available for H_2 formation and shows no indication of chemical equilibrium up to ∼20 Myr. The gas will eventually become fully H_2 unless the molecular cloud is destroyed by stellar feedback such as photoevaporation by HII regions and protostellar outflows. On the

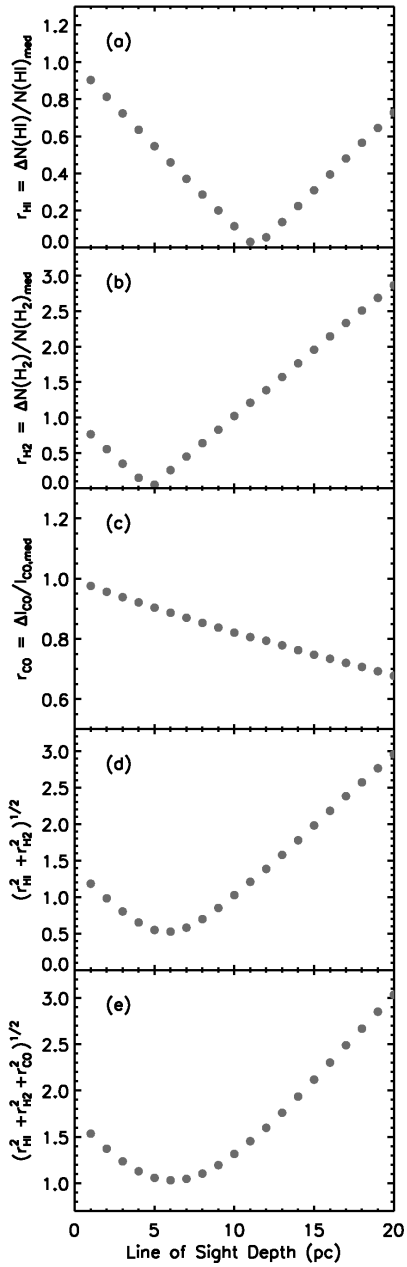

Fig. 4.18. — (a) The difference between the observed median N(HI) and the simulated median N(HI) normalized by the observed median N(HI), $r_{\rm HI} = \Delta N({\rm HI})/N({\rm HI})_{\rm med}$, is plotted against the line of sight depth. (b) Same with (a) but for $N(H_2)$. (c) Same with (a) but for $I_{\rm CO}$. (d) The sum of the two normalized differences in quadrature, $\sqrt{r_{\rm HI}^2 + r_{\rm H2}^2}$, is plotted against the line of sight depth. (d) The sum of the three normalized differences in quadrature, $\sqrt{r_{\rm HI}^2 + r_{\rm H2}^2 + r_{\rm CO}^2}$, is plotted against the line of sight depth. Note that the line of sight depth of 6 pc results in the minimum discrepancy between our data and the simulated data.

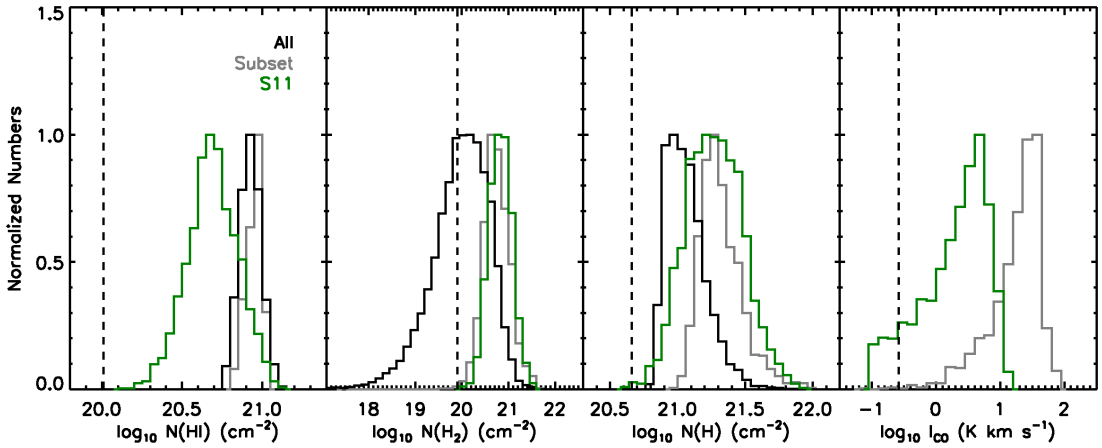

Fig. 4.19. — Normalized histograms of $N(\mathrm{HI})$, $N(\mathrm{H_2})$, $N(\mathrm{H})$, and I_{CO}. The histogram in black, grey, and green is constructed using the data points with positive $N(\mathrm{H_2})$, shown in Figure 4.4, and from the S11 model, respectively. See Section 7.2.2 for details. The black dashed line in each panel shows the median 3σ uncertainty of each quantity calculated for the data points with $N(\mathrm{H_2}) > 0$ cm^{-2} and $I_{\mathrm{CO}} > 0$ K km s^{-1}.

other hand, the CO abundance is controlled by photodissociation and reaches equilibrium within ∼2 Myr.

4.7.2.2 Comparison with Observations: Global Properties

We first compare our data with the S11 model by constructing normalized histograms of $N(\mathrm{HI})$, $N(\mathrm{H_2})$, $N(\mathrm{H})$, and I_{CO} in Figure 4.19. To construct the histograms, we use the data points with $N(\mathrm{H_2}) > 0$ cm^{-2} in Figure 4.2 ("All" histograms in black), as well as those shown in Figure 4.4 ("Subset" histograms in grey). While the grey histograms are limited to the regions where CO emission is detected, the black histograms represent the whole Perseus cloud. The simulated data (scaled for the LoS depth of 6 pc, smoothed, regridded, and the observational thresholds applied) result in "S11" histograms in green, which can be directly compared with the grey histograms. We find the followings.

First, the black and grey $N(\mathrm{HI})$ histogram are nearly identical. This results from the small variation of $N(\mathrm{HI})$ across the whole Perseus cloud, as discussed in Section 4.2.1. The green histogram, on the other hand, has a peak at a factor of ∼2 smaller $N(\mathrm{HI})$ and even more importantly a factor of ∼6 broader distribution than the observed data (the black and grey histogram).

Second, the grey and green $N(\mathrm{H_2})$ histogram agree extremely well: both peak at a similar $N(\mathrm{H_2})$, have a similar width, and show a lognormal-like distribution. The black histogram, on the other hand, has a tail toward small $N(\mathrm{H_2})$. However, note that this tail is mostly below our median 3σ uncertainty of $N(\mathrm{H_2})$.

Third, the green N(H) histogram has a peak at a similar N(H) compared to the grey histogram, while showing a broader (a factor of $\sim$2) and lognormal-like distribution. The simulated distribution is broader mainly because the simulated N(HI) has a greater range than what is observed across Perseus. The black and grey histogram, on the other hand, have a tail toward $N(\mathrm{H}) \gtrsim 10^{21.4} \sim 2.5 \times 10^{21}$ cm^{-2}. This tail is consistent with Kainulainen et al. (2009) who found a deviation from the lognormal distribution at $A_V \gtrsim 3$ mag for Perseus (corresponding to $N(\mathrm{H}) \sim 2.7 \times 10^{21}$ cm^{-2}, with DGR $= 1.1 \times 10^{-21}$ mag cm^2) and interpreted it as a result of self-gravity.

Lastly, we find the most significant difference between the simulated and observed data in the case of I_{CO}: the (simulated) green histogram shows a peak at a factor of $\sim$9 smaller I_{CO} than the (observed) grey histogram. In addition, the green histogram has the maximum $I_{\mathrm{CO}} \sim 15.1$ K km s^{-1}, which is a factor of $\sim$5 smaller than that of the grey histogram, and a prominent tail toward $I_{\mathrm{CO}} \lesssim 10^0 \sim 1$ K km s^{-1}. While the exact factor for the discrepancy is somewhat uncertain because of the nontrivial scaling of I_{CO} with the LoS depth, we stress that the simulated I_{CO} becomes comparable to the observed I_{CO} only if we use the whole simulation box of 20 pc. Figure 4.19 also shows that the simulated histogram is slightly broader than the observed one. This can be partly due to the limited spatial coverage of the COMPLETE I_{CO} image. For example, the five regions in the COMPLETE I_{CO} image are up to a factor of $\sim$2 smaller than the same regions in the CfA I_{CO} image selected with more restricted criteria (Tables 4.1 and 4.2).

In summary, we find that the S11 model reproduces the observed range of $N(\mathrm{H_2})$ extremely well. While the predicted N(HI) has a relatively similar median value compared to the observed N(HI), it has a broader distribution and this leads to a broader range of N(H) in the simulation. I_{CO} predicted by the S11 model, on the other hand, is systematically smaller than our observations. In particular, the observed maximum $I_{\mathrm{CO}} \sim$ 50–80 K km s^{-1} in Perseus is not reproduced in the simulation.

4.7.2.3 Comparison with Observations: Molecular Fraction and X_{CO}

We plot N(HI) against N(H) for each dark and star-forming region and show the prediction from the S11 model in Figure 4.20. While the observed $N(\mathrm{HI}) \sim 9 \times 10^{20}$ cm^{-2} is in the range of the predicted N(HI), the relation between N(HI) and N(H) found in the S11 model is different from what we find in Perseus: not only does the simulated N(HI) have a broader distribution, but the S11 model predicts a factor of $\sim$8 increase of N(HI) for the range of N(H) in Perseus where we observe less than a factor of 2 variation in N(HI). This suggests that N(HI) positively correlates with N(H) in the S11 model and we

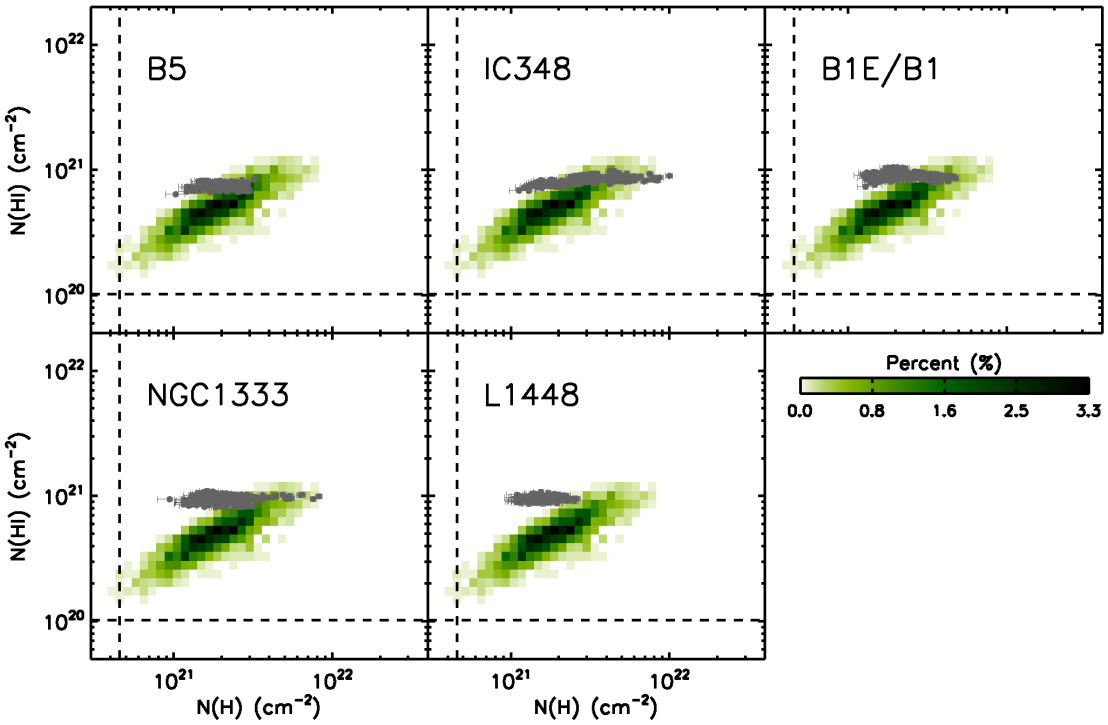

Fig. 4.20. — Comparison with the S11 model for N(HI) vs N(H) = N(HI) + 2N(H_2). The median 3σ uncertainties of N(HI) ($\sim$1.02 $\times$ 10^{20} cm^{-2}) and N(H) ($\sim$4.56 $\times$ 10^{20} cm^{-2}) calculated for the data points with $N(H_2) > 0$ cm^{-2} and $I_{CO} > 0$ K km s^{-1} are shown as dashed lines.

indeed estimate the Pearson correlation coefficient $r \sim 0.8$. The linear increase of N(HI) with N(H) is expected in the equilibrium models of H_2 formation for column densities below the threshold (or shielding) column density required for H_2 formation, where gas remains purely atomic (e.g., Figure 11 of Lee et al. 2012). The linear trend observed in the S11 model has nothing to do with H_2 shielding: as shown in Figure 4.21, R_{H2} is significant throughout the simulated data.

In addition, the S11 model predicts a factor of $\sim$2 smaller N(HI) for a given N(H) on average. As a result, R_{H2} is slightly larger in the S11 model for a given N(H) and increases with N(H) with a slope smaller than what we observe in Perseus (Figure 4.21). While our observations show $R_{H2} < 1$ for the outskirts of the five regions, the simulated $R_{H2} > 1$ everywhere.

We next plot COMPLETE I_{CO} as a function of A_V in Figure 4.22 with the prediction from the S11 model and find that the S11 model describes the relation between I_{CO} and A_V reasonably well: the steep increase of I_{CO} at $A_V \lesssim 2$ mag and the hint of the saturation of I_{CO} at $A_V \gtrsim 2$ mag. However, the S11 model predicts a more gradual increase of I_{CO} with a large scatter, while our observations indicate a sharp

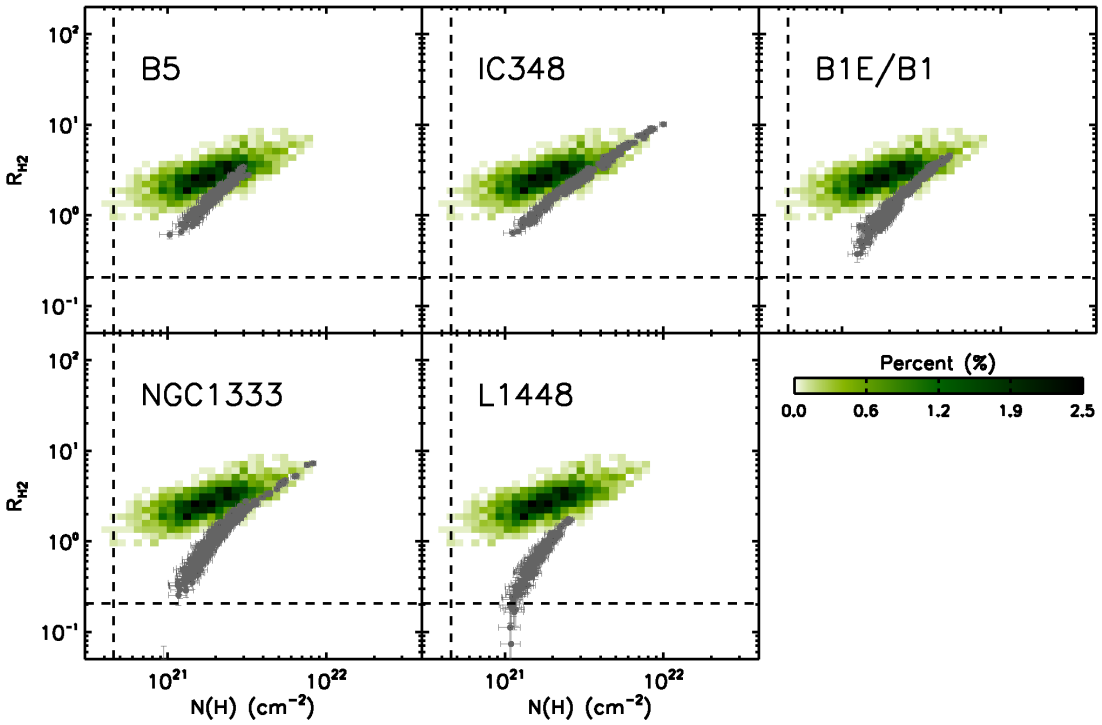

Fig. 4.21. — Comparison with the S11 model for $R_{\rm H2} = 2N({\rm H_2})/N({\rm HI})$ vs $N({\rm H}) = N({\rm HI}) + 2N({\rm H_2})$. The median 3σ uncertainties of $R_{\rm H2}$ ($\sim$0.21) and $N({\rm H})$ ($\sim 4.56 \times 10^{20}$ cm^{-2}) calculated for the data points with $N({\rm H_2}) > 0$ cm^{-2} and $I_{\rm CO} > 0$ K km s^{-1} are shown as dashed lines.

increase of $I_{\rm CO}$ (a factor of $\sim$6 more gradual for 0.1 K km s^{-1} $< I_{\rm CO} <$ 10 K km s^{-1} compared to our data). The scatter is larger at the low end of the A_V range, likely due to density fluctuations in the S11 model. In addition, the S11 model does not reproduce the data points with $I_{\rm CO} \sim$ 50–80 K km s^{-1}.

Considering that the shape of the $X_{\rm CO}$ vs A_V profile is primarily determined by how $I_{\rm CO}$ changes with A_V, we expect that the S11 model reproduces the observed shape of the $X_{\rm CO}$ vs A_V profile reasonably well. The COMPLETE $X_{\rm CO}$ vs A_V profile for each dark and star-forming region is shown in Figure 4.23 with the S11 model. We find that the predicted $X_{\rm CO}$ vs A_V profile shows a characteristic decrease at small A_V and increase at large A_V, similar with what is found in our observations except that it is offset to larger $X_{\rm CO}$ due to the smaller $I_{\rm CO}$ in the S11 model. The simulated $X_{\rm CO}$ shows a significant scatter at small A_V, while the scatter becomes smaller at the high end of the A_V range. The transition from decreasing to increasing $X_{\rm CO}$ at $A_V \sim 2$ mag is comparable with what we find for IC348 and B1E/B1.

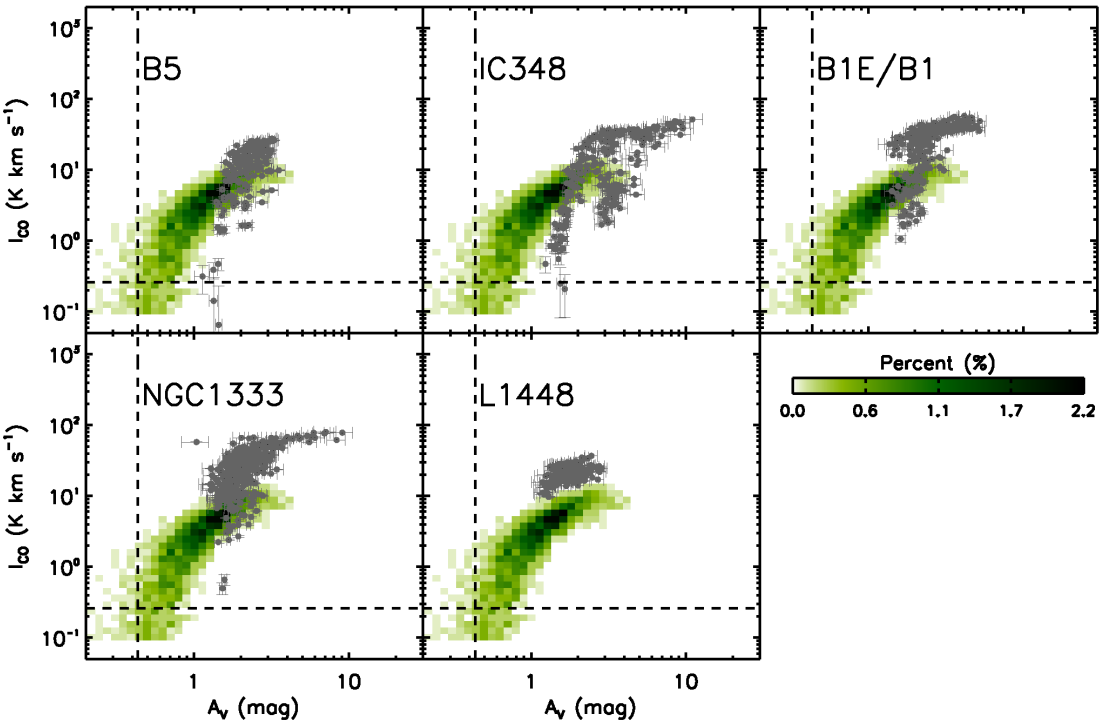

Fig. 4.22. — Comparison with the S11 model for $I_{\rm CO}$ vs A_V. The median 3σ uncertainties of $I_{\rm CO}$ ($\sim$0.26 K km s^{-1}) and A_V ($\sim$0.43 mag) calculated for the data points with $N({\rm H_2}) > 0$ cm^{-2} and $I_{\rm CO} > 0$ K km s^{-1} are shown as dashed lines.

4.8 Discussion

4.8.1 $X_{\rm CO}$ in Perseus and Comparison with Previous Studies

As we have shown throughout most of this chapter, we find significant variations of $X_{\rm CO}$ across Perseus. In general, all regions in Perseus have $X_{\rm CO}$ smaller than the typical value assumed for the Milky Way, $X_{\rm CO} \sim 1.8 \times 10^{20}$ (Dame et al. 2001) (Table 4.1). This is a factor of $\sim$6 larger than our median $X_{\rm CO} \sim 2.8 \times 10^{19}$. As shown in Bolatto et al. (2013), there is an assuring degree of uniformity among the values of $X_{\rm CO}$ obtained in previous studies through a variety of observational methods and at different resolutions. In this section, we attempt to understand why our result is different from previous studies.

The main issue appears to be the angular resolution of HI data. If we follow what Dame et al. (2001) did by smoothing the CfA $I_{\rm CO}$ image to 36′ angular resolution (limited by their use of the LDS HI data at 36′ angular resolution), we find that $I_{\rm CO}$ decreases by a factor of $\sim$10 (COMPLETE $I_{\rm CO} \sim 20$ K km s^{-1} at 4.3′ resolution vs CfA $I_{\rm CO} \sim 2$ K km s^{-1} at 36′ resolution). If we smooth our $N({\rm H_2})$ image

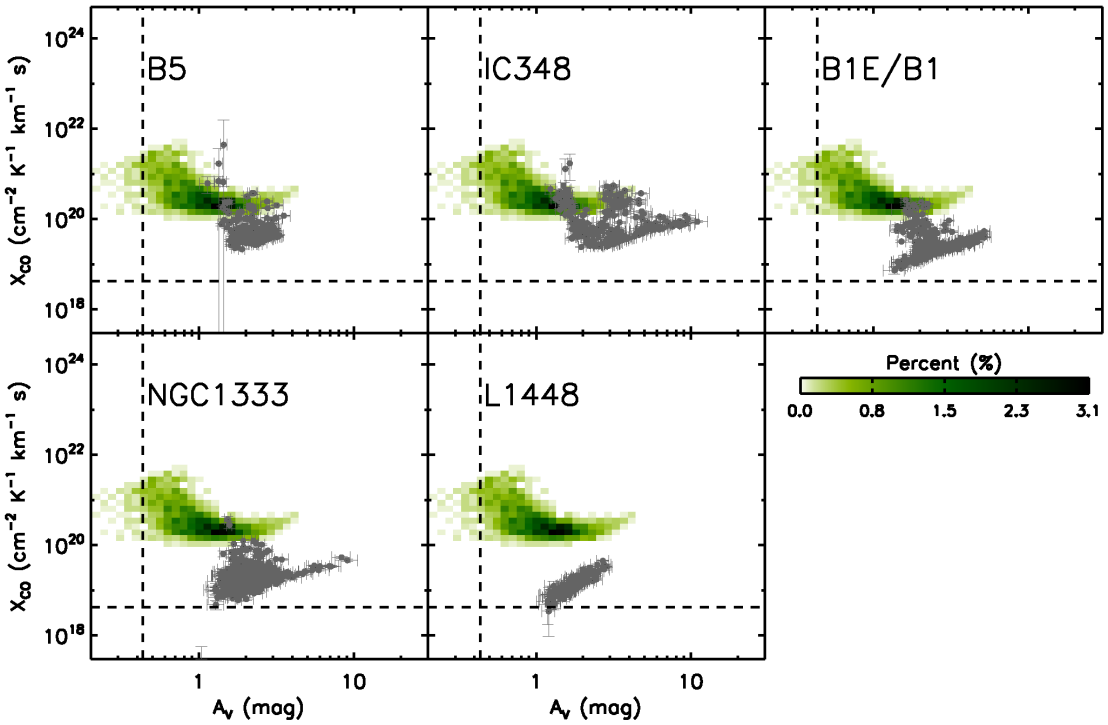

Fig. 4.23. — Comparison with the S11 model for $X_{\rm CO}$ vs A_V. The median 3σ uncertainties of $X_{\rm CO}$ ($\sim$4.19 $\times$ 10^{18}) and A_V ($\sim$0.43 mag) calculated for the data points with $N({\rm H_2}) > 0$ cm^{-2} and $I_{\rm CO} > 0$ K km s^{-1} are shown as dashed lines.

to the same angular resolution, we derive $X_{\rm CO}$ much closer to the canonical $X_{\rm CO} \sim$ (1–3) $\times$ 10^{20}. The CO distribution appears to be clumpier than the H_2 distribution and therefore $X_{\rm CO}$ strongly depends on angular resolution. Several studies of local molecular clouds in the Milky Way were limited to $\sim$36′ angular resolution as their HI data came from the LDS survey (e.g., Abdo et al. 2010; Paradis et al. 2012). The GALFA-HI survey with its angular resolution of $\sim$4′ provides a much sharper view of the HI distribution across molecular clouds, matching well the angular resolution of available infrared data (in particular from *IRAS*) and enabling for the first time high resolution studies of $X_{\rm CO}$ for many molecular clouds in the Milky Way.

The dependence of $X_{\rm CO}$ on spatial resolution has been noticed by other studies as well. For example, Rubio et al. (1993) calculated $X_{\rm CO}$ for molecular clouds in the SMC and found that $X_{\rm CO}$ depends on the spatial scale of R such as $X_{\rm CO} \propto R^{0.7}$. Based on this empirical relation, a decrease of angular resolution from 4.3′ to 36′ would result in a factor of $\sim$4 larger $X_{\rm CO}$. This is comparable with the discrepancy between our median $X_{\rm CO}$ and the canonical $X_{\rm CO} \sim 1.8 \times 10^{20}$ for the Milky Way derived by Dame et al. (2001).

We note that several high resolution studies of Galactic molecular clouds have also derived $X_{\rm CO} \sim$ (1–3) $\times$ 10^{20} (e.g., Lombardi et al. 2006; Pineda et al. 2008; Pineda et al. 2010). While estimating $X_{\rm CO}$ at similar $\sim 4'$ angular resolution, most of these studies made the following assumptions: (1) all hydrogen traced by A_V is in the form of H_2 and (2) Galactic DGR $\sim 5.3 \times 10^{-22}$ mag cm^{-2} (a factor of $\sim$2 smaller than our local DGR for Perseus $\sim 1.1 \times 10^{-21}$ mag cm^{-2}). If we follow those assumptions, either by totally ignoring the contribution from HI to the total gas column density or by assuming a canonical DGR without deriving it for our particular conditions, we find a very similar $X_{\rm CO}$.

In summary, the discrepancy between our $X_{\rm CO}$ in Perseus and previous estimates of $X_{\rm CO}$ in the Milky Way primarily results from the superior angular resolution of our HI data and the role that HI plays in estimating the DGR and the molecular hydrogen column density.

4.8.2 $X_{\rm CO}$ in Molecular Clouds

In Section 4.6.1, we found potentially a large-scale trend in $X_{\rm CO}$: it decreases by a factor of $\sim$3 from the northeastern (B5 and IC138) to southwestern (B1E/B1, NGC1333, L1455, L1448, and Westend) regions in Perseus. Our investigation of the large-scale trends in G and $\sigma_{\rm CO}$ points out that a slightly stronger G and up to a factor of $\sim$2 smaller $\sigma_{\rm CO}$ could result in a factor of $\sim$3 larger $X_{\rm CO}$ in the northeastern part of Perseus. In addition, our comparison with the modified W10 model suggests that variations in n and/or A_V can contribute to the observed variations of $X_{\rm CO}$ among the different regions as well as within the individual regions (Section 4.7.1.2). These results are in good agreement with previous theoretical studies that have shown $X_{\rm CO}$ to be sensitive to local ISM conditions.

By zooming in on the individual dark and star-forming regions, we found large variations in $X_{\rm CO}$. Within a single region with a size of $\sim$6 pc, $X_{\rm CO}$ can vary by up to a factor $\sim$80 (Section 4.6.3). In addition, we found that $X_{\rm CO}$ shows a characteristic trend with A_V, particulary evident for IC348 and B1E/B1 where we probe a large range of A_V: the steep decrease of $X_{\rm CO}$ at $A_V \lesssim 3$ mag and the moderate increase of $X_{\rm CO}$ at $A_V \gtrsim 3$ mag. This relation between $X_{\rm CO}$ and A_V results from the strong dependence of $I_{\rm CO}$ on A_V. The location at which most carbon is locked in CO primarily depends on dust shielding (e.g., W10; Glover & Mac Low 2011). Once dust shielding becomes sufficiently strong to prevent photodissociation ($A_V \sim 1$ mag in Perseus; Section 4.6.2.1), the CO abundance and emission strength sharply rise, resulting in decreasing $X_{\rm CO}$ with A_V. $I_{\rm CO}$ then saturates to a certain value as CO becomes optically thick with increasing depth. This causes increasing $X_{\rm CO}$ with A_V. For those regions where CO is optically thick, therefore, using a

single $X_{\rm CO}$ will only provide a lower limit of $N(\rm H_2)$. While this characteristic dependance of $X_{\rm CO}$ on A_V has been theoretically studied, our study provides the first observational confirmation.

Overall, our results suggest that one needs to be careful in adopting a single $X_{\rm CO}$ to derive $N(\rm H_2)$ for a system that likely has a diverse range of physical parameters. The first reason stems from a limited dynamic range of CO as a tracer of $\rm H_2$. The traceable $N(\rm H_2)$ by $I_{\rm CO}$ is bounded at bottom by the required minimum dust shielding against photodissociation and at top by opacity and/or depletion (e.g., Goodman et al. 2009). The complex dependence of $X_{\rm CO}$ on various physical parameters is the second reason. The combination of these two reasons can hamper the derivation of the accurate $N(\rm H_2)$ distribution.

4.8.3 Insights from the Microturbulent Equilibrium Model

The good agreement found between our data and the modified W10 model with the "core-halo" structure (Section 4.7.1.2) suggests that the main assumptions of the model, e.g., $\rm H_2$/CO formation in chemical equilibrium, the microturbulent approximation for CO spectral line formation, and the "core-halo" density distribution, are valid for Perseus on ∼0.4 pc scales. This result is consistent with Lee et al. (2012) who found that N(HI) and $N(\rm H_2)$ in Perseus conform to the equilibrium $\rm H_2$ formation model by K09. We now turn to a couple of interesting aspects of the modified W10 model and discuss their implications.

4.8.3.1 The Importance of Diffuse HI Halo for $\rm H_2$ and CO Formation

The modified W10 model that is comparable to the observations of Perseus adopts the "core-halo" structure motivated by previous studies of molecular clouds (Section 4.7.1). We showed that the model with the uniform density distribution predicts N(HI) much smaller than the uniform $N(\rm HI) \sim 9 \times 10^{20}$ cm^{-2} measured across Perseus. The uniform density model with the largest density of $n = 10^4$ cm^{-3} predicts the smallest N(HI), up to a factor of ∼160 smaller than what is observed. The reason why the uniform density model fails in reproducing the observed N(HI) is that $\rm H_2$ self-shielding alone counteracts $\rm H_2$ dissociation by UV photons. Traditionally, it has been known that G/n determines whether $\rm H_2$ self-shielding or dust shielding is more important for $\rm H_2$ formation and controls the location of the transition from HI to $\rm H_2$ in a PDR (e.g., Hollenbach & Tielens 1997). With $G = 0.5\ G_0'$ and $n = 10^3$ cm^{-3} in the uniform density model, G/n is 5×10^{-4} cm^3, small enough that dust shielding is negligible. In this case, most of HI is converted into $\rm H_2$ because of the strong $\rm H_2$ self-shielding. On the other hand, the "core-halo" model with $n_{\rm core} = 10^3$

cm^{-3} and $n_{halo} = 40$ cm^{-3} has $\langle n \rangle \sim 50$ cm^{-3} (Table 4.3), resulting in $G/n \sim 0.01$ cm^3. This increased G/n makes dust shielding more important for H_2 formation in the cloud outskirts and as a result, N(HI) remains at $\sim 9 \times 10^{20}$ cm^{-2} to provide enough shielding against H_2 dissociation.

The fact that the modified W10 model needs a diffuse HI halo to reproduce the observed N(HI) suggests that dust shielding is important for H_2 formation in Perseus. This importance of dust shielding is consistent with what Lee et al. (2012) found from the comparison between the observations of Perseus and the K09 model. The K09 model investigates the structure of a PDR in a spherical cloud based on H_2 formation in chemical equilibrium and predicts the following variable as one of the key parameters that determines the location of the transition from HI to H_2:

$$\chi = \frac{2.3(1 + 3.1Z'^{0.365})}{\phi_{CNM}}, \tag{4.3}$$

where Z' is the metallicity normalized to the solar neighborhood value and ϕ_{CNM} is the ratio of the actual CNM density to the minimum CNM density at which the CNM exists in pressure balance with the warm neutral medium (WNM). This χ is essentially comparable to G/n, except that it does not have a dependence on G due to the way the CNM density depends on G (Equations (4) and (5) of K09). Interestingly, K09 predicts $\chi \sim 1$ in all galaxies where the pressure balance between the CNM and the WNM is valid, suggesting that dust shielding and H_2 self-shielding are equally important for H_2 formation. By fitting the K09 model to the observed R_{H2} vs $\Sigma_{HI}+\Sigma_{H2}$ profiles, Lee et al. (2012) indeed found $\chi \sim 1$ for Perseus.

In the modified W10 model, a diffuse HI halo is also required to reproduce the observed steep increase of I_{CO} at $A_V \gtrsim 1$ mag and sharp decrease of X_{CO} at $A_V \lesssim 3$ mag (Section 4.7.1.3). The uniform density model predicts the shallower increase of I_{CO} at smaller $A_V \gtrsim 0.6$ mag, suggesting a less sharp transition from CII/CI to CO located closer to the surface of the gas slab. The more extended CO distribution eventually results in the reduced "CO-free" H_2 envelope and therefore the uniform density model with $n = 10^4$ cm^{-3} would have the smallest amount of "CO-dark" H_2. The CO distribution deep inside of the gas slab, on the other hand, does not appear to be affected by the presence of the diffuse HI halo because of the saturation of I_{CO}.

Even though the modified W10 model with the "core-halo" structure reproduces the observed N(HI), $N(H_2)$, and I_{CO} distribution, the agreement is likely to remain only if the density of the halo is not significantly larger than 40 cm^{-3}. The current density of $n_{halo} = 40$ cm^{-3} originates from the theoretical

(e.g., Wolfire et al. 2003) and observational (e.g., Heiles & Troland 2003) properties of the CNM. While large HI envelopes associated with molecular clouds have been frequently observed (e.g., Knapp 1974; Wannier et al. 1983, 1991; Reach et al. 1994; Rogers et al. 1995; Williams & Maddalena 1996; Imara & Blitz 2011; Lee et al. 2012), a number of fundamental questions still remain to be answered. What are the physical properties of the halos, such as density, temperature, and pressure? What is the ratio of the CNM to the WNM in the halos? Is there any correlation between the ratio and the H_2 abundance/star formation? Are the halos expanding or infalling? We are in the process of obtaining a large number of HI absorption spectra toward the outskirts of Galactic molecular clouds (Stanimirović et al. in prep) and they will be valuable to understand the role of diffuse HI halos on the formation and evolution of molecular clouds. The GALFA-HI survey opens the door to high resolution studies of diffuse HI halos around other Galactic molecular clouds in various ISM environments. In addition, further comparison between observations and theoretical models will be important to fully constrain the parameter space and density structure of diffuse HI halos.

4.8.3.2 Validity of Steady State and Equilibrium Chemistry

The timescale of H_2 formation on dust grains, $t_{\rm H2}$, dominates chemical timescales of PDRs (e.g., Hollenbach & Tielens 1997). For the modified W10 model with the "core-halo" structure, dense regions have $\langle n \rangle \sim 300$ cm^{-2} where gas is completely molecular ($n_{\rm H2} \sim 0.5n$). In this case, $t_{\rm H2} = 0.5/\mathcal{R}\langle n \rangle \sim 1.8$ Myr, where $\mathcal{R} = 3 \times 10^{-17}$ cm^3 s^{-1} is the rate coefficient for H_2 formation (Wolfire et al. 2008). In diffuse regions with $\langle n \rangle \sim 50$ cm^{-3}, on the other hand, gas is mostly atomic ($n_{\rm H2} \sim 0.1n$) and therefore $t_{\rm H2} = 0.1/\mathcal{R}\langle n \rangle \sim 3.5$ Myr. Because $t_{\rm H2}$ of the model is well within the expected age of Perseus, $t_{\rm age} \sim 10$ Myr, the assumption of chemical equilibrium is valid. In other words, Perseus is old enough to reach chemical equilibrium and therefore it is not surprising that the equilibrium chemical model (W10) fits our observations very well.

However, for steady state chemistry to be valid, $t_{\rm H2} \lesssim t_{\rm age}$ is not enough: $t_{\rm H2}$ should be short compared to a dynamical timescale of the molecular cloud, $t_{\rm dyn}$. For Perseus, this requires $t_{\rm dyn} \gtrsim 10$ Myr. As a rough estimate, we calculate a crossing timescale $t_{\rm cross} = L/\sigma \sim 100$ pc/3.5 km s^{-1} ~ 28 Myr, where we choose L as the size of the whole Perseus cloud and σ as the average HI velocity dispersion in Perseus (Ridge et al. 2006). This $t_{\rm cross} \sim 28$ Myr satisfies the condition for $t_{\rm dyn} \gtrsim 10$ Myr. However, many dynamical processes are involved with the formation and evolution of molecular clouds (e.g., cloud-cloud

collisions, spiral shocks, stellar feedback; Mac Low & Klessen 2004; Mckee & Ostriker 2007) and therefore it is difficult to pin down the exact process that is most relavant to the formation of molecular gas. The good agreement between our data and the modified W10 model with the "core-halo" structure suggests that the characteristic $t_{\rm dyn}$ for the formation of molecular gas in Perseus should be $\gtrsim$ 10 Myr.

4.8.4 Insights from the Macroturbulent Non-equilibrium Model

4.8.4.1 The Choice of the Input Parameters in the MHD Simulation

In Section 4.7.2.2, we found that the S11 model predicts $N(H_2)$ comparable to the estimated $N(H_2)$ in Perseus. This excellent agreement will likely hold even if some of the input parameters slightly change. For example, the S11 model adopts $G = 1\ G_0'$ and this is a factor of $\sim$2 stronger than what we measure across Perseus. Considering that S11 found no considerable difference in $N(H_2)$ for their models with $G = 1\ G_0'$ and 10 G_0' (Section 3.1 of S11), however, decreasing G from 1 G_0' to 0.5 G_0' to match the property of Perseus will not make a significant change in $N(H_2)$. In addition, increasing ζ from 10^{-17} s^{-1} to 10^{-16} s^{-1} to be consistent with the modified W10 model also will not affect $N(H_2)$ very much, based on the fact that Glover & Mac Low (2007b) found a negligible change in $N(H_2)$ when ζ increased from 10^{-17} s^{-1} to 10^{-15} s^{-1} in their MHD simulation with initial $n = 100$ cm^{-3} (Section 6.3 of Glover & Mac Low 2007b). Finally, the extension of the simulation run up to $t \sim 10$ Myr, comparable to the age of Perseus, will not significantly increase $N(H_2)$, considering that Glover & Mac Low (2011) found only a factor of $\sim$1.3 increase of the mass-weighted mean abundance of H_2 from $t \sim 5$ Myr to $t \sim 10$ Myr for their MHD simulation with initial $n = 100$ cm^{-3} (Section 3.3 of Glover & Mac Low 2011).

Similarly, small changes in the model parameters will likely make no substantial difference in $I_{\rm CO}$. For example, S11 showed that increasing G from 1 G_0' to 10 G_0' does not change $I_{\rm CO}$ for those regions where CO is well shielded against the radiation field (Section 3.1 of S11). Therefore, decreasing G from 1 G_0' to 0.5 G_0' will make only a minor change in $I_{\rm CO}$ at large column densities. In addition, we do not expect that running the S11 model up to $t \sim 10$ Myr drastically increases $I_{\rm CO}$, considering that the MHD simulation with initial $n = 100$ cm^{-2} in Glover & Mac Low (2011) predicts only a factor of $\sim$2 increase of the mass-weighted mean abundance of CO from $t \sim 5$ Myr to $t \sim 10$ Myr.

We therefore conclude that the input parameters used in the S11 model are reasonable for the comparison with the observations of Perseus and small (a factor of few) changes in the input parameters

will not result in significant changes in $N(H_2)$, N(HI), and I_{CO}. Considering that Perseus has most likely reached chemical equilibrium, it provides a suitable testbed for investigating whether results from the MHD simulation converge to the equilibrium chemistry model for molecular clouds that are evolved enough.

4.8.4.2 The Role of Turbulence in H_2 and CO Formation

As shown in Section 4.7.2.2, the S11 model produces the $N(H_2)$ distribution in excellent agreement with the observations of Perseus as well as the modified W10 model. This result suggests that the non-equilibrium H_2 formation model (S11) is consistent with the equilibrium H_2 formation model (W10) for low-mass, old molecular clouds such as Perseus. The similar conclusion has been made by Krumholz & Gnedin (2011), who found that time-dependent effects on H_2 formation become important only at extremely low metallicities of $Z \lesssim 10^{-2}\ Z_\odot$. While the median N(HI) in the S11 model is also in reasonably good agreement with the observations of Perseus, the simulated N(HI) distribution is a factor of ∼6 broader than the observed one and particularly has a more extended tail toward small $N(\mathrm{HI}) \lesssim 10^{20.5} \sim 3 \times 10^{20}$ cm^{-2}. This broad N(HI) distribution in the MHD simulation likely results from strong compressions and rarefactions by turbulence and results in a factor of ∼2 smaller R_{H2} for a given N(H) on average. The discrepancy becomes significant at small N(H) where the S11 model underesimates N(HI) by up to a factor of ∼10. Finally, the S11 model predicts that N(HI) increases with N(H), suggesting no minimum N(HI) beyond which the rest of hydrogen is converted into $N(H_2)$. In the modified W10 model with the "core-halo" structure, on the other hand, the diffuse halo remains atomic with $N(\mathrm{HI}) \sim 9 \times 10^{20}$ cm^{-2} and the dense core is fully converted into $N(H_2)$. Clearly, this N(HI) descrepancy between the simulation and the observations is significant and interesting. One potential avenue in exploring this in the future is using a mixture of neutral phases for initial conditions, mimicing in some way the "core-halo" structure in the modified W10 model.

The most significant descrepancy between the S11 model and the observations of Perseus is found for I_{CO} where the model predicts systematically smaller values than what we observe. To understand the origin of this discrepancy, we estimate $N(\mathrm{CO})_{obs}$ for B5, IC348, B1E/B1, and NGC1333 using the ^{13}CO($J = 1 \rightarrow 0$) excitation temperatures, optical depths, and integrated intensities provided by Pineda et al. (2008) and assuming $N(\mathrm{CO}) = 76N(^{13}\mathrm{CO})$ (Lequeux 2005). We find $N(\mathrm{CO})_{obs} \sim$ (1–2) $\times 10^{17}$ cm^{-2}, in excellent agreement with the predicted $N(\mathrm{CO})_{S11} \sim 3 \times 10^{17}$ cm^{-2}. This strongly suggests that the discrepancy in I_{CO} results from the radiative transfer calculations and/or the difference in velocity range.

In particular, the velocity range, Δv, directly affects $I_{\rm CO}$ via $I_{\rm CO} = \int T_{\rm B} dv$ and a smaller Δv will result in a smaller $I_{\rm CO}$ for the same $T_{\rm B}$. Our observations show $\Delta v \sim$ 10–15 km s^{-1} for IC348, B1E/B1, and NGC1333 (e.g., Figure 4 of Pineda et al. 2008). On the other hand, the S11 model has only $\Delta v \sim$ 3–6 km s^{-1} for the simulation with the LoS depth of 6 pc.

The smaller Δv in the S11 model could result from several factors. First, CO-emitting clumps could be heavily overlapped in velocity space. Shetty et al. (2011b) indeed showed that two lines of sight with a similar number of clumps can have very different $I_{\rm CO}$ if one line of sight has overlapping clumps in velocity space, while the other line of sight has widely distributed clumps. Superpositions of physically disconnected clumps in velocity space have been found in other MHD simulations as well (e.g., Ballesteros-Paredes et al. 1999; Ostriker et al. 2001; Lazarian et al. 2001; Ballesteros-Paredes & Mac Low 2002) and in particular Ballesteros-Paredes & Mac Low (2002) showed that velocity crowding can be severe for low density tracers (e.g., CO) and large driving wavenumbers. Second, missing stellar feedback processes in the S11 model could result in the smaller Δv. For example, the observed Δv is particularly large for B1E/B1 and NGC1333, where a large number of H-H objects likely contribute to broad CO spectra (Section 4.6.1).

It is also interesting to notice that $I_{\rm CO}$ increases more gradually with a large scatter in the S11 model. This could result from large density fluctuations in a turbulent medium. The gas in the S11 model would be strongly compressed and rarefied by turbulence and the density of gas for a given A_V can vary over several orders of magnitude (e.g., Figure 14 of Glover et al. 2010). In this case, CO can form in dense clumps even at small A_V and $I_{\rm CO}$ therefore shows a large scatter. This scatter is reduced at large A_V where $I_{\rm CO}$ eventually saturates to a certain value. Finally, turbulent mixing could spread the CO distribution, resulting in the more gradual increase of $I_{\rm CO}$.

In general, our study shows that the MHD model by S11 is successful in reproducing the chemical state of Perseus, which is a low-mass, old molecular cloud most likely in chemical equilibrium. We have revealed two important areas of future attention: (1) the role and physical properties of diffuse halos around molecular clouds and (2) the velocity superposition and stellar feedback effect that could result in the predicted velocity range smaller than what is observed. Finally, future work should include similar analyses of molecular clouds less evolved and/or forming more massive stars (therefore more turbulent) than Perseus, where the difference between the MHD and PDR model is likely to be more pronounced.

4.9 Summary

In this chapter, we combine high resolution H_2 and CO measurement to investigate X_{CO} across the Perseus molecular cloud. We derive the X_{CO} image at ∼0.4 pc spatial resolution by using $N(H_2)$ estimated by Lee et al. (2012) and I_{CO} provided by the COMPLETE survey. To study the large-scale spatial variations of X_{CO} and their correlations with local ISM conditions, we additionally derive the X_{CO} image at ∼0.7 pc spatial resolution by combining the same $N(H_2)$ from Lee et al. (2012) with the CfA I_{CO} data.

The COMPLETE X_{CO} image and the $N(HI)$ and $N(H_2)$ data from Lee et al. (2012) allow us to test two theoretical models of H_2 and CO formation: the modified W10 model (microturbulent equilibrium model) and the S11 model (macroturbulent non-equilibrium model). For several dark and star-forming regions in Perseus (B5, B1E/B1, L1448, IC348, and NGC1333), we investigate X_{CO} vs A_V, $N(HI)$ vs $N(H)$, and R_{H2} vs $N(H)$ and compare the results with predictions from the modified W10 model and the S11 model. We summarize our main results as follows.

1. We derive the median $X_{CO} \sim 2.8 \times 10^{19}$ for Perseus. This median X_{CO} is a factor of ∼6 smaller than previous estimates of $X_{CO} \sim$ (1–3) $\times 10^{20}$ for the Milky Way and the discrepancy mainly arises due to the high resolution of our HI data and the consideration of HI in deriving the DGR and the molecular hydrogen column density.

2. We find a factor of ∼3 region-to-region variations in X_{CO}. The larger X_{CO} in the northeastern part of Perseus (B5 and IC348) can result from the larger G and/or the smaller σ_{CO}. Additionally, variations in n and/or A_V can contribute to the observed regional variations in X_{CO}. Within the individual dark and star-forming regions, X_{CO} varies up to a factor of ∼100.

3. The observed X_{CO} vs A_V profiles have two characteristic features: the steep decrease of X_{CO} at small A_V and the gradual increase of X_{CO} at large A_V. Among the five dark and star-forming regions, IC348 and B1E/B1 clearly show the transition from decreasing to increasing X_{CO} at $A_V \sim 3$ mag.

4. The modified W10 model with the "core-halo" structure reproduces the observed X_{CO} vs A_V profiles, particularly well for IC348 and B1E/B1. In addition, the model matches the nearly constant $N(HI)$ $\sim 9 \times 10^{20}$ cm^{-2} and predicts the linear increase of R_{H2} with $N(H)$, consistent with what we find in Perseus.

5. The modified W10 model with the uniform density distribution reproduces the observed $N(H_2)$ reasonably well but underestimates N(HI) by a factor of ∼10–160. As a result, the model overestimates R_{H2} for a given N(H) by up to a factor of ∼700. In addition, while matching the observed saturation of I_{CO} at $A_V \gtrsim 3$ mag, the model predicts the more gradual increase of I_{CO} at $A_V \lesssim 3$ mag. This results in the X_{CO} vs A_V profile whose increasing portion at $A_V \gtrsim 3$ mag is consistent with the observed one but decreasing portion at $A_V \lesssim 3$ mag is shallower than our data.

6. The S11 model predicts $N(H_2)$ comparable to what we estimate in Perseus. However, N(HI) increases with N(H) by a factor of ∼8 in the S11 model and this is in contrast with the observed small variation of N(HI) with N(H) (less than a factor of 2). In addition, the S11 model predicts that I_{CO} increases more gradually at $A_V \lesssim 2$ mag with a large scatter and saturates to a systematically smaller value at $A_V \gtrsim 2$ mag. As a result, the predicted X_{CO} vs A_V profile has a shape relatively similar with what we observe in Perseus but is offset to larger X_{CO}.

Our study shows that X_{CO} can vary by up to a factor of ∼100 on ∼0.4 pc scales and depends on local ISM conditions such as G, σ_{CO}, n, and A_V. Interestingly, X_{CO} has a characteristic relation with A_V, mainly driven by how I_{CO} changes with A_V. At small A_V, X_{CO} steeply decreases with A_V, because CO becomes sufficiently shielded against photodissociation and I_{CO} sharply increases. X_{CO} then gradually increases with A_V, resulted from the saturation of I_{CO}. Our results confirm previous theoretical predictions of the X_{CO} vs A_V profile for the first time. However, the precise shape of the X_{CO} vs A_V profile, e.g., the location where the transition from decreasing to increasing X_{CO} occurs, the slopes of the decreasing and increasing portion, etc., again depends on local environmental parameters (e.g., Bell et al. 2006). In general, our results suggest a careful adoptation of X_{CO} to derive $N(H_2)$ for a system that covers a range of environments.

The detailed comparison between our high resolution data and theory provides important insights into H_2 and CO formation in molecular clouds. For example, the good agreement we found with the modified W10 model suggests that the steady state and equilibrium chemistry and the microturbulent approximation for CO spectral line formation work well for Perseus on ∼0.4 pc scales. Perseus appears to be old enough to achieve chemical equilibrium and the timescale of the dynamical process(es) most revelant for the formation of molecular gas is likely $\gtrsim$ 10 Myr. The good agreement, however, is valid only if the density distribution has a diffuse HI halo component. In the modified W10 model, the halo provides dust

shielding against H_2 and CO dissociation and is essential to reproduce the observed N(HI), R_{H2}, and I_{CO} distribution. While our results indicate the importance of the diffuse HI halo for the distributions of two most abundant molecular species, H_2 and CO, the properties of the halo have not been observationally well constrained. Our future work on a large number of HI absorption spectra obtained toward the HI envelopes of Galatic molecular clouds (Stanimirović et al. in prep) will reveal the physical properties of the halo and eventually be valuable to investigate the role of the halo in the formation and evolution of molecular clouds.

Despite the lack of tuning to match the characteristics of Perseus, the S11 model reproduces the observed N(HI), $N(H_2)$, and I_{CO} properties well. In particular, the predicted range of $N(H_2)$ is in excellent agreement with our data. These results suggest that non-equilibrium chemistry is generally consistent with equilibrium chemistry for low-mass, old molecular clouds such as Perseus. However, there are several interesting discrepancies and they likely result from the nature of turbulence in the S11 model. The strong compressions and rarefactions by turbulence result in the large range of N(HI) and unlike the modified W10 model, there is no minimum N(HI) beyond which the rest of hydrogen is converted into $N(H_2)$. Because of the complex velocity field in the S11 model, gas clumps are not uniformly distributed in velocity space and in combination with missing stellar feedback processes, this results in the smaller Δv and consequently the smaller I_{CO}. In addition, density fluctuations allow the formation of dense clumps even at small A_V and I_{CO} increases with a large scatter in the S11 model. Finally, turbulent motions mix the CO distribution and I_{CO} increases with A_V more gradually. Future studies of a large number of molecular clouds, in particular those clouds much less evolved and/or forming more massive stars (therefore more turbulent) than Perseus, will be important for systemstic tests of the PDR and MHD model.

References

Abdo, A. A., Ackermann, M., Ajello, M., et al. 2010, ApJ, 710, 133

Ballesteros-Peredes, J., Vázquez-Semadeni, E., & Scalo, J. 1999, ApJ, 515, 286

Ballesteros-Peredes, J., & Mac Low, M.-M. 2002, ApJ, 570,‘0i 734

Bally, J., Walawender, J., Johnstone, D., Kirk, H., & Goodman, A. A. 2008, Handbook of Star Forming Regions, Volume I: The Northern Sky, ed. B. Reipurth (ASP Monograph Publications, Vol. 4; San Francisco, CA: ASP), 308

Bell, T. A., Roueff, E., Viti, S., & Williams, D. A. 2006, MNRAS, 371, 1865

Bensch, F. 2006, A&A, 448, 1043

Bevington, P. R. & Robinson, D. K. 2003, Data Reduction and Error Analysis for the Physical Sciences, 3rd ed. (Boston: McGraw-Hill)

Bigiel, F., Leroy, A. K., Walter, F., et al. 2008, AJ, 136, 2846

Bohlin, R. C., Savage, B. D., & Drake, J. F. 1978, ApJ, 224, 132

Bolatto, A. D., Wolfire, M. G., & Leroy, A. K. 2013, arXiv:1301.3498

Boulanger, F., Abergel, A., Bernard, J.-P., et al. 1996, A&A, 312, 256

Černis, K. 1990, Ap&SS, 166, 315

Dalgarno, A. 2006, Proc. Natl. Acad. Sci., 103, 12269

Dame, T. M., Hartmann, D., & Thaddeus, P. 2001, ApJ, 547, 792

Draine, B. T. 1978, ApJS, 36, 595

de Vries, H. W., Thaddeus, P., & Heithausen, A. 1987, ApJ, 319, 723

Feldmann, R., Gnedin, N. Y., & Kravtsov, A. V. 2012a, ApJ, 747, 124

Feldmann, R., Gnedin, N. Y., & Kravtsov, A. V. 2012b, ApJ, 758, 127

Frerking, M. A., Langer, W. D., & Wilson, R. W. 1982, ApJ, 262, 590

Glover, S. C. O., & Mac Low, M.-M. 2007a, ApJS, 169, 239

Glover, S. C. O., & Mac Low, M.-M. 2007b, ApJ, 659, 1317

Glover, S. C. O., Federrath, C., Mac Low, M.-M., & Klessen, R. S. 2010, MNRAS, 404, 2

Glover, S. C. O., & Mac Low, M.-M. 2011, MNRAS, 412, 337

Glover, S. C. O., & Clark, P. C. 2012, MNRAS, 426, 377

González Hernández, J., Iglesias-Groth, S., Rebolo, R., et al. 2009, ApJ, 706, 866

Goodman, A. A., Pineda, J. E., & Schnee, S. L. 2009, ApJ, 692, 91

Gratier, P., Braine, J., Rodriguez-Fernandez, N. J., et al. 2010, A&A, 512, 68

Heiles, C., & Troland, T. 2003, ApJ, 586, 1067

Herbig, G. H., & Jones, B. F. 1983, AJ, 88, 1040

Herbig, G. H. 1998, ApJ, 497, 736

Heyer, M. H., & Brunt, C. M. 2004, ApJ, 615, 45

Hollenbach, D. J., & Tielens, A. G. G. M. 1997, ARA&A, 35, 179

Hollenbach, D. J., Kaufman, M. J., Neufeld, D., Wolfire, M., & Goicoechea, J. R. 2012, ApJ, 754, 105

Imara, N., & Blitz, L. 2011a, ApJ, 732, 78

Imara, N., Bigiel, F., & Blitz, L. 2011b, ApJ, 732, 79

Indriolo, N., & McCall, B. J. 2012, ApJ, 745, 91

Israel, F. P. 1997a, A&A, 317, 65

Israel, F. P. 1997b, A&A, 328, 471

Kainulainen, J., Beuther, H., Henning, T., & Plume, R. 2009, A&A, 508, 35

Knapp, G. R. 1974, AJ, 79, 527

Kaufman, M. J., Wolfire, M. G., Hollenbach, D. J., & Luhman, M. L. 1999, ApJ, 527, 795

Kaufman, M. J., Wolfire, M. G., & Hollenbach, D. J. 2006, ApJ, 644, 283

Kennicutt, R. C. Jr. 1989, ApJ, 344, 685

Kennicutt, R. C. Jr., & Evans, N. J. 2012, ARA&A, 50, 531

Krumholz, M. R., McKee, C. F., & Tumlinson, J. 2009, ApJ, 693, 216 (K09)

Krumholz, M. R., & Gnedin, N. Y. 2011, ApJ, 729, 36

Krumholz, M. R. 2012, ApJ, 759, 9

Lada, C. J., Lombardi, M., & Alves, J. F. 2010, ApJ, 724, 687

Lagos, C., Bayet, E., Baugh, C. M., et al. 2012, MNRAS, 426, 2142

Lazarian, A., Pogosyan, D., Vázquez-Semadeni, E., & Pichardo, B. 2001, ApJ, 555, 130

Lee, M.-Y., Stanimirović, S., Douglas, K. A., et al. 2012, ApJ, 748, 75

Lequeux, J. 2005, The Interstellar Medium (Berlin: Springer)

Le Bourlot, J., Pineau Des Forets, G., Roueff, E., & Flower, D. R. 1993, A&A, 267, 233

Le Petit, F., Nehmé, C., Le Bourlot, J., & Roueff, E. 2006, ApJS, 164, 506

Leroy, A. K., Bolatto, A. D., Stanimirović, S., et al. 2007, ApJ, 658, 1027

Leroy, A. K., Bolatto, A. D., Bot, C., et al. 2009, ApJ, 702, 352

Leroy, A. K., Bolatto, A. D., Gordon, K., et al. 2011, ApJ, 737, 12

Lombardi, M., Alves, J., & Lada, C. J. 2006, A&A, 454, 781

Luhman, K. L., Rieke, G. H., Lada, C. J., & Lada, E. A. 1998, ApJ, 508, 347

Mac Low, M.-M. & Klessen, R. 2004, RvMP, 76, 125

Maloney, P., & Black, J. H. 1988, ApJ, 325, 389

McKee, C. F., & Ostriker, E. C. 2007, ARA&A, 45, 565

Miville-Deschênes, M.-A. & Lagache, G. 2005, ApJS, 157, 302

Muench, A. A., Lada, E. A., Lada, C. J., et al. 2003, AJ, 125, 2029

Narayanan, D., Krumholz, M. R., Ostriker, E. C., & Hernquist, L. 2012, MNRAS, 421, 3127

Nelson, R. P., & Langer, W. D. 1999, ApJ, 524, 923

Norman, M. L. 2000, Rev. Mex. AA Ser. Conf., 9, 66

Ossenkopf, V. 1997, New Astron., 2, 365

Ostriker, E. C., Stone, J., & Gammie, C. F. 2001, ApJ, 546, 980

Papadopoulos, P. P., Thi, W.-F., & Viti, S. 2002, ApJ, 579, 270

Paradis, D., Dobashi, K., Shimoikura, T., et al. 2012, A&A, 543, 103

Peek, J. E. G., Heiles, C., Douglas, K. A., et al. 2011, ApJS, 194, 20

Pineda, J. E., Caselli, P., & Goodman, A. A. 2008, ApJ, 679, 481

Pineda, J. L., Goldsmith, P. F., Chapman, N., et al. 2010, ApJ, 721, 686

Rahman, N., Bolatto, A. D., Xue, R., et al. 2012, 745, 183

Reach, W. T., Koo, B.-C., & Heiles, C. 1994, ApJ, 429, 672

Ridge, N. A., Di Francesco, J., Kirk, H., et al. 2006, AJ, 131, 2921

Rogers, C., Heyer, M. H., & Dewdney, P. E. 1995, ApJ, 442, 694

Sakamoto, S. 1996, ApJ, 462, 215

Rubio, M., Lequeux, J., & Boulanger, F. 1993, A&A, 271, 9

Sakamoto, S. 1999, ApJ, 523, 701

Sancisi, R. Goss, W. M., Anderson, C., Johansson, L. E. B., & Winnberg, A. 1974, A&A, 35, 445

Sandstrom, K. M., Leroy, A. K., Walter, F., et al. 2013, arXiv:1212.1208

Schmidt, M. 1959, ApJ, 129, 243

Schlegel, D. J., Finkbeiner, D. P., & Davis, M. 1998, ApJ, 500, 525

Schruba, A., Leroy, A. K., Walter, F., et al. 2011, AJ, 142, 37

Shetty, R., Glover, S. C., Dullemond, C. P., & Klessen, R. S. 2011a, MNRAS, 412, 1686 (S11)

Shetty, R., Glover, S. C., Dullemond, C. P., et al. 2011b, MNRAS, 415, 3253

Shetty, R., Kelly, B. C., & Bigiel, F. 2013, MNRAS, 430, 288

Smith, P. A., Brand, P. W. J. L., Mountain, C. M., Puxley, P. J., & Nakai, N. 1991, MNRAS, 252, 6

Sobolev, V. V. 1957, SvA, 1, 678

Stone, J. M., & Norman, M. L. 1992, ApJS, 80, 753

Taylor, S. D., Hartquist, T. W., & Williams, D. A. 1993, MNRAS, 264, 929

Tielens, A. G. G. M., & Hollenbach, D. 1985, ApJ, 291, 722

Wannier, P. G., Lichten, S. M., & Morris, M. 1983, ApJ, 268, 727

Wannier, P. G., Lichten, S. M., Andersson, B.-G., & Morris, M. 1991, ApJS, 75, 978

Williams, J. P., & Maddalena, R. J. 1996, ApJ, 464, 247

Wolfire, M. G., Hollenbach, D., & Tielens, A. G. G. M. 1993, ApJ, 402, 195

Wolfire, M. G., McKee, C. F., Hollenbach, D., & Tielens, A. G. G. M. 2003, ApJ, 587, 278

Wolfire, M. G., Tielens, A. G. G. M., Hollenbach, D., & Kaufman, M. J. 2008, ApJ, 680, 384

Wolfire, M. G., Hollenbach, D., & McKee, C. 2010, ApJ, 716, 1191 (W10)

Young, J. S., Goldsmith, P. F., Langer, W. D., Wilson, R. W., & Carlson, E. R. 1982, 261, 513

Chapter 5

Summary and Future Work

5.1 Summary

In this thesis, I have provided observational constraints on the formation of molecular clouds by confronting the latest theoretical models of H_2 and CO formation with high-resolution data of the Perseus molecular cloud in the Galaxy. In addition, I have explored how different galactic environments influence the formation of molecular clouds by investigating the properties of high-extinction regions in the SMC. The summary of each chapter is as follows.

In Chapter 2, I identified 55 high-extinction regions in the SMC by applying the unsharp-masking technique to the 24 μm image obtained with the *Spitzer Space Telescope*. This technique has been used in the Galaxy to search for cold and dense interstellar clouds, particularly infrared dark clouds (IRDCs). I found that those regions identified by high contrast against the diffuse background emission at 24 μm, so called high-contrast regions (HCRs), are mainly distributed on the periphery of CO clouds. The HCRs have a size of $\sim$8–14 pc and a peak contrast of $\sim$2–2.5% at 24 μm, which correpond to relatively large Galactic IRDCs in terms of size but with a factor of $\sim$2–3 smaller peak contrast. With a goal of constraining the physical properties of the HCRs, I performed NH_3, N_2H^+, HNC, HCO^+, and HCN (dense gas tracers, which have been frequently detected in Galactic IRDCs) observations toward one of the HCRs, HCR LIRS36–east, with the Australia Telescope Compact Array and the Mopra telescope. No molecular emission was detected but the upper limits to the column densities of molecular species suggest that the HCRs are most likely moderately dense with $n \sim 10^3$ cm^{-3}. In addition, the HCRs have $\Sigma_{\rm HI} \sim \Sigma_{\rm H2} \sim$ 50–100 M$_\odot$ pc^{-2}, suggesting that the HCRs have a significant amount of H_2 and trace the regions where the interstellar medium transitions from HI- to H_2-dominated. All these results indicate that the HCRs are less dense than Galactic IRDCs and therefore not counterparts of IRDCs in the SMC. However, alternative possibilities, e.g., the HCRs being counterparts of Galactic IRDCs with tiny molecular clumps with a size of $\sim$0.5 pc and/or being the regions with anomalous dust abundances, cannot be completely ruled out with the existing observations.

My investigation clearly demonstrates that galactic environments impact formation of molecular clouds. In the SMC, the interstellar medium appears to transition from HI- to H_2-dominated at $\Sigma_{\rm HI} + \Sigma_{\rm H2}$ $\sim$ 100–200 M$_\odot$ pc^{-2}, which is a factor of $\sim$5–10 larger than what is found in the Galaxy (e.g., Lee et al.

2012). The discrepancy is comparable to the difference in metallicity between the Galaxy and the SMC. This suggests that the formation of molecular clouds in low-metallicity environments requires much larger column density to achieve enough dust shielding against dissociating photons. As being more sensitive to dust shielding than H_2, CO forms in much denser clumps deep inside a molecular cloud, which are embedded in a large "CO-dark" H_2 envelope.

In Chapter 3, I focused on the Perseus molecular cloud in the Galaxy, where available high-resolution data allow me to study the formation of molecular clouds in great detail. In particular, I examined the transition from HI to H_2 across Perseus by deriving the $\Sigma_{\rm HI}$ and $\Sigma_{\rm H2}$ distributions on $\sim$0.4 pc scales. I found a relatively uniform $\Sigma_{\rm HI} \sim 6$–8 $M_\odot$ pc^{-2} and a linear increase of $\Sigma_{\rm H2}/\Sigma_{\rm HI}$ with $\Sigma_{\rm HI} + \Sigma_{\rm H2}$ for both dark and star-forming regions in Perseus, in agreement with theoretical predictions from Krumholz et al. (2009; K09). The K09 model estimates the H_2 abundance in a spherical cloud based on the balance between H_2 formation on dust grains and dissociation by far-ultraviolet photons and predicts a minimum $\Sigma_{\rm HI}$ required to shield H_2 against photodissociation. This minimum $\Sigma_{\rm HI}$ for H_2 formation is inversely proportional to metallicity ($\Sigma_{\rm HI} \sim 10$ $M_\odot$ pc^{-2} for solar metallicity) but interestingly only weakly depends on the strength of a radiation field. Once the minimum $\Sigma_{\rm HI}$ is achieved, all additional $\Sigma_{\rm HI}$ is converted into $\Sigma_{\rm H2}$, resulting in a uniform $\Sigma_{\rm HI}$ distribution and a linear increase of $\Sigma_{\rm H2}/\Sigma_{\rm HI}$ with $\Sigma_{\rm HI} + \Sigma_{\rm H2}$. In addition, I examined the relative distribution of H_2 and CO in Perseus and found that H_2 is more extended than CO by a factor of $\sim$1.4 on average. The fraction of "CO-dark" H_2 was estimated to be $\sim$0.3 and varies across the cloud by a factor of $\sim$3.

Considering that the K09 model is intended primarily to predict H_2 distributions in galaxies on $\sim$kpc scales and does not take into account any dynamical processes (e.g., spiral arms, stellar feedback, interstellar turbulence), the excellent agreement with the observational data of Perseus on $\sim$0.4 pc scales is surprising. This suggests that H_2 formation in Perseus can be described by the "classical" model, where molecular clouds are long-lived and the chemical and dynamical evolution of gas are not strongly coupled, so that molecular abundances can be calculated under the steady state and equilibrium approximation. The agreement with the K09 model holds for both dark and star-forming regions, indicating that internal radiation fields do not affect H_2 formation if embedded stars are not of early spectral types (later than B3 V, in the case of Perseus).

In Chapter 4, I investigated the relation between H_2 and CO in Perseus in depth by deriving the

distribution of the "CO-to-H_2 conversion factor" or "X-factor" on ∼0.4 pc scales. I found that Perseus has a median X_{CO} of $\sim 2.8 \times 10^{19}$ cm^{-2} K^{-1} km^{-1} s and X_{CO} varies by up to a factor of ∼100 within individual dark and star-forming regions. While showing large spatial variations, X_{CO} has a characteristic dependence on A_V: X_{CO} sharply decreases at $A_V \lesssim 3$ mag and gradually increases at $A_V \gtrsim 3$ mag. This dependence is primarily due to the sensitivity of I_{CO} to A_V and the transition from decreasing to increasing X_{CO} occurs where I_{CO} becomes optically thick and saturates to ∼50–80 K km s^{-1} in Perseus. In an attempt to further evaluate the previous conclusion that the chemical model based on the steady state and equilibrium approximation describes H_2 formation in Perseus, I then compared the measured N(HI), $N(H_2)$, I_{CO}, and X_{CO} with two contrasting models of H_2 and CO formation: (1) a one-dimensional photodissociation region (PDR) model originally developed by Tielens & Hollenbach (1985) and modified by several authors including Wolfire et al. (2010; W10), and (2) a three-dimensional magnetohydrodynamic (MHD) model by Shetty et al. (2011; S11). I found that the modified W10 model successfully reproduces the HI, H_2, and CO distributions in Perseus but requires a density distribution with a large diffuse halo. The S11 model generally matches the data as well, while showing several systematic discrepancies: a broader range of N(HI), a smaller I_{CO}, and a more gradual increase of I_{CO} with A_V along with a large scatter. Both models predict the X_{CO} vs A_V profile whose shape is in agreement with what is found in Perseus.

My study clearly shows that X_{CO} can vary over two orders of magnitude on sub-parsec scales. In addition to the characteristic dependence on A_V, changes in density, radiation field, and/or non-thermal gas motion can result in the variations in X_{CO}. Such high variability of X_{CO} observed in Perseus urges caution about adopting a single X_{CO} for a system that has a wide range of physical parameters. In addition, the fact that the median $X_{CO} \sim 2.8 \times 10^{19}$ cm^{-2} K^{-1} km^{-1} s in Perseus is a factor of ∼6 smaller than the canonical $X_{CO} \sim 1.8 \times 10^{20}$ cm^{-2} K^{-1} km^{-1} s in the Galaxy (e.g., Dame et al. 2001; Lombardi et al. 2006; Pineda et al. 2008; Abdo et al. 2010; Paradis et al. 2012) stresses the importance of high-resolution HI data for deriving the dust-to-gas ratio and the molecular hydrogen column density. Finally, the good agreement with the PDR model (W10) suggests the validity of steady state and equilibrium chemistry for CO, as well as H_2 in Perseus. Considering that the MHD model (S11) reproduces the estimated $N(H_2)$ and N(CO) reasonably well, time-dependent effects on H_2 and CO formation appear not to be significant for low-mass, old molecular clouds such as Perseus. However, the discrepancies in N(HI) and I_{CO}, which likely result from the highly complex spatial and kinematic structure of the gas in the MHD model, call for

further investigations.

5.2 Future Work

While providing important constraints on the formation of molecular clouds, this thesis poses several interesting questions and I plan to address them in the future work.

(1) *Effect of high optical depth HI*: The uniform $\Sigma_{\rm HI} \sim 6$–$8\ {\rm M}_\odot\ {\rm pc}^{-2}$ across Perseus could alternatively be due to the presence of high optical depth HI. To assess the effect of high optical depth HI in Perseus, I have been working on the estimation of optical depth corrections using the HI absorption line data that were obtained with the Arecibo telecope toward ∼30 compact radio sources located behind Perseus. This work is still in progress but the preliminary results suggest that the $\Sigma_{\rm HI}$ distribution increases by a factor of ∼1.4 on average but is still relatively uniform (Stanimirović, Lee et al. in prep).

(2) *Physical properties of the diffuse HI halo*: One of the main findings in this thesis is the importance of the diffuse HI halo for H_2 and CO formation in Perseus. I plan to examine the physical properties of the diffuse HI halo by utilizing the HI absorption, OH, and [CII] data of Perseus. The Arecibo HI absorption line data will provide fundamental parameters of the halo, e.g., HI spin temperature, number density, sonic Mach number, ratio of the cold neutral medium (CNM) to the warm neutral medium (WNM). In addition, the OH and [CII] emission line data (obtained with the Green Bank Telescope in 2009 and with the *Herschel Space Observatory* in 2012 respectively) will allow me to revisit the discrepancies in N(HI) and $I_{\rm CO}$ that were pronounced for diffuse regions in the S11 model and provide further constraints on the MHD model (both line transitions are good tracers of diffuse gas).

(3) *The formation of molecular gas in different interstellar environments*: Finally, with a goal of understanding the formation of molecular gas in different interstellar environments, I plan to extend my analyses of Perseus to other molecular clouds in the Galaxy and the Magellanic Clouds (the LMC and the SMC). To achieve this goal, I will first choose a substantial number of molecular clouds that cover a wide range physical parameters such as metallicity, radiation field, stellar feedback, and cloud evolutionary stage. I will then measure the $\Sigma_{\rm HI}$ distribution across each selected molecular cloud using both HI emission and absorption data. HI absorption line observations of 9 Galactic molecular clouds are already in progress (5 with the Arecibo telescope and 4 with the Karl G. Jansky Very Large Array) and the existing HI emission data (e.g., the GALFA-HI and Effelsberg-Bonn HI surveys) can be used for those clouds. For the molecular

clouds in the Magellanic Clouds, I will make use of HI emission and absorption data from the GASKAP survey, which is scheduled to begin this year. The measured $\Sigma_{\rm HI}$ distributions will be then compared with the K09 model. The analyses I plan to do with Perseus using the *Herschel* [CII] data can be also done for the selected molecular clouds using publicly available *Herschel* or SOFIA data.

References

Abdo, A. A., Ackermann, M., Ajello, M., et al. 2010, ApJ, 710, 133

Dame, T. M., Hartmann, D., & Thaddeus, P. 2001, ApJ, 547, 792

Krumholz, M. R., McKee, C. F., & Tumlinson, J. 2009, ApJ, 693, 216 (K09)

Lee, M.-Y., Stanimirović, S., Douglas, K. A., et al. 2012, ApJ, 748, 75

Lombardi, M., Alves, J., & Lada, C. J. 2006, A&A, 454, 781

Paradis, D., Dobashi, K., Shimoikura, T., et al. 2012, A&A, 543, 103

Pineda, J. E., Caselli, P., & Goodman, A. A. 2008, ApJ, 679, 481

Shetty, R., Glover, S. C., Dullemond, C. P., & Klessen, R. S. 2011, MNRAS, 412, 1686 (S11)

Tielens, A. G. G. M., & Hollenbach, D. 1985, ApJ, 291, 722

Wolfire, M. G., Hollenbach, D., & McKee, C. 2010, ApJ, 716, 1191 (W10)